Growth and Characterisation of ZnO Nanostructures: Excitonic Properties and Morphology

By

Mahua Biswas
School of Physical Sciences
Dublin City University

A thesis submitted for the degree of

Doctor of Philosophy

to

Research Supervisor

Dr. Enda McGlynn

April 2010

Declaration

I hereby certify that this material, which I now submit for assessment on the programme of study leading to the award of Ph.D is entirely my own work, that I have exercised reasonable care to ensure that the work is original, and does not to the best of my knowledge breach any law of copyright, and has not been taken from the work of others save and to the extent that such work has been cited and acknowledged within the text of my work.

Signed: _____ ID No.: 56114354

Date: _____

Acknowledgement

This is a wonderful opportunity for me to acknowledge the people without whom it would not have been possible to complete my doctoral degree. Truly, words are not enough to express my gratitude to all of them.

First of all, I would like to express my deepest appreciation to my supervisor Dr. Enda McGlynn. I was very fortunate to have such a wonderful person as my Ph.D supervisor. Many thanks for your support, encouragement and raising my confidence up. This thesis would not have been possible without your help, support and patience. Your guidance and advices have been invaluable to me on both academic and personal level.

My heartfelt thanks to my senior colleagues Dr. Justina Grabowska, Dr. James Fryer and Dr. R. T. Rajendrakumar for their time and knowledge to introduce me to the world of “ZnO” and teach experimental techniques. A special thanks to Mr. Daragh Byrne for helping me with the thesis corrections and for providing samples. I am grateful to Prof. Martin Henry and Prof. Greg Hughes for their supports and advices during my Ph.D. I am thankful to Prof. Daniel Le Si Dang, Prof. Hong Koo Kim and Dr. Simon Newcomb for providing their experimental facilities and valuable discussion. Thanks to my group members Mr. Kumar Kumarappan, Mr. Barry Foy and Mr. Connor McLoughlin for their co-ordination and helps. I would like to take the opportunity to thank Ms. Lisa Peyton, Mr. Des Lavelle, Mr. Mike Aughey, Mr. Alan Hughes, Mr. Ray Murphy in physics department and Ms. Veronica Dobbyn in chemistry department for their help. I deeply thank Mr. Pat Wogan for his many many assistances during my Ph.D and helping me in my experimental setup.

Thanks to Science Foundation Ireland, the NCPST and the School of Physical Sciences for the financial support and facilities.

I owe my uncle Dr. Bhajan Biswas, who gave me the motivation for pursuing Ph.D. I am indebted to my aunty Ms. Rita Baidya and my cousins Barshan and Sayan for their invaluable love and support in an important stage of my life. I would like to acknowledge the love of all my family members including my sister-in-law Gouri. I

am fortunate to have Jaydip Neogi as my true friend. Many thanks to my friends Shantanu, Arundhati, Rani, Sukanta and Gopali to share all of my sadness and laughter during my stay at Dublin.

To my parents, my elder brother Shantanu and my husband Uttam, all I can say is, this small space is not enough to acknowledge your contributions up to this stage of my life. Many thanks to Uttam for encouraging and criticising me throughout my Ph.D, and for being my great support. Thanks to my brother for supporting me and showing faith on me. And to my parents I just want to say, it was your dream which made my journey up to this possible. Lastly, my love and gratitude to my grandmother for her priceless love and company, and thanks for all your lovely fighting.

To my

Grandmother....

Abstract

The growth mechanism of aligned ZnO nanostructures, grown by the vapour phase transport (VPT) growth method, specifically with nanorod and nanowall morphologies has been studied. The thesis begins with an introductory chapter on ZnO nanostructures and related topics, and the second chapter introduces the various experimental techniques used. The main thesis work involves five distinct studies. Firstly, the conditions to grow nanorod and nanorod/nanowall structures on sapphire using a ZnO/graphite powder mixture as a growth source are studied and the optimum conditions for each morphology identified. Secondly, the effects on ZnO nanostructure growth on sapphire of using activated carbon and carbon black powders, rather than graphite powder are studied. Nanostructures can be grown at significantly lower temperatures with carbon black and activated carbon, though with different morphologies, compared to graphite. Thirdly, low temperature cathodoluminescence spectroscopy measurements of ZnO nanostructures grown on Si substrate are presented. These data show significant inhomogeneity in the spatial distribution of emission throughout the sample for the Al-related donor bound exciton emission at 3.3605 eV and the Al-related emissions are compared to the other spectral features seen for these samples. The possible origin of this inhomogeneity is discussed. Fourthly, the microscopic origin of a unique photoluminescence peak at ~3.367 eV, which is known as surface exciton peak, has been studied in detail and its behaviour is studied after samples have been subjected to various post-growth treatments such as plasma treatment, UV exposure in vacuum and exposure to high voltages. Finally, post-growth passivation of nanostructures has been done using PVP and HF on ZnO nanostructure samples. The effects of these chemicals on the optical emission from these samples are studied and the potential for these to act as effective passivation agents is discussed. The thesis concludes with a summary of the work done, some general conclusions and comments on possible future directions.

Contents

List of Acronyms

AE	Auger Electrons
BE	Bound Exciton
BET	Braunauer–Emmett–Teller
BSE	Back Scattered Electrons
CB	Conduction Band
CBD	Chemical bath deposition
CL	Cathodoluminescence
CL-SEM	Cathodoluminescence Scanning Electron Microscopy
CTR	Carbothermal Reduction
CTR-VPT	Carbothermal Reduction-Vapour Phase Transport
CVD	Chemical Vapour Deposition
DBE	Donor Bound Exciton
EDX	Energy Dispersive X-ray
e-h	Electron-Hole
FE	Free exciton
FESEM	Field Emission Scanning Electron Microscopy
FT	Fourier Transform
HTSA	High Total Surface Area
ICP-RIE	Inductively Coupled Plasma Reactive Ion Etching
LD	Laser Diode
LED	Light Emitting Diode
LTSA	Low Total Surface Area
MBE	Molecular Beam Epitaxy
MEMS	Microelectromechanical system
MOCVD	Metal Organic Chemical Vapour deposition
MPS	Methacryloxypropyl-trimethoxysilane
M-PL	Macro-Photoluminescence
MWNT	Multi Walled Nano Tube
NR	Non-Radiative
PL	Photoluminescence

PLD	Pulsed Laser Deposition
PVP	Polyvinylpyrrolidone
RF	Radio Frequency
SAED	Selected Area Electron Diffraction
SC	Specimen Current
SE	Secondary Electrons
SEM	Scanning Electron Microscopy
SSA	Specific Surface Area
STM	Scanning Tunnelling Microscopy
SWNT	Single walled Nano Tube
SX	Surface Exciton
TE	Transmitted Electrons
TEM	Transmission Electron Microscopy
TSA	Total Surface Area
UV	Ultraviolet
VB	Valence Band
VLS	Vapour - Liquid – Solid
VPT	Vapour Phase transport
VS	Vapour Solid
XRD	X-ray Diffraction
XPS	X-ray Photoelectron Spectroscopy
μ-PL	Micro-Photoluminescence

List of Figures

The captions listed here are not full captions but concise ones.

List of Tables

List of Publications

1. R. T. Rajendra Kumar, E. McGlynn, **M. Biswas**, R. Saunders, G. Trolliard, B. Soulestin, J. R. Duclere, J. P. Mosnier, M. O. Henry, "*Growth of ZnO nanostructures on Au-coated Si: Influence of growth temperature on growth mechanism and morphology*", **Journal of Applied Physics**, 104, 084309, (2008).
2. **M. Biswas**, E. McGlynn, M. O. Henry, "*Carbothermal reduction growth of ZnO nanostructures on sapphire – comparisons between graphite and activated charcoal powders*", **Microelectronics Journal,** 40, 259, (2009).
3. **M. Biswas**, E. McGlynn, M. O. Henry, M. McCann, A. Rafferty, "*Carbothermal reduction vapour phase transport growth of ZnO nanostructures: Effects of various carbon sources*", **Journal of Applied Physics**, 105, 094306, (2009).
4. **Mahua Biswas**, Ho-Sang Kwack, Le Si Dang, Martin O. Henry, Enda McGlynn, "*Spatial inhomogeneity of donor bound exciton emission from ZnO nanostructures grown on Si*", **Nanotechnology**, 20, 255703, (2009).
5. R. B. Saunders, E. McGlynn, **M. Biswas**, M. O. Henry, "*Thermodynamic aspects of the gas atmosphere and growth mechanism in carbothermal vapour phase transport synthesis of ZnO nanostructures*", **Thin Solid Films**, in press.
6. D. Byrne, E. McGlynn, K. Kumar, **M. Biswas**, M.O. Henry, G. Hughes, "*A study of drop-coated and chemical bath-deposited buffer layers for vapour phase deposition of large area, aligned, zinc oxide nanorod arrays*", accepted in **Crystal Growth and Design**.
7. Susanta Kumar Das, **Mahua Biswas**, Daragh Byrne, Martin Bock, Enda McGlynn, Markus Breusing, Ruediger Grunwald, "*Multiphoton-absorption induced UV luminescence of ZnO nanorods irradiated by few-nJ broadband fs-pulses of a Ti:sapphire laser oscillator*", submitted in **Journal of Applied Physics**.
8. **M. Biswas**, E. McGlynn , Y. S. Jung, H. K. Kim, K. Kumarrappan, G. Hughes, S. Newcomb, M. Henry, "*Microscopic origin of the surface exciton peak at 3.367 eV of ZnO nanostructures*", **Manuscript in preparation**.

List of Presentations

1. K. Kumar, G. Hughes, **M. Biswas**, B. Doggett, J-P. Mosnier and E. McGlynn, "XPS study of ZnO single crystal, thin film and nanorod", **European Conference on Surface and Interface Analysis,** Brussels, Belgium, 9^{th} – 14^{th} September 2007.

2. **M. Biswas**, E. McGlynn and M. O. Henry, "Carbothermal reduction growth of ZnO nanostructures on sapphire – comparisons between graphite and activated charcoal powders", Presented as a Poster at EMRS conference, **EMRS spring meeting 2008**, Strasbourg, France, 26^{th} – 30^{th} May 2008.

3. R. B. Saunders, E. McGlynn, **M. Biswas** and M. O. Henry, "Thermodynamic aspects of the gas atmosphere and growth mechanism in carbothermal vapour phase transport synthesis of ZnO nanostructures", Presented as a Poster at EMRS conference, **EMRS spring meeting 2009**, Strasbourg, France, 8^{th} – 12^{th} June 2009.

4. S. K. Das, M. Bock, **M. Biswas**, E. McGlynn, and R. Grunwald, "Strong Multiphoton-Absorption-Induced UV Luminescence from ZnO nanorod Arrays Grown by Vapour-Liquid-Solid Mechanism", Presented as a poster at CLEO Europe conference, **CLEO Europe-EQEC 2009**, Munich, Germany, 14^{th} -19^{th} June 2009.

Chapter 1

Introduction

In this chapter the general background of the thesis topics are discussed, including the basic properties of zinc oxide (ZnO) as a semiconductor and more specific background information on ZnO nanostructure growth. The various advantages and applications of nanostructured ZnO are also introduced.

1.1 General Background

Since the invention of the semiconductor transistor in 1947 by scientists at Bell Laboratories, the semiconductor industry has developed at an incredible pace. Fabrication of faster, smaller, and more powerful devices while manufacturing in larger volume with lower cost is advancing continually to the present day. Despite the first transistor being manufactured from germanium (Ge) due to its relative ease of processing, silicon (Si) has since come to a dominant position in the global semiconductor industry in fields such as communications, data storage and computing. The vast expansion in the Si based semiconductor industry is due to its exceptional material properties and compatibility with conventional processing. However, the performance of Si devices may be approaching their limit due to the material's physical properties, including its energy bandgap, type and the apparent impossibility of dramatic future developments in power devices (for e.g. switched mode power supply). Perhaps most importantly, Si (with its indirect bandgap) is a

very unsuitable material for optoelectronic devices, where a direct bandgap is needed for efficient optical emission (so that less probable three body transitions including crystal momentum-conserving phonons are not required in band to band transitions). At present a number of semiconductors are considered more suitable than Si for optical applications. Among these, gallium arsenide (GaAs), a direct bandgap semiconductor with superior electron transport properties and many suitable optical properties, is the most studied for this purpose and other applications. GaAs has a higher carrier mobility and higher effective carrier velocity than Si, which leads to faster devices [1]. These properties make GaAs (and related materials such as InGaAs and AlGaAs) very suitable for high speed integrated circuits and optoelectronic applications such as laser diodes and light emitting diodes (LEDs). However with its many advantages, GaAs and related III-V materials do not possess all the properties required for the range of desired applications including high power devices, high temperature electronics, and blue / ultraviolet (UV) light emitters. Hence research has continued over the past four decades to investigate other materials which exhibit the required properties for these applications, i.e. larger (direct) bandgaps, high electron mobility and higher breakdown field strengths for optoelectronic devices and high power, high temperature electronics. Among the many materials investigated, wide (direct) bandgap semiconductors are of particular interest.

ZnO has a very interesting and broad-ranging history in various applications. ZnO is and has been used extensively as a pigment in paints and enamel coatings and as an ingredient in cements, glass, tires, glue, matches, white ink, reagents, photocopy paper, flame retardant, fungicides, cosmetics and dental cements with ~ 100,000 tonnes of ZnO being produced per annum, as reported by Klingshirn [2]. These diverse applications rely on various properties of ZnO such as the white colour of the material, its chemical activity, UV absorption capability, thermal conductivity and bioactivity.

Apart from the above mentioned commercial usages, ZnO can also be considered as an ‘old’ semiconductor which has attracted research attention for a long time for many applications in scientific and industrial fields. The first demonstration of the

semiconducting properties of ZnO was performed in the 1920s. A thin copper wire (known as “cat’s whisker”) was used as a contact on sensitive spots on ZnO crystals. The metal/semiconductor junction allows current flow in only one direction and converts the incoming waves from alternating current to direct current in a radio circuit [3]. As this example demonstrates it is not a newly discovered material and research has been in progress for many decades now. Synthesis and characterization of ZnO has been reported from as early as 1935 [4]. Recent improvements in the growth of high quality, single crystalline ZnO, in bulk and epitaxial forms have renewed interest in ZnO. Originally research efforts in ZnO growth were made for GaN epitaxy. From about the 1960s on, synthesis of ZnO thin films has been an attractive field because of the strong potential for applications such as sensors, transducers and catalyst. Nanostructures of ZnO have attracted huge attention in recent times due to their potential technological applications and advantages [5-10]. From 1940s it has been known that ZnO can be grown in the form of nanostructures under variety of growth conditions [2, 11-13]. In the last few decades, especially since the United States of America led the initiative of nanotechnology, low dimensional material study became the leading edge in nanoscience and nanotechnology. The work of Look and his colleagues played a major role in the renewed interest on ZnO, as discussed by Klingshirn [2]. They organized the ‘First Zinc Oxide Workshop’ in 1999 that brought a great deal of new work and ideas on ZnO from different research communities together. At present, the interest in this material is at a peak. It is recognized as one of the most promising materials for applications related to optoelectronics in the blue and UV range due to its wide (direct) bandgap, promising physical and optical properties [14-16]. As the name implies, a ‘wide bandgap’ semiconductor is one having a relatively large bandgap energy (forbidden bandgap), typically 3 eV or greater. This in turn is directly applicable to the potential uses of such materials as blue/UV optical emitting devices and as constituents in various visible optical emitting devices. During the 1990s research activities in the field of wide bandgap semiconductors increased dramatically following the first successful operation of blue LEDs using nitride-based materials and the opening up of potential application areas which are beginning to be realised in e.g. Blu-Ray disc systems etc.

Zinc oxide (ZnO) and gallium nitride (GaN) are two wide band gap semiconductors which are very suitable for a range of (opto) electronic applications. GaN and ZnO can be used for many of the same applications, as some of the properties of these two materials overlap for optoelectronic applications; however ZnO has some distinct advantages over GaN–

i) Exciton binding energy of ~60 meV [17] which is much larger than that of GaN (~21-25 meV) [18], means the free exciton is stable at 300 K .
ii) Large size single crystal substrates are available [19, 20].
iii) Wet chemical processing is possible, and is compatible with Si technology [21].
iv) It has a greater resistance to radiation damage [22].
v) It is biocompatible [23].
vi) It has a lower power threshold for optical pumping and lasing [21, 24].

The large excitonic binding energy of ~60 meV makes ZnO more attractive for optoelectronic application than GaN because the higher exciton binding energy increases the exciton stability. The higher exciton binding energy enhances the luminescence efficiency by increasing the probability of radiative recombination. ZnO has gained substantial interest in the research community because of this higher exciton binding energy which may lead e.g. to lasing action based on exciton recombination at or even above room temperature.

ZnO also shows good potential for applications in a diverse range of other areas, including spintronic devices [25], biomedical sciences [23] and sensor applications [26-28]. It shows promise for space and nuclear applications, due to higher radiative resistance [21, 29]. ZnO can also be used as a material for piezoelectric transducers [30], varistors [31], phosphors [32] and transparent conducting films [33]. For these later applications mostly polycrystalline material is suitable, however for light-emitting devices and other high-end electronic devices single crystal thin films or other high crystal quality morphologies are required. More recently extensive research on nanostructured ZnO has made this material even more attractive for various applications. The reduction in size introduces novel electrical, mechanical, chemical and optical properties, which are believed to be due to surface and quantum

confinement effects in addition to major improvements in crystal quality for growth on lattice-mismatched substrates due to the smaller nanostructure "footprint" compared to thin films. Low dimensional nanostructures of ZnO may improve the efficiency and compactness of electronic and photonic devices including LEDs, optical waveguides and sensors. The structural, electrical, mechanical, chemical and optical properties of such devices have already been improved by the reduced size of ZnO nanostructures. The technological fields where ZnO nanostructures are highly promising for application are summarized in section 1.6.

While ZnO has already many industrial applications due to its piezoelectric properties and bandgap in the near UV range, its use in optoelectronic based devices has not been successful yet because of the unavailability of proper and reliable *p*-type epitaxial layer. In general, it is difficult to obtain *p*-type doping in wide bandgap semiconductors. There have been a significant number of reports regarding *p*-type conductivity of ZnO using various growth methods and group-V dopant elements like N [34], P [35], As [36] and Sb [37] but a reliable and reproducible technique producing high quality *p*-type conductivity has not yet been achieved. It remains one of the most dominant topics in the ZnO community, with a large proportion of the research efforts being directed towards solving this problem. In order to overcome this issue a clear understanding of some ZnO physical processes is necessary. In spite of many decades' research, some basic properties have remained unclear. These include-

i) The nature of the residual *n*-type conductivity in undoped ZnO film, whether it is due to impurities of native defect, or defects.
ii) The mode of incorporation of potential *p*-type dopants either group I or V and complexing.
iii) The presence of autocompensation.

Although *p*-type doping is difficult to achieve, the advantages of ZnO are being utilized by other alternative methods like heteroepitaxy. Here *p*-*n* heterostructures can be realised by using *n*-type ZnO and a second *p*-type material, while still utilizing ZnO as an active layer. Progress has been made in this area. For example, high-intensity UV emission has been observed from the *n*-ZnO/*p*-AlGaN

heterojunction in which ZnO served as the active layer [38]. Another attractive potential ZnO application is in devices where homoepitaxy is sufficient. One example of this is field emission devices.

Apart from the difficulty in achieving *p*-type conductivity for all types of ZnO materials (bulk, thin film and nanostructures), the reproducible growth of nanostructures is also an issue which is a concern for many researchers in this field. From the discussions at a variety of international meetings and conferences by several authors (including recent EMRS meetings, Photonics West, EU SOXESS meetings and others), it is widely acknowledged in the community that the morphology of ZnO nanostructures is highly sensitive to the growth environment (i.e. parameters such as temperature, pressure, and substrate choice and gas flow). This sensitivity makes it very difficult to control the growth process to a sufficient degree to achieve large area uniform growth and to obtain a specific desired morphology reproducibly. In general it has proven very difficult to take a published growth recipe from one laboratory and reproduce the results using the same conditions in another laboratory. However, certain growth techniques such as metal organic chemical vapour deposition (MOCVD) (discussed in section 1.4.2 below) show a greater degree of reproducibility than others in this respect [5]. To control growth sufficiently to synthesize a single desired nanostructure morphology reproducibly and uniformly over a large area substrate will be one of the key challenges facing the ZnO research community in the coming years.

This thesis presents the results of research work on ZnO nanostructure growth and characterisation, concentrating specifically on ZnO nanorod and nanowall systems on sapphire and Si substrates. The growth mechanisms of aligned ZnO nanostructures on sapphire which has already been investigated by other workers in our group have been investigated further. The growth technique used in our laboratory is the vapour phase transport (VPT) method and our investigations centre almost exclusively on material grown by this technique. The morphological, structural and optical properties of nanostructures on various substrates, grown with various source materials have been studied.

The thesis consists of eight chapters. In broad outline, the first part of the thesis experimental results deals with the growth mechanism of ZnO nanostructures and the effects of various growth parameters, and the later parts of the thesis experimental results deal with the characterisation (and control) of various physical properties of ZnO nanostructures.

Chapter 1 introduces the general background, material properties, nanostructure growth issues and applications of ZnO. The treatment will of necessity be a selective summary rather than a comprehensive review given the volume of published material on ZnO nanostructures in the literature[*].

Chapter 2 describes the basic concepts of the experimental techniques employed during the course of the research work and specifically how those techniques are used to study ZnO nanostructures. The experimental methods used in this thesis work include

(a) Growth

i) The VPT system

(b) Characterization

i) The Fourier Transform (FT) low temperature photoluminescence (PL) spectroscopy system,
ii) The X-ray diffractometer (XRD)
iii) Various scanning electron microscopy (SEM) systems including field emission systems and
iv) The low temperature cathodoluminescence (CL) spectroscopy system.

Other measurements such as transmission electron microscopy (TEM) and x-ray photoelectron spectroscopy (XPS) have been facilitated by collaborators and some results are included in later chapters. The details of such systems are not discussed in chapter 2 but are summarised in the relevant chapter where the data appears.

[*]Recorded return by the search on keywords “ZnO” is 33,795, by “zinc oxide” 21,137, by “ZnO and nano*” 11,154 and “zinc oxide and nano*” 5,430 in the ISI Web of Science (conducted on 12th January 2010).

Chapter 3 describes the growth mechanism of aligned ZnO nanostructures and more specifically the control of nanostructure morphology to vary between the so-called nanorod and nanorod/nanowall morphologies on *a*-plane sapphire substrates.

In chapter 4, the effects of different carbon source powders (a carbon/ZnO powder mixture is used as the source material in our VPT system – a carbothermal reduction of the ZnO by the carbon yields a Zn vapour source) on nanostructure growth and morphology is described.

Chapter 5 presents a low temperature CL study of ZnO nanostructures on different substrates with the purpose of studying the distribution of (mainly unintentional) dopants within the nanostructures.

In chapter 6 the so-called surface exciton (SX) peak observed in the low temperature PL spectrum of some ZnO nanostructures is studied in detail. The origin of this peak is being studied by several research groups worldwide but with no definitive answer as yet. The microscopic origin of this peak and methods to influence the peak intensity have been investigated since this surface-related peak is often correlated with a rapid decay of overall PL intensity with increasing temperature.

In chapter 7 the effects of various post growth passivation techniques on PL from ZnO nanostructures is reported. These passivation techniques are studied with the hope of improving the optical quality i.e. the luminescence intensity of nanostructures, by minimizing non-radiative recombination.

Finally, chapter 8 contains a summary of the research work performed, some general conclusions and comments on possible future directions.

1.2 Overview of ZnO material properties

1.2.1 Crystal structure of ZnO

The crystal structure of most of the group-II-VI binary compound semiconductors are either the cubic zinc-blende or hexagonal wurtzite structures where each anion is surrounded by four cations forming a tetrahedron and *vice versa*. The tetrahedral coordination implies sp^3 hybridised covalent bonding, though in all cases there is partial ionicity in the bonds as well. The group II-VI semiconductor ZnO is no exception, and it has an ionicity in between covalent and ionic semiconductors, in the region where tetrahedral coordination is expected [39]. At ambient pressure and temperature, ZnO crystallizes in the wurtzite (B4 type) structure as shown in *Fig 1.1 (a)*. Although this is the most stable phase at room temperature and atmospheric pressure, two other allotropic crystal structures are possible under certain conditions. These are (i) rocksalt (B1 type) and (ii) zinc-blende (B3 type) as shown in *Fig 1.1 (b)* and *(c)*, respectively. Most of the II-VI materials, such as ZnS, ZnTe, and ZnSe are stable thermally with zincblende phases, while the II-VI oxide materials crystallize in the rocksalt (MgO and CdO) and wurtzite (ZnO and BeO) phases. For ZnO the zinc-blende structure is stable only for growth on cubic substrates [40], whereas the rocksalt structure is the stable phase only at high pressures (~ 9-10 GPa) which also is a metastable phase when the pressure is lowered [41, 42]. In the present work (and the majority of the work in the ZnO community), conducted at or below atmospheric pressures, the crystal structure of material grown is always the wurtzite structure and thus we will give a brief description of the ZnO wurtzite structure only.

The lattice parameters of the hexagonal unit cell are *a* and *c*. In an ideal wurtzite crystal, the axial ratio *c/a* and the u parameter (which is the measure of the amount by which each atom is displaced with respect to the next atom along the *c*-axis.) are correlated by the relationship $uc/a = (3/8)^{1/2}$, where $c/a = (8/3)^{1/2} = 1.6329$, and $u = 3/8 = 0.375$. The wurtzite ZnO crystal deviates slightly from both of these ideal values. Experimentally, it has been shown that the experimental values of *u* and *c/a* for ZnO lie in the range $u = 0.3817\text{-}0.3856$ and $c/a = 1.593\text{-}1.6035$, respectively [43-45].

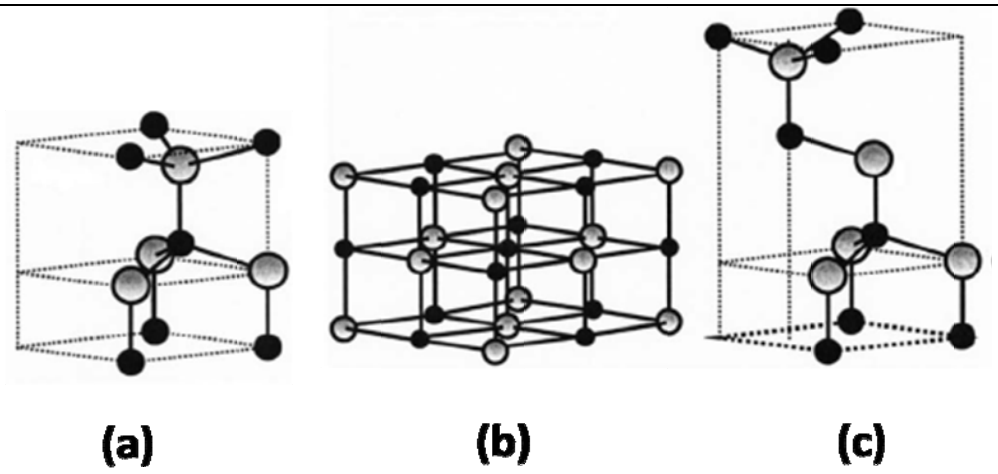

Fig 1.1: (a) The hexagonal wurtzite structure (b) cubic rocksalt (c) zinc-blende phases of ZnO. The shaded gray, and black spheres denote Zn and O atoms, respectively [24].

The tetrahedronal structure gives rise to polar symmetry along the hexagonal axis. This polarity is responsible for number of properties like piezoelectricity, spontaneous polarization and is also a key factor during crystal growth and defect generation. The lack of a centre of symmetry in the wurtzite structure combined with large electromechanical coupling results in strong piezoelectric and pyroelectric properties. Consequently ZnO has been used in mechanical actuators and piezoelectric sensors. The commonly observed face terminations of wurtzite ZnO are (surface energies in parenthesis)-

Basal crystal faces-

i) Polar Zn terminated (0001) (*c*-axis oriented)
(Surface energy 1.6 J/m^2)

ii) Polar O terminated (000-1) (*c*-axis oriented)
(Surface energy 1.6 J/m^2)

Prismatic crystal faces-

iii) Non-polar (11-20) (*a*-axis oriented)
(Surface energy 2.0 J/m^2)

iv) Non-polar (10-10) (*m*-axis oriented)
(Surface energy 3.4 J/m^2)

Mixed faces-

v) Mix-polar (11-21) (*r*-axis oriented)
(No reported surface energy value found)

Each face displays different chemical activity and stability, and the surface energies vary considerably [46-48], as given in the list above [48].

Recently, new developments have been reported in theoretical studies of ZnO thin film growth and nanowire stress loading. It has been predicted by theoretical studies that during the initial nucleation of ZnO films, the wurtzite film may grow as a non-polar graphitic structure which fixes the *c*-axis orientation [49, 50]. During the next stage of growth, transition to the wurtzite structure proceeds with a low or zero energy barrier. These theoretical predictions have been recently validated by surface XRD and scanning tunnelling microscopy (STM) by Tusche *et al.* [51]. According to the prediction by Kulkarni *et al.* wurtzite to graphitic transformation should occur under unaxial tensile loading of ~10 GPa in (01-10) oriented nanowires [52]. This new phase of ZnO will be of interest to understand the nucleation and growth of nanostructures and aspects of their behaviour under stress.

1.2.2 Electronic bandstructure

The electronic band structure of a semiconductor is crucial to determining the material's potential technological usefulness. The band structure gives the electronic one-particle (i.e. electron or hole) states. Zinc oxide is a wide bandgap semiconductor material with band gap energy of ~ 3.3 eV at room temperature [24].

ZnO is a direct bandgap semiconductor having the uppermost valence and the lowest conduction bands (VB and CB, respectively) at the same point in the Brillouin zone (i. e. at the Γ-point), namely at K=0 (K is the crystal momentum).

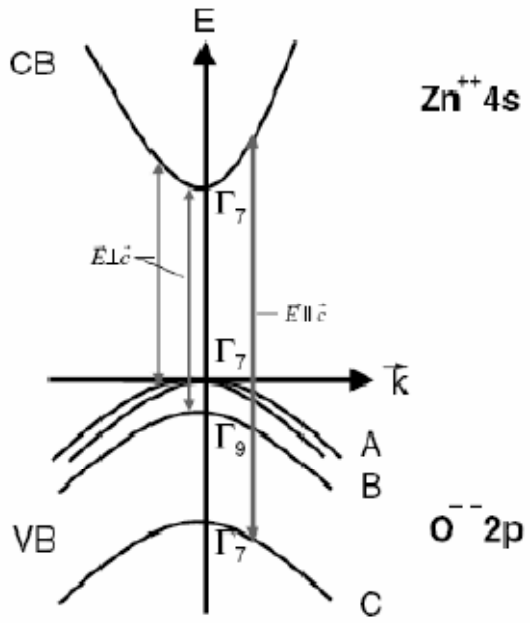

Fig 1.2: The valence band (VB) and conduction band (CB) of ZnO in the vicinity of fundamental bandgap [53].

In the Brillouin zone centre, the bottom of the CB is formed from the empty 4s states of Zn^{2+} , while the top of the valence band is formed from the occupied 2p states of O^{2-}. The group theoretical compatibility tables [54] show that the bottom of the CB has Γ_1 symmetry without involvement of spin, and symmetry $\Gamma_1 \otimes \Gamma_7 = \Gamma_7$ with spin. Without spin the VB is split into two states Γ_1 and Γ_5 under the influence of the hexagonal crystal field. And incorporation of spin gives a further splitting into three twofold-degenerated sub-VBs of symmetries $(\Gamma_1 \oplus \Gamma_5) \otimes \Gamma_7 = \Gamma_7 \oplus \Gamma_9 \oplus \Gamma_7$ (*Fig 1.2*). These VBs are labelled from highest to lowest energies as A, B and C bands. The energies of the three bandgaps correlated with the VBs A, B and C are 3.445, 3.448 and 3.487 eV, respectively, at 4.2 K [55]. There is a continual debate about the ordering of the VBs, whether it is of the "normal" form ($A\Gamma_9$, $B\Gamma_7$, $C\Gamma_7$) [56] or if it is $A\Gamma_7$, $B\Gamma_9$, $C\Gamma_7$, so called "negative spin-orbit splitting" or inverted ordering of the top two VB compared to most other wurtzite semiconductors [57, 58]. In 1966 Park *et al.* assigned the ordering as $A\Gamma_9$, $B\Gamma_7$, $C\Gamma_7$ but erroneously identified the intrinsic A exciton reflectance and PL features as an extrinsic ionized donor bound exciton feature [59]. Despite the majority of research groups supporting the initial

conclusions by Hopfield and Thomas for the inverted ordering [57, 58], including direct evidence from Rowe *et al.* in 1968 [60], the controversy continues with both theoretical and experimental papers being published recently by Reynolds *et al.* (1999) [17], and Gil (2001) [61] in favour of the "normal" ordering, i.e. $A\Gamma_9$, $B\Gamma_7$, $C\Gamma_7$ ordering.

1.3 ZnO Nanostructures: General issues

ZnO shows a huge variety of nanostructure morphologies compared e.g. to GaN. A wide variety of nanostructures such as nanobelts [62], nanorod arrays [63], nanocombs [64], nanorings [65], nanoneedles [66] have been demonstrated and grown by various research groups working in the area of ZnO nanostructure growth.

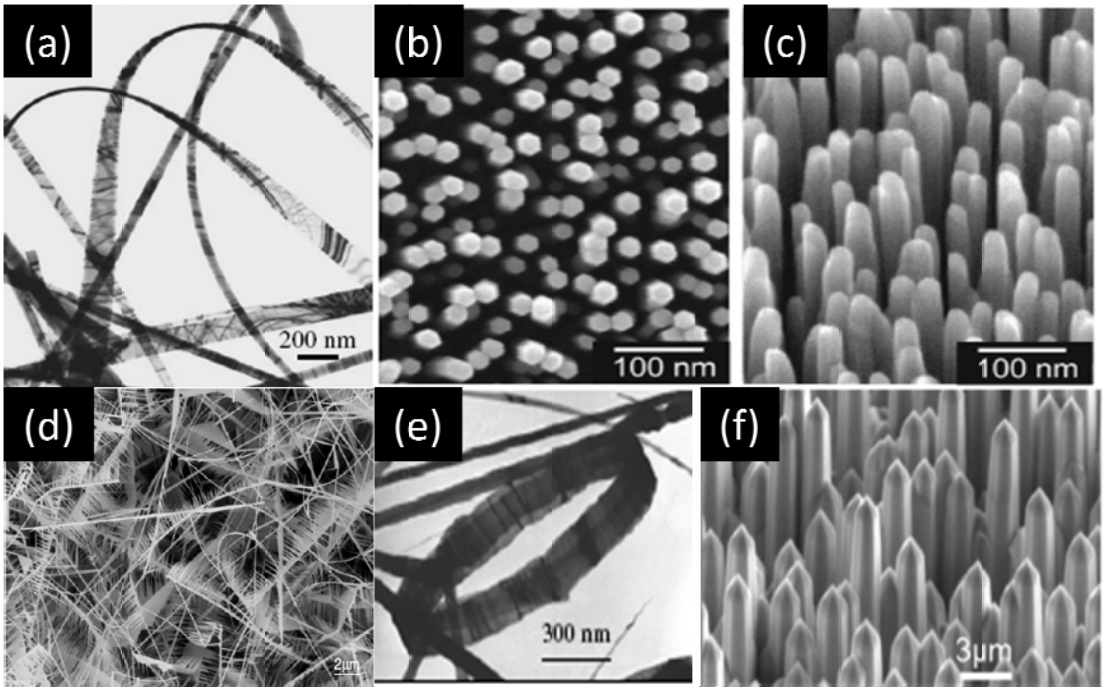

Fig 1.3: TEM/SEM images of ZnO nanostructures from the published literature including: (a) nanobelt from Z. W. Pan *et al.* [62], (b) and (c) nanorod array from W. I. Park *et al.* [63], (d) nanocomb from Z. L Wang *et al.* [64], (e) nanoring from X. Y. Kong *et al.* [65], (f) nanoneedle from M. Lorenz *et al.* [66].

As mentioned in section 1.1, the fabrication of ZnO nanostructures in an effective, scalable and controllable way remains the most challenging issue for current researchers. Consequently significant efforts in the last few years have been made in controlling nanostructure deposition and improving crystal quality of the grown structures. Nanolithographic techniques such as e-beam writing, proximal probe patterning and x-ray lithography have been used to fabricate uniform ZnO nanostructure arrays [67, 68]. However these techniques are limited by the need for sophisticated manipulation methods, expensive and slow preparation and procedures, due to their serial nature. For nanoscale electronic and optoelectronic devices, it is very important that the growth of nanostructures is repeatable and cost effective. This suggests that self-assembly techniques may offer substantial advantages over conventional processing techniques. The epitaxial orientation relationship between ZnO nanorods and certain substrate causes well-aligned growth perpendicular to the surface. Using this relationship, aligned nanostructures can be grown on suitable substrates using self assembly techniques. This can be combined with area-selective growth on metal catalysts or other seed/buffer layers to achieve a degree of positional control in addition to alignment. One example of this self assembly approach is the use of epitaxially matched *a*-plane sapphire with Au coating as a substrate to grow well-aligned nanorods. Usually in ZnO growth, the fastest growth rate is observed along the *c*-axis, which results in nanorod/nanowire type structures. By controlling the growth kinetics, it is possible to modify the growth behavior. Recently most of the research work on growth is concentrated on growing uniform and controllable nanostructures with various growth conditions i.e. changing various parameter of growth using various techniques [69, 70].

Among the various ZnO nanostructures, nanorod- and nanowall-like structures have potential for use in high performance device and may be key material morphologies for future nanotechnology devices [24, 71]. For example, recently a report of room temperature lasing action of a highly oriented ZnO nanorod arrays has demonstrated that the design of ZnO nanomaterials in a highly oriented and ordered manner is of crucial importance for such devices [72]. Their most useful features include their high aspect ratio (length/diameter) and excellent crystal quality.

1.4 Various growth methods for ZnO nanostructures

To date a great deal of the research on ZnO nanostructures has focused on synthesis in addition to characterization. There are a large variety of growth mechanisms of one-dimensional ZnO nanostructures. The large surface area to volume ratio and other characteristics make these nanostructures very attractive for sensing and biomedical applications as discussed earlier. The most notable methods which have been used for nanostructure growth include-

i) Chemical Vapour Deposition (CVD) [6]
ii) Molecular Beam Epitaxy (MBE) [7]
iii) Chemical solution Method [73, 74]
iv) Vapour Phase Transport (VPT) [10]

These are summarized below-

1.4.1 Chemical Vapour Deposition (CVD)

CVD is a process based on pyrolitic reactions. The precursor compound, usually an organic-based compound, used in CVD systems has reasonable vapour pressures and low melting points. A carrier gas transports the vapour of the reacting species i.e. the precursor to the substrate. The reaction then proceeds on the substrate surface which is heated to the growth temperature. There are several modifications of this method depending on the nature of the precursors used, for example metal organic (MO) systems used in MOCVD or halide CVD where $ZnCl_2$ is used as precursor. MOCVD is the most widely used method among all the CVD processes. MOCVD is different from conventional CVD in its choice of MO precursors as the reactant species. These MOs have only one dangling bond and can be easily converted into chemical vapours. This allows the use of a lower deposition temperature. MOCVD methods have been widely used for epitaxial film growth. It is less commonly used however for one-dimensional nanostructures growth [75]. For well aligned nanorod deposition lattice matched substrates are necessary for this technique. Using MOCVD nanorods

can be grown at low temperatures ~400^{o}C compared to VPT growth. Some of the advantages of CVD techniques are chemical and thermodynamic dependent growth, control at the atomic level, large area deposition capabilities and high growth rates. The need for metallic catalysts or buffer layers is negated in MOCVD method, and hence the use of MOCVD reduces the amount of unintentional impurities like metallic species that are often incorporated into the nanostructures during VPT growth (where gold is often used as a catalyst). Despite these advantages, the CVD deposition process is complicated by the introduction of controlled chemical vapour concentration, and incorporation of large amounts of impurities within the nanostructures grown which is detrimental for devices. The system configuration of a CVD setup makes it costlier than VPT and it is quite complex to control the chamber pressure with accurate masses or partial pressure of reactant and carrier gases. In addition toxic and corrosive gases are produced as waste.

1.4.2 Molecular Beam Epitaxy (MBE)

MBE is a widely used thin film deposition technique involving the reaction of one or more thermal beams of atoms or molecules with a crystalline surface in an ultrahigh vacuum (~10^{-8} Pa) [76]. MBE allows delicate control of atomic level deposition and dopant species. Gas phase MBE has been used to grow ZnO nanorods and nanowires [77]. During MBE depositions, site-selective catalyst driven growth is also possible. The ability to synthesize nanorods at arbitrary locations at moderate temperatures is possible and makes this technique excellent for nano-device integration. During this process the background base pressure should be low and well controlled and for ZnO growth an oxygen/ozone mixture is required as oxidising source. This requirement for ozone makes the system expensive to operate, in addition to the high costs associated with the ultra-high vacuum (UHV) operation.

1.4.3 Chemical solution method

In the chemical solution method of growth, aqueous solutions of zinc compounds are used at low temperature. In this method, the notable advantage is that the nanostructure can be grown at very low temperatures, even below 100^{o}C. This is an

encouraging feature for large scale low cost ZnO nanomaterial synthesis and for growth on diverse substrates such as plastics [74]. Ordered nanorod arrays can be grown even on lattice mismatched Si substrates. Prior to growth, a ZnO thin film generally has to be deposited for aligned growth to occur. Also the crystal quality of the nanostructures is not good (as determined by e.g. bound exciton linewidths in low temperature PL) compared to high temperature evaporation methods. To utilize ZnO nanostructures in devices it is very important that the crystal quality is good which in turn will generate a higher optical emission signal.

1.4.4 Vapour Phase Transport (VPT)

In the VPT method, Zn vapour is generated by various methods, generally at high temperatures and transported to the substrate by a carrier gas, which enables ZnO nanostructure growth. The main advantage of this method is its compatibility with the vapour-liquid-solid (VLS) mechanism for the growth of well-aligned ZnO nanostructures on specific areas of a substrate where a catalyst has been deposited. In this method a very simple setup can be used with a normal high temperature furnace. No pressure control is required.

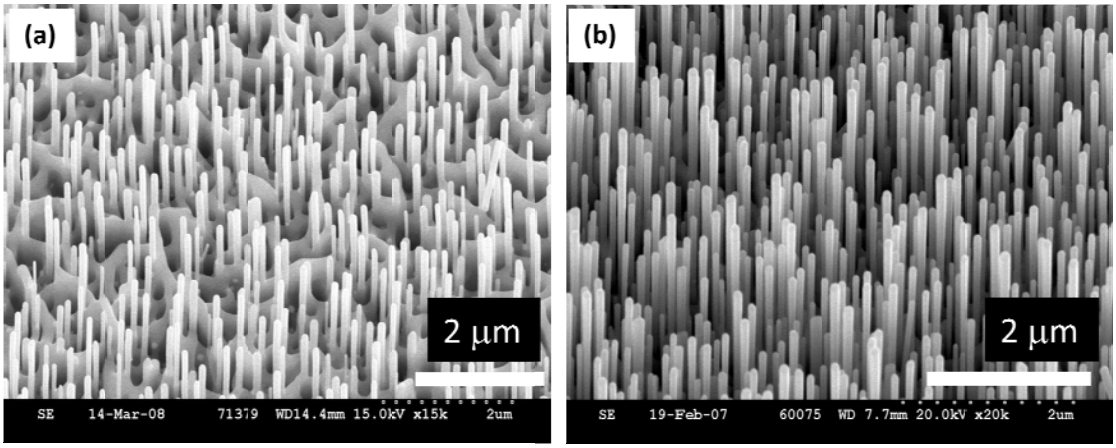

Fig 1.4: ZnO nanostructures grown by VPT/VLS on *a*-plane sapphire (a) nanorod/nanowall (900^{o}C) (b) nanorod structures (950^{o}C).

One disadvantage of this technique is the relatively high temperature necessary compared to methods such as MOCVD, CVD and chemical solution growth. This

disadvantage is offset by the fact that the crystal quality and luminescence efficiency of ZnO depositions are excellent compared to most of the other techniques. As the VLS method is catalyst driven, selective area growth of nanostructures is possible. To reduce the cost and complexity for mass production, a lower temperature growth method with excellent reproducibility is highly desirable. If a lower temperature growth is possible using the VPT method then this technique may prove to be very useful for applications that require high quality depositions. This is discussed in chapter 4 of this thesis.

Among the various growth techniques, VPT is one of the most widely adopted methods. This is probably due to the simplicity of the required facilities. The alternative lower cost solution based methods which are also technically simple are not promising because of poorer crystal quality. The disadvantages of the other methods are described above.

For this reason in this thesis, nanostructure deposition is performed using a VPT method. Various studies of parameter variation during VPT growth in order to control the deposit morphology and properties are studied as part of this work in chapter 3 and 4.

1.5 Properties of ZnO nanostructures; Specific motivations of this work

Apart from research concerning the growth methods and mechanisms of nanostructures, there is also significant amount of research being undertaken to understand the properties of ZnO nanostructures. To make these structures effective for future optoelectronic applications it is necessary to understand the optical and electrical properties, particularly the surface-related phenomena, properly. In this thesis, in addition to the growth methods, the optical properties of ZnO nanostructures have been mainly studied.

As discussed above in section 1.1, doping of ZnO, both *n*- and *p*-type is a heavily studied area, with important applications in transparent conducting oxides and bipolar light emitting devices. The as-grown ZnO has always been found to be *n*-type. *p*-type doping is an extensively studied area to achieve controllable and repeatable *p*-type conductivity. To utilize ZnO in bipolar devices, it is very important to overcome this problem. Doping of ZnO nanostructures is in an early stage but some attempts have already been reported [78, 79]. The properties and distribution of donors within ZnO thin films and nanostructures is also another important issue. Usually in as-grown ZnO, a range of *n*-type dopants can be observed due to Al, Ga and In contamination. For ZnO bulk crystals, a range of sharp peaks in the UV photoluminescence spectrum have already been observed by several authors, which have been labeled as the I_0 to I_{11} peaks [80]. From previous luminescence studies of ZnO crystals, the I_6, I_8 and I_9 lines are known to correspond to the previously mentioned dopants, respectively. We have measured the distribution of these dopants in ZnO nanostructures including their emission peak energy using low temperature CL-SEM. This CL study of dopant distributions in as-grown ZnO nanostructures is discussed in chapter 5.

The surface properties of ZnO bulk material have already been reported by several groups [81, 82]. ZnO has been effectively used as a gas sensor material based on the near-surface modification of charge carrier distributions with certain surface-absorbed species [83]. ZnO nanorods will provide significant enhancement in sensitivity due to their high surface-to-volume ratio. ZnO is also piezoelectric and is used in surface acoustic wave devices [84]. These measurements have often concentrated on electrical properties of the surface and their alteration following application of different processing conditions. To use ZnO nanostructures in devices, it is very important to know the geometry of the surface. It is also important to understand the microscopic origins of the optical and electrical properties. Two of the more effective morphologies to study near surface region optical properties are nanorods and nanorod/nanowall structures. As stated earlier the optical and electrical properties of nanoscale devices are often dominated by surface-related phenomena due to its large surface-to-volume ratio. This large ratio may have advantages in certain applications, but also can lead to e.g. surface quenching of luminescence, and

deterioration in the optical properties of nanostructures. This is particularly evident at room temperature.

Among the range of surface effects which can affect the ZnO nanostructure electrical properties, chemisorptions of oxygen is known to be important [85]. The adsorbed oxygen leads to charge transfer from the oxygen to the ZnO or *vice versa*. This phenomena alters the local Fermi level position in the ZnO relative to the bands, i.e. effectively acting as a dopant defect at the surface. Therefore the chemisorption of oxygen may have a substantial effect on the optical properties of ZnO. PL studies on ZnO nanostructures allow these effects to be observed. In the PL study of the nanorod/nanowall system, one surface related peak at ~3.367 eV has already been reported [86-88]. This peak is referred as a "surface exciton" (SX) peak. It has been confirmed that it associated with ZnO nanorod/nanowall morphology at low temperatures [86]. At higher temperatures (above ~ 25 K) this peak vanishes and it is a unique low temperature optical feature of this ZnO nanosystems. In bulk ZnO crystals it has not been observed. The peak observed at low temperatures may be responsible for the rapid decay of luminescence as the temperature increases. However, the microscopic origin of this peak is not known as yet. It has previously been assumed that this peak could be due to the chemisorption of oxygen at ZnO surfaces. Recent experiments are presented in chapter 6 of this thesis show that it may not be due to the adsorption of oxygen on the surface. A detailed study of this issue is presented in chapter 6.

Another surface related effect on optical properties of ZnO nanostructures is non-radiative (NR) surface recombination, which can strongly reduce the radiative efficiency, especially at room temperature. To utilize ZnO nanostructures in devices, it is essential that the luminescent efficiency is high at room temperature as the UV light emitting devices operate at room temperature. To overcome this problem some research has already been performed on ZnO nanoparticles [89, 90], nanocrystalline film [91] and quantum dots [92, 93]. Relatively few works have been published on ZnO nanostructures [94]. Most of these works have been focused on pre-growth passivation. To establish some methods to overcome the NR recombination after growth is an important and useful avenue of research. The attempt to find effective

post-growth passivation techniques is another significant part of this thesis and the finding are presented in chapter 7.

1.6 Summary of applications of ZnO nanostructures

Some useful applications of nanostructured ZnO have already been highlighted in section 1.1 and 1.5 while discussing the importance of this material. A number of attempts have been taken to utilize ZnO nanostructures in some technological areas, while in others it is believed that it has immense potential. Some of these applications are summarized below–

i) It is hoped that ZnO nanostructures will form an important component in next generation optoelectronic devices, such as light emitting diodes (LEDs) [16], laser diodes (LDs) [15].

ii) Nanosensors fabricated from ZnO with a larger surface-to-volume ratio have better characteristics than thin films [24, 95], and have the additional advantage of being insensitive to visible light. Visible blind UV sensor have a wide range of applications in military and non-military arenas that include missile plume detection for hostile missile tracking, flame sensors, UV source monitoring and calibration [95], in biological sensing and space communication [96, 97]. One major factor which stimulates the development of new UV photodetectors is the growing 'ozone hole' near the Antarctic linked to an increasing number of cancer and other skin conditions. ZnO nanostructures are also potential candidates for use as chemical sensors for detection of O_2 [98], toxic and flammable gases such as NO_2, NH_3 [28].

iii) Nanostructures of ZnO have already been used for Field Effect Transistors [99, 100].

iv) Thermoelectric performance can be improved using nanostructured ZnO. Reducing the object size cause radical changes in phonon modes and phonon densities of states change, resulting in unusual thermal transport phenomena in mesoscopic systems [8].

v) Cantilever based scanning probe microscopy (SPM) techniques are one of the most powerful approaches in imaging, manipulating and measuring nanoscale properties and phenomena. It has been reported that combining microelectromechanical system (MEMS) technology with self-assembled ZnO nanostructures leads to cost effective nanocantilevers with heightened sensitivity for a range of devices and applications [101]. The electric field induced mechanical resonance in ZnO nanobelt structures additionally makes it useful to use as a nanoresonator [102].

1.7 References

[1] C. Y. Chang and F. Kai, *GaAs High Speed Devices Physics Technology and Circuit Applications*, John Wiley & Sons, Inc., USA, Pg. 1, 1994.

[2] C. Klingshirn, Physica Status Solidi B-Basic Solid State Physics 244 (2007) 3027.

[3] C. Jagadish and S. J. Pearton, *Zinc Oxide Bulk, Thin Films and Nanostructures*, Elsevier Ltd., 2006.

[4] C. W. Bunn, Proceedings of the Physical Society London 47 (1935) 835.

[5] W. I. Park, D. H. Kim, S. W. Jung, and G.-C. Yi, Applied Physics Letters 80 (2002) 4232.

[6] J.-J. Wu and S. C. Liu, Advanced Materials 14 (2002) 215.

[7] Y. W. Heo, D. P. Norton, L. C. Tien, Y. Kwon, B. S. Kang, F. Ren, S. J. Pearton, and J. R. LaRoche, Materials Science and Engineering: R: Reports 47 (2004) 1.

[8] Z. L. Wang, Journal of Physics: Condensed Matter 18 (2004) R829.

[9] Z. L. Wang, Materials Today 7 (2004) 26.

[10] Z. W. Pan, S. M. Mahurin, S. Dai, and D. H. Lowndes, Nano Letters 5 (2005) 723.

[11] M. L. Fuller, Journal of Applied Physics 15 (1944) 164.

[12] Y. S. Park and D. C. Reynolds, Journal of Applied Physics 38 (1967) 756.

[13] E. Scharowsky, Zeitschrift Fur Physik 135 (1953) 318.

[14] A. Osinsky, J. W. Dong, M. Z. Kauser, B. Hertog, A. M. Dabiran, P. P. Chow, S. J. Pearton, O. Lopatiuk, and L. Chernyak, Applied Physics Letters 85 (2004) 4272.

[15] W. Yang, R. D. Vispute, S. Choopun, R. P. Sharma, T. Venkatesan, and H. Shen, Applied Physics Letters 78 (2001) 2787.

[16] A. Tsukazaki, A. Ohtomo, T. Onuma, M. Ohtani, T. Makino, M. Sumiya, K. Ohtani, S. F. Chichibu, S. Fuke, Y. Segawa, H. Ohno, H. Koinuma, and M. Kawasaki, Nat Mater 4 (2005) 42.

[17] D. C. Reynolds, D. C. Look, B. Jogai, C. W. Litton, G. Cantwell, and W. C. Harsch, Physical Review B 60 (1999) 2340.

[18] R. Dingle, Stokowsk.Se, P. J. Dean, and Zetterst.Rb, Physical Review B 3 (1971) 497.

[19] E. Ohshima, H. Ogino, I. Niikura, K. Maeda, M. Sato, M. Ito, and T. Fukuda, Journal of Crystal Growth 260 (2004) 166.

[20] J. M. Ntep, S. S. Hassani, A. Lusson, A. Tromson-Carli, D. Ballutaud, G. Didier, and R. Triboulet, Journal of Crystal Growth 207 (1999) 30.

[21] D. C. Look, Materials Science and Engineering B 80 (2001) 383.

[22] D. C. Look and D. C. Reynolds, Applied Physics Letters 75 (1999) 811.

[23] J. Zhou, N. S. Xu, and Z. L. Wang, Advanced Materials 18 (2006) 2432.

[24] U. Ozgur, Y. I. Alivov, C. Liu, A. Teke, M. A. Reshchikov, S. Dogan, V. Avrutin, S. J. Cho, and H. Morkoc, Journal of Applied Physics 98 (2005) 041301.

[25] S. Pearton, D. Norton, Y. Heo, L. Tien, M. Ivill, Y. Li, B. Kang, F. Ren, J. Kelly, and A. Hebard, Journal of Electronic Materials 35 (2006) 862.

[26] J. Xu, Q. Pan, Y. a. Shun, and Z. Tian, Sensors and Actuators B: Chemical 66 (2000) 277.

[27] X. Wang, J. Zhou, Song, J. Liu, N. Xu, and Z. L. Wang, Nano Letters 6 (2006) 2768.

[28] Z. Fan and J. G. Lu, Applied Physics Letters 86 (2005) 123510.

[29] M. Razeghi and A. Rogalski, Journal of Applied Physics 79 (1996) 7433.

[30] N. K. Zayer, R. Greef, K. Rogers, A. J. C. Grellier, and C. N. Pannell, Thin Solid Films 352 (1999) 179.

[31] K. Eda, Electrical Insulation Magazine, IEEE 5 (1989) 28.

[32] B. S. Jeon, J. S. Yoo, and J. D. Lee, Journal of the Electrochemical Society 143 (1996) 3923.

[33] H. Kim, C. M. Gilmore, J. S. Horwitz, A. Pique, H. Murata, G. P. Kushto, R. Schlaf, Z. H. Kafafi, and D. B. Chrisey, Applied Physics Letters 76 (2000) 259.

[34] K. Minegishi, Y. Koiwai, Y. Kikuchi, K. Yano, M. Kasuga, and A. Shimizu, Japanese Journal of Applied Physics Part 2-Letters 36 (1997) L1453.

[35] K. K. Kim, H. S. Kim, D. K. Hwang, J. H. Lim, and S. J. Park, Applied Physics Letters 83 (2003) 63.

[36] Y. R. Ryu, S. Zhu, D. C. Look, J. M. Wrobel, H. M. Jeong, and H. W. White, Journal of Crystal Growth 216 (2000) 330.

[37] T. Aoki, Y. Shimizu, A. Miyake, A. Nakamura, Y. Nakanishi, and Y. Hatanaka, physica status solidi (b) 229 (2002) 911.

[38] Y. I. Alivov, E. V. Kalinina, A. E. Cherenkov, D. C. Look, B. M. Ataev, A. K. Omaev, M. V. Chukichev, and D. M. Bagnall, Applied Physics Letters 83 (2003) 4719.

[39] J. C. Phillips, Reviews of Modern Physics 42 (1970) 317.

[40] A. Ashrafi and C. Jagadish, Journal of Applied Physics 102 (2007) 071101.

[41] J. E. Jaffe and A. C. Hess, Physical Review B 48 (1993) 7903.

[42] H. Liu, J. S. Tse, and H.-k. Mao, Journal of Applied Physics 100 (2006) 093509.

[43] L. Gerward and J. S. Olsen, Journal of Synchroton Radiation 2 (1995) 233.

[44] J. E. Jaffe and A. C. Hess, Physical Review B 48 (1993) 7903.

[45] E. H. Kisi and M. M. Elcombe, Acta Crystallographica C45 (1989) 1867.

[46] O. Dulub, L. A. Boatner, and U. Diebold, Surface Science 519 (2002) 201.

[47] B. Meyer and D. Marx, Physical Review B 67 (2003) 035403.

[48] N. Fujimura, T. Nishihara, S. Goto, J. F. Xu, and T. Ito, Journal of Crystal Growth 130 (1993) 269.

[49] C. L. Freeman, F. Claeyssens, N. L. Allan, and J. H. Harding, Physical Review Letters 96 (2006) 4.

[50] F. Claeyssens, C. L. Freeman, N. L. Allan, Y. Sun, M. N. R. Ashfold, and J. H. Harding, Journal of Materials Chemistry 15 (2005) 139.

[51] C. Tusche, H. L. Meyerheim, and J. Kirschner, Physical Review Letters 99 (2007) 4.

[52] A. J. Kulkarni, M. Zhou, K. Sarasamak, and S. Limpijumnong, Physical Review Letters 97 (2006) 4.

[53] C. Klingshirn, ChemPhysChem 8 (2007) 782.

[54] C. Klingshim, *Semiconductor Optics*, 3rd ed., Springer, Heidelberg, 2006.

[55] U. Rossler, *Landolt-Börnstein Numerical Data and Functional Relationships in Science and Technology, Semiconductors B: II-VI and I-VII Compounds,*, Springer-Verlag, Berlin and Heidelberg (on CD-ROM). 1999.

[56] D. C. Reynolds, C. W. Litton, and T. C. Collins, Physical Review 140 (1965) A1726.

[57] J. J. Hopfield and D. G. Thomas, Journal of Physics and Chemistry of Solids 12 (1960) 276.

[58] D. G. Thomas, Journal of Physics and Chemistry of Solids 15 (1960) 86.

[59] Y. S. Park, C. W. Litton, T. C. Collins, and D. C. Reynolds, Physical Review 143 (1966) 512.

[60] J. E. Rowe, M. Cardona, and F. H. Pollak, Solid State Communications 6 (1968) 239.

[61] B. Gil, Physical Review B 64 (2001) 201310.

[62] Z. W. Pan, Z. R. Dai, and Z. L. Wang, Science 291 (2001) 1947.

[63] W. I. Park, D. H. Kim, S. W. Jung, and G.-C. Yi, Applied Physics Letters 80 (2002) 4232.

[64] Z. L. Wang, X. Y. Kong, and J. M. Zuo, Physical Review Letters 91 (2003) 185502.

[65] X. Y. Kong, Y. Ding, R. Yang, and Z. L. Wang, Science 303 (2004) 1348.

[66] M. Lorenz, E. M. Kaidashev, A. Rahm, T. Nobis, J. Lenzner, G. Wagner, D. Spemann, H. Hochmuth, and M. Grundmann, Applied Physics Letters 86 (2005) 143113.

[67] T. Martensson, P. Carlberg, M. Borgstrom, L. Montelius, W. Seifert, and L. Samuelson, Nano Letters 4 (2004) 699.

[68] H. T. Ng, J. Han, T. Yamada, P. Nguyen, Y. P. Chen, and M. Meyyappan, Nano Letters 4 (2004) 1247.

[69] J. Grabowska, K. K. Nanda, E. McGlynn, J. P. Mosnier, and M. O. Henry, Surface and Coatings Technology 200 (2005) 1093.

[70] J. Grabowska, A. Meaney, K. K. Nanda, E. McGlynn, J. P. Monsnier, and M. O. Henry, in Opto-Ireland 2005: Nanotechnology and Nanophotonics, Vol. 5824, SPIE, Dublin, Ireland, 2005, p. 269.

[71] W. L. Hughes and Z. L. Wang, Journal of Americal Chemical Society 126 (2004) 6703.

[72] M. Huang, S. Mao, H. Feick, H. Yan, Y. Wu, H. Kind, E. Weber, R.Russo, and P. Yang, Science 292 (2001) 1897.

[73] Y.-J. Kim, C.-H. Lee, Y. J. Hong, G.-C. Yi, S. S. Kim, and H. Cheong, Applied Physics Letters 89 (2006) 163128.

[74] L. Vayssieres, Advanced Materials 15 (2003) 464.

[75] M. Yazawa, M. Koguchi, A. Muto, M. Ozawa, and K. Hiruma, Applied Physics Letters 61 (1992) 2051.

[76] T. Steiner, *Semiconductor Nanostructure for Optoelectronic Applicationss*, Artech House Inc., Norwood, MA, 2004.

[77] Y. W. Heo, M. Kaufman, K. Pruessner, D. P. Norton, F. Ren, M. F. Chisholm, and P. H. Fleming, Solid State Electronics 47 (2002) 2269.

[78] B. Q. Cao, M. Lorenz, A. Rahm, H. v. Wenckstern, C. Czekalla, J. Lenzner, G. Benndorf, and M. Grundmann, Nanotechnology (2007) 455707.

[79] M. Yan, H. T. Zhang, E. J. Widjaja, and R. P. H. Chang, Journal of Applied Physics 94 (2003) 5240.

[80] B. K. Meyer, H. Alves, D. M. Hofmann, W. Kriegseis, D. Forster, F. Bertram, J. Christen, A. Hoffmann, M. Straßburg, M. Dworzak, U. Haboeck, and A. V. Rodina, Physica Status Solidi (b) 241 (2004) 231.

[81] R. K. Swank, Physical Review 153 (1967) 844.

[82] R. J. Collins and D. G. Thomas, Physical Review 112 (1958) 388.

[83] W. P. Kang and C. K. Kim, Sensors and Actuators B 13/14 (1993) 682.

[84] F. C. M. V. d. Pol, Ceram. Bull. 69 (1990) 1959.

[85] J. Lagowski, J. E. S. Sproles, and H. C. Gatos, Journal of Applied Physics 48 (1977) 3566.

[86] J. Grabowska, A. Meaney, K. K. Nanda, J. P. Mosnier, M. O. Henry, J. R. Duclere, and E. McGlynn, Physical Review B 71 (2005) 115439.

[87] S. Savikhin, A. Freiberg, and V. V. Travnikov, JETP Letter 50 (1989) 122.

[88] V. V. Travnikov, A. Freiberg, and S. F. Savikhin, Journal of Luminescence 47 (1990) 107.

[89] L. Guo, S. Yang, C. Yang, P. Yu, J. Wang, W. Ge, and G. K. L. Wong, Applied Physics Letters 76 (2000) 2901.

[90] W. Feng, H. C. Tao, Y. Liu, and Y. C. Liu, Journal of Materials Science & Technology 22 (2006) 230.

[91] H. Y. Xu, Y. C. Liu, R. Mu, C. L. Shao, Y. M. Lu, D. Z. Shen, and X. W. Fan, Applied Physics Letters 86 (2005) 123107.

[92] C. L. Yang, J. N. Wang, W. K. Ge, L. Guo, S. H. Yang, and D. Z. Shen, Journal of Applied Physics 90 (2001) 4489.

[93] X. H. Li, C. L. Shao, Y. C. Liu, X. Y. Chu, C. H. Wang, and B. X. Zhang, Journal of Chemical Physics 129 (2008) 114708.

[94] J.-H. Choi, D.-Y. Khang, and J.-M. Myoung, Solid State Communications 148 (2008) 126.

[95] S. Hullavarad, N. Hullavarad, P. Karulkar, A. Luykx, and P. Valdivia, Nanoscale Research Letters 2 (2007) 161.

[96] H. K. Yadav, K. Sreenivas, and V. Gupta, Applied Physics Letters 90 (2007) 172113.

[97] L. Oleg, C. Lee, C. Guangyu, C. Leonid, L.-T. Olena, and H. Helge, physica status solidi (a) 205 (2008) 2673.

[98] Z. Fan, D. Wang, P.-C. Chang, W.-Y. Tseng, and J. G. Lu, Applied Physics Letters 85 (2004) 5923.

[99] P.-C. Chang and J. G. Lu, IEEE transactions on electron devices 55 (2008) 2977.

[100] M. S. Arnold, P. Avouris, Z. W. Pan, and Z. L. Wang, Journal of Physical Chemistry B 107 (2003) 659.

[101] W. L. Hughes and Z. L. Wang, Applied Physics Letters 82 (2003) 2886.

[102] X. Bai, E. G. Wang, P. Gao, and Z. L. Wang, Nano Letters 3 (2003) 1147.

Chapter 2

Experimental techniques

In this chapter, the details of the experimental techniques used to grow reproducible, good crystalline ZnO nanostructures and to study the physical, structural and optical properties of these nanostructures are discussed. These include (i) The Vapour Phase Transport (VPT) growth method using the Vapour-Liquid-Solid (VLS) and Vapour-Solid (VS) mechanism for ZnO nanostructures synthesis, (ii) Low temperature Fourier Transform Photoluminescence Spectroscopy (FT-PL), (iii) X-ray Diffraction (XRD), (iv) Scanning Electron Microscopy (SEM), and (v) Cathodoluminescence Spectroscopy (CL) to characterize ZnO nanostructures. These tools are central to the investigations of the properties of ZnO reported here. In this chapter, the working principle of these techniques, and how these techniques are used to study the properties of ZnO, are described.

2.1 Vapour Phase Transport (VPT) method

The fabrication of nanomaterials is the crucial beginning to experimentally understand and determine the fundamental properties of nanostructures, and hence the development of nanotechnologies. As mentioned in the previous chapter, several growth methods have been employed to grow ZnO nanostructures. Among those techniques, Vapour Phase Transport (VPT) is one of the simplest synthesis technologies, and hence, one of the most widely utilized methods of growth. A rich

variety of ZnO nanostructures can be grown using this method. This method is based on the transport of Zinc (Zn) and Oxygen (O) vapour to a substrate, where they react to form ZnO. The mixture of Zn and O vapour is usually produced either (a) by direct decomposition (sublimation) of ZnO powder, which occurs at relatively high temperature (>1975^{o}C), (b) by use of a ZnO + carbon powder mixture (referred as the carbothermal reduction method), where carbon lowers the decomposition temperature significantly (~900^{o}C or less in some cases), or (c) by evaporating Zn metal (~420^{o}C melting point) under an oxygen flow [1]. In the third method with Zn metal, the transport and reaction zones should be separated to avoid Zn and O reaction away from substrate. The nanostructure formation and its shape strongly depend on the Zn to O absolute pressures and their ratio. Naturally, aligned and patterned 1D nanostructure growth is important for device applications. Although various kinds of nanostructures can be obtained using a catalyst-free vapour-solid (VS) condensation process, control over nanostructure formation e.g. alignment, density and location can be achieved using the vapour-liquid-solid (VLS) process incorporating the use of catalysts, which initiate and guide the growth [2]. The details of the VLS mechanism is described in section 2.1.2, and before that the setup for the VPT growth of ZnO nanostructures used in our laboratory is described below. In fact in our system, even using metal catalyst, the growth proceeds by both VLS and VS pathways, because the catalysts provides an energetically suitable accommodation site for ZnO nucleation even without VLS taking place. This is discussed in chapter 3.

2.1.1 Growth setup

The VPT method via VLS mechanism is usually carried out in a horizontal tube furnace. The schematic is shown in *Fig 2.1*. This VPT setup is used in our laboratory to grow single crystalline ZnO nanostructures.

The furnace used is a single zone furnace (Lenton Thermal Design limited), the central part of which stays at the highest (nominal) temperature. The furnace is horizontal and cylindrical in shape. An alumina liner tube of inner diameter 46 mm is placed within the middle of the furnace horizontally. Within that tube a high

quality quartz tube of inner diameter 37 mm is placed. One end of the furnace is tightly closed by a vacuum fitting, and attached to a Mass Flow Controller (MFC) calibrated for Argon (Ar). The other side is the open side, and it is tightened loosely during growth. The source powders are placed on a small alumina or multisil boat, and the substrate is placed just beside (~3 cm away within the boat) or immediately above the powders.

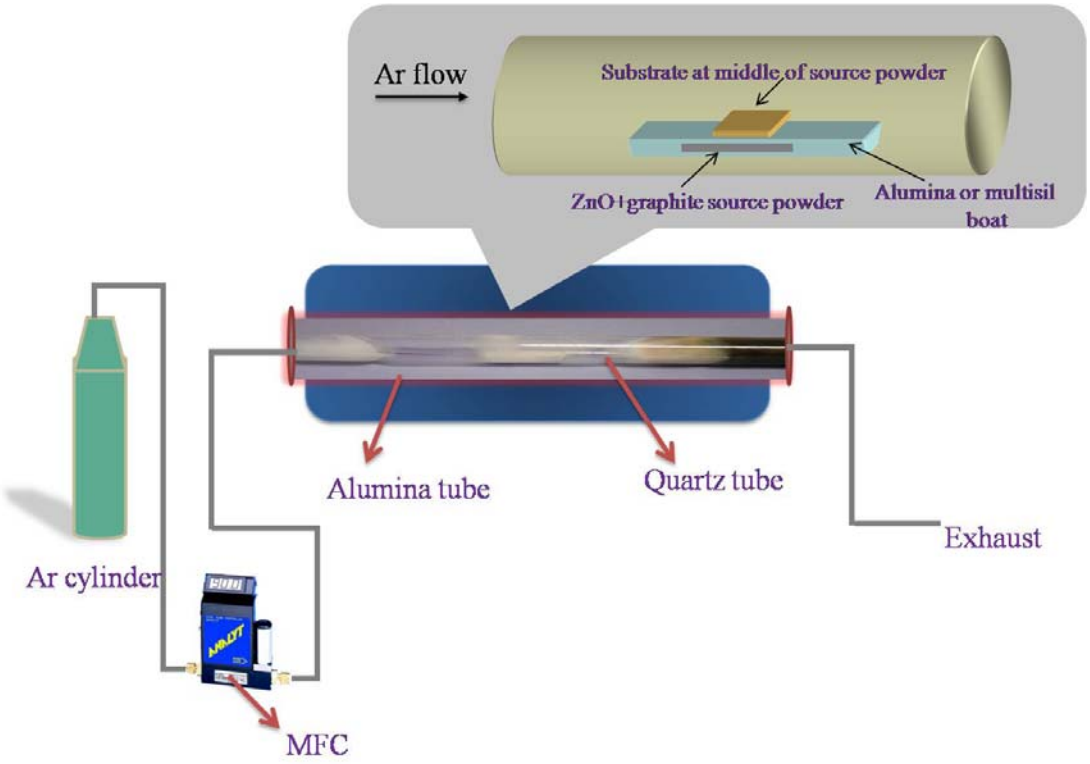

Fig 2.1: Experimental setup for growth of ZnO nanostructures

At the beginning of my Ph.D work, growth was done placing the sample beside powders, but the growth process became more reliable (run to run) by placing the substrate directly above the powders. By this arrangement, the minimum temperature at which nanostructure nucleation and growth starts become lower maintaining the same morphology, crystal quality and optical properties. The source powder usually used in this system is ZnO + graphite with mass ratio of 1:1 with a total mass of 0.012 gm. The carbon source used with ZnO powder acts as a reducing agent to

facilitate the availability of Zn vapour source at much lower temperature compared to the melting point temperature of ZnO (>1975^{o}C). This reduction method is popularly known as Carbothermal Reduction (CTR) method. The growth temperature usually varies in the range of 850 -1050^{o}C for growth on sapphire. For growth on Si, the temperature range may be even larger. Metal (in this case gold (Au)), which acts as a catalyst in VLS growth is deposited prior to growth using a thermal evaporator and normally nominal thickness of ~5 nm. An Ar gas flow of 90 sccm (controlled by the MFC) is introduced into the chamber. Prior to growth Ar gas is turned on into the chamber for 12-15 minutes to flush excess oxygen, and then growth is carried out for further 60 minutes in the presence of Ar gas. Growth is carried out at atmospheric pressure, and the oxygen source for growth is the residual O_2 in the chamber.

2.1.2 Vapour-Liquid-Solid (VLS) mechanism

Among all vapour based methods, the VLS process seems to be the most successful for generating nanowires with single crystalline structures in relatively large quantity. This mechanism was first proposed and demonstrated by Wagner and his co-workers in the 1960s during the study of large single-crystalline whisker growth of Si [3]. In this method, a catalyst like Au can play the role of impurity for liquid alloy formation. For ZnO nanostructure growth at temperature of ~900^{o}C, Zn vapour (formed e.g. by CTR) is transported to a Au-coated substrate, and at the same time Au melts on the substrate. Zn vapours immediately condense at the Au-coated regions preferentially, because the metal provides energetically favourable locations for nucleation, and then may dissolve in the Au.

The Au/Zn alloy becomes supersaturated, and Zn precipitates out and may react with the oxygen of the furnace (residual or deliberately introduced), and form ZnO nanorods. Au acts as a location for ZnO precipitation, but is not consumed in the growth, and we can say Au plays the role of a catalyst. Due to the continuation of this process, the alloy droplet becomes displaced from the substrate and stays on top of the growing nanorod as an Au “cap”. The growth process continues in the vertical direction perpendicular to the substrate, and generally the long axis of the nanorod is

along the ZnO (0001) direction as the ZnO (0001) planes have the lowest surface energy, and thus tend to align parallel to the substrate surface when an epitaxial match with the substrate is present, e.g. for sapphire.

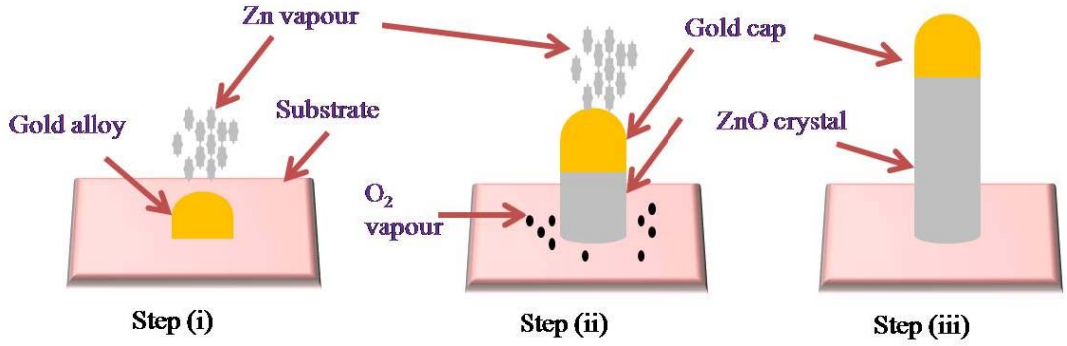

Fig 2.2: VLS mechanism- step (i) ZnO vapour deposition on gold alloy droplet, step (ii) & (iii) formation of ZnO nanorod growth in the interface of substrate and alloy.

The main characteristic of VLS growth is the presence of metallic nanoparticles (in this case Au nanoparticles) on top of the nanowires. We can observe from *Fig 2.3(a)* that each nanorod has a characteristic rounded tip instead of hexagonally faceted one, which is what is normally seen in catalyst free VS ZnO growth.

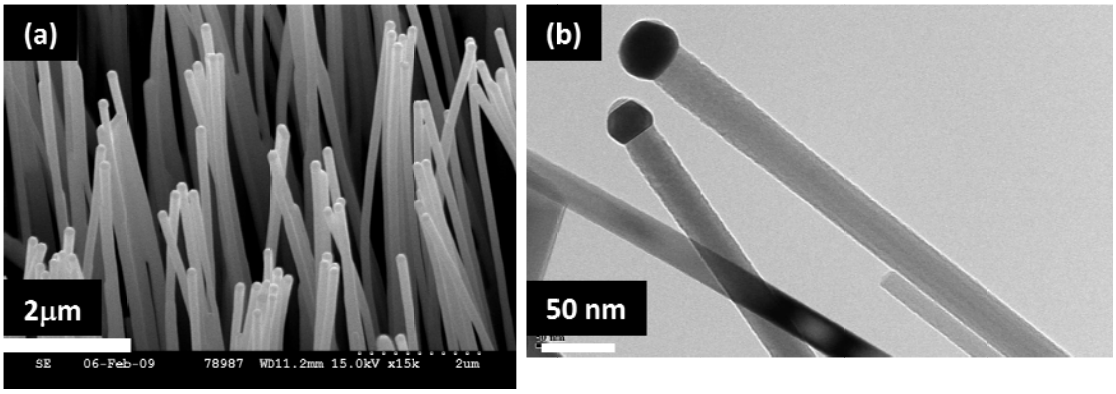

Fig 2.3: (a) FESEM image of ZnO nanorods grown at 950°C on *a*-sapphire with Au tip at top of nanorods showing evidence of VLS mechanism, (b) TEM image of sample grown at similar conditions showing further evidence of Au particle formation at the tips of ZnO nanorods.

The sample shown in *Fig 2.3(b)* presents evidence of the VLS mechanism where the dark, round tips represent the Au nanoparticles. The diameter of the ZnO nanorod

via VLS growth is primarily determined by the liquid alloy droplet which is dependent on the initial Au layer thickness.

Controlled growth can be achieved through appropriate use of catalysts in patterns or films on the substrate surface. *p-n* junctions and heterojunctions can be made; also dislocation free nanowire crystals can be grown.

2.1.3 Vapour-Solid (VS) mechanism

VS mechanism is another vapour based method which is of relevance in the growth of the nanostructures in this thesis. It is a catalyst free method that involves direct vapourization of solids at higher temperature followed by deposition of nanostructure at lower temperature. In this work for the VS mechanism Zn vapour is also produced by CTR method followed by transportation and condensation of Zn vapour directly on the substrate at liquid alloy droplet locations. Then oxidation of Zn vapour occurs, and forms nanostructures as discussed in section 2.1.2. This method has the advantages of producing impurity free pure nanostructures, and selective area growth is possible due to the nucleation droplet locations in the growth process.

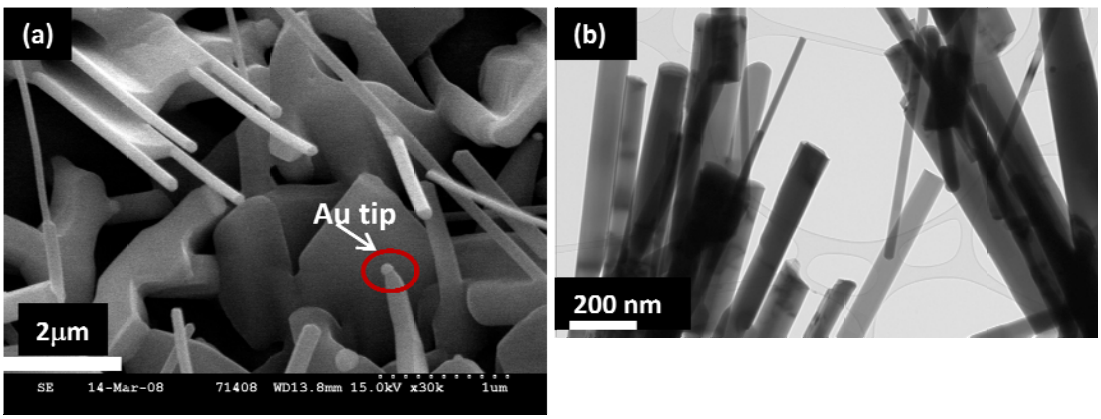

Fig 2.4: (a) FESEM image of ZnO nanorods grown at 900^0C on Si with most of the nanorods without Au tip at top showing presence of VS mechanism along with VLS mechanism (b) TEM image of sample grown at similar conditions on *a*-sapphire showing further evidence of the presence of VS mechanism.

Usually we observe the presence of both the VS and the VLS mechanisms simultaniously for the nanostructures grown in our laboratory. We can observe many nanorods without Au tip, growth of which can be explained by VS mechanism as shown in *Fig 2.4*. In *Fig 2.4 (a)* although we can see one nanorod with Au at tip, most of the nanorods are without Au tips, and TEM data confirm this.

2.2 Fourier Transform Photoluminescence (FT-PL)

Luminescence is generally defined as emitted light from cold objects (due to non-equilibrium excitation levels), in contrast to incandescence, which is the light emitted by hot bodies. There are various types of luminescence, named according to the type of excitation causing the light emission. These include-

- **Photoluminescence** (PL) – When the exciting source is electromagnetic radiation, with a photon energy greater than the material bandgap.
- **Chemiluminescence** – When the light is emitted as a result of chemical reactions
- **Bioluminescence** – When the chemical reaction takes place within a living organism and luminescence is due to biochemical reactions
- **Triboluminescence** – When the light is produced because of mechanical excitation
- **Cathodoluminescence (CL)** – When the luminescence is due to material excitation by a high energy (in kV) electron beam

The study of PL spectroscopy, a technique to obtain the relation between the intensity and the wavelength of the luminescence, has become one of the most powerful techniques for the comprehensive and (mostly) non-destructive assessment of many materials. It yields a large amount of information about the electronic structure of the materials under study [4]. The heart of this optical measurement is a spectrometer, which is used to discriminate among emissions at different photon energies, resulting in a plot of light intensity as a function of energy. Grating monochromators are often used for this purpose while dispersive prisms are the

oldest instrument to separate light into its component wavelengths. However, Fourier Transform (FT) Spectrometer is a very powerful spectroscopic technique for PL studies and is the main technique used in this work.

2.2.1 Theory of PL

Three processes are involved in the luminescence as shown in *Fig 2.5*-

- Excitation
- Energy transfer and thermalisation
- Radiative transition of the carriers

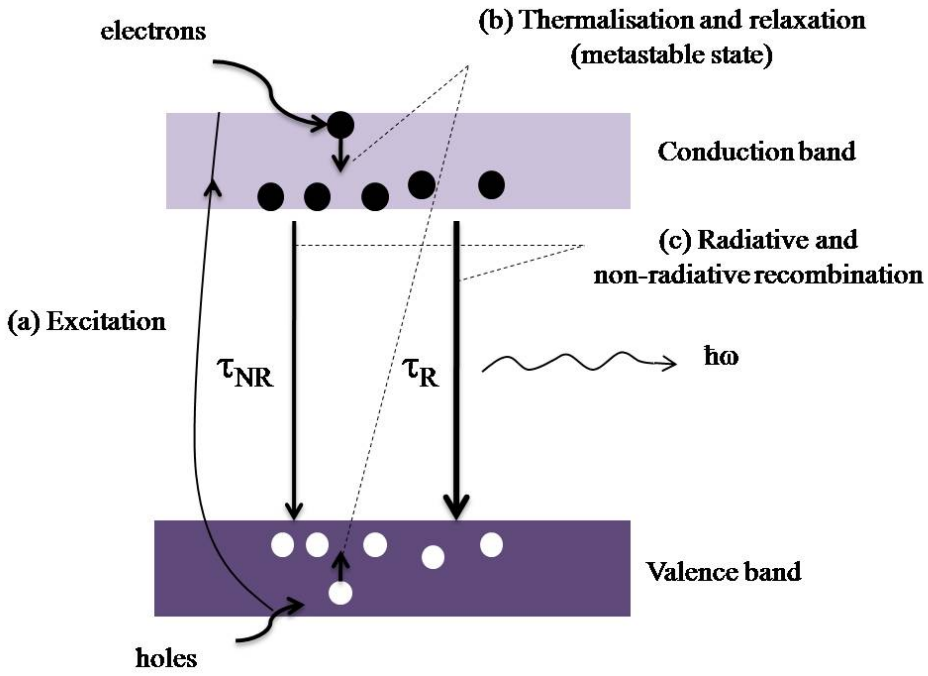

Fig 2.5: Schematic diagram of the general process of luminescence (a) Excitation by an external source (b) thermalisation and relaxation to create metastable e-h pairs denoted as excitons (c) recombination which can be of two types; radiative (τ_R) and non-radiative (τ_{NR}). The emission of photon due to radiative recombination detected as luminescence.

When light is the excitation energy source the process is called photoluminescence, as mentioned above. In a semiconductor absorption of photons of energy higher than the bandgap results in the creation of free electrons and holes, which is a non-equilibrium distribution of electron-hole (e-h) pairs. The electrons and holes, respectively, thermalise quickly (~5 ps) to reach thermal equilibrium amongst themselves, and thus reach a quasi-thermal equilibrium described by quasi-Fermi levels in a short time compared to the time it takes for e-h recombination (typically > 200 ps). This thermalisation creates a population of electrons and holes close to the conduction and valence band edges, respectively. In pure materials (where stray electric field effects are small) and at low temperatures, the Coulomb attraction between the electron and hole causes their motion to be correlated, and the resultant Coulombically bound e-h pair is known as an **exciton**.

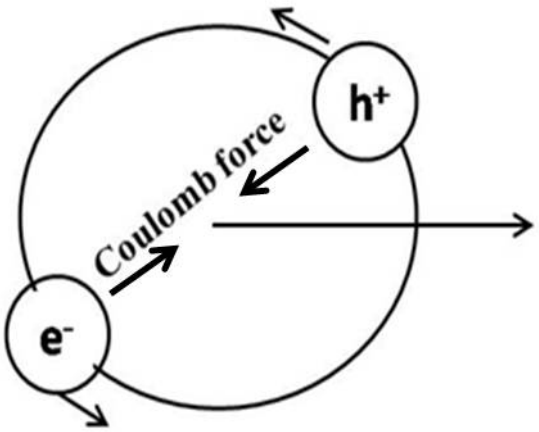

Fig 2.6: Exciton showing the electron and hole attracted by the Coulomb force with the centre-of-mass motion of the exciton indicated by the arrow pointing to the right, adapted from [5].

The development of the study of excitons began with prediction of these excitations by Frenkel in 1931. This was followed by Mott and Wannier's development of a theory of more loosely bound excitons in 1937 [6, 7]. The active experimental investigation of excitons began in 1951 after the discovery of the appearance of exciton features in light absorption spectra of cuprous oxide crystals by Gross and Kar'ev [8].

Because the exciton is a bound electron and hole pair, its formation energy is slightly less than that of an unbound electron and hole pair. The excitonic particle can be considered as an electron and hole orbiting around a common centre-of-mass and bound together in a Bohr atom-like way. The binding energy, Bohr radius etc. of the exciton in many cases can be calculated using the equations of the Bohr model, and taking into account the effective masses of the particles and the dielectric constant of the semiconductor.

Excitons are generally divided into two types-

- **Frenkel excitons**: Frenkel proposed a model of this quantum of excitation propagation in 1931 (it was not referred as an exciton at that time) in insulating crystals [6]. These excitons are very tightly bound with a small radius. When a material's dielectric constant is very small, the Coulomb interaction between electron and hole becomes very strong, and the exciton radius tends to be very small, of the same order as the unit cell. As a result, the electron and hole essentially can be viewed as "sitting" on the same cell and the exciton can hop from cell to cell. This Frenkel exciton has typical binding energy in the order of 1.0 eV. Frenkel excitons are realized in alkaline halide crystals and in many crystals of aromatic organic molecules. So for the Frenkel exciton in alkaline halide or strongly ionic insulators the excitation dimension is limited to a single atom or molecule.
- **Mott-Wannier exciton**: The model of Frenkel exciton is inadequate for many insulators and semiconductors which have larger dielectric constants. In such cases, the exciton radius is much larger and the electron can be considered to orbit many unit cells distance from the hole. This type of excitons has much larger radius than the lattice spacing. The electron and hole are separated by many interatomic spacing. This happens mostly in semiconductors where the dielectric constant is generally large, and as a result screening tends to reduce the Coulomb interaction between electrons and holes. As a result, the effect of the lattice potential can be incorporated into the effective masses of the electron and hole, and because of the lower masses and the screened Coulomb interaction, the binding energy is usually much less, typically on the order of 0.1 eV or less.

A charge-transfer exciton is an intermediate form between the Frenkel and Mott-Wannier exciton models.

For ZnO, the exciton binding energy is ~ 60 meV, and the Bohr radius of the exciton is ~ 2 nm and it may be considered a Mott-Wannier exciton. In a pure material at a sufficiently low temperature (where kT < exciton binding energy), the exciton is a stable particle and will not be thermally dissociated. The exciton may also be destabilized in highly impure materials with many defects where stray DC electric fields can cause the exciton to dissociate.

In a pure material without any defect or impurities (intrinsic semiconductor) the exciton centre of mass is perfectly free to move throughout the material, and thus such a particle is called a **free exciton** (FE) [9]. In most materials, there are finite concentrations of impurities or defects. Any disruption of the periodicity of a lattice (impurities, vacancies, dislocations and even large scale defects such as surfaces) may either destroy an exciton or localize it. The possibility of localization of Mott-Wannier exciton on impurities was predicted by Lambert (1958) and observed by Haynes (1960) in the form of narrow peaks below the free exciton level in Si [8]. Impurities can trap a FE, and bind the exciton to the defect location with a certain and impurity specific localization energy. These trapped excitons are called **bound excitons** (BE). The localization energy is dependent on the nature of the defect (e.g. the chemical identity, symmetry, defect charge state etc.). Usually the localization energy of an exciton on an impurity, measured from the free exciton line, is a fraction of the ionization energy of the impurity (e.g. E_A for acceptor, E_D for donor) which localizes the exciton. For ZnO $E_{loc}= 0.1E_A$, $E_{loc}=0.2E_D$ (Haynes rule) [8]. At low temperatures, most of the free excitons in real materials are trapped and bound at defects due to thermalisation effects. As the temperature is raised, these are gradually released to form free excitons.

Before explaining the next step of the luminescence process, the differences between direct and indirect bandgap semiconductors are briefly described. The first point to note is that in any transition involving free carriers in a crystal, both energy and

momentum (crystal momentum for carriers and excitons) must be conserved, taking into account the carriers, photons and other excitations (e.g. phonos).

There are two basic types of configurations of the CB and VB in semiconductor materials. In a direct bandgap semiconductor, the upper (conduction) band and the lower (valence) band have their minimum and maximum at the same value of K (crystal momentum), and are thus laid directly above and below each other in a graph of energy (E) versus crystal momentum (K) as shown in *Fig 2.7 (a)*. In the case of direct bandgap semiconductors, after being excited by photon with energy greater than bandgap energy, the electrons and holes thermalise down to the CB and VB edges respectively, and the electron may later radiatively recombine with the hole and emit a photon with an energy given by-

$$\hbar\omega \cong E_g \qquad \text{Eqn. 2.1}$$

Where $\hbar\omega$ is the photon energy, E_g is the bandgap energy.

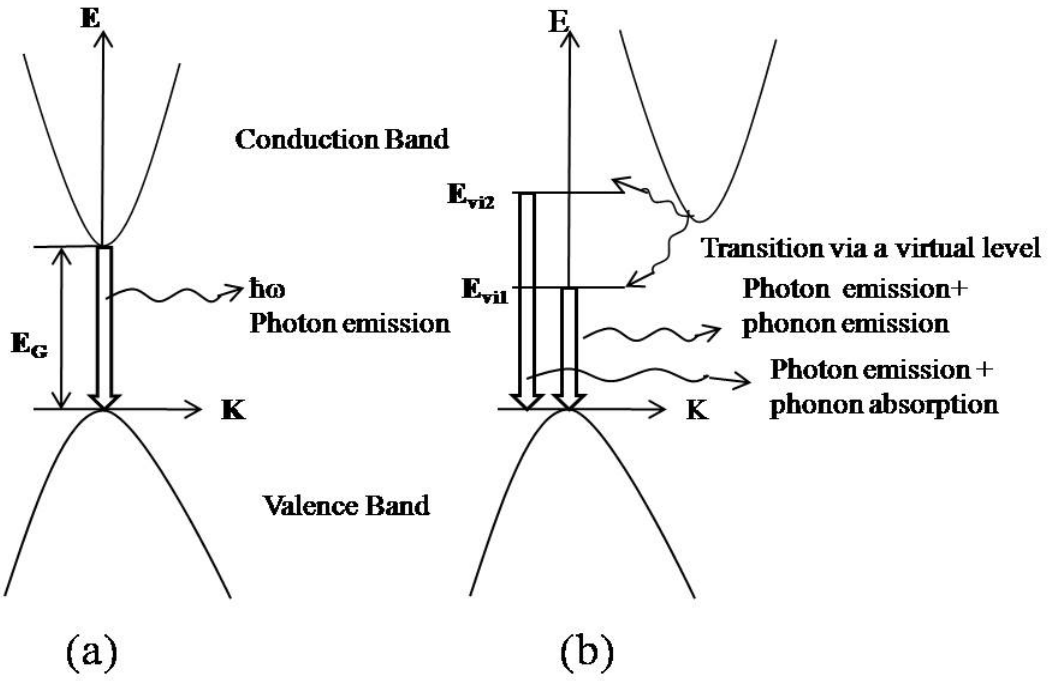

Fig 2.7: Example of (a) direct bandgap, and (b) indirect semiconductors. E_G is the bandgap energy of a particular semiconductor. E_{vi1} and E_{vi2} are the virtual level of transition for conservation of momentum via phonon emission and phonon absorption, respectively.

The transition is a two-body, i.e. electron + photon, process, and both energy and crystal momentum can be conserved because the photon momentum (c/λ) is very

small compared to the Brillouin zone dimension (~π/a). Thus the transition due to a photon only is "vertical" on an E-K diagram and thus can directly connect the CB and VB directly. The two body nature of the process means its quantum mechanical matrix element (probability) is quite high compared to NR recombination and thus direct gap materials are efficient optical emitters (and absorbers).

On the other hand, indirect bandgap semiconductors have a displacement in K in between the upper and lower bands. This develops additional constraints upon the emission of radiation. For such material, a phonon (or other exciton such as magnon, but most commonly a phonon) must be emitted or absorbed (to supply a change in momentum) at the same time a photon is emitted in order to conserve the momentum as shown in *Fig 2.7 (b)*.

The energy of the emitted photon in this case is given by-

$$\hbar\omega \cong E_g \pm \hbar\Omega \qquad \text{Eqn. 2.2}$$

Where $\hbar\Omega$ is the energy of the momentum-conserving phonon and the ± sign corresponds to phonon absorption and emission respectively [10]. Because a three body process (electron, photon and phonon) is needed in an indirect gap material, the quantum mechanical matrix element for indirect transitions is reduced compared to direct transitions and becomes dependent on the phonon population. At normal temperatures (below 300 K) the phonon density is so low that the photon emission + phonon emission channel is overwhelmingly likely compared to the photon emission + phonon absorption channel. In indirect gap materials the radiative transition probability is much less than for direct gap materials and competing NR transitions are much more important and thus indirect gap materials are less efficient optical emitters (and absorbers).

The consideration of K-conservation above apply both to free electron, free hole and FE transitions and also to transitions of loosely BE or carriers, whose wavefunctions are similar to FE or free carriers. For tightly bound species the K-conservation rules are strongly relaxed, but such transitions are not the focus of this work.

Si are Ge are examples of indirect bandgap semiconductors, and ZnO and GaAs are examples of direct bandgap semiconductors. The combination of a direct bandgap and a relatively large exciton binding energy (means a strong e-h wavefunction overlap and thus a large quantum mechanical optical transition matrix element) means ZnO is a very efficient optical emitter and absorber.

In an impure material (as in the usual case), e.g. a doped material or one with lattice defects, new states can occur in the forbidden gap. Carriers can relax or be trapped in these states and recombination from these states can dominate the luminescence spectra at low temperatures. In the event of **radiative** recombination from such levels, one photon with an energy equal to the difference in energy between the initial and final state is emitted.

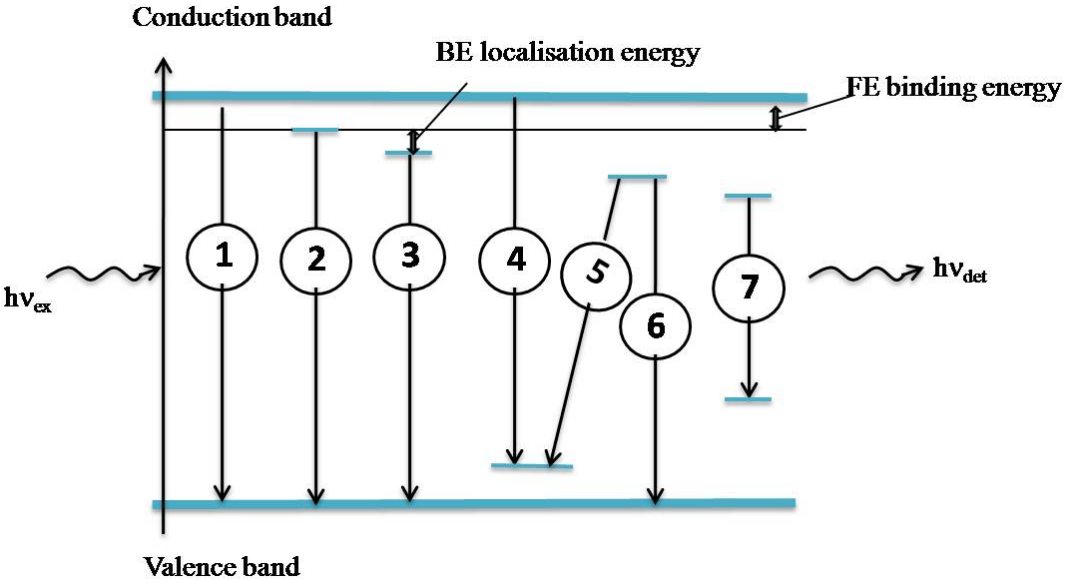

Fig 2.8: Illustration of recombination process in semiconductor: Radiative recombination; band to band (1) Free exciton (FE) (2), bound exciton (BE) (3), conduction band electron to acceptor (e,A), (4) donor to acceptor (D,A) (5), and valence band hole to donor (h,D) (6) recombination. Deep level intra-impurity recombination (7).

The emitted photon in radiative recombination is detected as PL light. Radiative processes, leading to photon emission can be of many types depending on the defect nature. Different radiative recombination paths are shown in *Fig 2.8*. The balance between intrinsic (i.e. free electron to free hole and/or FE) recombination and defect-

related recombination is dependent both on temperature and defect concentrations. At higher temperatures excitons or carriers trapped at defects tend to be thermally released (with a Boltzmann-factor dependence $\propto \exp\left(-\frac{\Delta E_{localisation}}{kT}\right)$) and intrinsic (bandedge) emission dominates, whereas at lower temperatures the carriers/excitons remain localized (trapped) at defects and defect-related emission dominates.

In addition to the radiative recombination process there is another possible recombination process for excited carriers in semiconductors known as **non-radiative** (NR) recombination. In NR recombination, the excited state energy is converted to e.g. vibrational energy of lattice atoms i.e. phonons. Thus, the electron energy is converted into energy forms other than light at the desired photon energy. For obvious reasons, NR processes are unwanted in photonic applications. There are several physical mechanisms by which NR recombination can occur. Defects in the crystal structure and multi-phonon emission are two common causes for this type of recombination. Defects may include unwanted foreign atoms, native defects, dislocations and any complexes of such defects. All such defects may form one or several energy levels within the forbidden gap of semiconductor. These energy levels can be efficient NR recombination centers, in particular if the level is close to the middle of the gap. These deep levels or traps kill or quench the luminescence [11, 12]. At higher temperatures, as trapped carriers/excitons are thermally released from defects and become mobile they can diffuse through the crystal and encounter various defects which increase the probability of NR recombination at such defects. Thus at higher temperature the fraction of NR recombination increases and the material's optical emission efficiency generally reduces.

The PL photon energy produced in most materials is typically close to the bandgap energy (called near bandedge PL). In the case of recombination of FE in a direct bandgap material, the emitted photon energy equals the bandgap minus the free exciton binding energy. In the case of recombination of BE in a direct bandgap material, the emitted photon energy equals the bandgap minus the FE binding energy minus the defect localization energy. Thus, as stated above the BE emission spectrum is slightly lower in energy than the FE emission energy, and each different species of defect leads to BE emission at specific photon energies, which enables one

to use this emission to identify and study certain specific defects. An example of ZnO near bandedge PL is shown in *Fig 2.9* below.

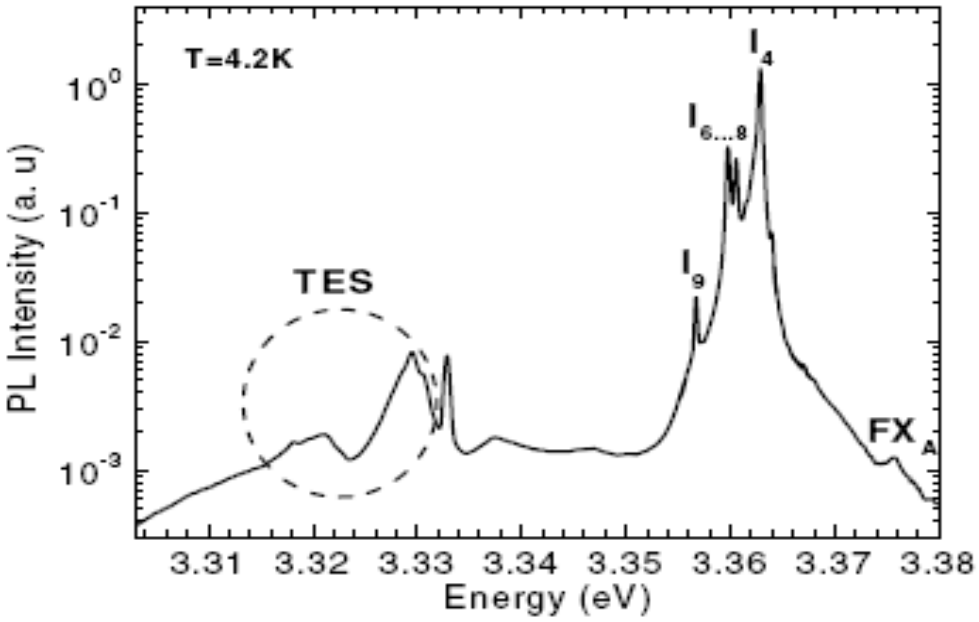

Fig 2.9: PL spectrum of bulk ZnO in the excitonic range. FX_A is the transversal free exciton, I_4 to I_9 are BE lines. The region where the two-electron-satellite (TES) transitions occur is indicated (HeCd excitation). Spectrum is taken from Meyer *et.al* [13].

The luminescence from bulk ZnO extends from the bandedge (near UV ~3.3 eV) to the green/orange spectral range. PL study of both ZnO bulk and nanostructured material by various groups reveals some near bandedge excitonic emission lines, mostly donor bound exciton (DBE) lines at low temperature. These lines are mostly well understood and named as I_0 to I_{11} as discussed by Meyer *et. al* [13]. From *Fig 2.9* we can see the spectrum is mostly dominated by BE lines I_4, $I_{6..8}$ and I_9. The origin of most of those lines is known, such as I_4 is due to H, I_6 due to Al, I_8 due to Ga, I_9 due to In. The peak positioned at 3.375 eV in *Fig 2.9* is the free exciton emission (FX_A) involving a hole in the A-valence band. In the lower energies from 3.34 to 3.31 eV one can expect the two-electron satellite (TES) recombination lines of the neutral DBEs, which means that during the recombination of an exciton bound to a neutral donor the donor final state is left in the 2s, 2p states (TES-line) rather than the ground 1s state as is most usual. The energetic distance between the D^0X

and its TES is consequently the difference between the donor energies in the 1s and 2p states.

2.2.2 PL Setup

The components of a basic PL spectroscopy setup consist of a source to excite the sample, a cryostat to keep the sample cold (measurement is carried out at low temperature as (i) the optical efficiency is highest and (ii) the defect related spectroscopic feature for ZnO such as bound excitonic emission peaks can be visible only at low temperature and specifically the peak at 3.367 eV studied in chapter 6 known as SX peak in ZnO nanostructures can be observed only at temperatures below 25 K), and an instrument to measure the emitted PL signal as a function of wavelength. The exact configuration of these components is adjusted wherever possible to suit a particular PL feature of interest. ZnO luminescence falls in the near UV range of the spectrum. In this thesis, the PL spectra have been taken using FT-PL spectroscopy. The principle of the FT-PL spectroscopy is summarized in this section.

The FT spectrometer used for our PL study is a Bomem Hartmann & Braun DA8 FT spectrometer. The detector of the light is a photomultiplier tube (PM tube, model number IPH8200L). The excitation source for PL was an IK series He-Cd laser emitting at 325 nm with power of ~40 mW unfocused on the sample. To achieve low temperatures for PL (~20K or less), a closed cycle cryostat (Janis research Co. Inc.) is used. The PL set up is shown in *Fig 2.10* below.

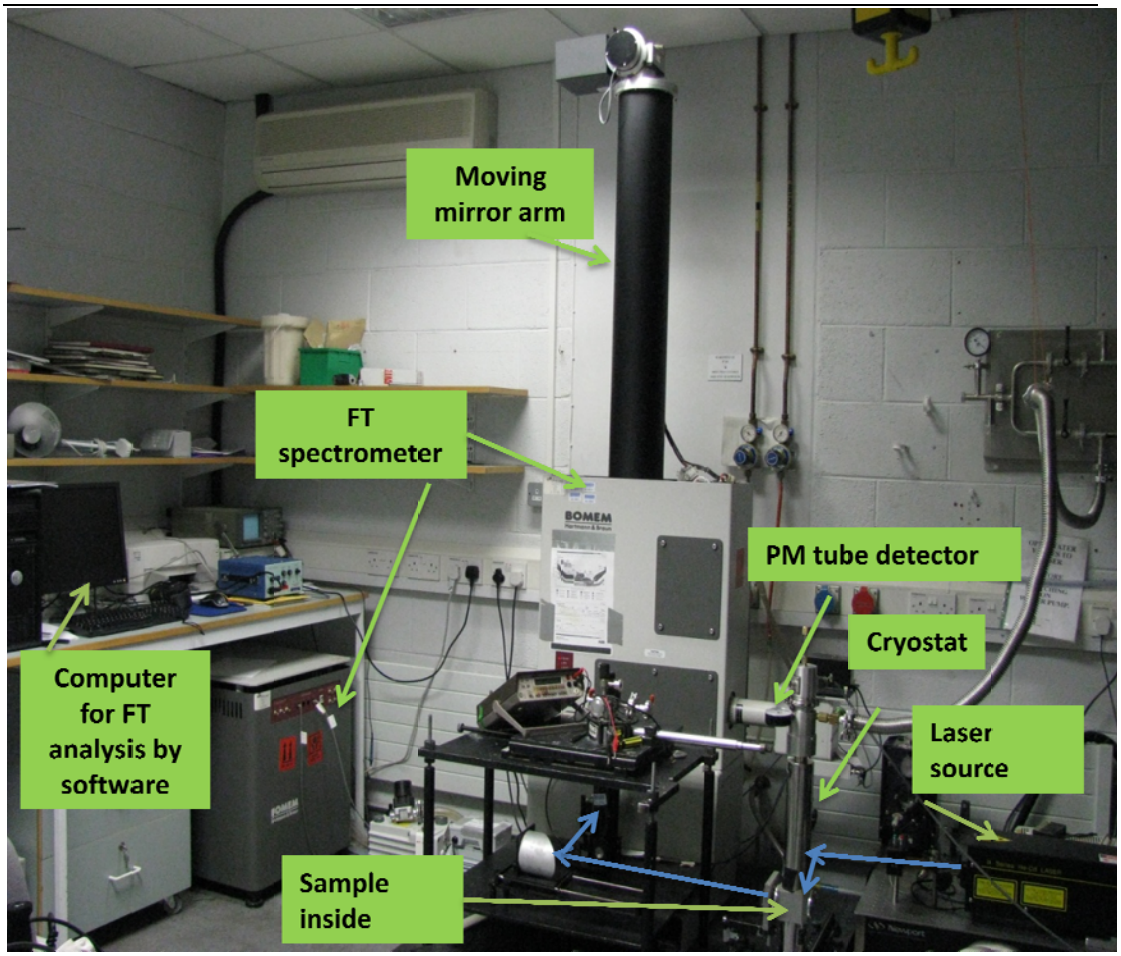

Fig 2.10: FT-PL setup for ZnO nanostructure optical study; the blue arrows showing the laser path from laser source to spectrometer aperture after striking the sample within cryostat.

2.2.3 Basic principle of FT-PL

The foundation of modern FT spectroscopy is the two beam Michelson interferometer. The spectroscopic information is contained in the fact that an interferogram and its spectrum are related by a Fourier Transform. The modern developments in computing have enabled the application of the fast FT to spectroscopic measurements routinely. The basic optical components of a FT spectrometer are shown in *Fig 2.11.*

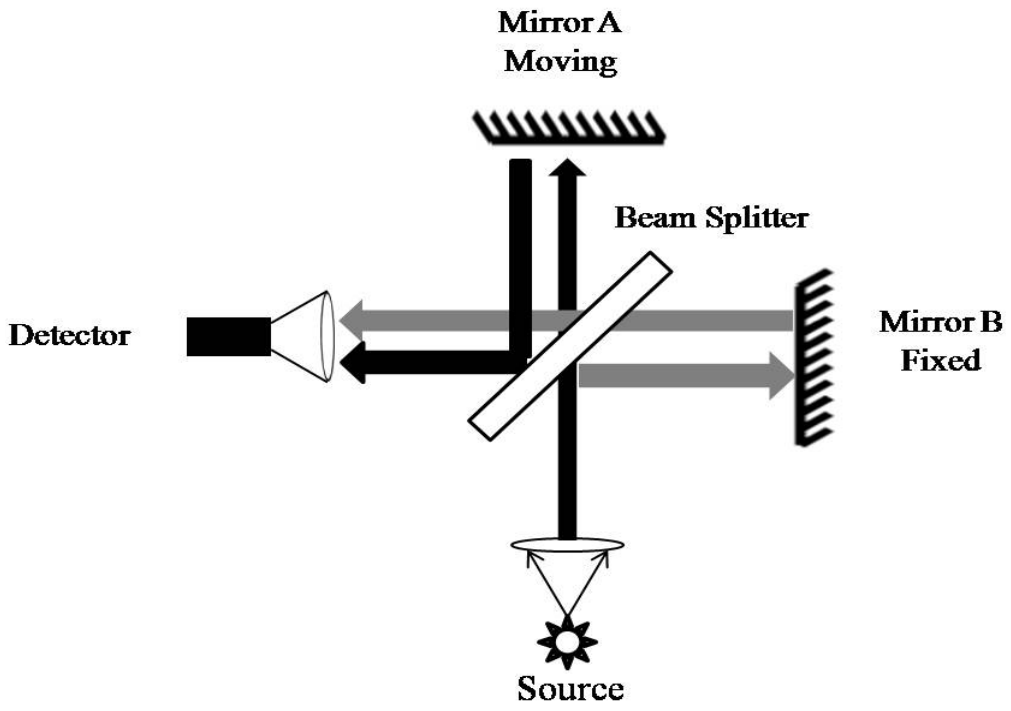

Fig 2.11: Schematic of Michelson Interferometer

In FT spectroscopy, unlike prism and grating spectrometers, different wavelengths are not spatially dispersed. In a FT system, light from a UV source (in this work, ZnO luminescence is in the near-UV range) is collimated and collected through an entrance aperture, and separated into two beams by a beam splitter. An ideal beam splitter creates two separate optical paths by reflecting 50% of the incident light, and transmitting the remaining 50%. As shown in *Fig 2.11,* a fixed mirror B reflects one beam, and the other beam is reflected by a moving mirror A. Then two beams recombine in the beamsplitter itself. As mirror A moves, the optical path travelled by the beam in arm A of the system changes with respect to the optical path travelled by the beam in arm B. So when these two beams recombine at the beam splitter, there will be a phase difference between them, which can be altered by changing the position of the mirror A. The resultant interference pattern is detected as a function of mirror position in the detector.

In the case of a monochromatic source, after passing through the beamsplitter we consider the electric field intensity of two light waves as –

$$E_1 = E_0 \, sin(kx - \omega t) \qquad \text{Eqn. 2.3}$$

$$E_2 = E_0 \sin(kx - \omega t + \phi)\,, \qquad \text{Eqn. 2.4}$$

where ϕ is the relative phase of the two waves, E_0 is the electric field amplitude, and k is the wavenumber, related to wavelength λ by

$$k = \frac{2\pi}{\lambda}$$

ω can be expressed as 2πf, where f is the frequency of light. Now, to obtain a relationship between relative phase ϕ and the mirror position, we assume the position of the moving mirror A relative to the position of the moving mirror B as D/2, and define D/2 as zero, when the paths length of A and B are equal (known as the zero path difference (ZPD point)). The number of additional wavelengths travelled by the beam in path A as the mirror moves can be expressed as-

$$N = \frac{D}{\lambda} \qquad \text{Eqn. 2.5}$$

To turn Eqn. 2.5 into a phase angle in radians, we multiply it by 2π, and we get the phase angle in terms of D as-

$$\phi = \frac{2\pi D}{\lambda} = kD \qquad \text{Eqn.2.6}$$

If we add two light beams whose electric fields are given by Eqn. 2.3 and 2.4, the equation of electric field of the resultant wave can be expressed as-

$$E_T = E_1 + E_2$$

$$= E_0[\sin(kx - \omega t) + \sin(kx - \omega t + \phi)]$$

$$E_T = 2E_0 \sin\left(kx - \omega t + \frac{\phi}{2}\right)\cos\left(\frac{\phi}{2}\right) \qquad \text{Eqn.2.7}$$

The light intensity of the detector can be obtained by taking the time average of the electric field squared-

$$I = < {E_T}^2 > = {E_0}^2 + {E_0}^2 \cos(kD) \qquad \text{Eqn.2.8}$$

So from Eqn. 2.8, we can see that the detector intensity varies in a cosinusoidal manner as a function of mirror movement D and with a period determined by the wavelength of the source (through k).

The plot of detector intensity versus mirror position is called the interferogram. *Fig 2.12 (a)* is an example of interferogram for a quasi-monochromatic light source. If

the source consists of more than one monochromatic light output, then each of the wavelength will produce a cosinusoidal signal in the interferogram, and each will have characteristic periods as the mirror moves. The amplitude of this cosinusoidal contribution is proportional to the spectral line strength. Hence, the total interferogram is obtained by adding or integrating all the cosinusoidal contributions over the source spectrum, which all add incoherently.

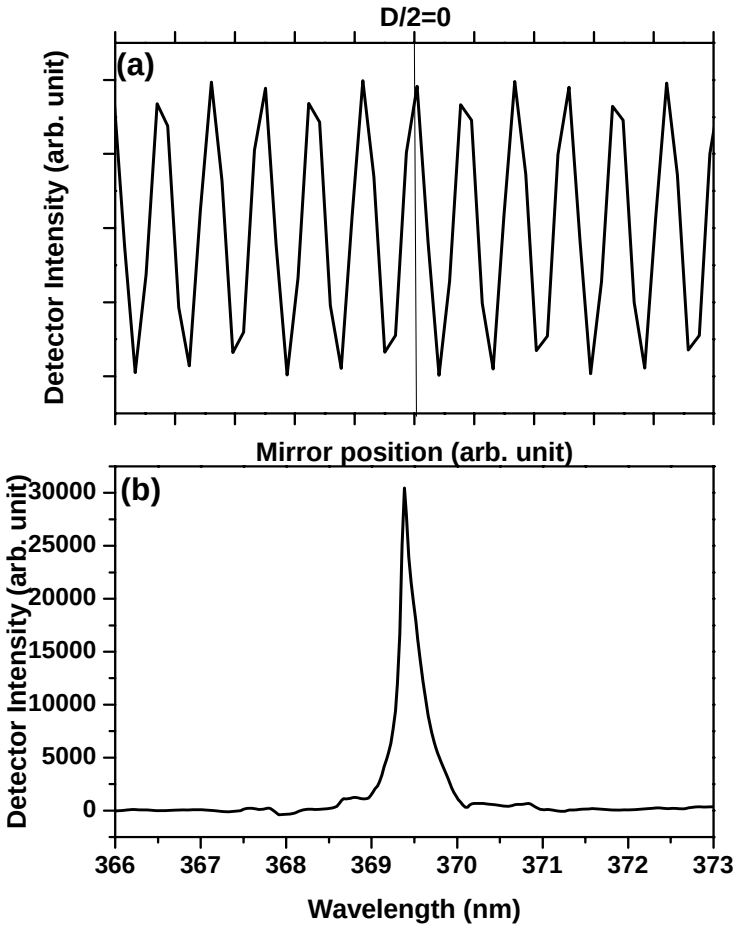

Fig 2.12: (a) Example of interferogram of indium doped ZnO nanostructures at 20 K. (b) Spectrum of the same sample and the peak is a BE peak (known as I_9 according to Meyer *et. al.* [13]) related to indium impurity. This original spectrum at (b) we get by performing FT on interferogram shown in (a).

So for a continuous wavelength distribution in the source across the spectrum, we get-

$$I(D) = \int_{-\infty}^{+\infty} I(k)\big(1 + cos(kD)\big)dk \qquad \text{Eqn.2.9}$$

Where I(k) represents the source spectrum.

The decomposition of this interferogram into its cosinusoidal signal will give us the source spectrum. By FT we can decompose an arbitrary interferogram into its cosinusoidal components. Considering the varying part of Eqn.2.9, and performing an FT on this part we get-

$$I(k) = \int_{-\infty}^{+\infty} I(D)cos(2\pi\, k.D)dD \qquad \text{Eqn.2.10}$$

Eqn. 2.10 decomposes the interferogram into its respective cosinusoids and one gets the original spectrum e.g. shown in *Fig 2.12 (b)*.

From Eqns. 2.9 & 2.10, we can see that limits of the FT spectrometer are assumed from -∞ to +∞ i.e. mirror A can move infinitely far. But practically, this is not possible for any instrument and this limits the system instrumental resolution so that the minimum resolvable Δk for the instrument (i.e. the linewidth the instrument would yield when illuminated by an ideal monochromatic source) is given by

$$\Delta k \cong \frac{\pi}{D_{max}} \qquad \text{Eqn. 2.11}$$

Where D_{max} is the maximum distance the mirror can move.

With the advent of computers of high calculation capacity and small size, all the calculation involved in a FT can be done in seconds. The data are stored in digital form, and can easily be manipulated using different functions. In addition, many interferograms of a given sample can be collected and averaged for to give higher signal-to-noise ratio.

There are two unique features of the Bomem interferometer that makes it very suitable for semiconductor PL studies. The first is the real time numerical filtering which enables very fast collection of the interferogram, and subsequent calculation of the FT. The second feature is the dynamic alignment of the mirrors which is crucial in performing high resolution spectroscopy. The fixed mirror must remain parallel, to within a fraction of the wavelength of the light under study, to the moving mirror as it is scanned. At wavelengths of typical wide bandgap semiconductor luminescence, the technology must be much more sophisticated. The

Bomem accomplishes this by dynamically aligning the mirrors as the moving mirror is scanned. The dynamic alignment system uses the laser beam from a single mode He-Ne red laser (wavelength ~633 nm). The interference pattern from this laser is incident on a photodiode array and the signal from the photodiode array is used to control two servo motors, which adjust the angle of the fixed mirror so as to maintain the system alignment during the entire scan.

2.2.4 Advantages of FT-PL

The advantages of using an interferometer instead of a dispersive instrument like a prism or grating monochromators for PL studies are well-known. The most relevant advantages are-

i) Multiplex advantage: The multiplex advantage comes about because in interferometry the detector simultaneously samples all of the wavelengths in the emission, compared to scanning dispersive techniques where only one signal channel is sampled at a given time. That means the entire spectrum can be observed during the measurement of FT spectrum while only a small part of the entire spectrum is measured at a time in the normal monochromator. So an FT spectrum has a signal-to-noise advantage of √N for spectra with N spectral elements if only noise other than the photon noise is considered in the detector. Even for photomultiplier tube systems used in this work, where photon noise is important, the collection of the entire spectrum in one "go" is very useful.

ii) Throughput advantage: The throughput advantage arises because the width of the entrance slit monochromator must be two to three orders of magnitude smaller than the diameter of the aperture used in an interferometer, in order to obtain the same high spectral resolution. This means the collection solid angle for an interferometer is much larger than that for a monochromator at the same spectral resolution.

Other advantages of interferometry are the broad spectral range achievable, high spectral accuracy and ability to switch between very high resolution to low resolution without reconfiguring the apparatus. Thus one can quickly take a spectrum

over a very large wavenumber range with varying resolutions and with a minimum of configuration changes.

2.3 X-ray diffraction (XRD)

The phenomenon of XRD is based upon the interaction of X-rays with the periodic atomic structure of crystals. German scientist Max von Laue in 1912 first made the point that, "if crystals were composed of regularly spaced atoms which act as scattering centers for X-rays, and if X-rays were electromagnetic wave of wavelength about equal to the interatomic distance in crystals, then it should be possible to diffract X-rays by means of crystals" [14]. Under his direction the first attempt of experiments to test this hypothesis was made by Friedrich and Knipping, and they were successful (at their second attempt) in proving the wave nature of X-ray and the periodicity of atom arrangement in crystals. However, it was the English physicist W. H. Bragg and his son W. L. Bragg, who successfully analyzed the Laue experiment, and expressed the necessary conditions for diffraction in a simple mathematical form.

2.3.1 Basic concept of XRD

In case of XRD, X-rays impinge upon the different atoms in the crystal, and are scattered. When these scattered rays interfere with each other they cause a variation in amplitude for different scattered directions, those directions with large amplitude being considered as diffracted rays. In the scattering process, if there is a difference in the length of path travelled by the incident and scattered rays this leads to difference in phase and to different interference conditions and thus different strength diffraction in various directions. We can view the interaction of X-rays with a crystal as due to reflection from atomic planes, see *Fig 2.13*. In *Fig 2.13,* the necessary conditions for diffraction in a crystal are described. When an incident X-ray beam makes an angle θ with respect to the lattice planes (this angle θ is equal to the angle of reflection), a diffracted beam may be formed. The two rays 1 and 2 are reflected by planes P1 and P2 and the path difference between rays 1 and 2 is-

$$AC + BC = d\sin\theta + d\sin\theta = 2d\sin\theta$$

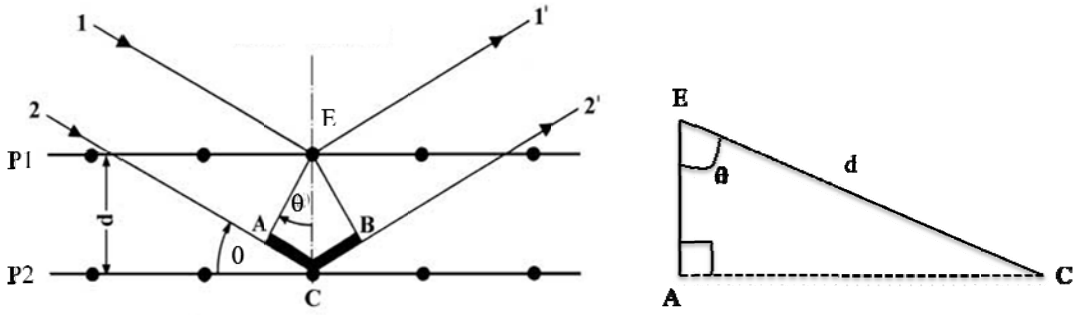

Fig 2.13: Diffraction of X-rays by a crystal, where *d* is the difference between crystal planes.

Reflected rays 1 and 2 will be completely in phase if this path difference is equal to whole number *n* of wavelength, or if

$$n\lambda = 2d\sin\theta. \qquad \text{Eqn. 2.12}$$

This relation was proposed by W. L. Bragg, and is known as **Bragg's Law**. It states the essential conditions which must be met if diffraction from a set of planes is to occur. *n* is called the order of diffraction. It may be any integral value which is consistent with $\sin\theta$ not exceeding unity, and is equal to the number of wavelengths in the path difference between rays scattered by adjacent planes. Therefore for fixed values of λ and *d*, there may be several angles of incidence $\theta 1$, $\theta 2$, $\theta 3$,… at which diffraction may occur, corresponding to $n = 1, 2, 3,\ldots$. So in a first order diffraction ($n = 1$), the scattered rays 1′ and 2′ of *Fig 2.12* would differ in path length (in phase) by one wavelength. The rays scattered by all the atoms in all the planes are therefore completely in phase, and reinforce one another (constructive interference) to form diffracted beam in the direction shown. In most other directions of space the scattered beams are out of phase, and null each another (destructive interference).The diffracted beam is generally weak compared to the incident beam as the planes reflect only a small fraction of the energy incident on them. So in summary we can say, in a perfect crystal where atoms are arranged periodically in space, in a few directions, those satisfying Bragg's law, the scattering is strong; as a result diffraction is observed. The angle at which diffracted beams are seen allow one to deduce the interplanar spacing *d* and thus to identify the composition of samples, their state of strain, material texture and epitaxial relation to substrate, among other aspects, such as crystallite size.

2.3.2 XRD setup

The next section describes the optics of the main parts of a Bruker Advance Diffractometer (the system used in this work) as shown in the diagram.

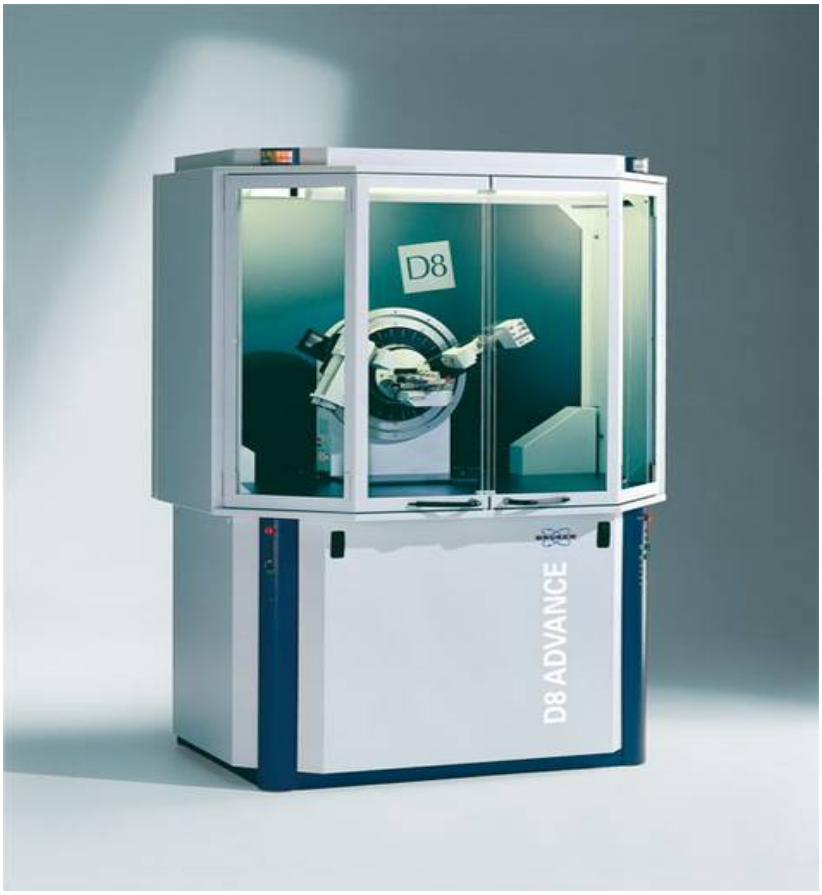

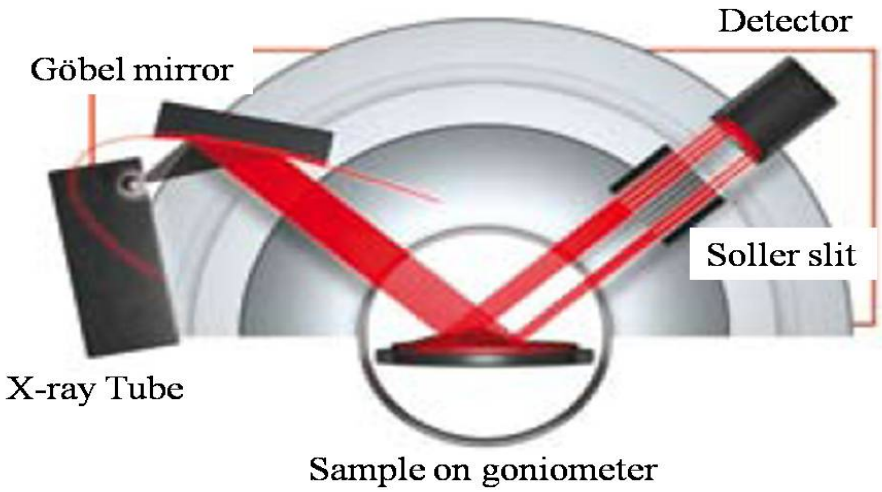

Fig 2.14: Bruker D8 Advance Texture Diffractometer [15], and a simple diagram of optics used in this instrument is shown below [16].

In XRD, a collimated beam of X-rays typically ranging from 0.5-2.5 Å is used as a source. For diffraction a monochromatic X-ray source is needed and the source is generally a metal anode bombarded by high energy electrons which gives off both characteristics line spectrum X-rays and continuum (bremsstrahlung) radiation. Generally the stronger Kα characteristic line radiation is used, and the Kβ radiation is filtered. In the Bruker system shown in *Fig 2.14* a Cu Kα X-ray source is used in which $\lambda = 1.54 \times 10^{-10}$ m (1.54 Å) is produced. The purpose of the Göbel mirror (a curved mirror) is to collimate the divergent beam coming from the point-like source in the X-ray tube anode. The mount in the diffractometer where the sample sits is called the goniometer. The goniometer allows the altering of orientation of the sample. Depending on the number of degrees of freedom of goniometer, and the allowed movement of the source and/or the detector the XRD system can be called a 'one-circle', 'two-circle' diffractometer …etc. The diffractometer used for this thesis work is a 'four-circle' diffractometer, a three circle goniometer plus a movable detector. The function of the soller slit is to remove any randomly scattered non-parallel X-rays. The detector used is a scintillation detector, which is a single photon detector. When the incident X-ray strikes the fluorescent crystal (scintillator) at the front of the detector a visible photon is produced. A photocathode struck by a photon ejects an electron. A series of dynodes after the scintillator/photocathode amplifies the electron into a detectable electrical pulse.

As stated earlier in the discussion of Bragg's law using XRD one can address issues related to crystal structure of solids. The crystal information which can be extracted includes-

- identification of unknown materials phases
- lattice constant and symmetry measurement
- orientation of single crystals and preferred orientation of polycrystals
- crystal quality (of bulk and thin crystal phases) measurement
- quantification of crystal defects, stress etc.

In addition it is a non-destructive technique.

Different XRD modes are used to examine the nanostructures grown in this work as follows-

- ***θ-2θ* mode** – This mode is used to study which crystallite planes are parallel to the substrate surface, and thus give evidence either for deposit polycrystallinity or texture. The angle between the source and the scattered beam (*2θ*) at which diffraction is seen defines the interplaner spacing (*d*) of the layers responsible. The symmetrical source/scatter beam arrangement means we only see contribution from planes parallel to the substrate.
- ***ω* (or rocking curve) mode** – In case any evidence is found for texture structure in the *θ-2θ* mode, this mode reveals the degree of preferential alignment.
- ***ϕ* mode** – This mode is to study the in-plane alignment to determine epitaxial relationship if there is evidence of highly textured growth.

2.4 Scanning Electron Microscopy (SEM)

An electron microscope is a type of microscope used to magnify objects on a very fine scale. It uses a particle beam of high energy electrons to illuminate a specimen, and create a highly-magnified image. The scanning electron microscope (SEM) is a type of electron microscope that builds up the images of the sample surface point by point in a time sequence by scanning it with a high-energy beam of electrons in a raster scan pattern. The electrons interact with the atoms that make up the sample producing signals that contain information about the sample's surface topography, composition and other properties such as electrical conductivity. A field emission SEM (FESEM) is a type of SEM where a field-emission cathode in the electron gun of a SEM provides narrower probing beams at low currents as well as high electron energy, resulting in both improved spatial resolution and minimized sample charging, and damage. It is used for applications which demand the highest magnification possible. Both FESEM and ordinary SEM with a thermoionic gun source have been used in this work. The types of signals produced by a SEM as shown in *Fig 2.15* include, secondary electrons (SEs), back-scattered electrons (BSEs), characteristic X-rays, light (CL), specimen current (SC), transmitted electrons (TEs) and Auger electrons (AE).

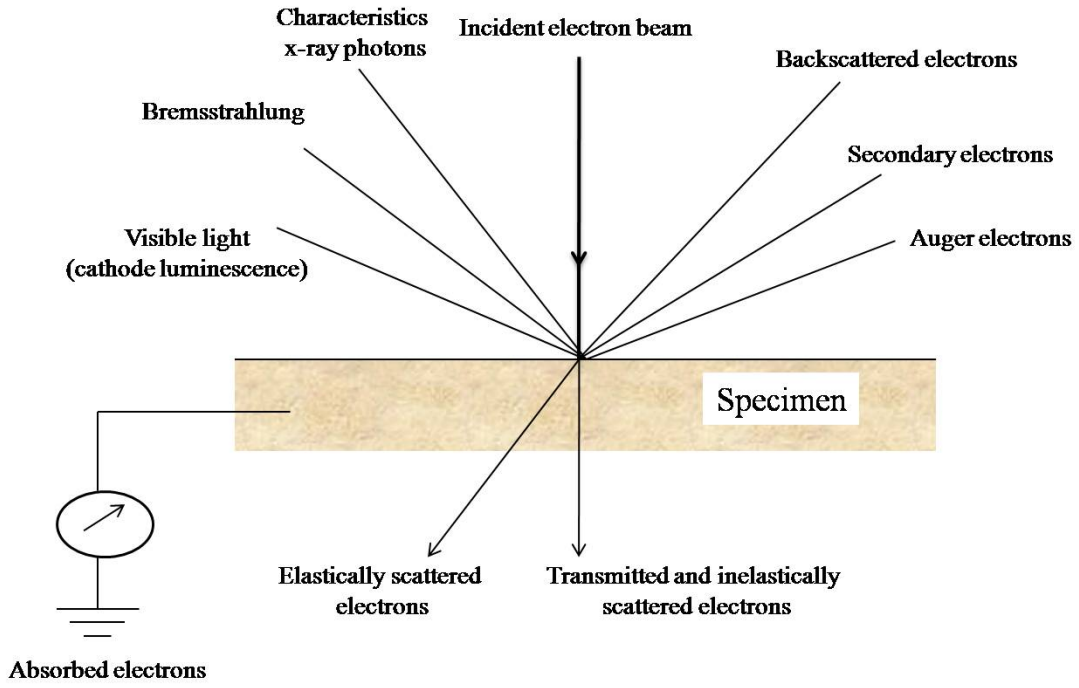

Fig 2.15: Types of emission from a specimen surface excited by the primary incident electrons in a SEM instrument.

SEs are sample electrons excited from the top surface layer of the specimen (0-10 nm). They are defined as having energy range 0-50 eV with the majority having energy of 3 to 5 eV. They produce the image of the surface of the sample and give information on sample topography. The emission of secondary electrons from each point on the specimen surface is dependent on its shape. BSEs are scattered beam electrons that emerge from greater depths in the sample. They are defined as electrons those having energy greater than 50 eV with the majority having energy approximately ¾ of the incident electron beam (probe energy). The number of BSEs that are emitted is strongly dependent on the mean atomic number of the specimen at the point of impact of the beam. So as the atomic number increases, the greater the number of electrons that are backscattered. BSEs give depth information and atomic number contrast within the image. Thus BSE images can provide information about the distribution of different elements in the sample. Characteristic X-rays are emitted when the electron beam removes an inner shell electron from the sample, causing a higher energy electron to fill the shell, and release energy as an X-ray with characteristic energy. These characteristic X-rays are used to identify the atomic composition, and measure the abundance of elements in the sample. CL light is

generated by some specimens that contain electroluminescent materials. CL will be described in more detail in the next section of this chapter. SC is the electron flow out of the specimen to earth, and if an amplifier is placed in the return path of electrons to earth its value can be measured, and can be also be used for imaging. TEs can be detected provided the sample is exceptionally thin. AE are unscattered electrons produced via ionization of sample atoms, and have energies characteristic of the atoms.

The most common or standard detection mode, secondary electron imaging or SEI is used to produce two dimensional scan with topographical feature information about the specimen. Secondary electron detectors are common in all SEMs, but it is rare that a single machine would have detectors for all possible signals. The signals result from interactions of the electron beam with atoms at or near the surface of the sample. SEM can produce very high resolution image at or near the sample surface revealing details at nm scales due to the small wavelengths of higher energy electrons which allows better microscopic resolution. In case of field emission this resolution is much better and produces clearer, less electrostatically distorted images. Also high quality, low voltage images are obtained with negligible electrical charging of samples.

Fig 2.16: Hitachi S-4300 field emission system [17]

The FESEM instrument used for much of the present thesis work is a Hitachi S-4300 field emission system as shown in *Fig 2.16*. The S-4300 is a computer controlled high resolution FESEM which produces exceptional images at both normal and low operating voltages. The resolution of this instrument is 1.5 nm at 15 kV and 2.5 nm at 5 kV. The accelerating voltage ranges from 0.5 to 30 kV.

2.5 Cathodoluminescence (CL)

CL is one type of luminescence technique where the excitation source is a beam of electron as described in section 2.2. In a typical SEM setup upon bombardment by beam electron, certain materials such as phosphors, semiconductors and insulators may emit photons in the UV and visible energy ranges along with SEs, BSEs, X-rays etc. It is possible to detect this light using appropriate equipment. The excitation process in CL is described schematically in *Fig 2.17* and the other steps are same as described in section 2.2.1. CL occurs because the injection of a high energy electron beam onto a semiconductor results in the promotion of electrons from the VB into the CB, leaving behind a hole. The various recombination processes are then just those found in any luminescent system, as discussed previously. However the small e-beam excitation spot size and scanning capability of SEM means that the CL-SEM optical information can be obtained with high spatial resolution. So CL spectroscopy has applications in the study of semiconductors, and impurity effect therein with spatial selectivity. While the spatial resolution of CL is not down to the nm level as in the case for SEs, it is still well within the 100's of nm range. The CL emitted is generally collected by an in-situ mirror and guided to a spectrometer external to the SEM system.

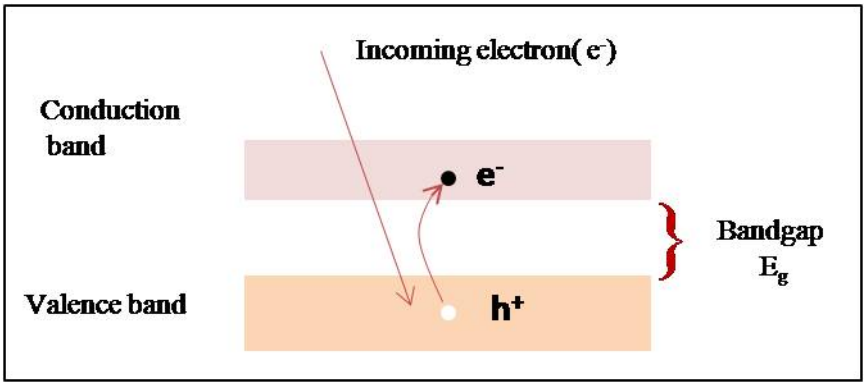

Fig 2.17: Schematic illustration of excitation process in CL where it shows the initial states before a beam of electron interacts with valence band electrons; the rest of the process of thermalisation and recombination is same as luminescence process described in *Fig 2.4.*

The CL study in this thesis for ZnO nanostructure sample is done using a variable temperature (5-300 K) CL setup mounted on a FEI quanta 200 SEM (the Institut Neel, CNRS, Grenoble, France). The Quanta 200 SEM from FEI is a special type of high performance SEM. It is equipped with a Schottky-type emission gun for good spatial resolution. The CL detection system consists of a parabolic mirror, a grating monochromator and a liquid-nitrogen-cooled CCD camera for measurements of CL spectra, and a photomultiplier tube for measurements of monochromatic CL images. The highly focused beam of electrons impinges on a sample and induces it to emit light from a localized area. This light is collected by an optical system, in this case a parabolic mirror. From there, a fibre optic transfers the light out of the microscope where it is separated by a monochromator, and then detected with a CCD camera or a photomultiplier tube.

2.6 References

[1] H. Morkoc and U. Ozgur, *Zinc oxide Fundamentals, materials and Device technology*, WILEY-VCH Verlag GmbH & Co. KGaA, 2009.

[2] R. S. Wagner and W. C. Ellis, Applied Physics Letters 4 (1964) 89.

[3] A. P. Levitt, *Whisker Technology*, Wiley-interscience, 1970.

[4] E. W. Williams and H. B. Bebb, Edited by R. K. Willardson and A. C. Beer (Academic, New York) Vol. 8 (1972) 181.

[5] G. F. Neumark, I. L. Kuskovsky, and H. Jiang, *Wide Bandgap Light Emitting Materials and devices*, Wiley-VCH, Germany, 2007.

[6] E. I. Rashba and M. D. Sturge, *Excitons*, North-Holland Publishing Company, Netherlands, 1982.

[7] D. C. Reynolds and T. C. Collins, *Excitons Their Properties and Uses*, Academic Press Inc. New York, 1981.

[8] V. I. Sokolov and K. A. Kikoin, *Excitons Bound to Impurities of 3d Elements in II-VI Compounds*, Soviet Scientific Reviews Published by Harwood Academic Publisher, 1989.

[9] P. Y. Yu and M. Cardona, *Fundamentals of Semiconductor, Physics and Material Properties*, Springer, Germany, Ed. 3, 345-369, 2005.

[10] S. Perkowitz, *Optical Characterization of Semiconductors: Infrared, Raman and Photoluminescence Spectroscopy*, Academic Press Ltd., London UK, 1993.

[11] E. F. Schubert, *Light-Emitting Diodes*, Cambridge University Press, Cambridge, UK, Ed. 2, 2006.

[12] J. Jimenez, *Microprobe Characterizations of Optoelectronic Materials*, Taylor and Francis Books, Inc., 2003.

[13] B. K. Meyer, H. Alves, D. M. Hofmann, W. Kriegseis, D. Forster, F. Bertram, J. Christen, A. Hoffmann, M. Straßburg, M. Dworzak, U. Haboeck, and A. V. Rodina, Physica Status Solidi (b) 241 (2004) 231.

[14] B. D. Cullity and S. R. Stock, *Elements of X-Ray diffraction*, Prentice-Hall, New Jersy, 2001.

[15] http://www.bruker-axs.de/d8_advance.html,

[16] http://www.bruker-axs.de/uploads/tx_linkselector/Goebel_Mirrors_DOC-S88-EXS030_V2_low.pdf,

[17] http://www.coax.co.th/ei/image/s4300.jpg,

Chapter 3

Well-aligned ZnO nanostructures growth and characterization

In this chapter, a detailed description of ZnO nanostructure growth is given. As mentioned in previous chapters, ZnO nanostructures are grown using the VPT technique. The main focus in this chapter is on growth of well-aligned and good crystalline quality ZnO nanostructures and methods to achieve this. Consistent reproducibility and two types of nanostructure morphology, nanorod and nanorod/nanowall have been investigated. Both types of morphology have been characterized using FESEM, TEM, XRD and PL.

3.1 Introduction

VPT is the most widely used method of ZnO nanostructure growth, which is already discussed in detail in chapters 1 and 2. Among various methods of source vaporization used in VPT including thermal evaporation (by heat), laser ablation (by photons), sputtering (by positive ions) and electron beam evaporation, thermal evaporation is widely used for 1D nanostructure growth. To some extent control over the shape and size of the nanostructures can be achieved by modification of the various parameters related to a particular method [1]. There are several processing parameters such as substrate type and orientation, carrier gas (including gas species and its flow rate), material source, substrate temperatures, evaporation time period,

which can be controlled and need to be selected carefully before and during the vaporization [1, 2]. For example, in ZnO growth on SiO_2 substrates by the MOCVD method, ZnO quantum dots have been obtained when nitrogen dioxide was used as the oxygen source [3], whereas 1D ZnO nanostructures were obtained when molecular oxygen was used as the oxygen source [4].

Supersaturation of vapour species is another important factor and is closely related to the growth behaviour of the nanomaterial. It is now generally accepted that the control of supersaturation is a prime consideration in obtaining 1D nanostructures, because there is strong evidence that the degree of supersaturation determines the prevailing growth morphology [5]. In principle, it is possible to process many materials into 1D nanostructures using VPT by controlling the supersaturation at relatively low levels. A low supersaturation is required to obtain whisker growth, where a medium supersaturation supports thin film or bulk crystal growth [6]. At high supersaturation, powders are formed by homogeneous nucleation in the vapour phase [7]. Supersaturation can be modulated through controlling the experimental parameters. So, for material synthesis, it is important to investigate the growth behaviour under different conditions which favour the controlled growth of nanostructures.

In the next section the variation in growth behaviour of nanostructures resulting from the variation of experimental parameters is discussed briefly. This discussion is built upon previously reported work by Grabowska *et. al* [8] in conjunction with the current work in this thesis. Later in this chapter we will discuss in detail the growth process for well aligned ZnO nanostructures using the VPT method and will draw conclusions about the growth conditions necessary for aligned nanostructure growth. Among the various types of nanostructures which are possible to grow using VPT, we will concentrate mainly on nanorod and nanorod/nanowall structures of the type shown in *Fig 1.2*. The nanorod morphology has good potential for device fabrication. In addition to this the presence of nanowalls can provide electrical connections to the aligned nanorods, as well as offering increased surface areas for e.g. sensor applications.

3.2 Parameters of growth

The main parameters which were varied in this work to investigate the growth behaviour and to yield different morphologies were the following –

- Substrate type and orientation
- Catalyst type
- Thickness of catalyst
- Growth temperature
- Carrier gas flow rate
- Ar flushing time before start of growth
- Growth duration

3.2.1 Substrate type and orientation

Proper substrate selection is necessary to achieve oriented (aligned) growth of nanostructures. Si, sapphire (Al_2O_3), and ZnO buffer layered Si (among others) have been used previously by many research groups to study the most suitable substrate for ZnO growth [1, 9-11]. Among these different substrates, ZnO nanostructure growth on Si is very common for the following reasons-

- Si is easily available and of relatively low cost.
- Doped Si is a good conductor, and thus for electrical applications of ZnO nanostructures, a Si substrate is very suitable.

However, growth on Si is complicated by two factors-

- Si generally has an amorphous native oxide (SiO_2) and on which one cannot achieve aligned growth.
- The lack of epitaxial matching to Si means that the nanostructures grown are generally not aligned normal to the substrate and the growth direction is random, even if the native oxide is removed.

ZnO *c*-plane and Al_2O_3 *a*-plane surfaces have less than 0.08% mismatch for certain directions, giving rise to a good epitaxial interface between the (0001) ZnO and the

(11-20) Al_2O_3 [12, 13]. Thus ZnO nanorods can be grown vertically on an *a*-plane (11-20) Al_2O_3 substrate. Since *m*-plane (10-10) Al_2O_3 substrate has a tilt angle of 30^o with respect to the *a*-plane, and ZnO (0001) is incompatible with the (10-10) plane, ZnO nanorod with a growth axis (0001) on *m*-sapphire will tilt 30^o with the substrate normal.

- Growth using other orientations of Al_2O_3 as substrates e.g. *r*-plane, *c*-plane Al_2O_3, does not yield as well-aligned nanostructures as on *a*-plane, due to epitaxial mismatch.
- The main disadvantages of sapphire are that it is an electrical insulator and expensive.
- ZnO nanostructure growth on ZnO buffer layers is less attractive due to the fact that ZnO buffer layer deposition on Si by e.g. Pulsed Laser Deposition (PLD) involves another growth step and increases the process cost and complexity.

3.2.2 Catalyst type

Metal catalyst islands on the substrate surface are used to act as nucleation sites, control the position of the nanorods and may also enable the VLS growth mechanism. For well aligned nanorod growth, VLS is the best mechanism in VPT growth as it is very straight forward. The only step before growth is the incorporation of a metal catalyst on substrate surface which will form the liquid alloy droplet at high temperatures. This metal catalyst can be placed either as particles or by deposition. In the VLS mechanism various metals including gold, platinum, nickel, silver, palladium or copper can be used as a catalyst [14]. The selection of a catalyst is an important factor and in some cases for VLS growth of compound crystal structures, metal compounds are used as catalyst [15, 16]. The selection of the catalyst depends on number of factors. Those factors are –

- Reaction temperature
- VLS interfacial energies
- Distribution coefficient and inertness of the reaction products

For ZnO nanostructure growth by the VPT method in our system, it was found that Au is the most suitable catalyst. It doesn't interact chemically with the sapphire substrate or the grown ZnO nanostructures and cross-contamination by Au appears quite small. The melting point of the catalyst is a very important factor for liquid alloy formation. The melting point of Au particles depends on their size as lower temperatures are required to melt smaller particles due to surface energy effects. If a deposited film of Au is used, the melting point changes with the thickness of the film. In this thesis work, all nanostructures of ZnO have been grown using evaporated Au thin films of nominal thickness 5 nm. The usual growth temperature in our system is >900^{o}C which is a very suitable temperature to form the Au liquid nanoclusters needed for the VLS mechanism, using 5 nm Au films, as discussed below.

3.2.3 Thickness of Catalyst

The thickness of the catalyst layer is found to be an important factor governing the aspect ratio and the density of ZnO nanorods. At elevated temperatures, Au forms nanoclusters due to capillary forces, which control the aspect ratio of nanorods. The nanoclusters size is dependent on the thickness of the evaporated film. It has been observed that in films of Au up to 50 Å thick, the number of nanoclusters i.e. density increases with increasing film thickness. The average diameters of nanoclusters are approximately constant up to the film thickness of 20 Å and increase slightly at 50 Å thickness. At film thickness of ≥50 Å the number of nanoclusters decrease and their diameters increase with the increase in film thickness [8]. Therefore, 50 Å thickness can be identified as a critical thickness after which the nature of clusters changes with increasing thickness. It has been found that the melting point of 50 Å Au thin film is ~977^{o}C [8, 17]. Another notable factor in informing our decision to use 50 Å thickness Au is the fact that, at different growth temperatures, 50 Å films can form either separated nanoclusters (higher temperature ~950^{o}C) or foam-like ZnO nanowall structures (lower temperature 900^{o}C), both of which have interesting properties. From the study performed by Grabowska *et al.* on the effects of Au thickness and in light of the nanostructure properties studied in this work, we have

thus chosen 50 Å Au film thickness to grow well-aligned ZnO nanorods and nanorod/nanowall morphologies.

3.2.4 Growth temperature

The temperature selection mainly depends on the volatility of the source materials, and catalyst type and thickness. Using a solid source, the temperature chosen is slightly lower than the melting point of the source material so as to achieve the required supersaturation levels. The usual growth temperature of ZnO nanostructures using graphite as a source powder for carbothermal reduction is ≥850^{o}C, when the substrate and source powder temperature is the same i.e. substrate is placed on top of powder. Otherwise it has been observed that if the substrate is placed beside the source powder (~3 cm downstream) the growth occurs only at ≥900^{o}C. In fact it is likely that at lower growth temperatures both the VLS and VS mechanisms are observable in our system. Due to high affinity of Zn towards Au molten nanoclusters, Zn may nucleate at Au nanoclusters and react with O_2 to form nanostructures via a VS mechanism even if the Au does not melt. In some cases where different carbon source powders are used, growth is found to occur at much lower temperatures (even down to 750^{o}C) by this mechanism. This is discussed in detail in chapter 4. In those cases ZnO itself is reduced to yield Zn vapour at a much lower temperature due to highly active carbon, i.e. the CTR occurs at lower temperature. In this work, for the normal growth using graphite we have concentrated mainly on two temperatures, 900^{o}C and 950^{o}C, where we obtain the nanorod/nanowall and nanorod morphologies, respectively.

3.2.5 Carrier gas flow rate

Among the various parameters mentioned above, Ar was selected as carrier gas from the beginning as successful depositions had been previously reported using this gas [2, 18]. The flow rate must be chosen to control the Zn vapour pressure and is therefore directly related to the rate of evaporation. The concentration of O_2 during growth is also an important factor. O_2 strongly influences the stoichiometry of the

deposit. If the amount of O_2 is higher or lower than the optimum range, ZnO nanostructure growth will be suppressed. In our growth system it has been found that an Ar flow rate of 90 sccm is optimal, for nanostructure growth.

3.2.6 Ar flushing time before growth starts

As mentioned previously Ar gas is used as a carrier gas for the vapour species during growth. Prior to growth Ar is switched on to flush out excess oxygen in the chamber, as the carbon which is used as a source powder is very reactive with O_2. Along with the flow rate, the flushing time is also an important factor to optimize the amount of O_2 required for growth. Typically 12-15 minutes flushing time is used before increasing the temperature to the growth value. Some experiments have been performed in this work with various flushing times so as to check the effect on growth. During the flushing time, the pre-growth preparation, including source powders measurement, mixing and placing powders and substrate in the proper position of boat is usually done. After placing the boat inside the furnace tube (~12-15 minutes after the Ar flow was started), the open end of the tube is closed and temperature ramping followed by growth is started immediately. In recent experiments we have observed that if we place the boat inside at the time mentioned above and start temperature ramping 30 minutes after Ar flow started (i.e. ~15-18 minutes after boat placed inside furnace) no growth is observed. If temperature ramping is started after 20 minutes instead of 30 minutes of Ar flushing, growth is observed. In other experiments, where the boat was placed inside the furnace immediately before the temperature ramping is started (not 12-15 minute after flow starts as mentioned above), growth is observed, even if the Ar flow is on for 1.5 hours prior to growth. In this case the tube end remains open to facilitate introduction of the boat and is closed only when temperature ramping begins. Also in the presence of O_2 flow (along with Ar) no growth was observed as the carbon powder quickly reacts with O_2. These all experiments indicate an optimum flushing time of ~15 minutes, to leave an optimum residual O_2 concentration in the tube or close to the boat at the sample and powder surfaces. Too long a flush removes all the

O_2 and too short leaves excess O_2 which reacts with the carbon and consumes it, preventing growth.

3.2.5 Growth duration

The growth duration is a very important factor to optimize the length of the nanostructures. It is observed that with increased duration of growth, the length of nanorods increases. Usually in our laboratory the growth temperature is maintained for 30 minutes or 60 minutes (excluding the time taken for the furnace to reach the set temperature, which is ~18 minutes) The length of nanorods is longer for 60 minutes growth than for 30 minutes, however the nanorod lengths are not proportional to growth times and it is expected that beyond 60 minutes the rate of growth will rapidly drop-off as the bulk of the residual oxygen in the growth chamber has been consumed during the deposition process, as well as being flushed out by the continuous Ar flow.

3.3 Experimental details

The experimental setup and procedure of the VPT method is described in more detail in section 2.1. For the experiments discussed in this work both Al_2O_3 and Si/SiO_2 substrates have been used for nanostructure growth though mainly Al_2O_3 in this chapter. For well-aligned nanostructures *a*-plane Al_2O_3 substrate was used. In both cases the substrate is first ultrasonically cleaned in alcohol (isopropanol) before the growth experiment and then dried by a nitrogen flow. The next step is the deposition of thin Au film on the substrate by a thermal evaporation process in an evaporation chamber (Bell jar). The nominal thickness of Au used here is 5 nm. The thickness is measured by a quartz crystal thickness monitor (model TM – 350 by Maxtek. Inc.). The source powder is prepared by mixing ZnO and graphite in the ratio 1:1 by mass with a total mass of 0.012g. The purity of ZnO powder and graphite powder is 99.9995% (Alfa Aesar) and 99.9999% (Alfa Aesar), respectively. Both powders are thoroughly mixed by a mortar and pestle. The source powders are placed on a small multisil (quartz) or alumina boat and the substrate is placed directly above the source

powders on the boat with the growth surface facing the powders or just beside the powders in some experiments performed at the beginning of my Ph.D work. The multisil or alumina boat is placed in the central part of furnace. A high purity (99.999%) Ar flow of 90 sccm is used from ~12-15 minutes prior to the start of the growth and during the growth period. The total growth time is 48/78 minutes (for all samples shown in *Fig 3.1, 3.2* and *3.4*). The first 18 minutes is the time required to reach the set temperature of the furnace and the next 30/60 minutes is the growth time. Following this the furnace is switched off and the samples are allowed to cool down to room temperature without quenching.

Samples were characterized by high resolution FE-SEM (Hitachi S-4300 field emission system), TEM (JEOL2000FX operating at 200 kV), XRD (Bruker AXS D8 advance texture diffractometer) and low temperature PL spectroscopy (Bomem Hartmann & Braun DA8 FT spectrometer).

3.4 Nanostructures study

The FESEM study has been performed for samples grown at various temperatures and on different substrates, and based on the FESEM images further TEM, XRD and PL studies have been undertaken for ZnO nanorod/nanowall and nanorod samples.

3.4.1 FESEM study

The FESEM images shown in *Fig 3.1* show the results of six different growth temperature experiments on *a*-sapphire. The images are 30^{o} tilted views of the samples.

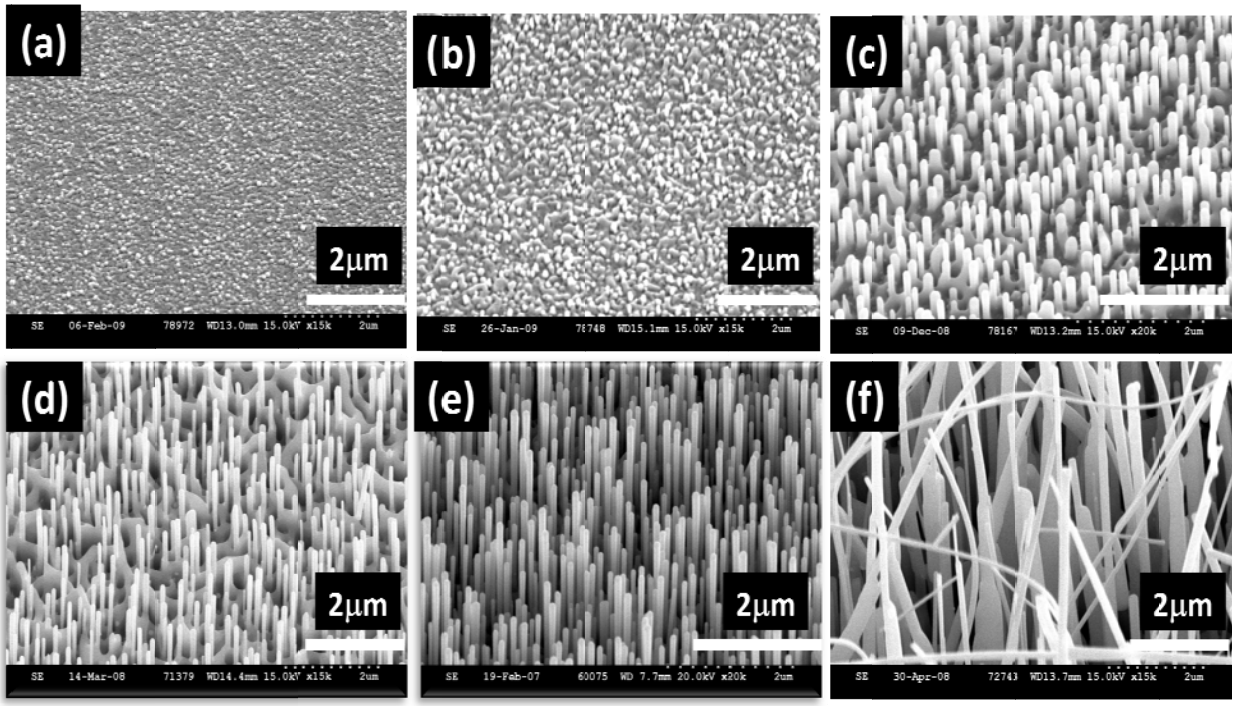

Fig 3.1: FESEM images of ZnO nanostructures sample on *a*-sapphire at (a) 750^{o}C (b) 800^{o}C (c) 850^{o}C (d) 900^{o}C (e) 950^{o}C (f) 1000^{o}C (In all cases the substrate was placed directly above the source powders).

Growth at different temperatures, with different gold thicknesses, with different substrates have been reported previously [1]. The parameters have been narrowed down based on previous work in our group and others as described earlier and my

investigation has been conducted in regions of parameter space where ZnO nanostructures are known to grow with reasonably good alignment.

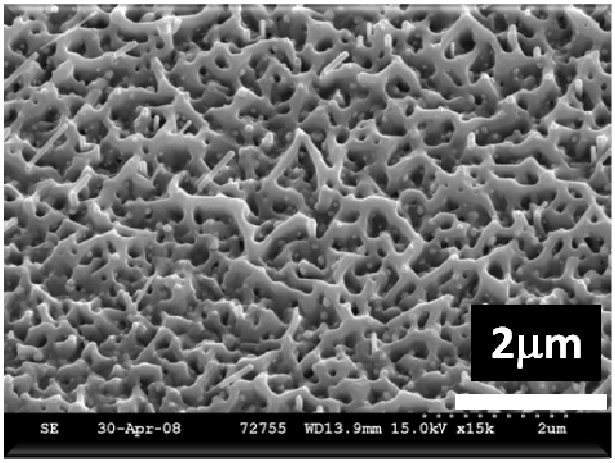

Fig 3.2: FESEM image of sample grown at 850^{o}C by placing substrate beside source powders.

From *Fig 3.1(a)* we can see, no growth occurs at 750^{o}C. At 800^{o}C nucleation commences, with significant nanostructure growth beginning at 850^{o}C. We found no growth is observed below 900^{o}C for samples where the substrate was placed beside source powders (substrate placing shown in *Fig 3.3 (b)*). This result is consistent with those reported previously by Dr. Justina Grabowska, a former member of our research group [8]. For substrates beside the source powder, nucleation of growth centres starts at 850^{o}C (*Fig 3.2*) and for substrates above the source powder, nucleation starts at 800^{o}C (*Fig 3.1 (b)*).

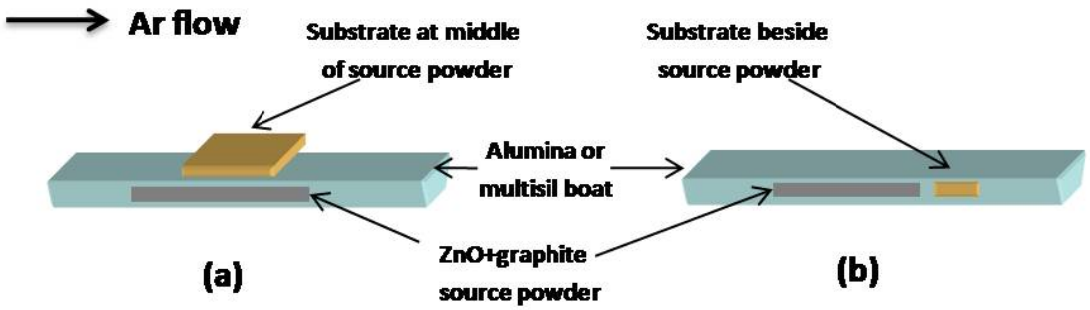

Fig 3.3: Substrate placing (a) directly above the source powders (b) beside the source powders at downstream.

In this thesis most of the growths were performed by placing the substrate directly above the source powders (as shown in *Fig 3.3 (a)*), ensuring the same temperature for both the source powder and substrate. This allows us to establish more consistent growth conditions and enhance deposition in the lower region of the temperature range. In *Fig 3.1(c)* grown at 850^{o}C, the nanorods are aligned with some nucleated wall structures, but are of shorter in height and of reduced density in comparison to samples grown at 900^{o}C. *Fig 3.1 (d)* and *(e)* show very dense and well aligned nanostructures, which are generally found on samples grown at 900^{o}C - 950^{o}C. The nanostructures growth at 900^{o}C and 950^{o}C are exactly the same in terms of their morphology, density and dimensions for both types of substrate placing. From this and from observing a significant number of samples grown in our laboratory, we can conclude that the temperature range necessary for well-aligned and uniform nanostructure deposition is approximately 900^{o}C to 950^{o}C. At 900^{o}C we typically see the mixed nanorod / nanowall structure, while growth at 950^{o}C yields mainly well-aligned nanorods. This variation in growth at higher temperatures occurs because the Au film beads up into well-separated droplets, inhibiting nanowall formation. The presence of nanowalls may be related to the incomplete formation of well separated Au droplets at lower growth temperatures, i.e. the Au forms a film of Au dots in close proximity or even touching. The boundaries between touching Au dots/droplets are expected to be particularly active for the VLS mechanism, which may account for the initial growth of walls. This morphology is very interesting as the nanowalls can actually be used as, for example, electrical interconnections between the nanorods. This network-like morphology can provide good electrical connections in a device application. Above 950^{o}C the length of the nanorods increase, with decreasing width, leading to an overall improvement the nanorod aspect ratio. We can see long nanorod (nanowire-like structures) in *Fig 3.1 (f)*. Above 1100^{o}C no growth is observed for both types of substrate positioning. At lower temperatures the absence of growth is due to the very low Zn vapour pressure. The rate of release of Zn vapour due to the CTR by graphite is insufficient to start nanostructure growth. At high temperatures the Zn and CO vapour pressures are so high that all residual O_2 is displaced from the tube. As our system uses residual O_2 in the quartz tube and boat for growth, this displacement inhibits the growth and formation of ZnO nanostructures. Some experiments to overcome the high

temperature displacement of residual O_2, where a stream of O_2 was mixed with the Ar carrier gas were performed. However due to very high reactivity between graphite and O_2, the carbon source powder was rapidly consumed before CTR could take place, resulting in little or no nanostructure deposition.

FESEM images of ZnO nanostructures grown on Si/SiO_2 substrates are shown in *Fig 3.4 (a)*, so as to differentiate the types of morphology and alignment of growth from that of *a*-sapphire, keeping all other growth conditions identical. Growth on Si results in unaligned nanorod, nanowall and nanosheet types of morphologies as observed in *Fig 3.4 (a)*. *Fig 3.4(b)* shows the growth on a Si substrate, where a ZnO buffer layer was deposited prior to growth. The ZnO buffer layer was deposited using a PLD system. In this case no gold was deposited prior to growth, and all other growth conditions were identical to those mentioned previously. Nanostructures grown on buffer layer are dense and partially aligned, but not as perfectly aligned as on *a*-sapphire.

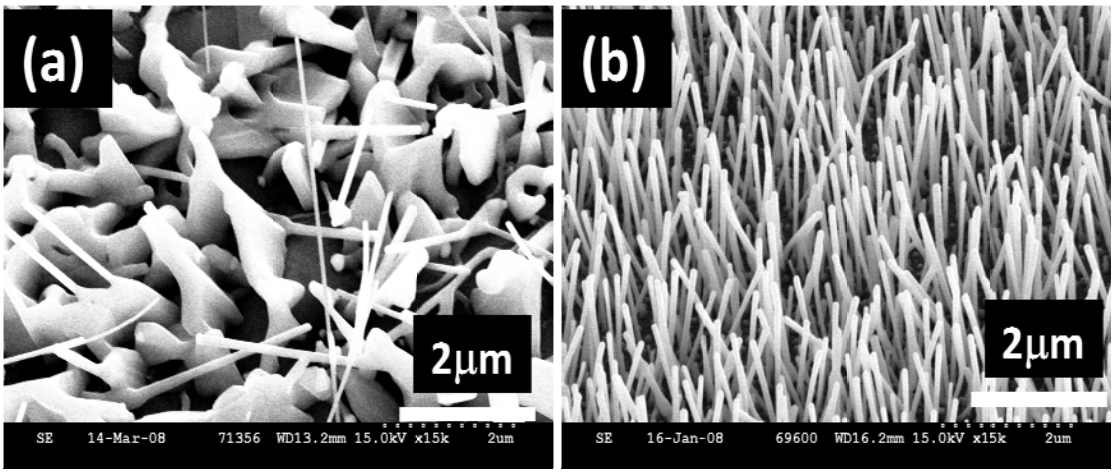

Fig 3.4: FESEM images of ZnO nanostructure grown (a) on Si/SiO_2 substrate at 900°C (b) on Si with ZnO buffer layer (thickness 50 nm) at 850°C. For both samples growth duration was 30 minutes.

In *Table 3.1* we summarize the growth conditions for well-aligned nanorod and nanorod/nanowall morphology. Studying the FESEM images it is found that using *a*-sapphire substrates, 900°C and 950°C are the most interesting temperatures, as two

different aligned morphologies can be observed. The optical and other properties of ZnO are expected to vary when growth is performed at these two temperatures, due to the presence of foam-like wall structures in the samples grown at 900^{o}C. These two types of morphology are also of interest for nanostructure device applications. This potential for applications is why, in further study of ZnO nanostructures we have concentrated on the samples grown at these two temperatures on *a*-sapphire.

Table 3.1 Conditions for well-aligned ZnO nanostructure growth

Morphology	**Temperature**	**Substrate**	**Gold Thickness**
Nanorod/Nanowall	900^{o}C	*a*-sapphire	5 nm
Nanorod	950^{o}C	*a*-sapphire	5 nm

3.4.2 TEM study

Fig 3.5 (a)-(b) show TEM * images of a sample grown at 900°C, while *(c)-(d)* show TEM images of a sample grown at 950°C. Sample sections for TEM microstructural evaluation were made using standard focused ion beam thinning (FEI FIB 200 workstation operating at 30 kV using a Ga ion source operating with beam currents of 11 nA and 150 pA for box milling and final polishing, respectively [19]).

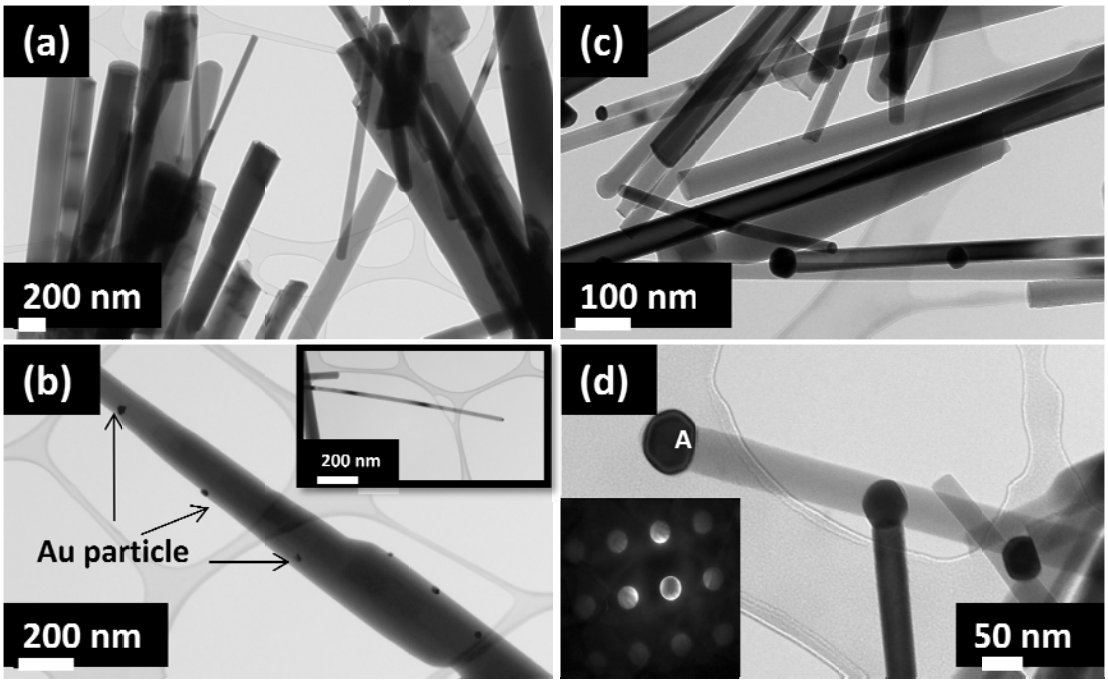

Fig 3.5: TEM image of samples grown on *a*-plane sapphire (a)-(b) at 900°C (b)-(c) at 950°C. Evidence of gold particles both at nanorod body and tip is shown in (b) and (d) respectively. The inset diffraction pattern at (d) was taken from the particle marked at A and shows a (233) Au zone normal.

In all of the TEM images we can see mostly good crystalline and defect-free nanorods. The sample grown at 900°C shows evidence that Au is not seen at the tip of all the nanorods (In *Fig 3.5 (a)* there is no evidence, but in other areas, one of which is shown in the inset of *Fig 3.5 (b),* we can see Au at the nanorod tip) which is expected for catalyst driven VLS grown samples. In *Fig 3.5 (b)* we also see evidence of Au along the nanorod body. Thus in the sample grown at 900°C, the VLS

* TEM was performed by Dr. Simon Newcomb of Glebe Scientific Ltd. Tipperary, Ireland.

mechanism did not work as predicted by theory [14]. Some of the Au particles stayed on the nanorod body and most of the tips of nanorods are without Au, showing evidence of both the VLS and VS growth mechanism as discussed earlier. Also as stated in section 3.4.1 due to the incomplete formation of separated Au droplets at lower growth temperatures, nanowalls may be formed but these are not seen in TEM due to the nature of specimen preparation. The continuous Au film might be unable to follow the normal VLS mechanism and thus this may explain the absence of Au particles at nanorod tips, at 900^{o}C.

The sample grown at 950^{o}C shows nanorods with Au at most of the tips (*Fig 3.5 (c)* and *(d))*. The selected area electron diffraction (SAED) pattern shown in the inset of *Fig 3.5 (d)* confirms the identity of the Au particles.

The TEM data shows, although both the VLS and VS mechanisms work from 900^{o}C, the VLS mechanism is more prominent from 950^{o}C. This data is consistent with the results published by Kumar *et. al* [20], and with the increased temperature resulting in Au melting, which facilitates the VLS mechanism.

3.4.3 XRD study

The XRD data of samples grown at 900°C and 950°C, showing nanorod/nanowall and nanorod morphologies are shown in *Fig 3.6.* From *Fig 3.6 (a)* and *(c)* we can see 3 prominent peaks which are ZnO (0002), ZnO (0004) and Al_2O_3 (11-20) at 34.46°, 72.58° and 37.78°, respectively. For the ZnO nanorod/nanowall sample (of the type shown in *Fig 3.1(d)* above and whose XRD data are shown in *Fig 3.6 (a)*) we can see an extra peak due to ZnO (10-11).

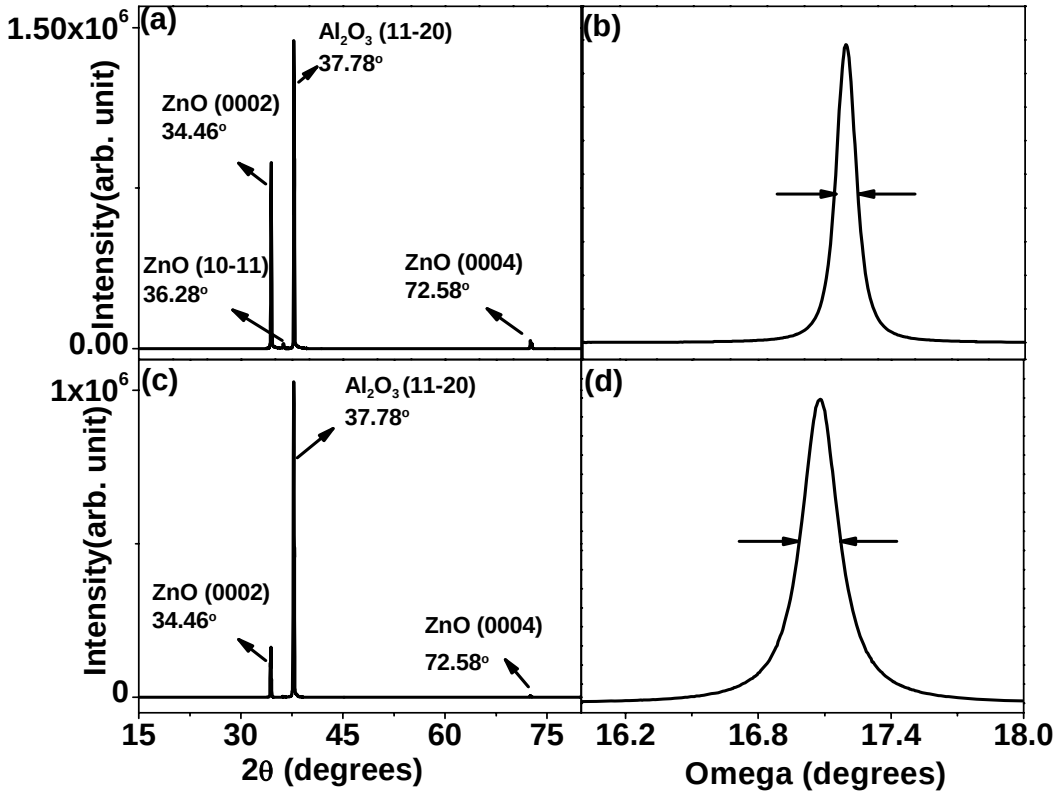

Fig 3.6: XRD data of two types of nanostructured samples grown at two temperatures. (a) and (c) are 2θ-ω scans of samples grown at 900°C and 950°C. (b) and (d) are rocking curve scans of the ZnO (0002) peaks of (a) and (c) respectively.

This extra peak is visible for ZnO nanorod/nanowall samples, while for samples with nanorods only (of the type shown in *Fig 3.1 (e)* above) the (10-11) peak is very weak and in some cases not detected at all. This provides some evidence that the ZnO (10-11) peak may be related to wall-like structures and some crystallite misalignment. In *Fig 3.6 (b)* and *(d)* we can see the rocking curve scans of the dominant ZnO (0002)

peaks shown at *Fig 3.6 (a)* and *(c)*, respectively. The FWHM of both samples indicated by the arrows are ~0.18^{o} and ~0.19^{o} respectively which indicated good crystallinity and alignment with respect to the substrate. The shift in centre omega angle is due to slight tilting of sample on the holder in XRD goniometer during specimen mounting.

3.4.4 Low temperature PL study

PL data is shown for the same two sample types discussed above, for which FESEM, TEM and XRD have been shown already. *Fig 3.7 (a)* and *(b)* (morphology shown in *Fig 3.1 (d)*) is the PL spectrum for nanorod/nanowall samples grown using alumina and multisil boat, respectively, and *Fig 3.7 (c)* and *(d)* is for the nanorod only samples (morphology shown in *Fig 3.1 (e)*) grown using alumina and multisil boat, respectively. These measurements were performed at 18 K. For all of the spectra, the same instrumental setup was used. The aperture of the detector in both cases enabled a spectral resolution of 5 cm^{-1}. The detector gain was set at 1 for both measurements. In terms of eV units, the spectral resolution was ~0.4 meV and number of co-added scans was 100. From *Fig 3.7 (a)-(c)* we can see three clear and dominant peaks at 3.3568 eV, 3.3608 eV and 3.3671 eV. As mentioned in previous chapters, for ZnO bulk crystals a range of sharp peaks in the UV PL spectrum have already been observed by several other authors and are labelled as I_0 to I_{11} peaks [21]. These peaks are associated with excitons weakly bound to defects (dopants in ZnO) [21]. According to the conventional labelling procedure, the peaks at 3.3568 eV and 3.3608 eV can be considered as the I_9 and I_6 peaks respectively, since for ZnO nanostructured samples, we can consider each nanorod as a single unstrained crystal of ZnO. To confirm this we used the XRD data in *Fig 3.6* and measured the interplanar spacing d (using Bragg's law $\rightarrow n\lambda = 2dSin\theta$) and compared this measurement with the literature value of d for a bulk ZnO crystal. For the ZnO (0002), (0004) and (10-11) peaks, the values of d are ~2.599 Å, ~1.300 Å and ~2.473 Å, respectively. The literature values for those peaks are 2.603 Å, 1.301 Å and 2.475 Å, which closely matches the value for d found in our experiments. Hence we can consider that the strain is minimal for our ZnO nanostructured samples.

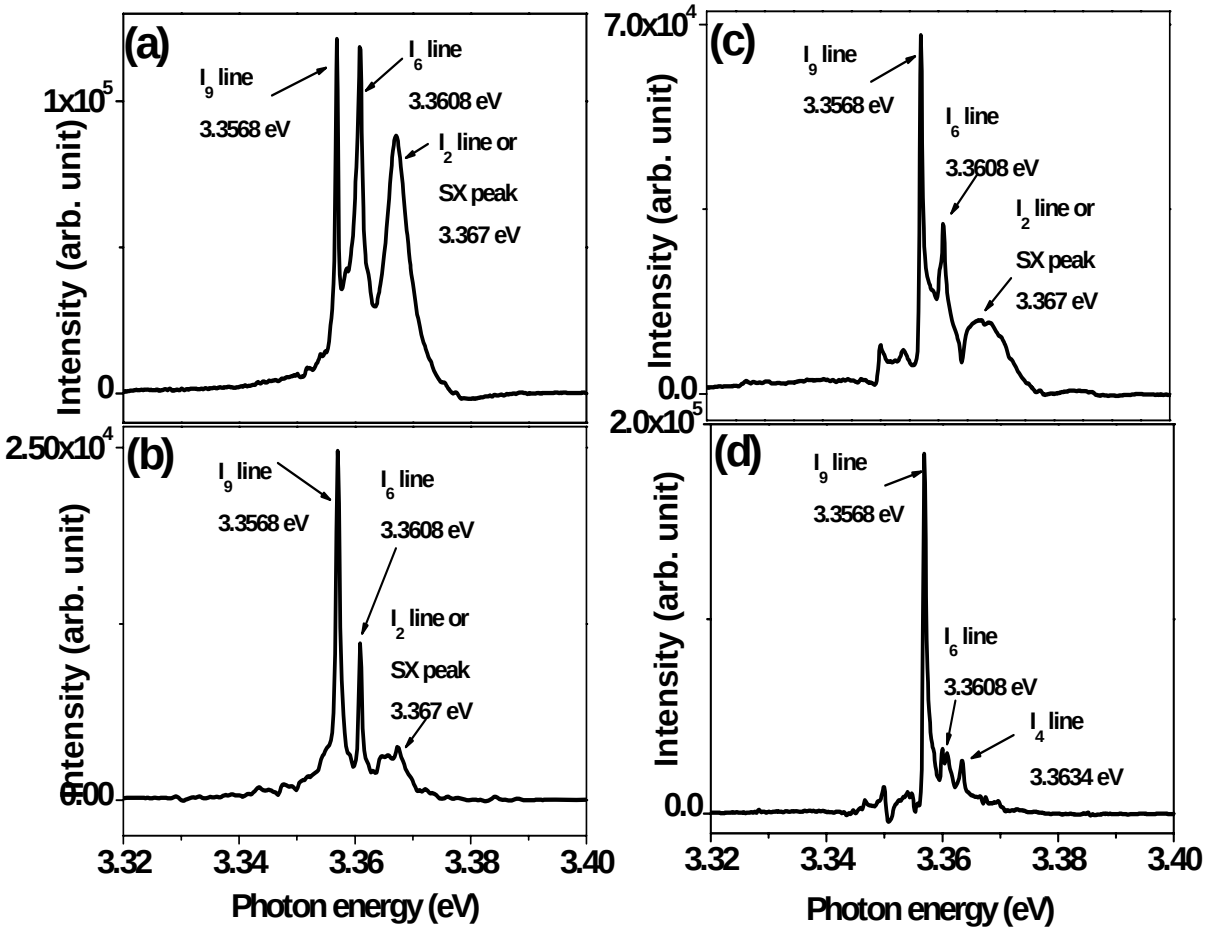

Fig 3.7: Low temperature (18K) PL data of samples grown at 900°C (a) using alumina boat (b) using multisil boat, and at 950°C (c) using alumina boat (d) using multisil boat.

The linewidths of the I_6 and I_9 lines for both samples are ~1.7 meV and ~0.6 meV, respectively which are comparable to bulk crystal values [21]. The peak at 3.3671 eV is referred to in the I-line series nomenclature as I_2. However, previous work from our group and others, as discussed above, has identified that this line is associated with ZnO nanostructures and we refer to it as the SX peak. The linewidth of the SX peak in the nanorod/nanowall sample is ~4.5 meV, noticeably broader than the other I lines, indicating that its origin may be quite different to the "normal" substitutional dopants. This line is seen mostly in the nanorod/nanowall sample and is detected in the nanorod only sample with some shorter basewalls and sidewalls.

Previous studies in the literature have identified the I_9 peak as due to an exciton bound at a substitutional In donor atom (i.e. In on a Zn site) [21, 22]. The ZnO powder which we use for the ZnO nanostructure growth in the VPT method contains a small amount of an In impurity at concentrations around the doping level. In our ZnO nanostructure growth we assume that the I_9 peak is due to this In impurity from the ZnO source powder. One previous report has suggested that In might preferentially aggregate at the surface of ZnO nanorods [23] but the various post-growth etching experiments we have undertaken on our nanorods do not support this suggestion.

The origin of the I_6 line is reported to be due to an exciton bound at a substitutional Al impurity. This has been discussed by Schilling *et al.* [24] who undertook implantation studies, where they found a correlation between Al implantation and successive annealing and an intensity increase of the I_6 line. In addition, according to Meyer *et al.* [21], secondary ion mass spectroscopy (SIMS) found Al was the dominant impurity in their ZnO samples, where the I_6 line was the dominant PL emission. In growth of ZnO on Al_2O_3, Al is always an important impurity due to diffusion from the substrate [25]. Two sets of data for each morphology have been shown to confirm the nature of this peak grown using different boats, as the alumina boat is also a source of Al and it might have some effect on the Al peak, while multisil i.e. quartz boat is not a Al source. From *Fig 3.7 (a)* and *(c)* (samples grown using alumina boat) we can see the Al peak intensity is comparatively higher compared to the two samples grown on multisil boat at *Fig 3.7 (b)* and *(d)*. But it is not very high, while with two source of Al from substrate and boat Al is expected to be the dominant peak compared to the I_9 peak and the multisil boat grown samples. Also from the PL data of large number of samples grown in our laboratory we found intensity of Al peak is inconsistent depending on which boat was used for growth. The peak at ~3.363 eV in *Fig 3.7 (b)* has recently been attributed to a hydrogen donor [26].

The most interesting and ambiguous PL feature is the line at 3.367 eV (the SX peak). It is generally observed in the ZnO samples which have high surface to volume ratios. It is reported that this peak is probably due to some surface related excitonic

emission [27]. However, at present there is no strong confirmation of the microscopic origin of the peak. Some suggestions have been made that this line is due to adsorbed O on the surface of ZnO crystals [28]. In our experiments we have observed the SX peak mostly in nanorod/nanowall samples. *Fig 3.7 (a)* represents a nanorod/nanowall sample, but *Fig 3.7 (c)* which is grown at 950^{o}C is labelled as nanorod sample also shows the SX peak with lower intensity. We have observed that the SX peak (whether strong or weak) is visible only in samples with clear evidence of a nanorod/nanowall morphology or with a nanorod morphology with base or side walls. In the sample grown at 950^{o}C nanowalls can be seen mostly at the bottom (some at side of nanorods) of the nanorod and very less in numbers and shorter in heights compared to 900^{o}C samples. The high intensity SX peak which can be seen in *Fig 3.7 (a)* has not been observed in any 950^{o}C grown sample, the intensity of SX peak in 950^{o}C grown samples are always same or less than shown in *Fig 3.7 (c)*. *Fig 3.7 (b)* shows that SX peak is not always very intense in dense nanowall sample also and indicates all ZnO nanostructure samples with nanorod/nanowall morphology do not show SX peak. In summary it can be conclude that the existence of the SX peak in PL spectra is always dependent on the presence of nanowalls, but the presence of nanowalls does not guarantee the presence of the SX peak. The surface-to-volume ratio of the nanorod/nanowall structures is similar or less to that of the nanorod only structures, which implies that the argument that the origin of the SX peak is solely due to adsorbed species such as O is incomplete. Our XRD data is also relevant for comparison with the PL data. In the XRD studies of samples with big and broad SX peak in PL, we found the ZnO (10-11) peak with significant intensity, whereas the peak intensity is below detection limit for samples without SX peak. The presence of the (10-11) peak in XRD indicates that there is crystalline inhomogeneity in the ZnO material in the nanowall/nanorod sample with some crystallites showing different orientations. There appears to be some correlation between the presence of the SX peak in PL and the (10-11) peak in XRD, which may hint that the origin of the SX emission in PL is related to defects associated with the differing crystallite orientations. The detailed study of the microscopic origin and nature of the peak is discussed in chapter 6. A detailed study including plasma treatments, UV exposure at high vacuum (a process conventionally used to desorb oxygen from ZnO surfaces)

and application of voltage at high vacuum and in various gas atmospheres have been performed in order to try to identify the origin of this peak.

3.5 Conclusion

From our FESEM data of samples grown at various temperatures, on different substrates and also from the previous work done by Dr. Justina Grabowska we can optimize the conditions to get reproducible well-aligned nanostructures. The nanorod-only morphology can be achieved at 950^{o}C and the nanorod/nanowall morphology at 900^{o}C. In our work we have found the growth of nanostructures is very reproducible. To use ZnO in nanodevices these two types of morphology are of great interest and the methods used here can produce high quality nanostructures showing excellent properties in TEM, XRD and PL studies. Nanowall structures are very interesting as they may serve as interconnections between nanorods and can be used as electrical networks. The optical properties of these two types of morphology have some differences and some of these properties and differences have been studied in more detail later in this thesis.

3.6 References

[1] J. Grabowska, K. K. Nanda, E. McGlynn, J. P. Mosnier, and M. O. Henry, Surface and Coatings Technology 200 (2005) 1093.

[2] Z. L. Wang, Journal of Physics: Condensed Matter 18 (2004) R829.

[3] S.-W. Kim, S. Fujita, and S. Fujita, Applied Physics Letters 81 (2002) 5036.

[4] S. Muthukumar, S. Haifeng, Z. Jian, Z. Zheng, N. W. Emanetoglu, and L. Yicheng, Nanotechnology, IEEE Transactions on 2 (2003) 50.

[5] Y. Yan, L. Zhou, L. Yu, and Y. Zhang, Applied Physics A: Materials Science & Processing 93 (2008) 457.

[6] W. B. Campbell, *Whisker Technology*, chapter 2, Wiley-Interscience, New York, 1970.

[7] N. Kobayashi, Y. Kawakami, K. Kamada, J. G. Li, R. Ye, T. Watanabe, and T. Ishigaki, Thin Solid Films 516 (2008) 4402.

[8] J. Grabowska, *Ph.D thesis*, Dublin City University, 2007.

[9] H.-M. Cheng, H.-C. Hsu, S. Yang, C.-Y. Wu, Y.-C. Lee, L.-J. Lin, and W.-F. Hsieh, Nanotechnology 16 (2005) 2882.

[10] Y. Li, M. Feneberg, A. Reiser, M. Schirra, R. Enchelmaier, A. Ladenburger, A. Langlois, R. Sauer, K. Thonke, J. Cai, and H. Rauscher, Journal of Applied Physics 99 (2006) 054307.

[11] R. T. R. Kumar, E. McGlynn, C. McLoughlin, S. Chakrabarti, R. C. Smith, J. D. Carey, J. P. Mosnier, and M. O. Henry, Nanotechnology 18 (2007) 215704.

[12] P. Kuppusami, G. Vollweiler, D. Rafaja, and K. Ellmer, Applied Physics A: Materials Science & Processing 80 (2004) 183.

[13] B. Nikoobakht, S. Eustis, and A. Herzing, The Journal of Physical Chemistry C 113 (2009) 7031.

[14] R. S. Wagner and W. C. Ellis, Applied Physics Letters 4 (1964) 89.

[15] M. Sacilotti, P. Cheyssac, G. Patriarche, J. Decobert, T. Chiaramonte, L. P. Cardoso, M. F. Pillis, M. J. Brasil, F. Iikawa, M. Nakaema, Y. Lacroute, J. C. Vial, and F. Donatini, Surface and Coatings Technology 201 (2007) 9104.

[16] R. Thapa, B. Saha, and K. K. Chattopadhyay, Journal of Alloys and Compounds 475 (2009) 373.

[17] P. Buffat and J. P. Borel, Physical Review A 13 (1976) 2287.

[18] C. C. Tang, M. Lamy de la Chapelle, P. Li, Y. M. Liu, H. Y. Dang, and S. S. Fan, Chemical Physics Letters 342 (2001) 492.

[19] S. B. Newcomb, in Electron Microscopy and Analysis 2003 (S. McVitie and D. McComb, eds.), Iop Publishing Ltd, Bristol, 2004, p. 357.

[20] R. T. R. Kumar, E. McGlynn, M. Biswas, R. Saunders, G. Trolliard, B. Soulestin, J. R. Duclere, J. P. Mosnier, and M. O. Henry, Journal of Applied Physics 104 (2008) 084309.

[21] B. K. Meyer, H. Alves, D. M. Hofmann, W. Kriegseis, D. Forster, F. Bertram, J. Christen, A. Hoffmann, M. Straßburg, M. Dworzak, U. Haboeck, and A. V. Rodina, Physica Status Solidi (b) 241 (2004) 231.

[22] D. S. S. Müller, M. Uhrmacher, H. Hofsäss, and C. Ronning, Applied Physics Letter 90 (2007) 012107.

[23] H. J. Fan, A. S. Barnard, and M. Zacharias, Applied Physics Letters 90 (2007) 143116.

[24] M. Schilling, R. Helbig, and G. Pensi, Journal of Luminescence 33 (1985) 201.

[25] C. Gonzalez, D. Block, R. T. Cox, and A. Herve´, Journal of Crystal Growth 59 (1982) 357.

[26] D. M. Hofmann, A. Hofstetter, F. Leitner, H. Zhou, F. Henecker, B. K. Meyer, S. Orlinski, J. Schmidt, and P. G. Baranov, Physical Review Letters 88 (2002) 45504.

[27] J. Grabowska, A. Meaney, K. K. Nanda, J. P. Mosnier, M. O. Henry, J. R. Duclere, and E. McGlynn, Physical Review B 71 (2005) 115439.

[28] V. V. Travnikov, A. Freiberg, and S. F. Savikhin, Journal of Luminescence 47 (1990) 107.

Chapter 4

Effect of various carbon sources on growth

In this chapter, growth of ZnO nanostructures has been investigated using different carbon powders, which is one of the source powders (along with ZnO powder) used in the VPT method. The main mechanism to generate Zn vapour is CTR of ZnO powder by carbon. The morphology of the nanostructures for different carbon powders and the effects of growth at different temperatures have been studied. The reason behind the lower temperature growths observed with particular types of carbon powder compared to graphite has been investigated and we conclude that the higher surface activity is the key factor.

4.1 Introduction

Carbothermal reduction (CTR) is the process by which a metal can be extracted from its corresponding metal oxide compound. In large industrial applications and in laboratory research the CTR mechanism is one of the most common and easy methods for metal extraction. The oxide form of metals is often the most easily naturally available compound of various reactive metals.

The CTR process involves the reaction of a metal oxide (from here on assumed to be ZnO) with carbon to form the metal and either carbon monoxide or dioxide, depending on the reaction temperature and molar ratio of oxide to carbon. The

energetics of the reaction are described by the so-called Ellingham diagram shown in *Fig 4.1* below [1]. The CTR reaction proceeds more readily (i.e. with a lower free energy barrier) than the direct dissociation of the metal oxide due to the competing formation of CO or CO_2. At low temperatures the free energy barrier for the CTR reaction equals the difference in Gibb's free energy between the dissociation of the ZnO (positive) and the formation of CO_2 (negative). At higher temperatures the free energy barrier for the reaction equals the difference in Gibb's free energy between the dissociation of the ZnO and the formation of CO. These reactions are shown in Eqn. 4.1 and 4.2 below.

$$ZnO(s) + \frac{1}{2}C(s) \rightarrow Zn(g) + \frac{1}{2}CO_2(g) \qquad \text{Eqn. 4.1}$$

$$ZnO(s) + C(s) \rightarrow Zn(g) + CO(g) \qquad \text{Eqn. 4.2}$$

The reaction proceeds strongly when there is a crossover between the Gibb's free energy of formation of ZnO and one of the gaseous carbon species. *Fig 4.1* shows that for ZnO this occurs at ~950^0C thus defining the temperature region in which we expect growth to proceed. While the reactions above appear to be solid-solid reactions between the ZnO and C, in fact the overall reaction proceeds via two intermediate heterogeneous reactions involving gas phase reactants and products as shown in Eqn. 4.3 and 4.4 below [2]. Kinetic studies of these two reactions previously published indicate that the rate of reaction in Eqn. 4.3 is substantially faster than that of Eqn. 4.4 [3].

$$ZnO(s) + CO(g) \rightarrow Zn(g) + CO_2(g) \qquad \text{Eqn. 4.3}$$

$$C(s) + CO_2(g) \rightarrow 2CO(g) \qquad \text{Eqn. 4.4}$$

The production of Zn vapour (and thus the growth of ZnO nanostructures) will be controlled by both the thermodynamics and kinetics of the CTR reaction. The CTR process is a very common and popular method used in the VPT growth of ZnO nanostructures and, as explained above CTR-VPT growth of ZnO nanostructures is usually done at temperatures >900 °C. The ability to grow ZnO nanostructures at lower temperatures is desirable as it would broaden the range of possible substrates and also reduce undesirable high temperature effects such as unwanted dopant

diffusion from substrate to nanorods (e.g., Al from Al_2O_3 substrates [4]) and substrate-nanorod reactions [5].

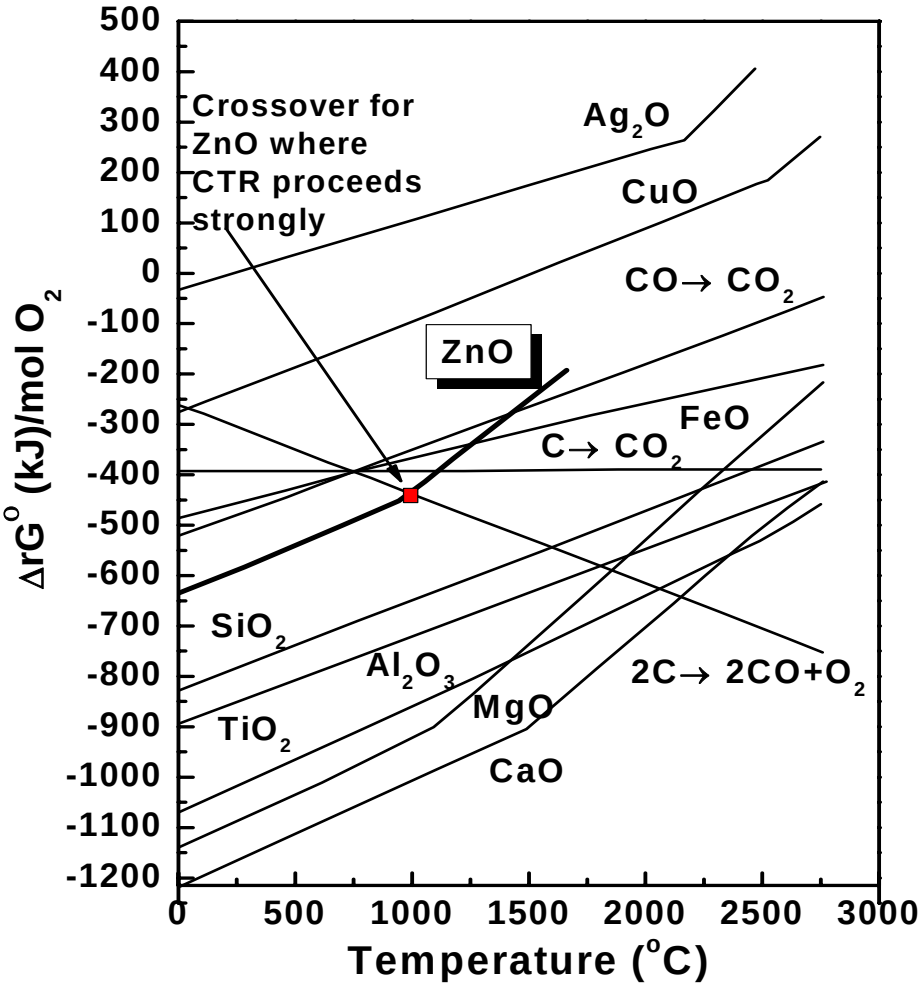

Fig 4.1: Ellingham diagram [1]

It has been observed experimentally that the use of other types of carbon such as carbon black, single walled nanotubes (SWNT), multi walled nanotubes (MWNT) and activated carbon can all be used to grow ZnO nanostructures at lower temperatures [5-8]. Interestingly, at certain temperatures, no growth at all was observed using graphite, whereas nanostructures were observed using the previously mentioned other carbon sources [5, 8]. This has been explained by previous authors in terms of the higher total surface area (TSA) of nongraphite carbon sources (such as those mentioned above) leading to an increase in released Zn vapour responsible for nanostructure growth [5] and by others as due to the effects of lower purity in the

carbon source [8]. At the initial stage of our experiments with different carbon powder we questioned the former explanation and commented that as well as surface area one must also consider factors such as differences in free energy of different carbon sources and effects on the reaction energetics [9]. Additionally, the surface activity of nongraphite carbon sources (originating in edges and defects of the carbon layers and the presence of heteroatoms such as oxygen, hydrogen, sulfur and nitrogen, which introduce active sites on the carbon surface) is known to play a considerable role in the surface chemistry of the material [10]. The surface activity is related to the surface area (and is expected to scale with surface area for otherwise identical materials) but is not correlated solely with changes in the surface area as the density of active sites is strongly dependent on material preparation methods. Hence, different carbon materials with identical surface areas can have different surface activities due to differences in preparation [10]. Finally, the available purity levels of these nongraphite carbon sources is often or even generally inferior to the available purity levels in graphite and impurities can affect nanostructure growth, e.g., contamination of the growth system with In is known to significantly alter the growth morphology and alignment of ZnO nanostructures in CTR-VPT growth [11]. The need to ensure reproducibility and control of nanostructure morphology is in general an even more important consideration than unwanted high temperature effects. Hence, the appropriate selection of the carbon source is an important factor as the relative effects of the carbon source surface area, surface activity, thermodynamic stability and purity remain unclear. In this chapter, we present a study of CTR-VPT growth of ZnO nanostructures at different temperatures using the following carbon powders –

- Carbon black
- Activated carbon
- Graphite

We have directly compared the observed ZnO deposit where identical total carbon surface areas for graphite and carbon black were used to test the previously reported hypothesis of a kinetic limitation on growth due to surface area. We have also studied the effects of using very high surface area activated carbon, compared both

to carbon black and graphite. The ZnO deposits grown using carbon black and activated carbon are similar and differ significantly in quantity and morphology from those grown with graphite. We find that ZnO nanostructures grow at 750°C using carbon black and activated carbon, but no growth is seen at this temperature when using graphite even where identical TSAs compared to carbon black are used. We discuss this data and comment on the effect of the Ellingham diagram of differences in Gibb's energy for different carbon powders, in addition to differences in impurity levels. We conclude that these differences are largely insignificant and that the high surface activity of activated carbon and carbon black sources compared to graphite is the most likely explanation for our results. Before presenting the results of CTR-VPT using different carbon powders, carbon allotropic structures are reviewed briefly below. As the element carbon has a large family of structures and varieties, the discussion below is mainly focused on the types of carbon allotropes used in our experiment.

4.2 Carbon allotropic structures

Carbon is a unique solid material which can exist in more than one form of crystal structure i.e. it is polymorphic [12]. There are several forms of carbon but mainly we can classify it in the following way –

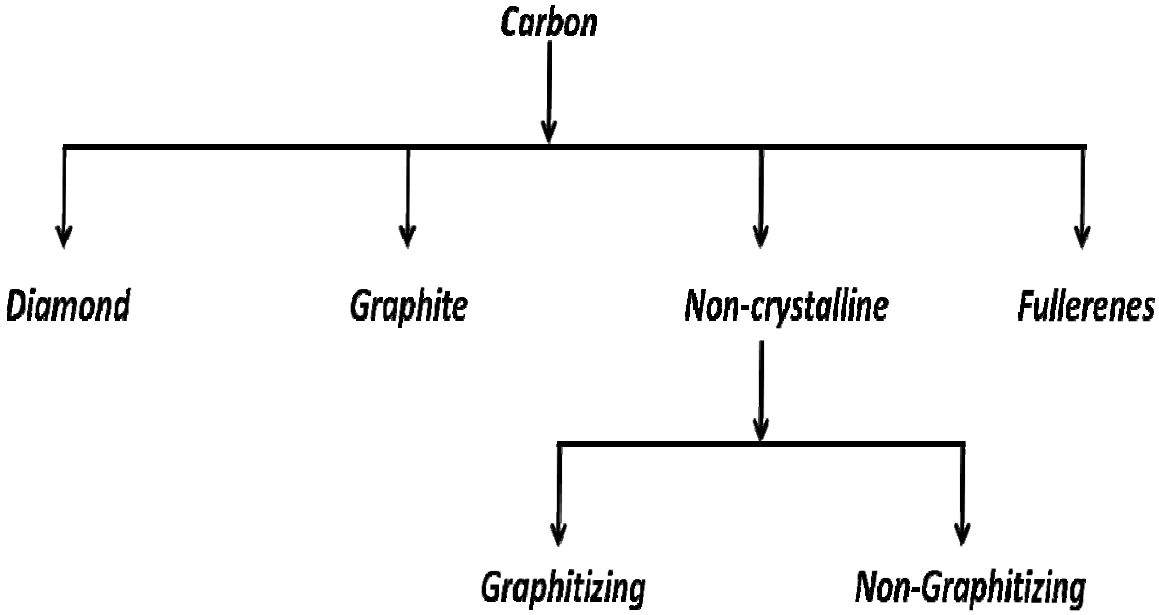

The above is the simplest version of carbon family. In our discussion next focus is given mainly on the carbon types mentioned in the charts.

Among the crystalline carbons the main difference between graphite and diamond is their carbon atom bonding. Graphite is sp^2 (trigonal) hybridized and diamond is sp^3 (tetrahedral) hybridized. As a result diamond has a three-dimensional crystal structure (solid covalent network) whereas graphite consists of carbon layers (with covalent and metallic bonding within each layer). In graphite the layers are stacked in an AB sequence and are linked by weak van der Walls interaction [12]. In *Fig 4.2 (a*) and *(b)* the structures of graphite and diamond are shown, respectively. Due to the metallic bonding within layers, graphite is a good electrical conductor within the layer, unlike diamond.

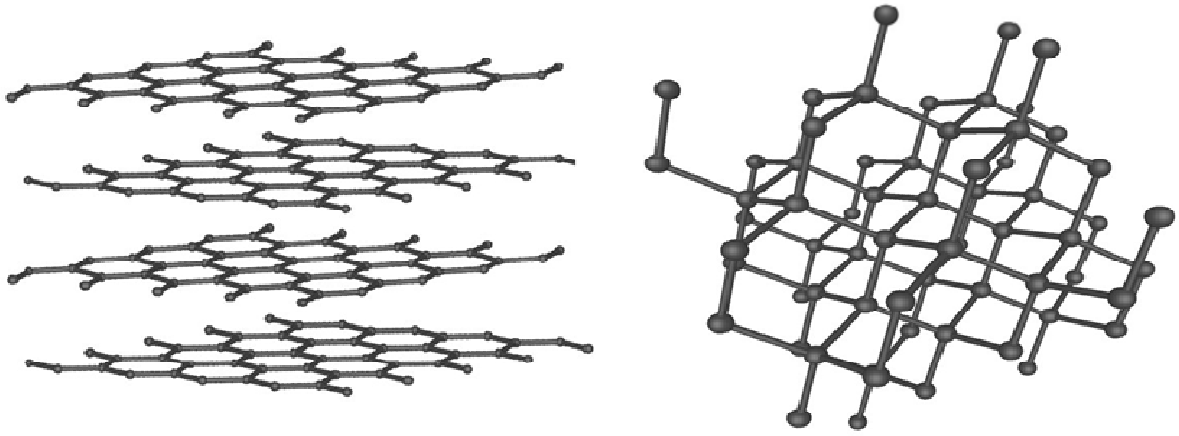

(a) (b)

Fig 4.2: Structure of (a) graphite (b) diamond

The fullerenes category of carbon generally consist of molecules composed entirely of carbon, in the form of a hollow spheres, tubes etc. The structures of fullerenes are very similar to graphite, being composed of sheets of linked hexagonal (mainly) and pentagonal rings. Fullerenes are predominantly sp^2 hybridized carbon atoms which are bent to form closed sphere or tube. *Fig 4.3* is an example of C_{60}, the archetypal fullerene [13].

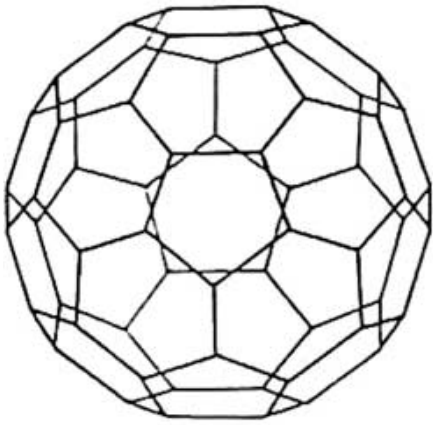

Fig 4.3: Structure of archetypal fullerenes (C_{60}) [13]

There are also higher atomic weight fullerenes like C_{100}, C_{540}. These numbers in the subscript indicate the number of atoms in a single molecule. The stability of fullerenes increases with molecule size. The carbon nanotube structures discovered by Iijima [14] are a more recent discovery in fullerene-type carbon structures.

Carbons produced by solid-phase pyrolysis of organic materials can be referred as non-crystalline or amorphous carbons. In this type of carbon the bonding of atoms and molecule structures are locally similar to graphite but there is no long range order. The AB stacking order found in graphite is not present and layers are not flat [12]. This type of carbon can be distinguished by two classes according to Franklin [15].

- **Non-graphitizing carbons** shown in *Fig 4.4 (a)* cannot be transformed into crystalline graphite even via annealing at 3000^{o}C or higher temperatures. This type of carbon is hard and has a low density. It has a highly porous internal structure with a very high surface-to-volume ratio.
- **Graphitizing carbon** shown in *Fig 4.4 (b)* can be transformed into crystalline graphite by heating in the range of 2200^{o}C-3000^{o}C. This type of carbon is soft, has a high density (i.e. close to that of graphite) and is non-porous.

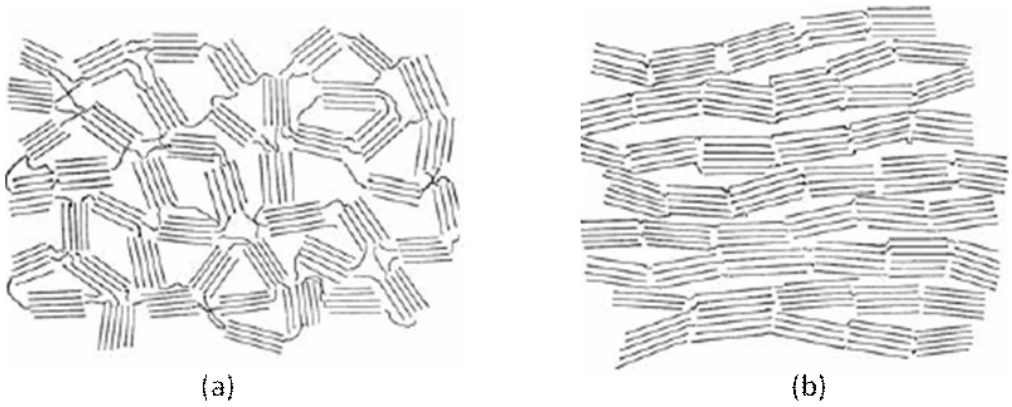

Fig 4.4: Franklin's representation of (a) non-graphitizing (b) graphitizing carbon [15]

According to Franklin the inability of non-graphitizing carbon to convert into graphite is due to the structure of this type of carbon, consisting of randomly ordered crystallites, held together by residual cross-linking and van der Walls forces. At high temperatures, even though the cross-links can be broken, very high activation energies are needed to change whole crystallite orientations to enable graphite formation, energies which cannot be readily supplied. In graphitizing carbon the carbon crystallites are nearly parallel to each other, reducing the energetic difficulties associated with a transformation into graphite. In non-graphitizing carbon the structure is micro porous which gives this type of carbon very high surface area. This surface area can be increased more by activation i.e. mild oxidation by gas or chemical processing. After this activation those carbons are referred as 'active carbon'. Two of the three types of carbon powder which we used in our carbothermal reduction growth of ZnO nanostructures are graphite and activated carbon.

Carbon black is another type of non-crystalline or amorphous carbon is a pure form of soot (impure carbon particles resulting from the incomplete combustion of a hydrocarbon), is manufactured industrially on a large scale primarily for the filler in rubber products. Among variety of industrial processes of manufacturing, the most important is the "furnace black" process, which involves the partial combustion of petrochemical or coal tar oils.

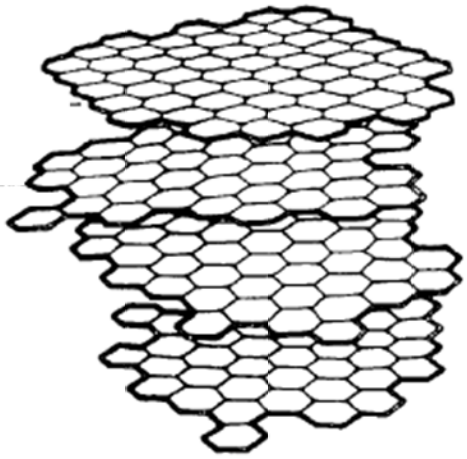

Fig 4.5: Typical crystallite in carbon black presented by Heidenreich *et al.* [16].

A review of early TEM studies of carbon black was given by Heidenreich, Hess, and Ban in 1968 [16]. These authors interpreted the TEM results in terms of the model shown in *Fig 4.5*. In this model, the basic structural units are rather flat graphene planes, arranged in a concentric manner around a hollow centre. From XRD studies of most commercial carbon black powder [16], it is observed that they are made up of crystallites which have dimensions of about four graphite layer planes. The layer planes are roughly parallel and equidistant but do not have the long range AB sequence of hexagonal graphite which is consistence with results from ref [12]. At the highest temperature anneals such as 2500^{o}C-3000^{o}C, carbon blacks do begin to approach the structure of graphite but the long range three dimensional graphite structure cannot be achieved extensively [16].It is therefore referred to as partially graphitized carbon.

From the above discussion we can presume that for the three types of carbon powders which we used one is crystalline graphite while the other two are non-graphitizing amorphous carbon with high internal surface area (active carbon) and partially graphitized carbon (carbon black). XRD 2θ-ω scans were performed on both graphite and active carbon powders to assess their crystallinity.

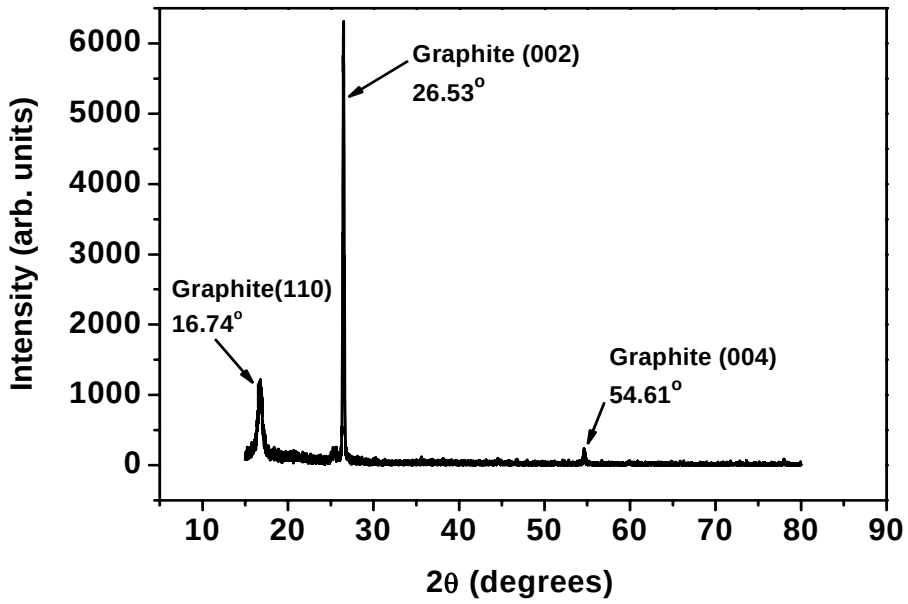

Fig 4.6: *2θ-ω* XRD data of graphite, peaks at 16.74°, 26.53° and 54.61° for graphite (110), (002) and (004), respectively.

In *Fig 4.6* we can see the *2θ-ω* scan data of graphite powder. The peaks at 16.74°, 26.53°, 54.61° are associated with reflections from the graphite (110), (002) and (004) planes, respectively. The lattice structure for these peaks is hexagonal. During an XRD *2θ-ω* scan, using identical conditions no peaks were observed for activated carbon and carbon black. From these scans further we can confirm that carbon black and active carbon which we used is an amorphous form of carbon. In chapter 3 the optimal growth temperature of ZnO nanostructures on Al_2O_3 using graphite source powder has been reported. Our key motivation in performing ZnO nanostructure growth with different types of carbon powder was to explore the possibility of good nanostructure growth at lower temperatures other than the usual 900°C and 950°C and to understand the major factors affecting the growth. The experimental details are described below.

4.3 Experimental procedure

To study the effect of different carbon powders ZnO nanostructures have been grown using the CTR-VPT method on the *a*-plane (11-20) sapphire using the VLS mechanism. The growth mechanism used for these experiments is exactly the same as the mechanism described in chapters 2 and 3. Growth was carried out for a period of 60 minutes for all the samples studied in this chapter. The only alteration between some of the experiments is the type of carbon source powder used or the mass of carbon powder used, with all other parameters being kept exactly the same. Zn vapours are produced by CTR of high purity ZnO powder (Alfa Aesar; 99.9995%). Three types of carbon powder source have been used:

i) Carbon black (Micromeritics: 99% purity—a partially graphitizing carbon)
ii) Activated carbon (Sigma-Aldrich; untreated activated carbon, 99% purity— a nongraphitizing carbon).
iii) Graphite (Alfa Aesar; 99.9999% purity; -325 mesh).

Different purity and different mesh size graphite powders were also used as the source powder while studying the exact reason behind the lower temperature growth. Other graphite carbons which have been used apart from the ones mentioned above are –

iv) Graphite powder (Sigma Aldrich; 99% purity)
v) Graphite flake(Alfa Aesar; 99.9% purity; -10 mesh)

Mesh size is the scale used to determine the particle size distribution of a granular material. Sieving or screening is a method of categorizing a powder's particle size by running the powder through a specific sized screen. A particular size of screen through which most of the particles of a powder can pass is denoted by that mesh size. A "-" before the sieve mesh indicates the particles pass through the sieve. For larger sieve opening sieve size is designated in inches, but smaller sieve "mesh" sizes are designated by the number of openings per linear inch in the sieve. For e.g. the type (v) graphite powder mentioned above (mesh size of this powder is -10) the

particles can pass through 10 openings per linear inch in the sieve. For ease of understanding the particle size of above powders are shown in micron in *Table 4.1* below –

Table 4.1: Particle size in micron and mesh size of the graphite powders used in experiments:

Powder Name	Mesh size	Microns
Graphite type (iii)	-325	44
Graphite type(v)	-10	2000

Different mesh sized graphite powders were used during this study to also check whether different particle sizes have any effect on specific surface area (SSA) of the powder. If the SSA was different due to different particle sizes then different graphite powders with different SSA would have been necessary to check the effect of surface area.

The specific surface area (SSA) of all five types of powder was measured using the Braunauer–Emmett–Teller (BET) method [17]. Adsorption isotherms using nitrogen were obtained for each of the powders using a Nova 2200® surface area analyzer (Quantachrome Instruments). The SSA is the TSA per unit mass for porous solids, may be attributed predominantly to the total internal surface area of open pores. The Quantochrome instrument enables the accurate, precise and reliable characterization of powdered and porous materials. This instrument works using a gas adsorption method of solids. The tendency of all solid surfaces to attract and ultimately capture surrounding gas molecules is called gas adsorption. Monitoring the gas adsorption process provides a wealth of useful information about the characteristics of solids such as surface area and pore size. For accurate surface area measurements, the temperature and pressure of an inert gas are adjusted to cause a single layer of gas molecules to be adsorbed over the entire surface of a solid, be it porous, non-porous or powdered. The sensors of the instrument respond quantitatively to the amount of gas adsorbed. Using this data and by means of the BET equation one may compute the surface area of a sample which is usually reported as the specific surface area

(i.e. surface area per unit mass, usually m^2/g). The BET theory is a well-known method for describing the physical adsorption of gas molecules on a solid surface, which forms the basis of the analysis technique for the measurement of the specific surface area of a material.

As mentioned in previous chapters the ZnO and carbon source powders are well mixed using mortar and pestle before CTR-VPT. SSA measurements before and after this mechanical procedure indicate that the mixing process does not affect the SSA of either species. Our "normal" procedure uses ZnO powder and carbon powder masses of 0.060 g each (1:1 mass ratio giving a molar excess of C). In some experiments we equalized the total carbon surface area between growths with carbon black and graphite by varying the relative mass of graphite powder to ZnO powder. Therefore, since the SSA of graphite powder used is lower than that of carbon black, in these experiments we used a larger mass of graphite to equalize the TSAs.

The relative difference in SSA between graphite and carbon black was such that the surface are equalization process could be performed while maintaining the growth chamber's physical configuration in a nearly identical fashion; however, the relative difference in SSA between graphite and activated carbon was too large for this procedure to be used, as a very large graphite mass would have been required, leading to a significant alteration of the growth chamber's physical configuration. Samples were characterized by high resolution FESEM (Hitachi S-4300 field emission system or Tescan Mira II field emission system) and XRD (Bruker AXS D8 advance texture diffractometer).

4.4 Results

We begin by noting again the details of the reactions that govern generation of Zn vapour above 700°C for the ZnO nanostructures [3]. These reactions are as follows:

$$ZnO(s) + C(s) \rightarrow Zn(g) + CO(g) \quad \text{Eqn. 4.2}$$

$$ZnO(s) + CO(g) \rightarrow Zn(g) + CO_2(g) \quad \text{Eqn. 4.3}$$

$$C(s) + CO_2(g) \rightarrow 2CO(g) \quad \text{Eqn. 4.4}$$

At the normal range of growth temperatures (>700 °C), the gases produced by reaction (1) are Zn(*g*) and CO(*g*), although at lower temperatures CO_2 may also be produced even for molar equalities or excesses of C [3]. The overall reaction (at temperatures >700°C) is given by Eqn. 4.2 and it is known that this proceeds by two intermediate reactions shown in Eqns. 4.3 and 4.4, so the actual reaction pathway is via solid-gas reactions and thus may be sensitive to the solid surface area. Previous work has established that the step contained in Eqn. 4.4 (the producer gas reaction) is the slower one and thus carbon surface area and activity may be the key factors in CTR-VPT growth of ZnO nanostructures [3]. For this reason, we have examined the effects of changes in the carbon surface area only and kept the ZnO powder surface area constant.

The BET calculated SSA results are presented in *Table 4.2*. For reference, the ZnO powder surface area is constant in all experiments. Since the carbon black SSA is 10.9 times higher than that of graphite, for certain experiments (samples shown in *Figs 4.8 (a)–4.8 (c)*) a graphite weight of 10.9 × 0.06 g (=0.654 g) was used (keeping the amount of ZnO powder identical, i.e., 0.06 g), yielding an equivalent carbon surface area (1.7 m^2) for both graphite and carbon black powders. Since there remains a molar excess of C, the thermodynamics of reactions (4.2)–(4.4) are not affected [3]. This allowed a direct comparison of the effect of the kinetics due to the surface area.

Table 4.2 SSA values for the various carbon source powders used in the CTR process and the ZnO powder.

Powder	SSA (m^2/g)
Graphite (type iii)	2.6
Graphite (type iv)	11.2
Graphite (type v)	1.6
Carbon Black	28.5
Activated carbon	1000
ZnO	7.9

Fig 4.7 shows the high resolution FESEM of the samples in the Au-deposited region of the substrate for CTR-VPT growth using graphite and carbon black at different temperatures with the normal mass of carbon (0.060 g). The left column images *(a)*, *(b),* and *(c)* correspond to ZnO nanostructures grown using carbon black and the right column images *(d)*, *(e)*, and *(f)* correspond to ZnO nanostructures grown using graphite (750°C [*(a)* and *(d)*], 800°C [*(b)* and *(e)*], and 850°C [*(c)* and *(f)*]). Further experiments were carried out in the temperature range of 700–950°C for both types of powder. Differences in growth and morphology can be observed in these images for the two different carbon source powders, which are especially visible for growths at 750 and 800°C, although the morphology for growth at 850°C is also quite different, with substantially longer, generally narrower, higher density and less well-aligned nanostructures being grown using carbon black compared to graphite. *Fig 4.8* shows the 2θ-ω XRD data of the same samples. The left columns again show data for samples grown using carbon black and the right column are for samples grown using graphite (750°C [*(a)* and *(d)*], 800°C [*(b)* and *(e)*], and 850°C [*(c)* and *(f)*]).

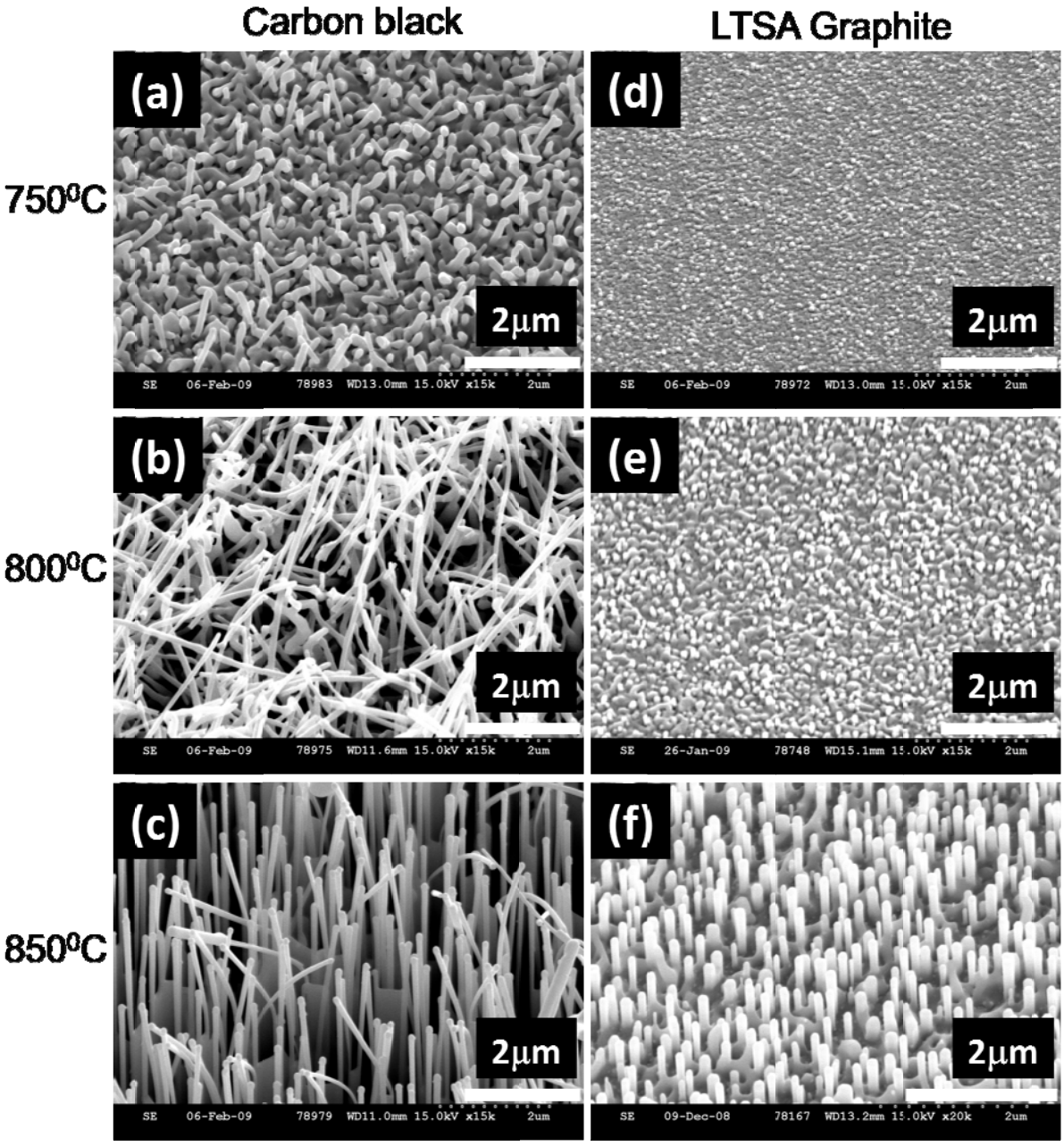

Fig 4.7: FESEM images of samples grown using carbon black at (a) 750°C, (b) 800°C, and (c) 850°C and using graphite at (d) 750°C, (e) 800°C, and (f) 850°C (using a carbon powder mass of 0.06 g in both cases).

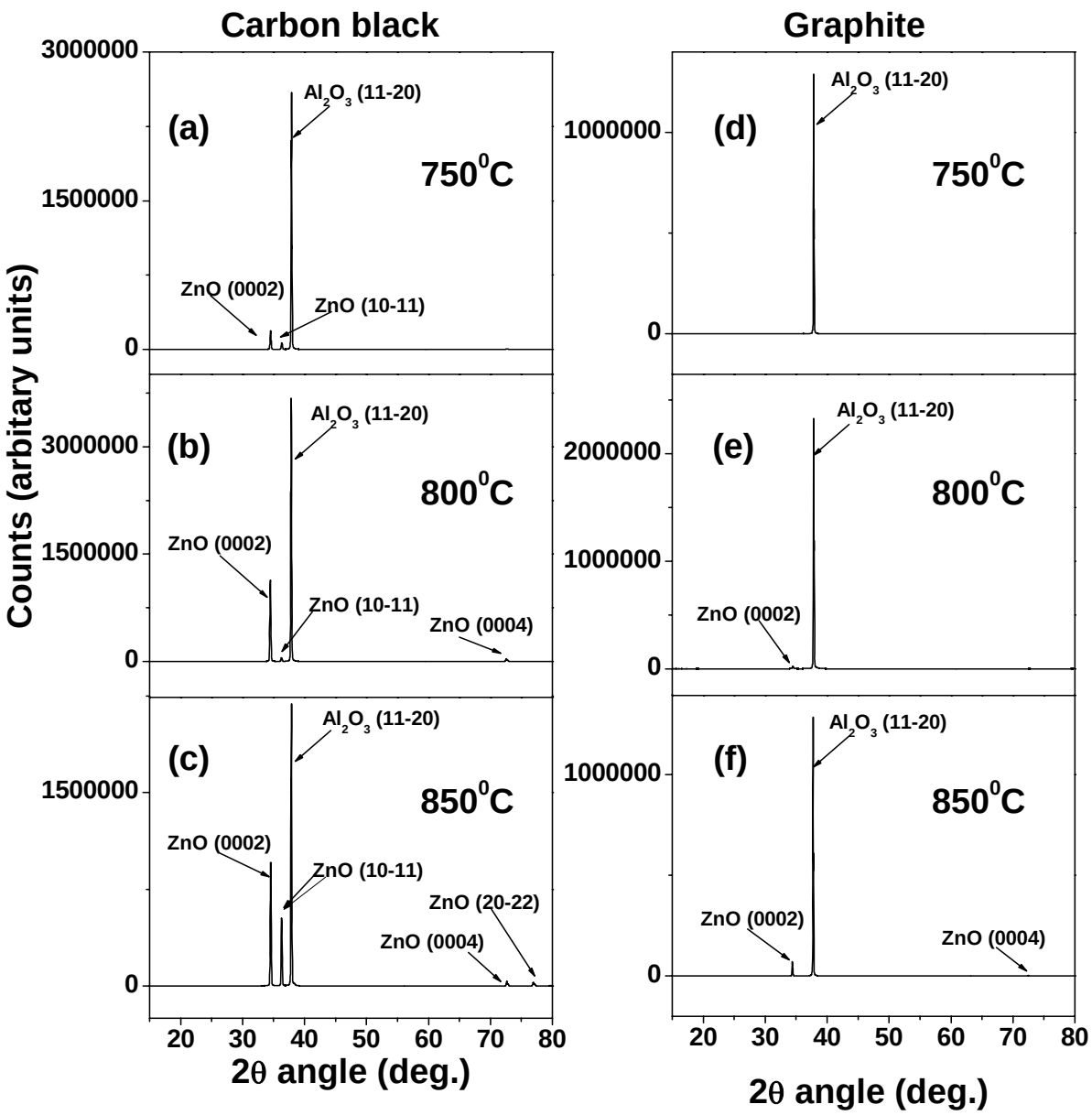

Fig 4.8: *2θ-ω* XRD data of the samples grown using carbon black at (a) 750°C, (b) 800°C, (c) 850°C and using graphite at (d) 750°C, (e) 800°C, (f) 850°C (using a carbon powder mass of 0.06 gm in both cases).

All samples show the Al_2O_3 (11-20) peak at 37.78° due to the sapphire substrate. Peaks corresponding to ZnO are seen in all samples, except that grown using graphite at 750°C, where the ZnO peaks are below the detection limit. No XRD peaks corresponding to other phases are seen [18]. For samples grown with carbon black the ZnO (0002) peak at 34.42° and ZnO (10-11) peak at 36.25° are seen in all samples, consistent with the unaligned growth of ZnO nanostructures seen in *Figs*

4.7 (a)–4.7 (c). For samples grown with graphite, the (0002) peak is seen as the dominant peak in *Figs. 4.8 (e)* and *4.8 (f),* consistent with the *c*-axis aligned growth seen in *Figs. 4.7 (e)* and *4.7 (f);* although some slight evidence of the (10-11) peak is also seen due to unaligned crystallites. The fact that no ZnO peaks are observed above the detection limit of the instrument in *Fig 4.8 (d)* is consistent with the absence (or a very small quantity) of the observed ZnO growth in *Fig 4.7 (d)*. The higher order ZnO (0004) (72.50°) peak is seen in *Figs. 4.8 (b), 4.8 (c),* and *4.8 (f)*, while the ZnO (20-22) peak (76.90°) is seen in *Fig 4.8 (c)* only.

Fig 4.9 shows SEM images of samples grown using graphite with different TSAs from 750 to 850°C. As stated above, we varied the TSA by varying the weight of the graphite powder keeping all other conditions identical. The high TSA (HTSA) sample in *Figs 4.9 (a)–4.9 (c)* had a carbon TSA of 1.7 m^2 [the same TSA as the carbon black used to grow the samples shown in the *Figs 4.7 (a)–4.7 (c)*] and the low TSA (LTSA) sample in *Figs 4.9 (d)–4.9 (f)* had a carbon TSA of 0.156 m^2 [mentioned above as the normal procedure, and identical to the samples in *Figs 4.7 (d)–4.7 (f)*]. However, it is clear that the ZnO morphology and deposit quantity are very similar for both samples. There is a slightly greater volume of deposit for the HTSA sample at all temperatures—the nanorod density determined from the SEM data for the LTSA sample at 850°C (LTSA density 18×10^8 cm^{-2}) is slightly >80% of the density for the HTSA sample (HTSA density 10×10^8 cm^{-2}) at the same temperature, and the LTSA nanorods are slightly shorter and narrower than the HTSA nanorods.

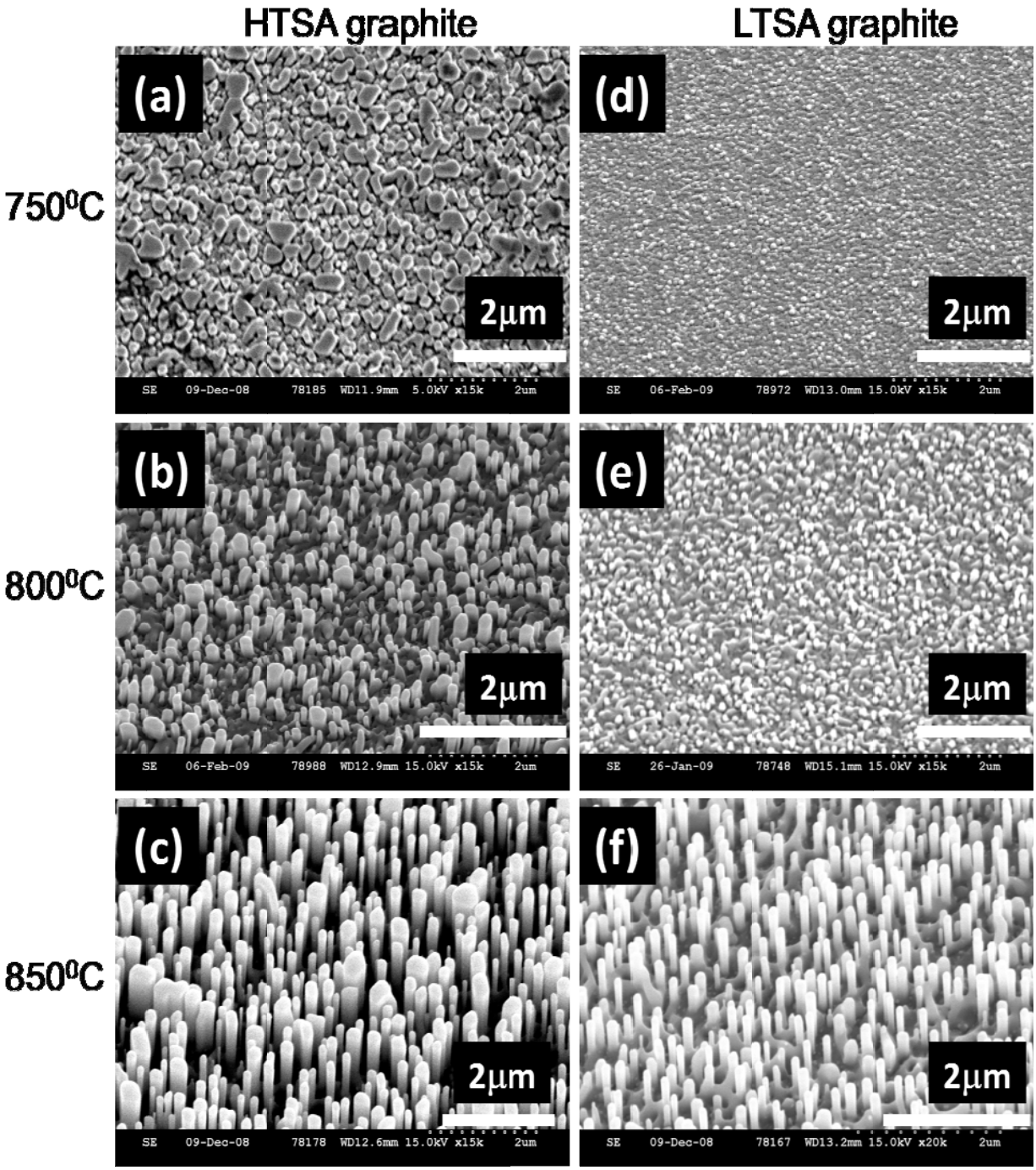

Fig 4.9: FESEM images of samples grown using HTSA graphite (mass = 0.654 gm) at (a) 750^{o}C, (b) 800^{o}C, (c) 850^{o}C and using LTSA graphite (mass = 0.06 gm) at (d) 750^{o}C, (e) 800^{o}C, (f) 850^{o}C.

4.5 Discussion

The data shown above in *Fig 4.7* (and supported by *Fig 4.8*) clearly demonstrate that the ZnO nanostructures grown with carbon black have a very different yield and morphology to those grown with LTSA graphite, with, e.g., large deposits of partially aligned and thin nanowires (diameters of ~50 nm and lengths of ~10 μm) grown using carbon black at 850°C, while well-aligned nanorods (diameters of ~150 nm and lengths of <5 μm) are seen for growth using LTSA graphite at 850°C. In addition, while substantial ZnO deposits are seen using carbon black at 750 and 800°C, almost no deposit is seen at 750°C (some nucleation is seen) and only the beginnings of nanorod nucleation are seen for growth using LTSA graphite at 800°C. Further SEM and XRD results (not shown) indicate no observable growth is found at or below 700 °C for carbon black powder. When we equalized the total graphite surface area to that of the carbon black (HTSA), as shown in *Fig 4.9*, the growth morphology is very similar to that obtained using LTSA graphite. The reduced carbon surface area associated with the LTSA sample results in an almost negligible reduction in the quantity of nanostructure growth and no change in morphology. Previous work has compared growth with different carbon powders on Si substrates where in all cases unaligned growth is observed due to the absence of epitaxial growth conditions [5, 8]. The advantage of using *a*-sapphire substrates is that one can observe both clear changes in morphology from well aligned (using graphite, which is the normal situation due to the epitaxial growth of ZnO on sapphire) to poorly or unaligned (using carbon black or activated carbon) in addition to changes in yield. Our experiments thus have two methods for comparing changes in growth [9]. The conclusion we draw is that while the carbon powder source type is of extreme importance in determining the yield and morphology of the ZnO deposit and enables growth at lower temperatures, the origin of this effect is not in the differing surface areas of different carbon source powders, as hypothesized previously [5, 19]. There remain three possible sources of this effect;

i) differing free energies (which alter the Ellingham diagram [20])
ii) differing levels of impurities
iii) differing surface activities for the different carbon powders.

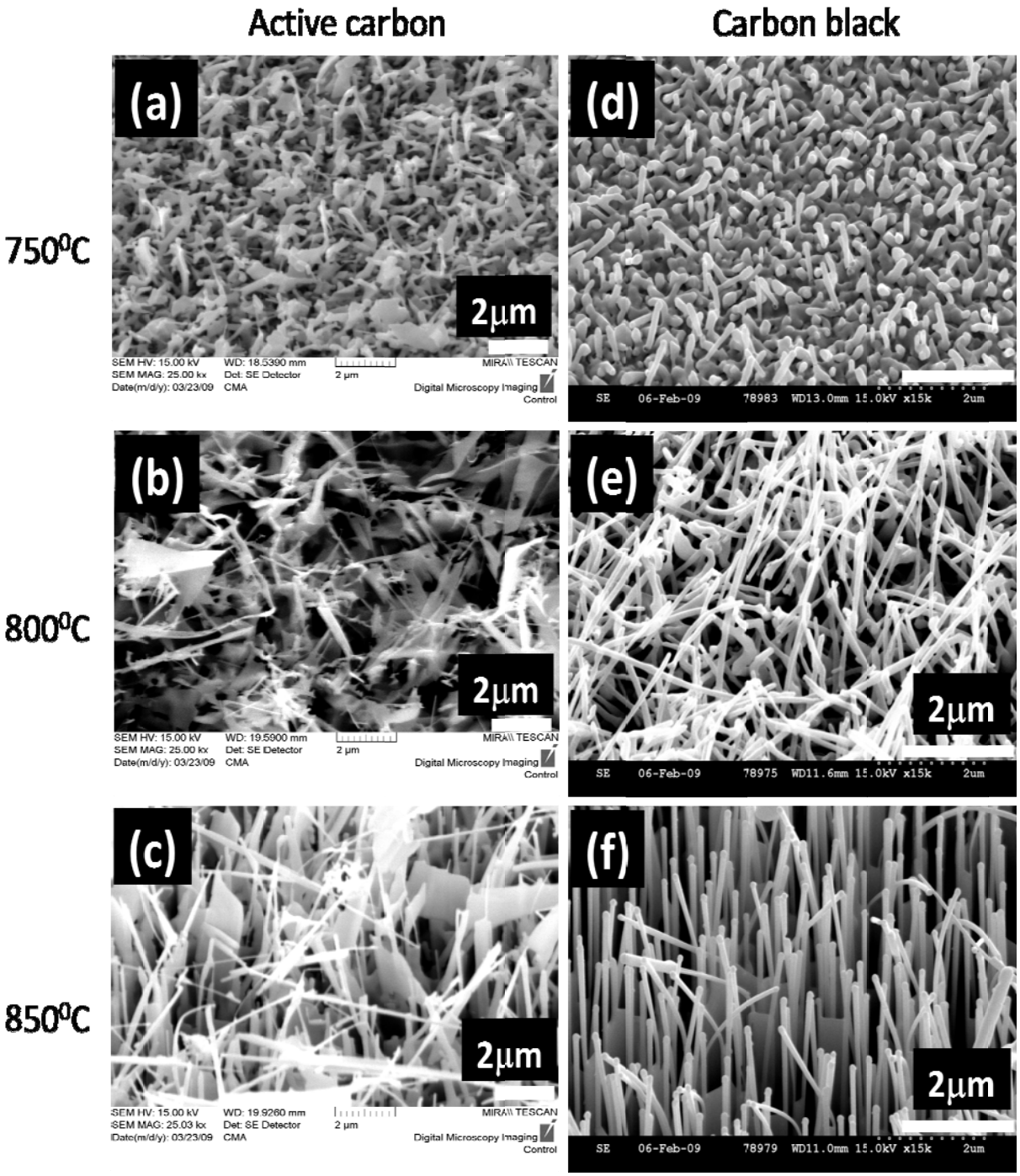

Fig 4.10: FESEM images of samples grown using activated carbon at (a) 750°C, (b) 800°C, (c) 850°C and using carbon black at (d) 750°C, (e) 800°C, (f) 850°C (using a carbon powder mass of 0.06 gm in both cases).

We discuss the effects of different carbon powder free energies first. Carbon black is a (partially) graphitizing form of carbon, while activated carbon is non-graphitizing [13, 21]. Graphite is the thermodynamically stable form of carbon and the specific

Gibbs free energies of other forms (including diamond and amorphous forms) are always larger than those of graphite [22]. The varying methods of production and the varying microstructure and chemical bonding of different carbons mean that a wide range of specific Gibbs free energies may be possible. In general the excess free energy for internal atoms (i.e., atoms not at edges and defects of the carbon layers or at locations where heteroatoms introduce active sites on the carbon layer surface) in turbostratic packing appropriate to carbon blacks and other graphitizing forms of carbon is above the graphite value is ~3–5 kJ/mol in the temperature regime used in this study [23, 24]. However, values of up to ~33 kJ/mol have been reported by other authors, for non-graphitizing forms, symptomatic of the varying microstructure and chemical bonding referred to above and especially the very distinct and porous microstructure of non-graphitizing forms [25]. The probable effects of the changes in Gibbs free energy for the samples of the type shown in *Fig 4.7* using graphite and carbon black can be judged in terms of shifts in the critical temperatures on the Ellingham diagram (*Fig 4.1*). In terms of moles of O_2, the $2C+O_2 \rightarrow 2CO$ line on the Ellingham diagram shifts downward by ~6–10 kJ for CTR using carbon black [23, 24]. This corresponds to a downward shift in the temperature where the $2Zn+O_2 \rightarrow 2ZnO$ line crosses the $2C+O_2 \rightarrow 2CO$ line of ~8–16°C. We can say that the effect of the differing free energy of the carbon black is to allow the CTR reaction to proceed at temperatures about 22 °C lower than with graphite. This is clearly insufficient to explain our data in *Fig 4.7*, where the differences in yield and morphology between growth using LTSA graphite at 800°C and carbon black at 800°C [*Figs. 4.7 (b)* and *4.7 (e)*] are not comparable to the differences in growth using LTSA graphite at 800 and 850°C [*Figs. 4.7 (e)* and *4.7 (f)*; a 50°C temperature difference]. Some other experiments at higher temperatures above the crossing points on the Ellingham diagram of the $2Zn+O_2 \rightarrow 2ZnO$ line with the $2C+O_2 \rightarrow 2CO$ line (>950°C) indicate that Gibbs free energy effects may lead to differences in deposit quantity for samples grown using carbon black compared to those grown with activated carbon, when the CTR reaction has a negative free energy change and is strongly favoured. We observed growth up to 900^{o}C and no growth from 950^{o}C onwards for activated carbon grown samples. In contrast, for carbon black grown samples, growth is seen up to 1000^{o}C and growth stops from 1050^{o}C (data not

shown). However, at the temperatures used for the samples considered here, below the crossing points on the Ellingham diagram, such effects do not explain our results.

Thus we conclude that the effects of differing Gibbs free energies between the graphite and carbon black powders cannot explain our data. These conclusions are valid also when comparing the differences in yield and morphology using HTSA graphite at 800 and 850 °C [*Figs. 4.9 (b)* and *4.9 (c)*] to the difference in yield and morphology between growth using carbon black at 800°C and HTSA graphite at 800°C [*Figs. 4.7 (b)* and *4.9 (b)*].

The conclusions that neither carbon source surface area nor thermodynamic stability explain our data are supported by the data for growth with the normal carbon weight (0.06 g) using activated carbon (a non-graphitizing carbon with a high surface area of 1000 m^2/g) shown in *Figs. 4.10 (a)–4.10 (c)* for growth at various temperatures [*Fig. 4.10 (a)*—750°C; *Fig. 4.10 (b)*—800°C; and *Fig. 4.10 (c)*—850°C]. The growths are not entirely similar in terms of morphology of the deposit to those found using carbon black at similar temperatures [shown for comparison in *Figs. 4.10 (d)–4.10 (f)* and identical to the samples in *Figs. 4.7 (a)–4.7 (c)*] but both powders grown samples show an unaligned structure, which is the main morphological feature of concern in the present study. The active carbon and carbon black grown nanostructures mostly show a nanowall/nanosheet morphology and an unaligned nanorod/nanrowire morphology, respectively. This is despite the fact that-

i) the activated carbon has a much (~30 times) higher SSA than carbon black and

ii) that it is a non-graphitizing carbon whose Gibbs free energy is probably larger than that of carbon black and thus likely to push the critical CTR reaction temperatures to even lower values.

Another possible factor to explain the results we see is the carbon purity. Previous reports have shown that the morphology of ZnO nanostructures is very dependent on the presence of In impurities in the growth system [11]. Impurities may in principle have two effects on the CTR-VPT growth. Firstly, enabling Zn vapour

production at lower temperatures which may occur either by direct ZnO reduction—common impurities such as Al, Si, Li, and Mg will all tend to reduce ZnO [22] or by catalysis of the CTR reaction, thus potentially increasing yields at lower growth temperatures. Secondly, impurities in the gas stream may affect the deposit morphology via alteration of surface energies of various ZnO facets, as shown by Fan *et al.* for In contamination [11] and discussed by Qi *et.al* [26]. However, CTR-VPT growth in our system using two much lower purity graphites with a range of metal and other impurities [as mentioned before type (iv) Sigma-Aldrich-Fluka; 99% purity graphite powder with 11.2 m^2 /g surface area and type (v) Alfa Aesar; 99.9% purity graphite flake with 1.6 m^2 /g surface area] show identical results both in terms of yield and morphology to *Figs. 4.7* and *4.9* above. We can observe for all three types of different purity graphite from *Fig 4.11* well-aligned nanorods/nanowall at 850°C and the beginnings of nanorod nucleation at 800°C. Almost no deposition is found at 750°C for both samples grown using lesser purity graphite powders (data not shown).

Thus we do not believe that impurities in the carbon are singularly responsible for the effects we observe. We note also that chemical analyses provided by the suppliers using inductively coupled plasma optical emission spectroscopy (ICP-OES) and our own energy dispersive X-ray (EDX) analyses of a selection of the carbon powders used in this work showed no evidence of In contamination, down to a detection limit of ppm (~0.0005% in percentage) using ICP-OES and of ~0.1% concentration using EDX.

We interpret our data to mean that the differences in growth we see are associated with the high surface activity of non-graphite carbon sources which is related to, but not completely determined by surface area, as discussed previously [10].

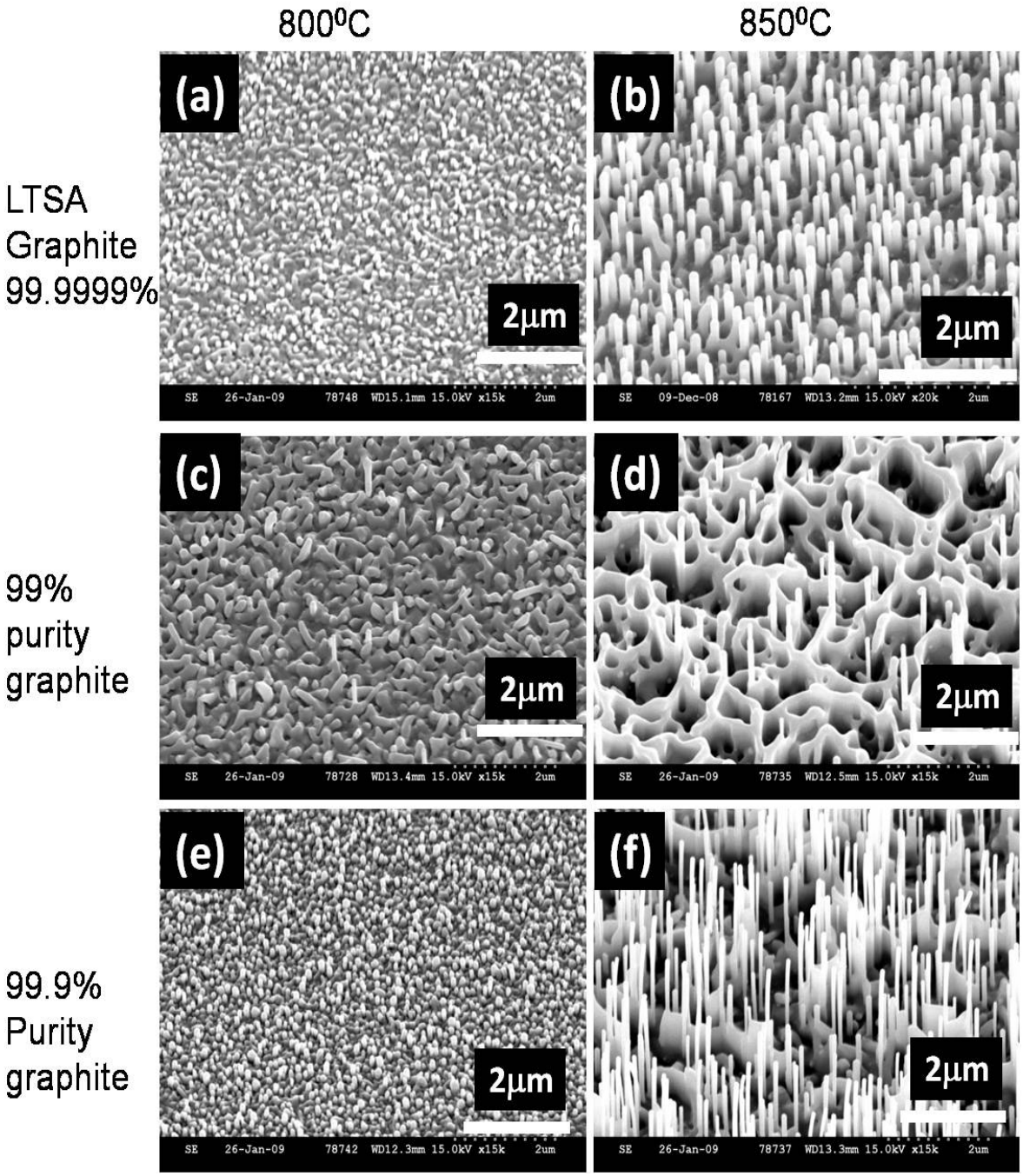

Fig 4.11: FESEM images of samples grown using LTSA graphite at (a) 800°C, (b) 850°C using 99% purity graphite at (c) 800°C and (d) 850°C and using 99.9% purity graphite flake at (e) 800°C, (f) 850°C (using a carbon powder mass of 0.06 gm in all cases).

4.5.1 Surface activity

Surface activity originates both at edges and defects of the carbon layers and at the locations of heteroatoms such as oxygen, hydrogen, sulfur and nitrogen, which introduce active sites on the carbon surface where carbon atoms can react preferentially with other species, compared to their normally rather inert behaviour in a perfect graphite structure. This surface activity is known to play a crucial role in the surface chemistry of the many carbon materials [10, 27]. *Fig 4.12* shows the presence of edges, defects and heteroatoms in different types of carbon which cause surface activity. It was realized as from the mid-1970s that neither the surface area nor its pore structure were sufficient to explain many of the properties of carbon supported catalysts [28, 29] and it was in the late 1980s when the neglected importance of carbon surface chemistry started to be analyzed in depth. Although carbon is considered to be an inert material in comparison with other catalyst supports such as alumina and silica, its surface has a number of active sites, constituted by unsaturated valences at the edges and defects of the graphitic hexagonal crystallites (graphene layers) formed by inert carbon atoms. Of course, the proportion of these active sites will increase as porosity and surface area increase. The presence of heteroatoms (mainly oxygen, hydrogen and nitrogen) also introduces active sites on the carbon surface and consequently, the carbon surface is not as inert as it could be expected. At the edge of the basal planes of carbon atoms in the graphite structure, where bonding in the plane is terminated, are unsaturated carbon atoms. These sites are associated with high concentrations of unpaired electrons and therefore, play a significant role in chemisorption. In crystalline graphite, the edge area is small compared to that of the basal plane and graphite does not exhibit significant chemisorption. However, microcrystalline carbons, like activated carbons, carbon black, carbon nanotubes have more disordered structures and more edge areas, which result in a larger propensity for chemisorption. In addition, the basal planes of the microcrystallites in the above mentioned non-graphitic carbons may contain various defects, dislocations and discontinuities, which are also sites for chemisorption [29]. In graphite, with a highly oriented structure, the adsorption takes place mainly by the dispersion component of the van der Waals forces. However, the random ordering of imperfect aromatic sheets in

activated carbon results in incompletely saturated valences and unpaired electrons, which influences the adsorption behaviour [30].

In general terms, although at low temperatures the adsorption is completely reversible, as the temperature is increased the chemisorption increases and the molecules dissociate into atoms that react chemically with the atoms of carbon to form surface compounds which are mostly carbon-oxygen compounds as shown in *Fig 4.12 (a)* and *(c)* [31].

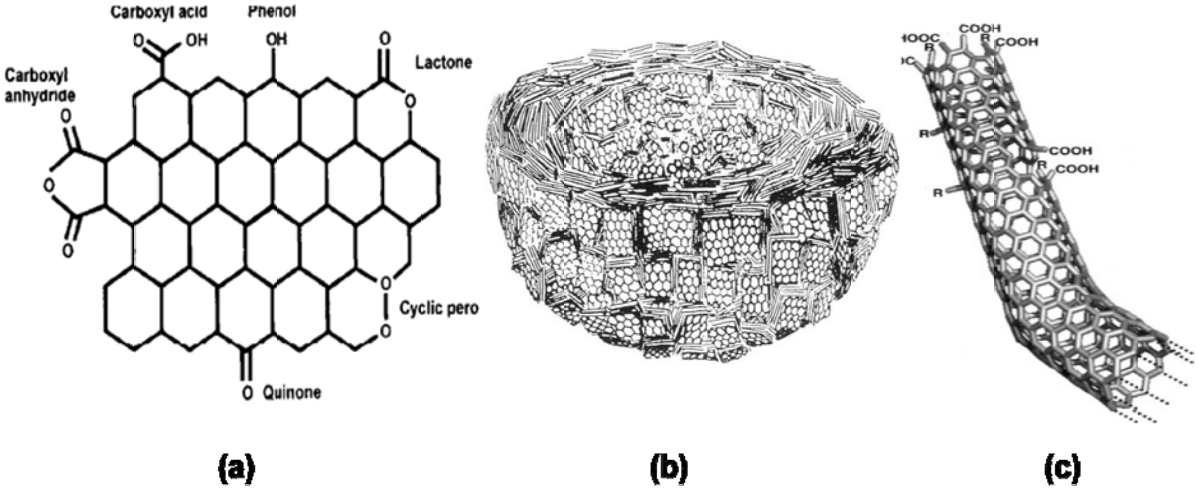

Fig 4.12: Edges and defects of the carbon layers and the presence of heteroatoms which causes higher surface activity. (a) In Activated carbon ref [10]; (b) In carbon black ref [16]; (c) In SWNT ref [31] (R = H and OH). This higher surface activity of CB and AC makes these more reactive at lower temperature compared to graphite.

Carbon-oxygen surface groups are not formed exclusively by reaction with oxygen but they can result also from reaction with many other oxidizing gases (ozone, nitrous oxide, nitric oxide, carbon dioxide, etc.), and with oxidizing solutions (nitric acid, sodium hypochlorite, hydrogen peroxide, etc.). These surface groups may originate from the original raw material, the activation process or introduction after preparation via post-treatment. Although some polymers (e.g. PVDC, phenol-formaldehyde) produce carbons free of oxygen and with only traces of hydrogen, these carbons may chemisorb oxygen, producing oxygen surface groups [10]. The nature and amount of oxygen surface complexes of a given carbon are affected by its

surface area, particle size and ash content, as well as temperature and degree of carbonization.

4.5.2 Explanation of our data with respect to surface activity

We note that the involvement of heteroatoms in the surface activity might be described as an impurity effect, which we have discussed above; however, the key point is that the presence of impurities alone is not the origin of the effects, but rather the specific binding to the carbon layers of such heteroatoms during the carbon synthesis which creates active carbon sites (in addition to intrinsic effects such as edges and defects of the carbon layers), thus enabling the CTR. The surface activity of carbon blacks may equal or exceed that of active carbons, despite the lower surface areas for the carbon blacks, especially for untreated active carbons, which is the type we have used [10, 32]. This conclusion is consistent with our data and also with the other reported data in literature since the surface activity of carbon blacks generally is quite high and will also be appreciable for other carbon species such as SWNT and MWNT where layer defects and edges are expected to be important [5, 8, 19, 31]. However, the surface activity of such powders is also a rather variable quantity and is crucially dependent on the material preparation and processing conditions so that variations from report to report in terms of the details of yield and morphology are expected due to the different sources of the carbon powders used [10]. The effects of higher surface activity of non-graphite carbons on the nanostructure yield are easily understood since the higher surface activity will enable the CTR reaction to proceed at much lower temperatures due to the availability of a suitable quantity of reactive carbon atoms/active sites and thus enable appreciable nanostructure yields at lower temperatures. The issue of why different nanostructure morphologies are observed using non-graphite carbons is less easily understood. Our studies with lower purity graphites indicate that impurities in the carbon source are not the single only origin of the differences in morphology in our experiments (unlike the results in ref. [11] for In contamination). There are some possible explanations; firstly the differences in morphology may be due either to the effects of higher Zn pressures on the nanostructure nucleation and the faster subsequent growth which may lead to defects which alter morphology. Secondly, the active sites

in the carbon, which are the source of the CTR reaction in carbon blacks in many cases, are the sites of heteroatom binding, which is in turn, the cause of the local surface activity. The CTR reaction, which occurs in the vicinity of such heteroatoms, may lead to the release of the heteroatoms or complexes containing heteroatoms into the Zn vapour stream which ultimately condenses at the substrate to form nanostructures. The presence of the heteroatoms in the condensing vapour stream may also lead to changes in the nanostructure morphology.

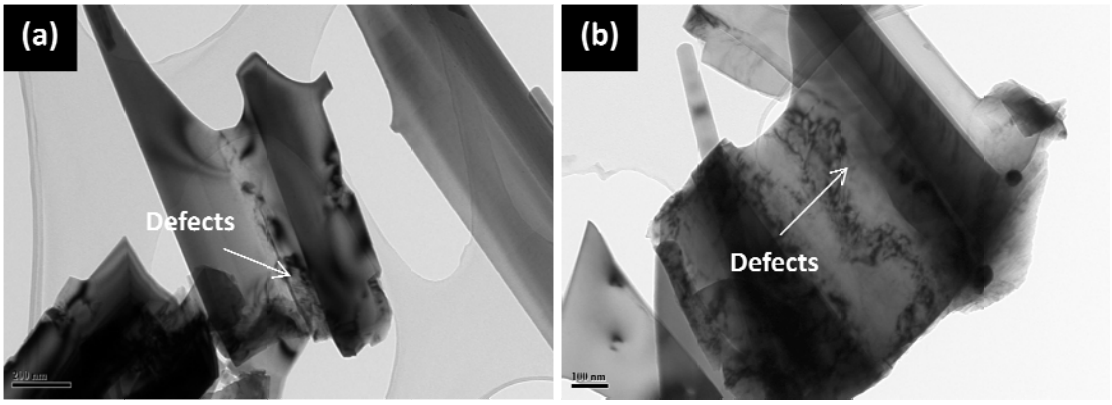

Fig 4.13: TEM images of sample grown by activated carbon at 850^{o}C temperature (a) a ZnO nanorod showing a characteristically variable diameter, (b) an example of defect formation in a nanostructure.

To investigate one aspect of the first possibility, that the faster growth rate causes crystal defects which alter morphology, TEM measurements have been performed on samples grown by activated carbon as shown in *Fig 4.13*. TEM sample preparation has been done by the same methods as mentioned in section 3.4.2. From *Fig 4.13 (b)* we can see significant amount of defects in the sample, also similar defects can be observed in some other areas investigated. We can see from the images that, the area of defects lies mainly in the nanowall, or in the base of the nanorod/nanowall structures. We cannot however conclude those defects are responsible for the unaligned structures, as in the area of the defects the crystals do not show any loss of texture.

These aspects related to the varying nanostructure morphology require significant further study to elucidate the details of the mechanisms responsible.

4.6 Conclusion

In conclusion, our data show that the different deposit yields and morphologies observed in CTR-VPT growth of ZnO nanostructures using different carbon powders cannot be explained by surface area, thermodynamic effects, or purity differences alone. Rather, the differing surface activities of the carbon powders are responsible for the observed variations in our experiments. The use of different types of carbon powder does enable growth at significantly lower temperatures and with different morphologies, including smaller nanowire diameters in certain temperature regions, which may be useful for applications in, e.g., field emission [33]. However, the negative side of this achievable diversity is that reproducible deposit yields and morphologies are more difficult to achieve with carbon powders whose chemical properties and specifically, surface activities are more variable. Clearly there is a trade-off between the relative advantages that lower temperature growth using non-graphite powders may offer in terms of nanostructure diversity and range of available substrates and the drive to develop industrial scale uses of ZnO nanostructures for which reproducibility and scalability are key considerations. For the latter applications, the use of graphite powder may be preferred, since, based on our data, the surface chemistry/activity of graphite powders appears quite reproducible from various sources and with varying purities and SSA.

4.7 References

[1] H. E. Catherine, *Chemistry : an introduction to organic, inorganic, and physical chemistry*, Pearson Education, ed. 3rd, 2006.

[2] L. Hong, H. Sohn, and M. Sano, Scandinavian Journal of Metallurgy 32 (2003) 171.

[3] C. G. Maier, U.S. Bureau of Mines Bulletin No. 324 (1930)

[4] J. R. Duclere, B. Doggett, M. O. Henry, E. McGlynn, R. T. R. Kumar, J. P. Mosnier, A. Perrin, and M. Guilloux-Viry, Journal of Applied Physics 101 (2007) 013509.

[5] Y. S. Lim, J. W. Park, M. S. Kim, and J. Kim, Applied Surface Science 253 (2006) 1601.

[6] G. Gundiah, F. L. Deepak, A. Govindaraj, and C. N. R. Rao, Topics in Catalysis 24 (2003) 137.

[7] Y. Hang Leung, A. B. Djurisic, J. Gao, M. H. Xie, and W. K. Chan, Chemical Physics Letters 385 (2004) 155.

[8] Y. H. Leung, A. B. Djurisic, J. Gao, M. H. Xie, Z. F. Wei, S. J. Xu, and W. K. Chan, Chemical Physics Letters 394 (2004) 452.

[9] M. Biswas, E. McGlynn, and M. O. Henry, Microelectronics Journal 40 (2009) 259.

[10] F. Rodríguez-Reinoso, Carbon 36 (1998) 159.

[11] H. J. Fan, A. S. Barnard, and M. Zacharias, Applied Physics Letters 90 (2007) 143116.

[12] D. Chung, Journal of Materials Science 37 (2002) 1475.

[13] P. J. F. Harris, Critical Reviews in Solid State and Materials Sciences 30 (2005) 235.

[14] S. Iijima, Nature 354 (1991) 56.

[15] R. E. Franklin, Proceedings of the Royal Society A209 (1951) 196.

[16] R. D. Heidenreich, W. M. Hess, and L. L. Ban, Journal of Applied Crystallography 1 (1968) 1.

[17] S. Brunauer, P. H. Emmett, and E. Teller, Journal of Americal Chemical Society 60 (1938) 309.

[18] JCPDS Card No. 36-1451 (for ZnO); JCPDS Card No. 46-1212 (for Al_2O_3).

[19] Y. S. Lim, J. W. Park, S. T. Hong, and J. Kim, Materials Science and Engineering: B 129 (2006) 100.

[20] P. W. Atkins, *Physical Chemistry*, Oxford University Press, Oxford, 1994.

[21] J.-B. Donnet, Carbon 32 (1994) 1305.

[22] Glushko Thermocenter of the Russian Academy of Sciences in the IVTANTHERMO database and listed at; http://www.chem.msu.su/rus/tsiv/Zn/table.Zn.6.html.

[23] B. S. Terry and X. Yu, Ironmaking and Steelmaking 18 (1991) 27.

[24] J. S. Speck, Journal of Applied Physics 67 (1989) 495.

[25] S. K. Das and E. E. Hucke, Carbon 13 (1975) 33.

[26] J. J. Qi, Y. Yang, Q. L. Liao, Y. H. Huang, J. Liu, and Y. Zhang, Acta Physico-Chimica Sinica 25 (2009) 1721.

[27] C. Poleunis, X. V. Eynde, E. Grivei, H. Smet, N. Probst, and P. Bertrand, Surf. Interface Anal. 30 (2000) 420.

[28] F. Rodríguez-Reinoso, *Porosity in Carbons: Characterizationand Applications*, ed. J. W. de Patrick. Edward Arnold, London, pg. 253, 1995.

[29] L. R. Radovic and F. Rodríguez-Reinoso, *Chemistry and Physics of Carbon*, ed. P. A. Thrower. Marcel Dekker, New York, Vol 25, pg. 243, 1997.

[30] R. C. Bansal, J. B. Donnet, and H. F. Stoeckli, *Active carbon*, Marcel Dekker, New York, 1988.

[31] S. Banerjee, T. Hemraj-Benny, and S. S. Wong, Advanced Materials 17 (2005) 17.

[32] A. Schroeder, M. Klueppel, and R. H. Schuster, Macromol. Mater. Eng. 292 (2007) 885.

[33] R. T. R. Kumar, E. McGlynn, C. McLoughlin, S. Chakrabarti, R. C. Smith, J. D. Carey, J. P. Mosnier, and M. O. Henry, Nanotechnology 18 (2007) 215704.

Chapter 5

Dopant distribution within ZnO nanostructures

In this chapter, the distribution of dopants within ZnO nanostructures is reported. Low temperature CL has been used to investigate the distribution of In and Al dopants by studying the donor bound excitonic emission at 3.3567 eV for In (I_9) and 3.605 eV for Al ($I_{6/6a}$) dopants in the CL spectrum. In the first part of this chapter the unintentionally introduced dopant distribution is studied in as-grown ZnO samples followed by experiments where ZnO doping has been performed deliberately. The In and Al doping process in the nanostructures is also described. The distribution nature i.e. whether it is homogeneous or not is an important factor for applications of ZnO nanostructures in device technology.

5.1 Introduction

The potential of ZnO for short wavelength optoelectronic devices applications such as UV LEDs and LDs [1-3] has been mentioned in previous chapters. Other possible applications are as transparent field effect transistors or field emission devices, which could serve as an active element in large area displays [4]. To realize these devices, the conductivity in ZnO and related materials must be controllable, an issue which has remained an extremely challenging affair and a significant obstacle to

device development. To attain the novel optical properties offered by ZnO and to utilize its potential in devices both high quality *n*- and *p*-type doping are critical, with carrier concentration well in excess of 10^{17} cm^{-3} being required for high quality *p*/*n* type doping [5]. ZnO with a wurtzite structure is naturally an *n*-type semiconductor because of its stoichiometric deviations, due to the presence of intrinsic defects such as O vacancies (V_o) and Zn interstitials (Zn_i), and also due to the relatively easy substitution of Zn atoms in the Zn lattice by some group III element including Ga, Al, In, which leads to large, controllable electron densities [6]. Normally undoped ZnO shows *n*-type conductivity in the order of 10^{14} – 10^{17} cm^{-3} typically [6-8], and as high as 10^{21} cm^{-3} [9]. Among various *n*-type dopants (such as group III elements B, Al, Ga, and In, group IIIB rare earth metals Sc and Y, group IV elements Si, Ge, and Sn and group VII elements F, Cl, and I [5]) group III elements Al, Ga and In acting as substitutional elements for Zn are probably the most suitable *n*-type doping agents, due to their lower vapour pressures compared to group VII elements. Among these group III elements, Al is highly reactive with O, and oxidation of Al sources for intentional doping during vapour phase growth of ZnO is problematic. Ga and In are less reactive than Al. Luminescence spectral features assigned to Al, Ga and In are seen in most ZnO samples. Nanostructured ZnO commonly exhibits Al, Ga and In-related spectral lines.

As mentioned in chapter 1 it is very difficult to obtain and control the degree of *p*-type doping in ZnO. This issue is not unique to ZnO but extends to most wide bandgap material e.g. GaN, ZnS, CdS, ZnSe. Group I elements on the Zn site, such as Li, Na, K, Cu, Ag, and Zn vacancies, and group V elements on the O site such as, N, P, Sb and As [5], are expected to act acceptors in ZnO. It is believed that the most promising *p*-type dopants are group V elements. The group I elements form deep acceptors or amphoteric which do not contribute strongly to *p*-type conduction. The *p*-type doping issue is a major bottleneck for ZnO material to be used in bipolar devices and several studies are ongoing in an attempt to overcome this problem. It is hoped that some progress can be made by co-doping, that is by using two different dopants simultaneously (e.g. ZnO:N,As) or combining a moderate concentration of donors with a high concentration of acceptors (e.g. in ZnO:Ga,N). The difficulties of achieving *p*-type doping and its causes are not described here in any more detail as

this chapter mainly focuses on *n*-type doping and its distribution within the nanostructures grown.

The distribution of dopants within ZnO thin films has been studied by various authors using micro-photoluminescence (μ-PL), CL spectroscopy and scanning probe electrical techniques [10-12]. Evidence has been seen in many cases for inhomogeneities in the emission; with the I_0/I_1 line having been shown to be strongest at grain boundaries in heteroepitaxial thin films, though the origin of such effects remains unclear. The peak wavelengths of the (Ga-related) I_8 line and other emissions have been shown to depend on the local strain in these samples and show greatest spectral shifts close to the substrate–film interface and at grain boundaries where crystallites have coalesced during growth [10, 12]. For homoepitaxial thin films the dominant I_6 (Al-related) emission is reported to be quite homogeneously distributed in the sample [11].

For ZnO nanostructures to be effectively utilized in devices, it must be possible to dope these structures effectively and homogeneously. This holds both for potential uses in bipolar, *p*–*n* junction devices and in unipolar devices such as field effect transistors and field emission devices. For example, inhomogeneous doping in nanostructures used in field emission devices will lead to local hot or cold spots, inhomogeneous electron emission and the possibility of local burn-out of nanostructures. Although doping of ZnO nanostructures is a topic in its infancy (relatively speaking), some attempts have been reported [13-16]. Given the relatively high crystalline quality of ZnO nanostructures one might expect a homogeneous distribution of dopants within these systems (unless specific materials engineering has been undertaken, e.g. in core–shell nanostructures or embedded quantum well structures). Where data has been reported on the spatial distribution of dopant-related optical emission from ZnO nanowires acceptor dopants have been reported to be homogeneously distributed along the nanowires, while evidence has suggested donors are distributed inhomogeneously [13, 14].

We have undertaken low temperature CL spectroscopy measurements of the band edge emission from nominally undoped ZnO nanostructures grown by VPT mainly

on Si substrates with some growths on sapphire. Measurements on intentionally doped ZnO nanostructures are also shown as supporting data. Our data show the presence of a range of donor species, deduced from the various I line DBE emissions seen in the spectra [17]. The entire range of the DBE emission shows some evidence of inhomogeneous distribution, probably partly due to variations either in CL collection efficiency or emitting volume below the incident electron beam, however the Al-related DBE emission at 3.3605 eV ($I_{6/6a}$, 368.95 nm vacuum wavelength) displays a very marked inhomogeneity, even more so than the emission from other donor species, in its distribution throughout the sample. Increased emission intensity is seen at various locations in nanorods and nanosheets, and specifically only at certain points where different nanostructures cross or coalesce (though not at all such points), which suggests an aggregation of Al donors in ZnO in regions of localized crystal structure disruption, consistent with a previous report and providing some clarification of the possible physical mechanism involved [13]. However, although increased $I_{6/6a}$ emission is seen only in such regions, not all such regions show increased emission, implying that the microscopic nature of the local crystal is important in determining the degree of Al aggregation.

5.2 Experimental details

The growth technique used for the samples is described in more detail in chapters 2 and 3. Briefly, ZnO nanostructures have been grown on Au-catalyzed SiO_2/Si(001) substrates using the VPT technique. The substrates have been cleaned ultrasonically and a 5 nm Au layer has been evaporated on the substrates in a bell jar evaporator. ZnO (99.9995%) + graphite (99.9999%) powders at a 1:1 mass ratio were mixed and spread in an alumina boat. The substrates have been then placed directly above the source powder on the boat with the growth surface facing the powder in a single zone tube furnace with a 90 sccm Ar carrier gas flow, with the other end of the tube open to the external atmosphere. The furnace temperature was set at 950^{o}C and the samples were grown for 60 min. Some samples were also grown on *a*-plane (11-20) sapphire, using the procedure described above.

In this work some samples have been intentionally doped with In and Al to verify further the distribution of the dopants within nanostructures. Two methods have been used for doping, and for doping with In only the first method has been implemented, while both methods were used to attempt Al doping.

- **Method 1**: A small amount (~0.002 gm or 3.3% of ZnO/C powder used) of In/Al powder of high purity (In purity 99.999% from Alfa Aesar; Al purity 99.95% from Sigma Aldrich) is mixed with the ZnO + graphite powders (mentioned above) by mortar and pestle thoroughly. The rest of the growth process used was the same as, normally used for growth. After this experiment we found the optical quality of ZnO nanostructure sample significantly degraded compared to normal samples. In the case of In doping the linewidth of the In peak (I_9) was very broad and in the case of Al doping no Al ($I_{6/6a}$) peak was found. The absence of any Al peak after attempting doping in the spectrum can be explained as due to the high oxidation reactivity of Al and a tremendous difference in vapour pressure between Zn and Al.

To overcome these two problems with In and Al we used the residual In/Al contamination of the growth chamber just immediately after the growth with In/Al powder i.e. the samples studied here grown by method 1 have been grown the next day after the growth with ZnO + graphite + In/Al powders, using only ZnO + graphite powder.

- **Method 2**: In this method samples have been grown by normal methods mentioned above. After growth very small quantity of Al powder has been placed on the area with nanostructures and then annealing was performed in an Ar atmosphere at 700^{o}C (melting point of Al is 660^{o}C).

After growth, samples were characterized by SEM (FEI Quanta 200) and XRD (Bruker AXS D8 advance texture diffractometer). CL measurements were made at 5K using a variable temperature CL setup (5–300 K) mounted on the FEI Quanta 200 SEM. The CL detection system consists of a parabolic mirror, a grating monochromator and a liquid-nitrogen-cooled CCD camera for measurements of CL spectra, and a photomultiplier tube for measurements of monochromatic CL images.

CL spectra in *Fig 5.4* and *5.6* were obtained with similar conditions for the same sample type (i.e. on Si or sapphire substrates) but differing from one sample type to another, the emission from the sample grown on sapphire being weaker than that from the sample grown on Si.

5.3 Results and discussion

The 2θ–ω XRD pattern of the deposit on Si was measured, as shown in *Fig 5.1*. All the peaks observed can be indexed either to the Si substrate or ZnO [18]. The 2θ peak values of the ZnO reflections match the reference values for unstrained ZnO to within the measurement uncertainty of ~0.1° ((0002)-experiment 34.49°; theory-34.45°: (10-11)-experiment 36.37°; theory-36.28°: (10-12)-experiment 47.59° theory-47.58°), indicating that the vast majority of the deposit is unstrained.

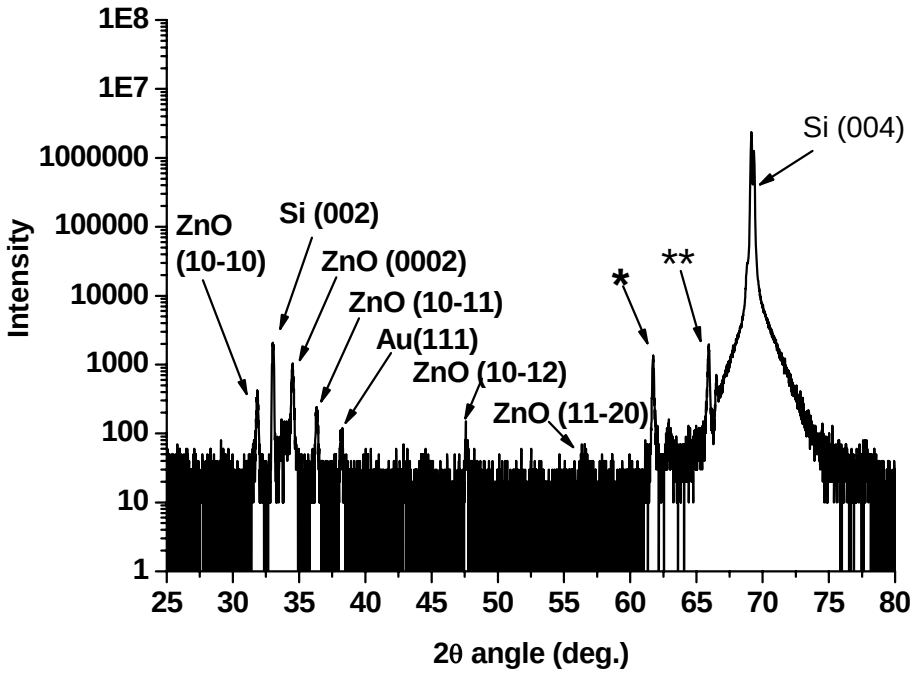

Fig 5.1: *2θ-ω* XRD data of ZnO nanostructures sample grown on Si. The feature marked "*" is due to *K*β radiation from the x-ray tube. The feature marked "**" is due to tungsten *L*α radiation from contamination of the x-ray tube.

Fig 5.2 (a) shows a SEM image from a region of the ZnO deposit. *Fig 5.2 (b)–(d)* show monochromatic CL-SEM images centred at 3.3661 eV (I_3/surface exciton-SX [19]), 3.3605 eV ($I_{6/6a}$) and 3.3567 eV (I_9), respectively. The slit width used corresponds to a spread in photon energy of ~0.3 meV. *Fig 5.3* shows a similar set of SEM and CL-SEM data taken from another area of the sample, with otherwise identical conditions[*].

The CL data from the majority of the deposit is broadly similar. In *Fig 5.2 (b), (d), 5.3 (b)* and *(d)* there are variations in CL signal across the images. In *Fig 5.2 (b)* and *(d)* especially these are similar and rather gradual. These variations are related to variations in the overall CL signal levels and may indicate some inhomogeneity in distribution of both the defect species responsible for the I_3/SX and I_9 emissions. The relative heights of these peaks do not vary greatly (as shown in CL spot scans in *Fig 5.4* below) and thus the variations may also be related either to slight changes in collection efficiency in the CL system or increased volume of excited material below the probe (and in all probability are at least partly explained by a combination of such effects). However, in both *Fig 5.2 (c)* and *5.3 (c)* there are regions where there are clear 'hot spots' of $I_{6/6a}$ emission intensity. These hot spots are labelled (i)–(iii) in *Fig 5.2* and *5.3. Fig 5.4 (a)–(c)* shows CL spot scans at the locations marked (i)–(iii) in *Fig 5.2* and *5.3. Fig 5.4 (d)–(f)* shows CL spot scans at the locations marked Ref1–Ref3 in *Fig 5.2* and *5.3*.

[*]In the monochromatic CL-SEM images, a darker shade indicates a higher CL intensity.

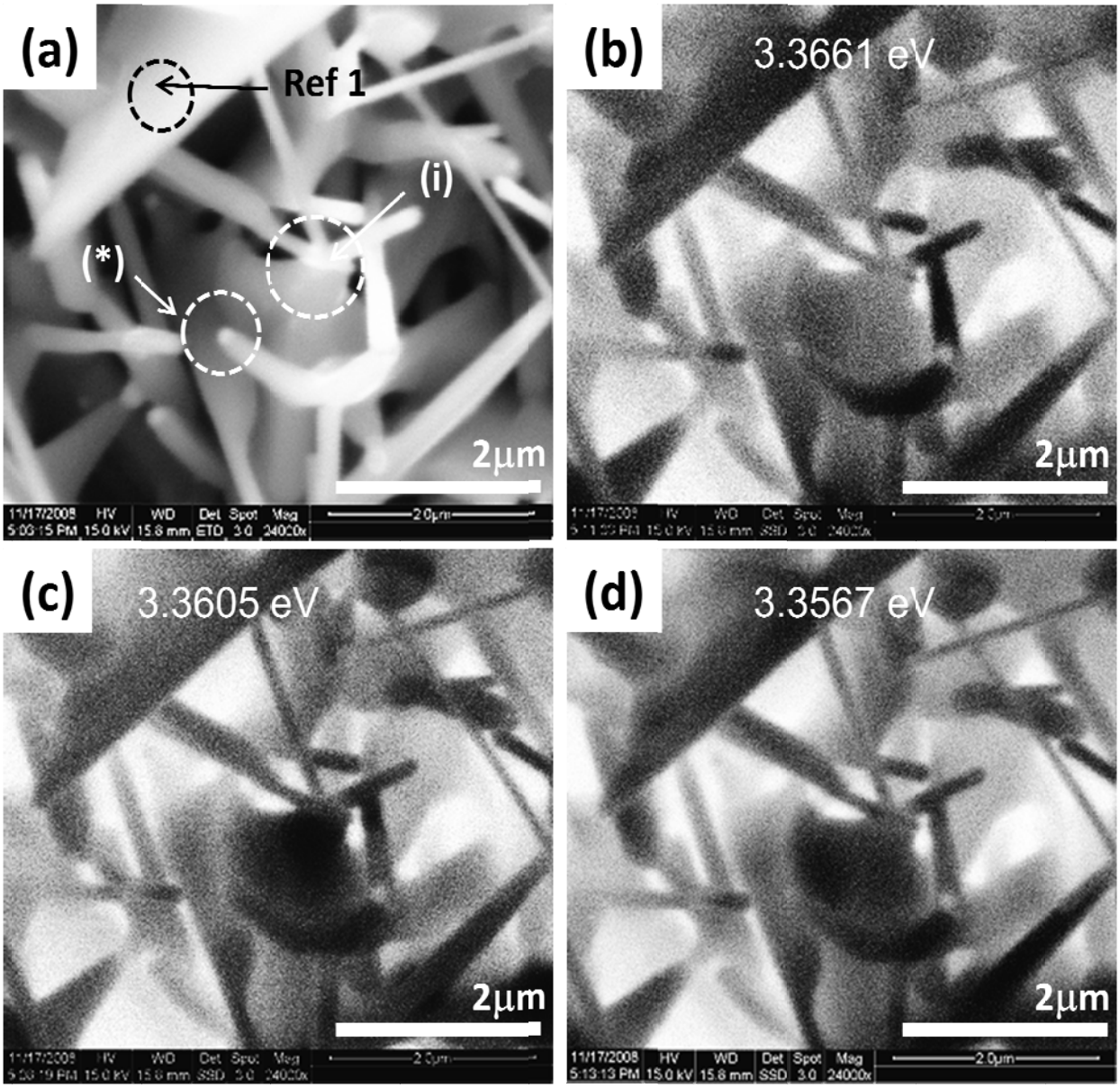

Fig 5.2: (a) SEM image from a region of the ZnO deposit on Si; monochromatic CL-SEM images centred at (b) 3.3661 eV (I_3/SX), (c) 3.3605 eV ($I_{6/6a}$) and (d) 3.3567 eV (I_9). The region marked by (∗) in (a) shows an Au droplet at the top of a nanorod.

These data clearly show that while the intensity variations seen in *Fig 5.2(b), (d), 5.3(b)* and *(d)* are associated with variations in CL signal with little change in relative height of the I_3/SX and I_9 peaks, the intensity variations seen in *Fig 5.2 (c)* and *5.3 (c)* clearly correspond to the increased intensity (and relative intensity compared to the I_3/SX and I_9 peaks) of the specific $I_{6/6a}$ DBE line associated with the

Al donor in ZnO [13]. Thus the $I_{6/6a}$ Al-related emission shows a very marked inhomogeneity, even more so than the emission from other donor species, in its distribution throughout the sample. The Al in the sample originates from inadvertent contamination by the alumina boat containing the source material, which can also undergo carbothermal reduction to a slight extent at elevated temperatures [20].

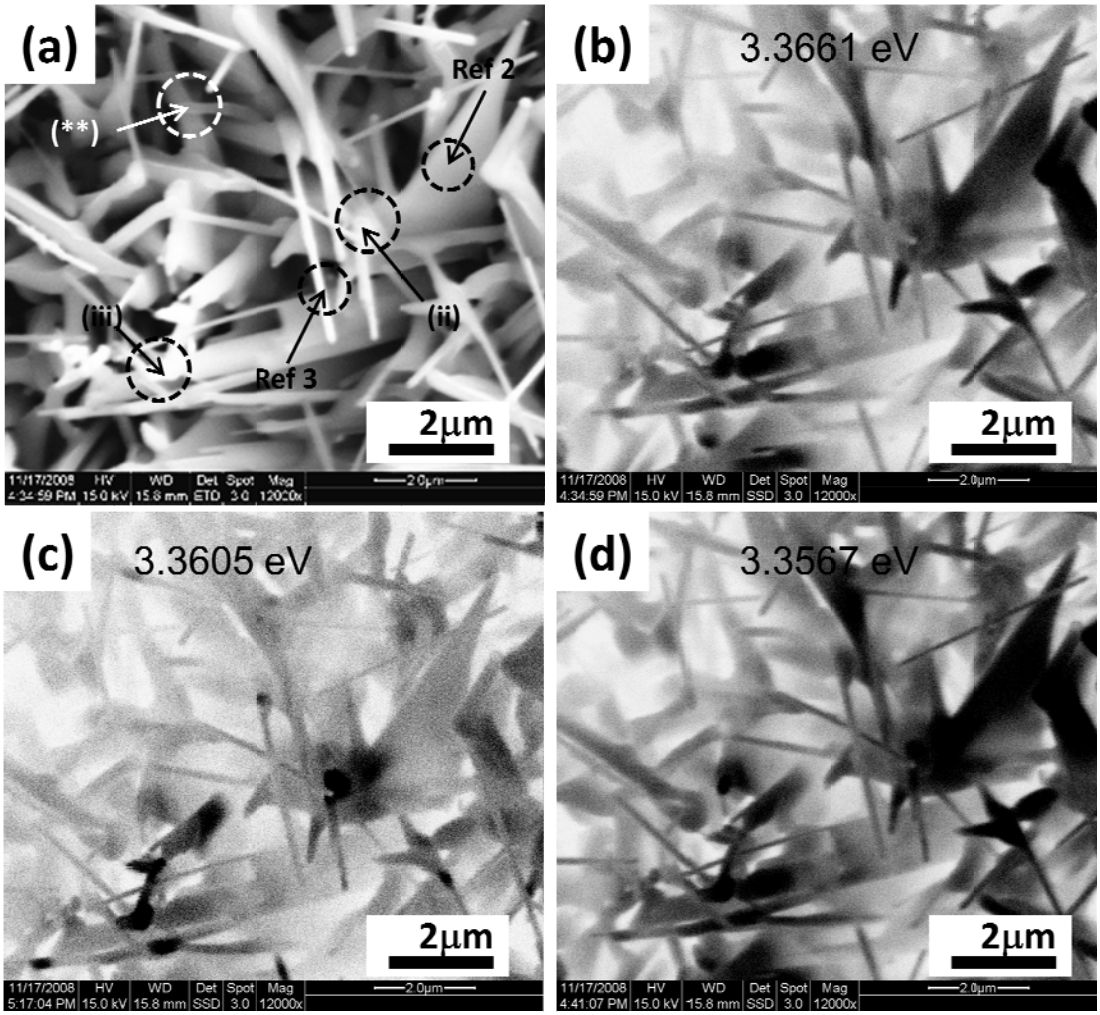

Fig 5.3: (a) SEM image from a different region of the ZnO deposit on Si; monochromatic CL-SEM images centred at (b) 3.3661 eV (I_3/SX), (c) 3.3605 eV ($I_{6/6a}$) and (d) 3.3567 eV (I_9).

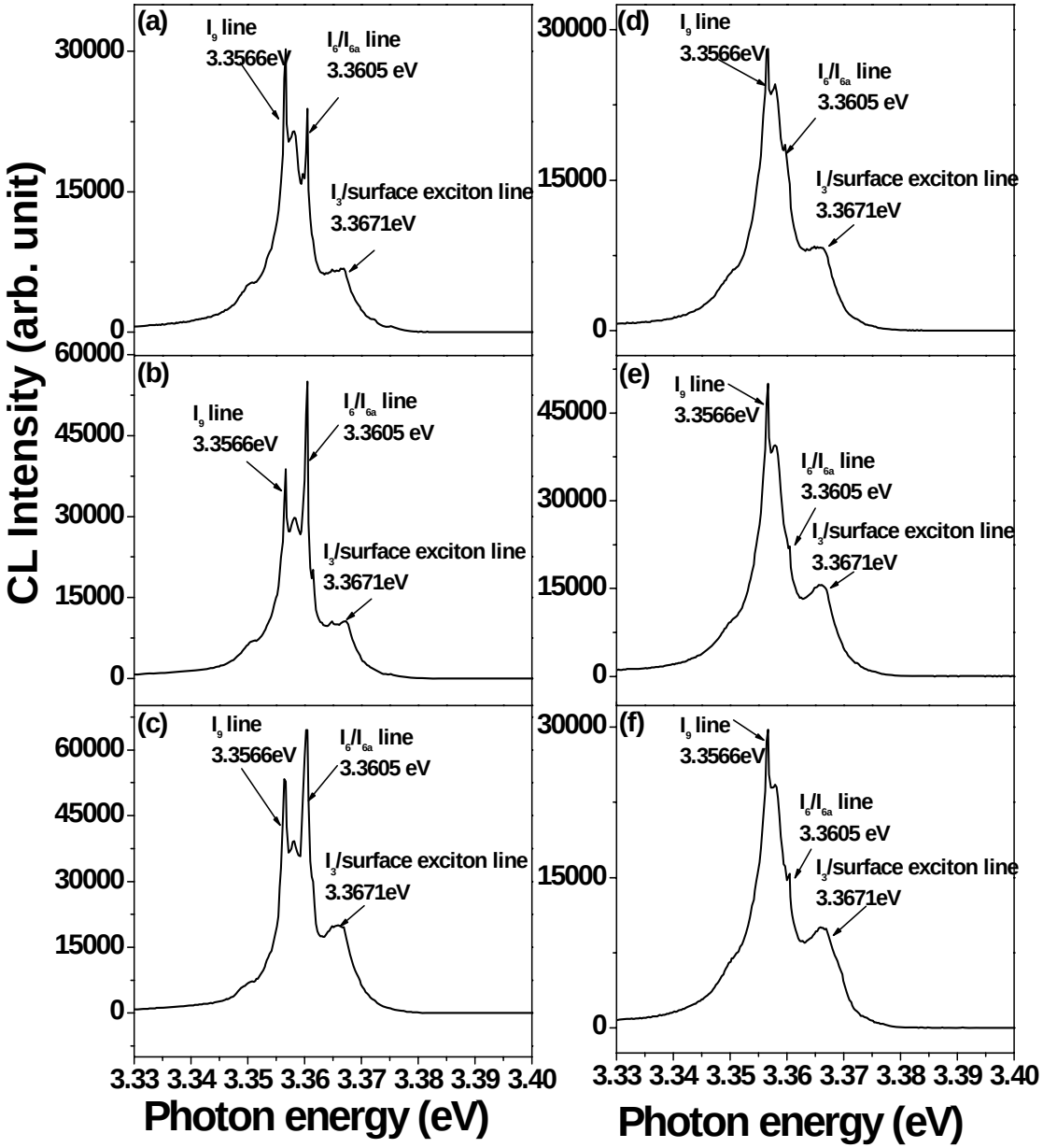

Fig 5.4: (a)–(c) CL spot scans at the locations marked (i)–(iii) in *Fig 5.2* and *5.3*; (d)–(f) CL spot scans at the locations marked Ref1–Ref3 in *Fig 5.2* and *5.3*, respectively.

The locations (i)–(iii) in *Fig 5.2* and *5.3* (and all other locations of $I_{6/6a}$ emission 'hot spots') correspond to locations where either we observe intersection of 2 nanostructures (e.g. (i) and (iii) in *Fig 5.2 (a)* and *5.3 (a)* correspond to the intersection of a nanosheet with a nanorod or a cluster) or secondary growth of one nanostructure from another (e.g. (ii) in *Fig 5.3 (a)*). These locations are likely, by

virtue of either the coalescence or secondary growth, to be regions of either localized strain or crystal structure disruption (e.g. grain boundaries) and the data suggest that these regions act as aggregation sites for Al dopants during growth. Not all such regions (e.g. location (∗∗) in *Fig 5.3 (a))* show increased $I_{6/6a}$ emission which indicates that the microscopic nature of the local crystal is relevant in determining if Al aggregation will occur at a particular location. We note that there is no evidence that 'hot spots' are associated with Au droplets, seen at certain locations (e.g. (∗) in *Fig 5.2 (a)).*

Furthermore, while strain in ZnO nanostructures can lead to appreciable lineshifts (see e.g. Nobis *et. al* [14]) in fact we see no evidence of lineshifts for the I_3/SX, $I_{6/6a}$ or I_9 lines at any of the marked locations in *Fig 5.2* and *5.3*, as shown in *Fig 5.4*. The lines occur at identical positions within the experimental uncertainty of 0.3 meV which is much less than the shifts seen by Nobis *et al*, which were of the order of some meV [14]. This is consistent with the absence of strain deduced from our XRD data. Thus we suggest that Al aggregation occurs in regions of localized crystal structure disruption such as grain boundaries and is dependent upon the microscopic nature of such structural defects.

We have tested this hypothesis by studying a ZnO nanostructure sample grown on *a*-sapphire (with very similar conditions to those described earlier and also described more fully in chapter 2 and 3). Nanorods grown on *a*-sapphire tend to be well-aligned normal to the substrate with no secondary growths or nanorod overlap or coalescence of the sort seen in unaligned samples grown on Si, and thus should not act as sites for Al aggregation. Cross-sectional SEM and monochromatic CL of this sample are shown in *Fig 5.5 (a)–(d),* under similar conditions to those in *Fig 5.2* and *5.3*. In this case *Fig 5.5 (b)–(d)* corresponds to scans centred at 3.3648 eV (at the high energy side of the sample emission close to I_3/SX), 3.3601 eV ($I_{6/6a}$/I_7) and 3.3565 eV (I_9).

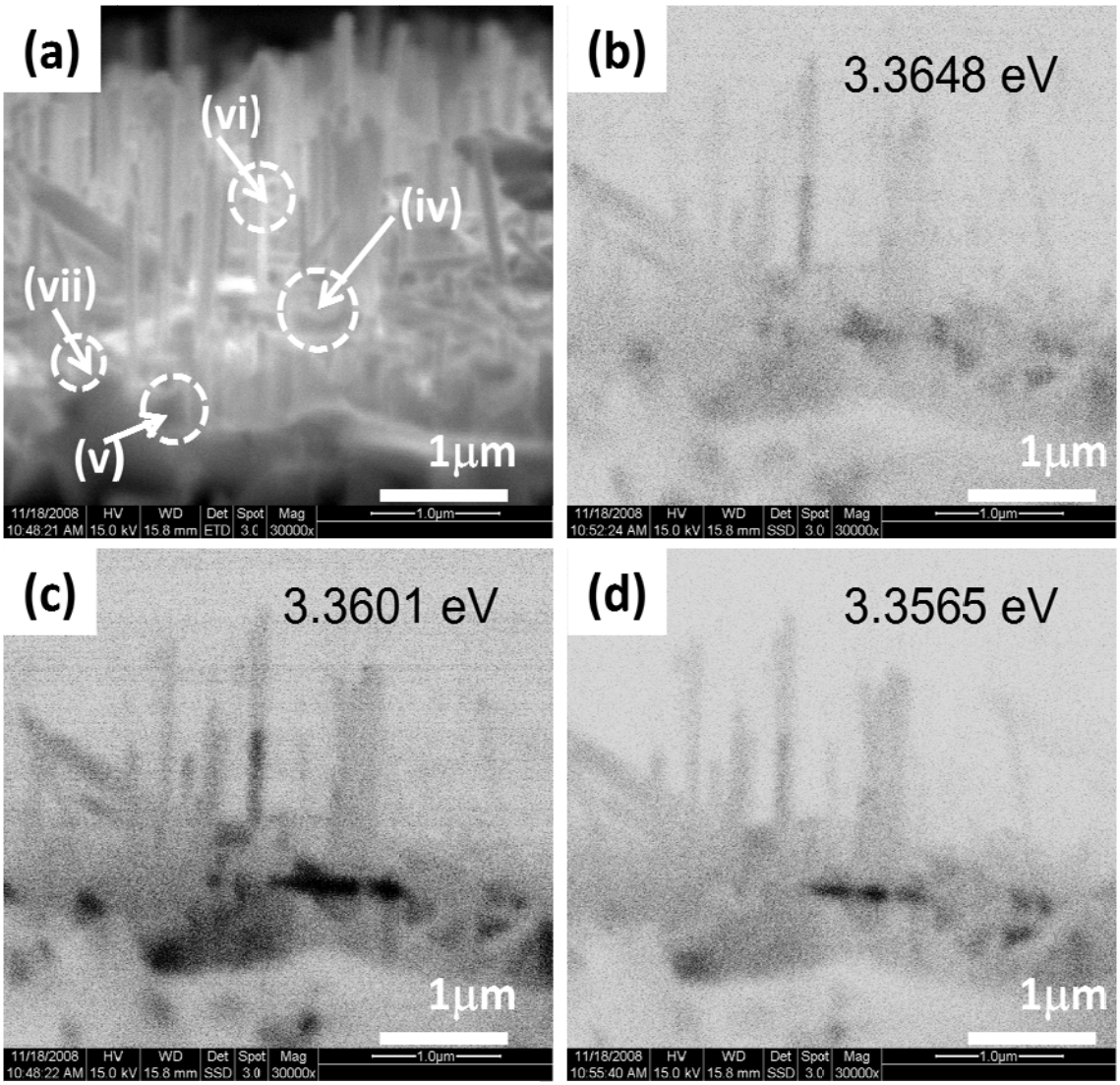

Fig 5.5: (a) SEM of sample grown on *a*-sapphire; monochromatic CL images centred at (b) 3.3648 eV (at the high energy side of the sample emission), (c) 3.3601 eV ($I_{6/6a}/I_7$) and (d) 3.3565 eV (I_9).

There is less evidence of the appearance of $I_{6/6a}/I_7$ emission 'hot spots' (and specifically no such spots are seen in the free standing nanorods which are expected to be single crystalline and do not intersect or overlap/coalesce with other nanorods or nanostructures; we note that the slightly enhanced emission at all wavelengths from location (vi) in *Fig 5.5 (a)* is due to two nanorods directly in line and thus both excited simultaneously by the electron beam-the enhancement is seen in all the monochromatic CL-SEM images in *Fig 5.5 (b)–(d)).*

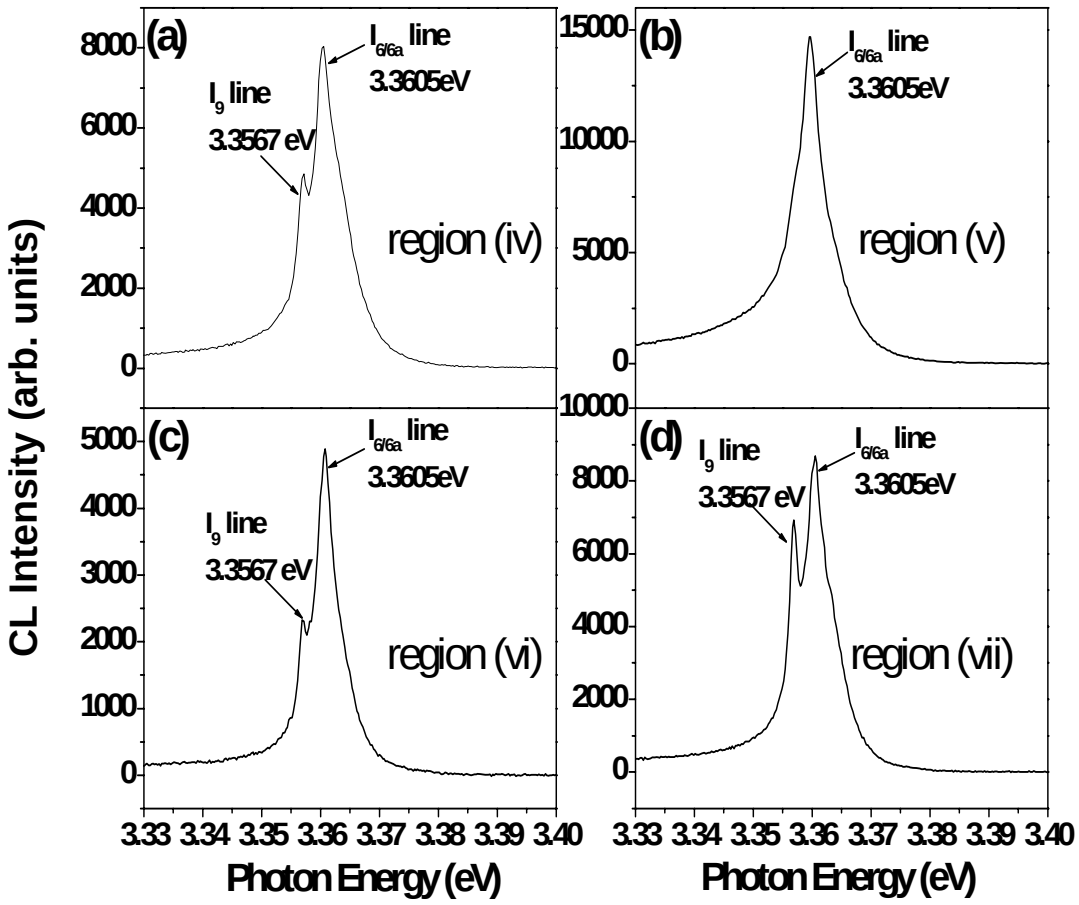

Fig 5.6: (a)-(d) is the CL spot scans from regions (iv)–(vii) marked in *Fig 5.5 (a)*.

CL spot scans of the regions marked (iv)–(vii) in *Fig 5.5 (a)* (which show local intensity increases in *Fig 5.5 (b)–(d))* are shown in *Fig 5.6 (a)–(d)*, respectively, and reveal no significant changes, specifically no new lines appearing from one scan to another. The intensity increases seen in *Fig 5.5 (b)–(d)* are thus mainly related to variations in the overall CL signal levels, as discussed previously. The In-related I_9 line intensity does change slightly from one scan to the next, which may indicate some degree of In aggregation in these samples (which was also seen in the samples grown on Si where some inhomogeneity in the distribution of the entire range of the DBE emission was noted) though this does not appear related to specific morphological features identifiable in SEM. The SEM data in *Fig 5.5 (a)* show that the ZnO nanorods in this sample are indeed well-aligned normal to the substrate (due

to mechanical effects some nanorods at the very edge of the sample have been knocked over). The growth of this sample on sapphire means that there is a stronger signal from the $I_{6/6a}$ Al-related DBE than was the case for the sample on Si, but it is seen to be quite homogeneously distributed, consistent with our hypothesis, specifically the absence of Al aggregation due to the lack of structural defects (associated with nanostructure overlap and coalescence) in the well-aligned nanorods of this sample.

5.4 Study of intentionally In and Al doped ZnO nanostructure sample

5.4.1 In-doping

The distribution of In within the ZnO nanostructures is studied using intentionally In doped samples. Method 1 mentioned in section 5.2 is used to grow ZnO nanostructures on both Si and *a*-sapphire to expand upon the data observed in nominally undoped samples.

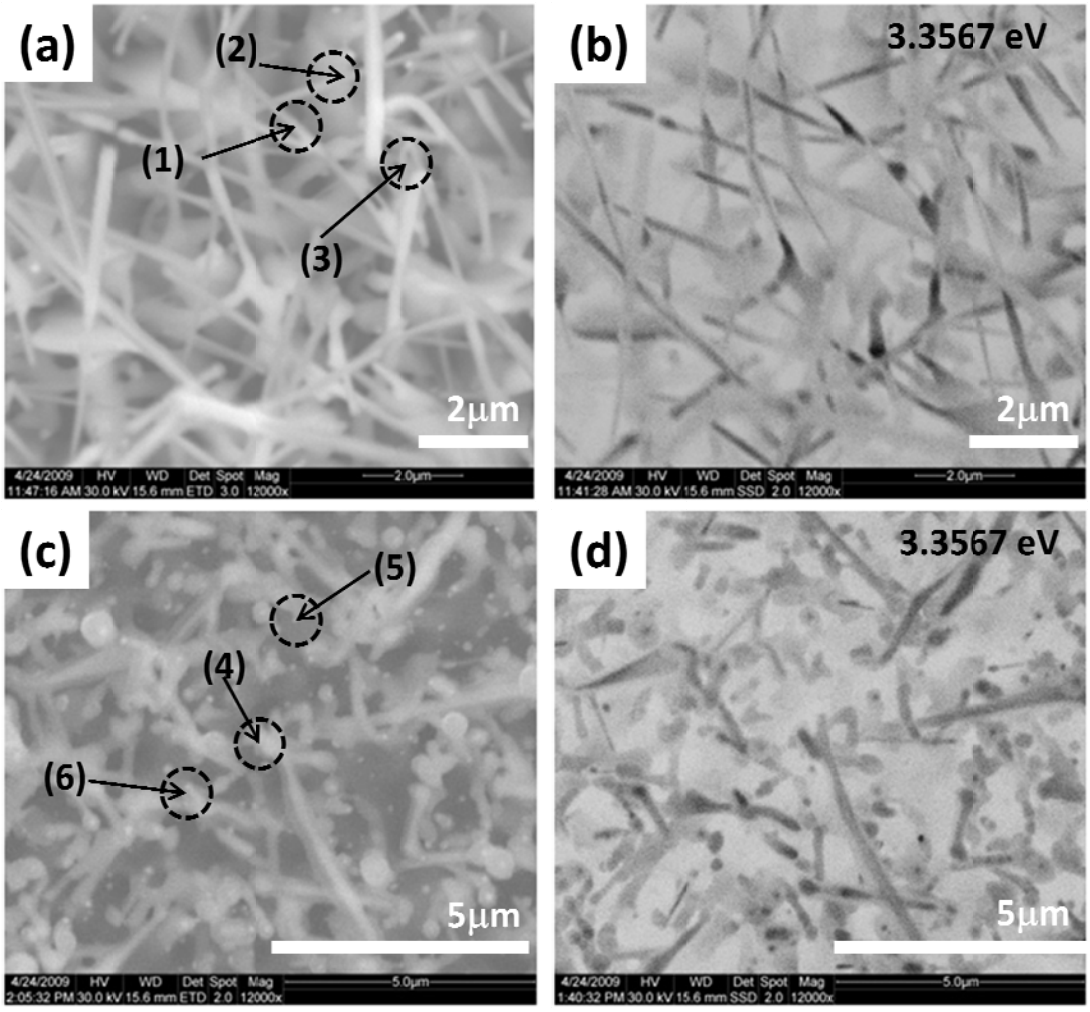

Fig 5.7: (a) and (c) SEM of In-doped sample grown on Si and *a*-sapphire respectively; (b) and (d) monochromatic CL images centred at 3.3565 eV (I_9).

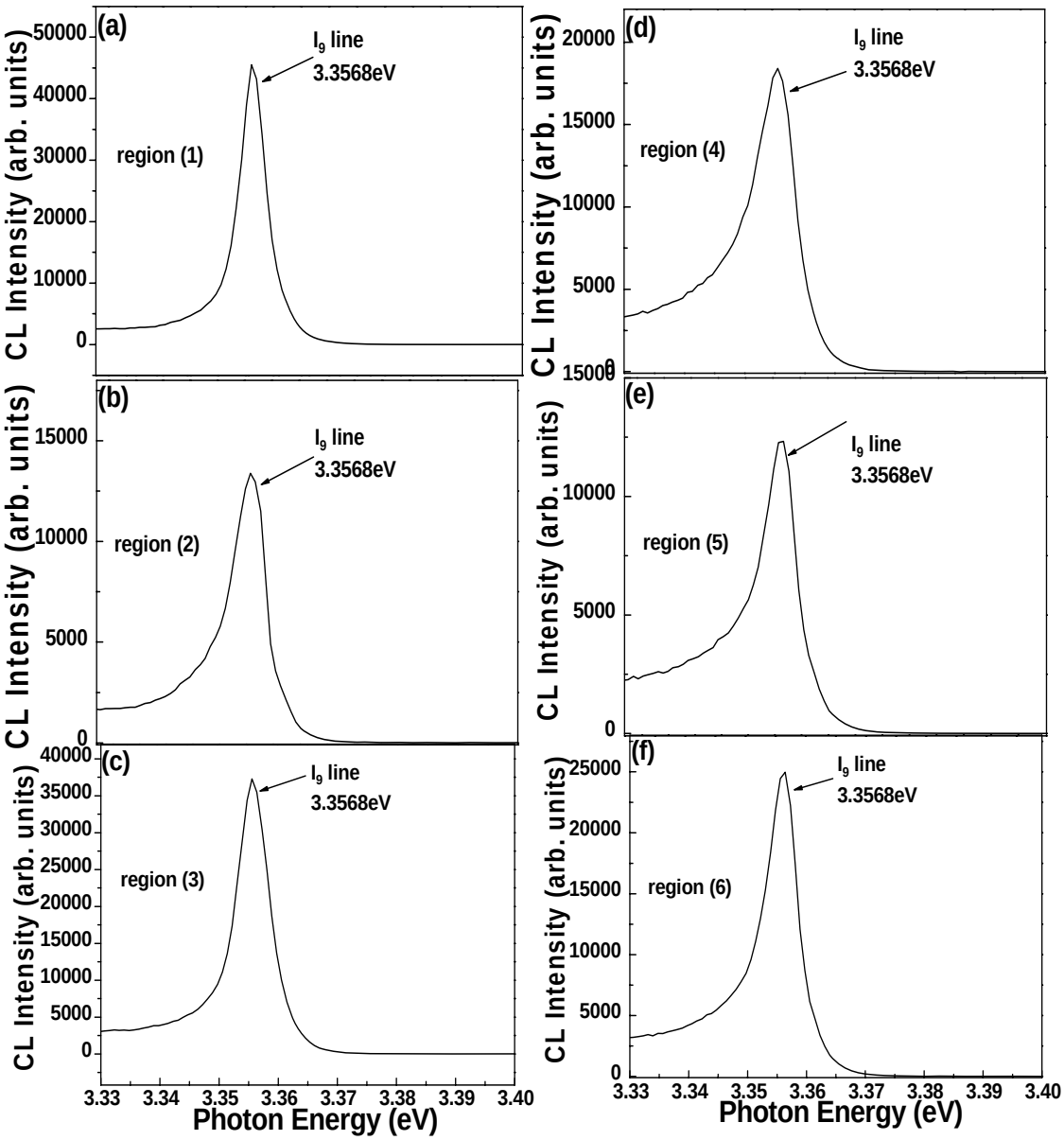

Fig 5.8: (a)-(c) is the CL spot scans from regions (1)–(3) marked in *Fig 5.7 (a)* and (d)-(f) is the CL spot scans from regions (4)–(6) marked in *Fig 5.7 (c)*.

Fig 5.7 (a) and *(c)* are the SEM images of samples grown on Si and *a*-sapphire, respectively. In *Fig 5.7 (c)* we can see the nanostructures are not aligned, while we get aligned nanorods in the normal samples (without intentional In doping) grown on

a-sapphire. The unaligned growth is clearly due to the In doping and has been already reported [21]. In the CL spectra in *Fig 5.8* we can only see a dominant peak of I_9 due to In DBE. The CL mapping has thus been taken centered only at 3.567 eV (I_9 line) for both samples. The CL spectra in *Fig 5.8 (a)-(c)* and *(d)-(f)* has been taken at the spots mentioned in *Fig 5.7 (a)* and *(c)* as (1)-(3) and (4)-(6), respectively. From *Fig 5.7 (b)* and *(d)* we can see no significant changes in CL signal, apart from the overall variations in the CL signal intensity discussed in the previous section. Spot (1) and (6) can be considered as a 'hot spot' compared to (2) and (3), and (4) and (5), respectively, but the CL spectra taken at these points in *Fig 5.8 (a)-(c)* and *Fig 5.8 (d)-(f),* respectively show little difference between the intensities. The CL lineshapes between these points are also very similar. As only one broad peak is visible and the intensity variation is also insignificant for these spectra, it may be concluded that the 'hot spots' observed are due to the overall CL signal variation.

5.4.2 Al Doping

Al doping was performed using both methods 1 and 2 mentioned in section 5.2. In this section only data from Al doped samples grown on Si by these two methods are shown (the Al doped samples grown on *a*-sapphire show similar data as shown in section 5.3 where well-aligned nanorods are obtained). *Fig 5.9 (a)* and *(d)* are the SEM images of the samples grown on Si by methods 1 and 2, respectively. *Fig 5.9 (b)* and *(e)* are the CL images centred at 3.3605 eV ($I_{6/6a}$ peak) for the two samples, respectively, and *Fig 5.9 (c)* and *(f)* are the CL images centred at 3.3567 eV (I_9 peak) for the same two samples, respectively. The CL spectra are taken at the spots shown in *Fig 5.9 (a)* and *(d)* marked as (7)-(9) and (10)-(12), respectively.

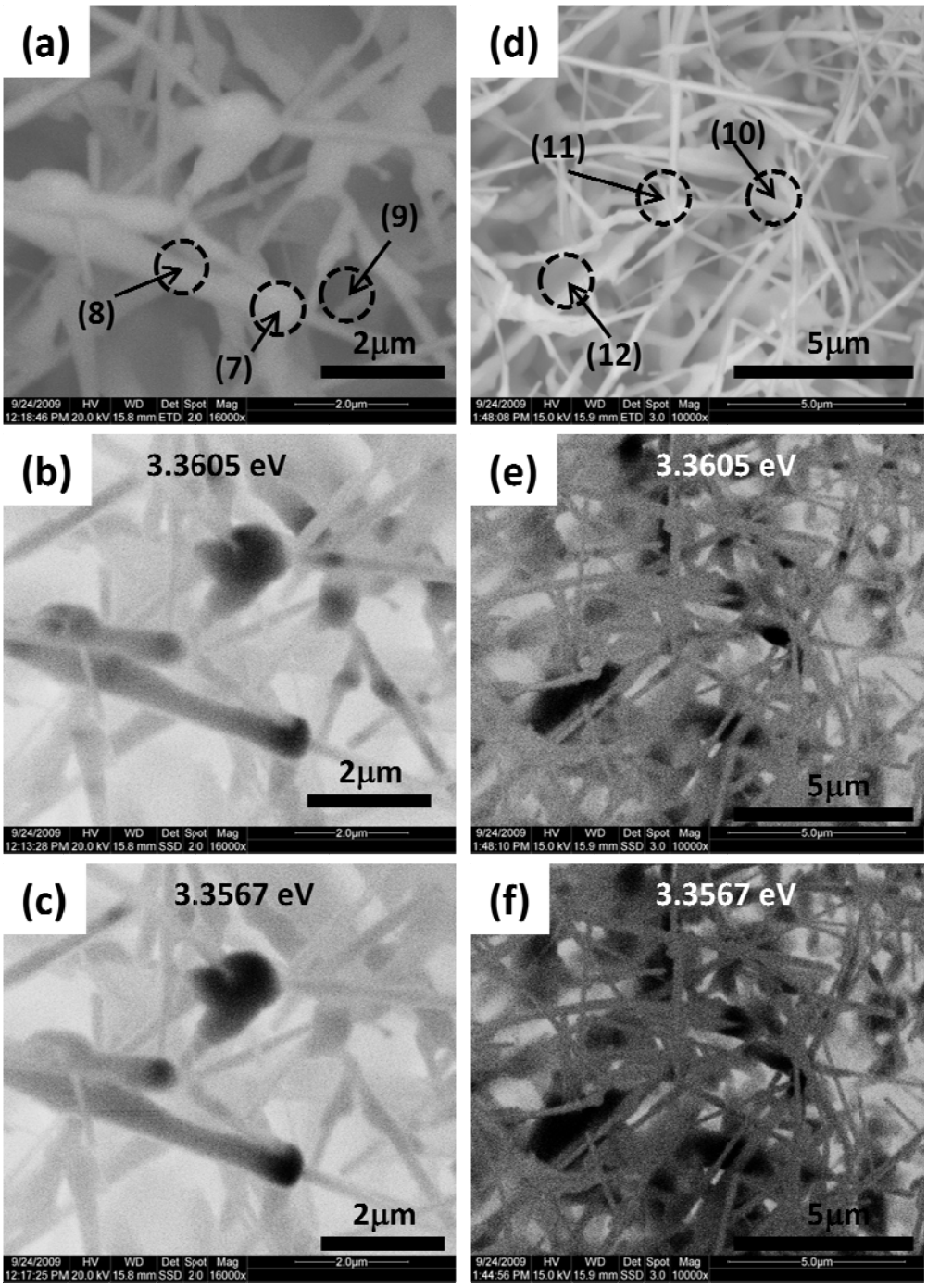

Fig 5.9: (a) and (d) SEM of two Al-doped samples grown on Si using doping methods 1 and 2 respectively; (b) and (e) monochromatic CL images centred at 3.3605 eV (I_6) and (c) and (f) monochromatic CL images centred at 3.3567 eV (I_9) for both samples, respectively.

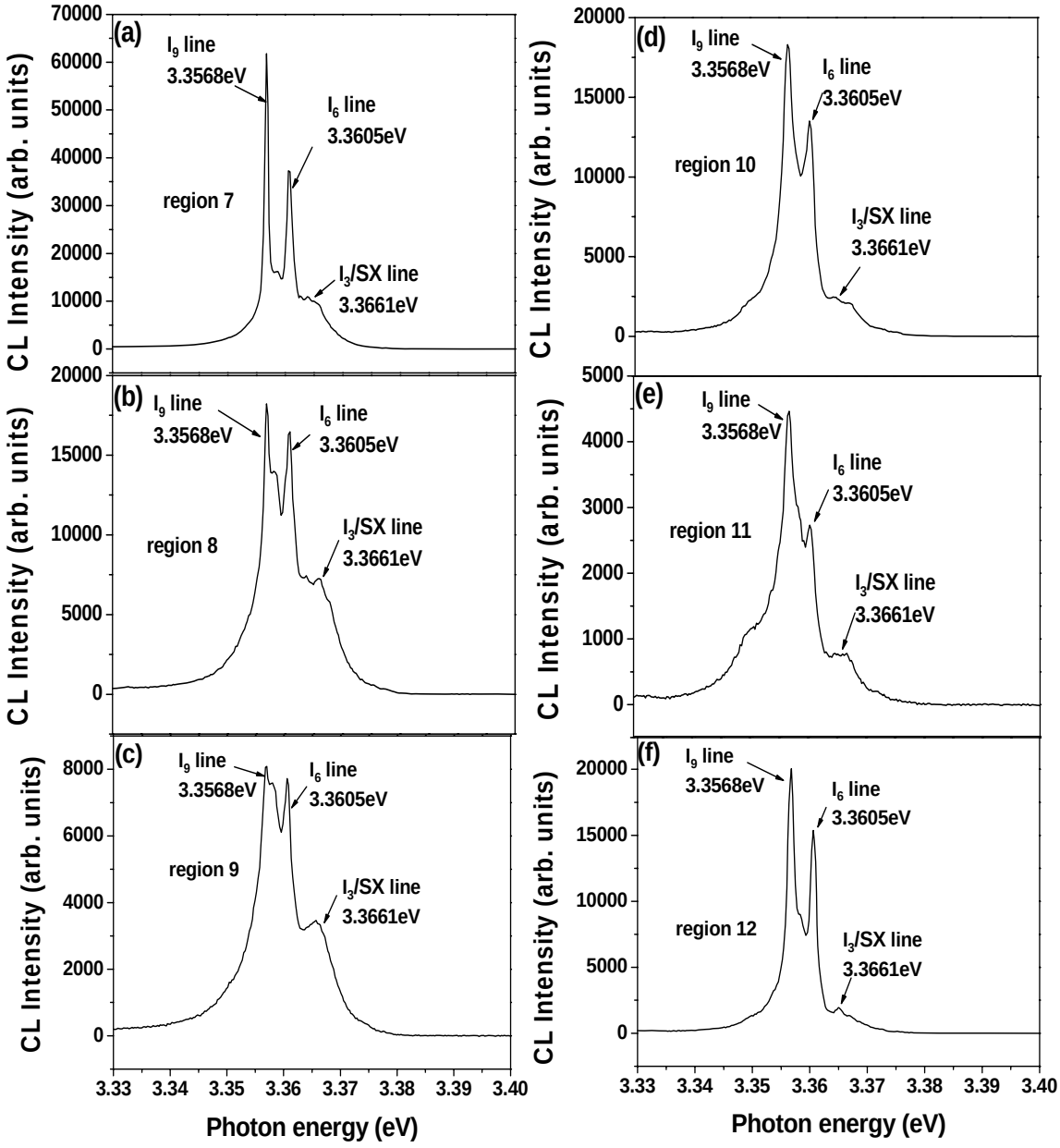

Fig 5.10: (a)-(c) is the CL spot scans from regions (7)–(9) marked in *Fig 5.9 (a)* and (d)-(f) is the CL spot scans from regions (10)–(12) marked in *Fig 5.9 (d)*.

There are clear overall variations in CL emission intensity (and also line broadening) in Al-doped samples grown by method 1 (*Fig 5.10 (a)-(c)*), but no hot spots of localised $I_{6/6a}$ emission in terms of relative intensity. The In-related I_9 line intensity also changes from one scan to the next, in addition to the $I_{6/6a}$ peak, which may indicate some degree of In aggregation in these samples (which was also observed in

the previous section with nominally undoped sample) though this does not appear related to specific morphological features identifiable by SEM. Also due to the reduction of entire signal intensity compared to undoped sample, some slight intensity variations for both the $I_{6/6a}$ and I_9 peaks are observable. However in the Al-doped samples grown by both methods there do appear to be localised hot spots of relatively higher $I_{6/6a}$ emission (see *Fig 5.10 (d)* and *(f)*, compared to *Fig 5.10 (e)* and *Fig 5.10 (a)* and *(b)*, compared to *Fig 5.10 (c)*) where the $I_{6/6a}$ lines are stronger relative to the I_9 and I_3/SX emissions). These corresponds to locations (10) and (12) in *Fig 5.9 (d)*. Once again these locations seem to coincide with locations of local crystal disruption, supporting the data and hypothesis of section 5.3.

So we conclude that the samples deliberately doped with Al powder have shown broadly similar results to those discussed in section 5.3 and thus support the hypothesis of an inhomogeneous distribution of Al dopants in ZnO nanostructures. The I_9 peak has shown some variation in relative intensity in the Al-doped samples, but not sufficient to support a hypothesis of In aggregation.

5.5 Conclusion

We have measured low temperature CL data on ZnO nanostructures grown on both Si and sapphire. The entire range of the DBE emission shows some evidence of inhomogeneous distribution for samples grown on Si, however the effect is much more pronounced for the Al-related $I_{6/6a}$ line and $I_{6/6a}$ 'hot spots' are seen only at locations in nanorods and nanosheets where different nanostructures cross or coalesce. This is suggestive of Al aggregation in regions of localized crystal disruption in the samples, such as grain boundaries, since no evidence for strain-induced lineshifts is observed. Localized crystal structure disruption appears to be a necessary rather than a sufficient condition for Al aggregation, since increased $I_{6/6a}$ emission is seen only in such regions, but not all such regions show increased emission and hence the aggregation appears to be dependent upon the microscopic nature of the structural defects. This hypothesis is consistent with further measurements of samples grown on sapphire and also with the data of Cao *et al.*,

who find an inhomogeneous distribution of donors for unaligned *p*-doped ZnO nanostructures grown on sapphire (where Al is the dominant donor species) by PLD [15]. Inhomogeneous distribution of the In-related I_9 and the I_3/SX lines is also observed in the various samples but the effect is not as pronounced as for the Al-related $I_{6/6a}$ emission and cannot be associated specifically with locations where different nanostructures cross or coalesce. Some of the inhomogeneity in the distribution of the I_9 and the I_3/SX lines may be partly related to variations either in CL collection efficiency or emitting volume below the incident electron beam. The intentionally Al-doped samples also support the hypothesis of an inhomogeneous distribution of Al dopants whereas the In-doped samples clearly show negligible inhomogeneity of I_9 emission.

In conclusion, Al donors appear to be significantly affected by localized crystal structure disruption in nanostructures and display a markedly inhomogeneous distribution throughout the sample as a consequence (even more so than the emission from other donor species). The presence of structural defects and regions of crystal disruption leads to Al aggregation at some of these locations and thence to Al-related $I_{6/6a}$ emission 'hot spots'. Further studies will be required to probe the microscopic details of the structural defects and correlate them with the CL emission distributions. Our findings may be important if *n*-doped ZnO nanostructures, doped using Al, are to be utilized for applications such as nanowire *p*–*n* junctions, field emitters etc., where dopant uniformity is a crucial parameter.

5.6 References

[1] W. Yang, R. D. Vispute, S. Choopun, R. P. Sharma, T. Venkatesan, and H. Shen, Applied Physics Letters 78 (2001) 2787.

[2] A. Tsukazaki, A. Ohtomo, T. Onuma, M. Ohtani, T. Makino, M. Sumiya, K. Ohtani, S. F. Chichibu, S. Fuke, Y. Segawa, H. Ohno, H. Koinuma, and M. Kawasaki, Nat Mater 4 (2005) 42.

[3] A. Osinsky, J. W. Dong, M. Z. Kauser, B. Hertog, A. M. Dabiran, P. P. Chow, S. J. Pearton, O. Lopatiuk, and L. Chernyak, Applied Physics Letters 85 (2004) 4272.

[4] R. L. Hoffman, Journal of Applied Physics 95 (2004) 5813.

[5] H. Morkoc and U. Ozgur, *Zinc oxide Fundamentals, materials and Device technology*, WILEY-VCH Verlag GmbH & Co. KGaA, 2009.

[6] U. Ozgur, Y. I. Alivov, C. Liu, A. Teke, M. A. Reshchikov, S. Dogan, V. Avrutin, S. J. Cho, and H. Morkoc, Journal of Applied Physics 98 (2005) 041301.

[7] C. Klingshirn, Physica Status Solidi B-Basic Solid State Physics 244 (2007) 3027.

[8] D. C. Look, D. C. Reynolds, J. R. Sizelove, R. L. Jones, C. W. Litton, G. Cantwell, and W. C. Harsch, Solid State Communications 105 (1998) 399.

[9] T. Minami, H. Sato, H. Nanto, and S. Takata, Japanese Journal of Applied Physics 24 (1985) L781.

[10] F. Bertram, D. Forster, J. Christen, N. Oleynik, A. Dadgar, and A. Krost, Applied Physics Letters 85 (2004) 1976.

[11] H. v. Wenckstern, H. Schmidt, C. Hanisch, M. Brandt, C. Czekalla, G. Benndorf, G. Biehne, A. Rahm, H. Hochmuth, M. Lorenz, and M. Grundmann, physica status solidi (RRL) - Rapid Research Letters 1 (2007) 129.

[12] F. Bertram, D. Forster, J. Christen, N. Oleynik, A. Dadgar, and A. Krost, Journal of Crystal Growth 272 (2004) 785.

[13] B. Q. Cao, M. Lorenz, A. Rahm, H. v. Wenckstern, C. Czekalla, J. Lenzner, G. Benndorf, and M. Grundmann, Nanotechnology 18 (2007) 455707.

[14] T. Nobis, E. M. Kaidashev, A. Rahm, M. Lorenz, J. Lenzner, and M. Grundmann, Nano Letters 4 (2004) 797.

[15] M. Yan, H. T. Zhang, E. J. Widjaja, and R. P. H. Chang, Journal of Applied Physics 94 (2003) 5240.

[16] H. Zhou, J. Fallert, J. Sartor, R. J. B. Dietz, C. Klingshirn, H. Kalt, D. Weissenberger, D. Gerthsen, H. Zeng, and W. Cai, Applied Physics Letters 92 (2008) 132112.

[17] B. K. Meyer, H. Alves, D. M. Hofmann, W. Kriegseis, D. Forster, F. Bertram, J. Christen, A. Hoffmann, M. Straßburg, M. Dworzak, U. Haboeck, and A. V. Rodina, Physica Status Solidi (b) 241 (2004) 231.

[18] JCPDS Card No. 27-1402 (for Si), JCPDS Card No. 36-1451 (for ZnO).

[19] J. Grabowska, A. Meaney, K. K. Nanda, J. P. Mosnier, M. O. Henry, J. R. Duclere, and E. McGlynn, Physical Review B 71 (2005) 115439.

[20] J. R. Duclere, B. Doggett, M. O. Henry, E. McGlynn, R. T. R. Kumar, J. P. Mosnier, A. Perrin, and M. Guilloux-Viry, Journal of Applied Physics 101 (2007) 013509.

[21] F. Hong Jin, F. Bodo, S. Roland, H. Cameliu, B. Andreas, L. Hartmut, D. Armin, K. Alois, C. Silke, G. Ulrich, and Z. Margit, Nanotechnology 17 (2006) S231.

Chapter 6

Study of the microscopic origin of the surface exciton peak seen in ZnO nanostructures

In this chapter, a PL peak seemingly unique to ZnO nanostructure at ~3.367 eV, known as the SX peak is studied in detail. PL, SEM and XRD studies have been used to try to determine the nature of this peak. It was previously assumed in several reports that the peak is due to surface adsorbed species, especially adsorbed oxygen at the surface of ZnO nanostructures; however the microscopic origin of the peak has remained an ambiguous issue. We have investigated whether the feature's origin is related to adsorbed oxygen by measuring the PL spectra of the nanostructures exposed to UV light under high vacuum conditions, and treated by plasma, both of which are well known processes leading to desorbtion of oxygen. Additionally, localised high voltage application has been performed in high vacuum and in different gas atmospheres. We have found no consistent effects on the SX peak as a result of the UV illumination at high vacuum or as a result of either oxygen or argon plasma treatments. The result of the voltage application studies shows a consistent variation of the peak in vacuum and different atmospheres. X-ray photoelectron spectroscopy (XPS) and TEM studies are also used to help interpret the probable microscopic origin of the SX peak. A model of the origin of the SX peak is outlined, consistent with our data and other reports in the literature. This model, although tentative, may provide a useful starting point for further studies.

6.1 Introduction

ZnO nanostructures provide an ideal system to study the influence of surface effect on optical properties due to their large surface-to-volume ratios. The influence of the near-surface region considerably increases with decreasing rod or wire diameter. As mentioned previously PL studies of both bulk ZnO and ZnO nanostructured material reveals a range of near bandedge excitonic emission lines, mostly DBE lines at low temperature. These lines are mostly well known and named as I_0 to I_{11} by e.g. Meyer *et al*.[1]. The microscopic origin of some of these lines are known, e.g. I_4 is due to H, I_6 due to Al, I_8 due to Ga and I_9 due to In impurities [1]. These peaks are visible both in bulk and nanostructured ZnO material. However, a broad peak at ~3.367 eV, denoted as I_2 by Meyer *et al.*, and regarded by various authors as a surface exciton (SX) peak, can be seen mostly in nanostructured materials [2-7]. The linewidth of the peak is much wider (~4.5 meV) compared to the other I lines. A similar kind of peak was observed in cleaved ZnO crystals as reported by Travnikov *et al.* [8], almost two decades ago, but the SX peak is reported more recently in emission from ZnO nanostructures with high surface-to-volume ratios [2, 3, 5, 6, 9, 10]. In other II-VI semiconductors e.g. CdS [11-13], CdSe [11] and in III-V semiconductors e.g. GaAs [14], GaN [4] similar peaks have been observed, which are generally regarded as exciton peaks related to the crystal surface. This type of surface related peak was first observed in CdS crystals, and later in ZnO crystals a similar type of peak was assigned to SX related emission [8, 12]. It was assumed that in CdS crystals the SX peak line shape, and especially the tail observed on the low-energy side, was due to excitons localized at centres which have different distances to the sample surface. A similar conclusion was also reached in studies of the ZnO SX peak more recently [2]. A report has been published very recently on GaN where direct evidence of SX emission has been shown while studying the macro-PL (M-PL) and μ-PL of single GaN nanowires [4]. These authors also concluded that the broadening observed for the nanowire ensemble is a natural consequence of the energy dispersion of surface BE states as a function of their distance from the surface, similar to the cases of ZnO

and CdS materials. However, they did not reach any conclusion as to the nature of the surface species responsible.

In the last few years this peak has been studied by the ZnO community with increasing interest due to its association with surface related phenomena generally which are important issues for applying nanostructures in e.g. optical devices [2, 5, 7-9, 15, 16]. Usually the SX peak is visible only at temperature below 25 K. The large surface-to-volume ratio of nanostructures is regarded as the main possible reason of its appearance mostly in nanostructured material. Additionally, in nanostructures showing the SX peak the bandedge intensity decays rapidly with increasing temperature as shown experimentally by Grabowska *et. al* [7]. It appears that the surface conditions responsible for this SX peak at low temperature lead also to temperature activated NR recombination processes at higher temperature. Wischmeier *et al.* reported time dependent spectroscopic studies of this peak and also concluded that origin was excitons trapped at near surface states [2]. The inhomogeneously broadened line shape was concluded to be due to BEs with either different distances to the surface or to differences in interaction with additional surface centres of an inhomogeneous nature (such as reconstructions, dangling bonds, impurities etc.) [2, 17]. The thickness of the surface layer from which the SX band is emitted has been reported as 25 nm by Voss *et. al.* [10], and 5nm by Yang *et. al.*[6].

To utilize ZnO nanostructures in devices it is very important to understand the surface related phenomena which underlie this peak emission. The microscopic origin of this peak is not reported clearly yet, but it is believed that adsorbed species in the near surface region of ZnO (with a lot of attention centering on O) are the trapping centers responsible for this BE. The chemisorbtion process in semiconductor and in ZnO is reasonably well known and species such as O^{2-}, O^{-}, OH^{-}, H_2O etc. are common adsorbates at the surface of ZnO [18] and have been considered as possible origin of the trapping centre of the excitons responsible for the SX band [5, 6, 9, 16].

Additionally, Richters *et al.* reported a significant increase in the SX peak intensity in polymer coated ZnO nanowires and ZnO/Al_2O_3 core/shell nanowires compared to as-grown ZnO nanowires [5, 9]. They explained in terms of, the polymer/Al_2O_3 layer acting as a dielectric medium, which reduce the near surface band bending by screening the charge carriers located in the near surface region. The wavefunction overlap of electrons and holes and thus exciton formation increase due to this reduced band bending, hence creating a higher density of near surface excitons. This increased amount of near surface free excitons which may be trapped by the adsorbates responsible leads to significant enhancement in the SX peak. Thus the SX intensity depends on three coinciding factors-

i) The high surface-to-volume ratio of nanostructures
ii) The presence of suitable adsorbates on the nanostructure surface to trap free excitons and
iii) A reduction in surface band bending allowing a higher concentration of near surface free excitons.

To understand the exact microscopic origin of this broad surface related peak it is necessary to perturb the sample surface in a way which may alter the amount of the adsorbed species. Size dependent PL and μ-PL studies are not suitable methods to study this aspect, as they can interpret the presence and distribution of the peak, but not its origin. Hence, surface treatments are needed and we are especially interested in those which affect adsorbed O concentrations. In this work we have studied the effects on the SX peak of ZnO nanostructures of attempting to desorb surface species using different surface treatments, and allowing re-adsorbtion of such species again. Desorbtion of surface species is a well known process and there are several publications which show direct evidence of desorbtion of species like O^-, O^{2-}, OH^- from ZnO surface [19-28]. UV illumination is the most effective method to desorb species such as O^- and O^{2-}, where photolysis occurs when UV light of energy more than bandgap energy is incident on ZnO samples in high vacuum [20, 24, 25, 27, 29-31]. These experiments have mostly been done to observe the photocurrent response, i.e. the conductivity of ZnO and in some cases for cleaning of ZnO crystal surfaces

[18, 23-25, 29, 30, 32]. As grown ZnO materials are usually *n*-type and adsorbate species like O, OH captures free electrons from *n*-type ZnO, chemisorbing on the surface and create depletion layers near the ZnO surface.

$$O_2\,(g) + e^- \rightarrow O^{2-}\,(s) \qquad \text{Eqn. 6.1}$$

UV illumination creates photogenerated holes which can be move to the surface and these holes recombine with negatively charged ions and, desorb the species.

$$O^{2-}\,(s) + h^+ \rightarrow O^2\,(g) \qquad \text{Eqn. 6.2}$$

Hence, if the SX is due to such species, desorbtion of these from ZnO nanostructures after UV illumination at high vacuum should cause the SX band to reduce or disappear. In fact, we have not seen any significant and consistent change in the SX band due to such UV illumination in vacuum.

Also we report the effect of surface plasma treatments on the SX band intensity. Kim *et al.* reports the effect of plasma treatment on ZnO epitaxial films, where it is found that O plasma treatment suppress the chemisorbtion sites effectively and helps to diffuse surface O within the ZnO bulk which in turn reduces adsorbed species at the surface [33]. The same plasma treatment and also plasma treatments with Ar plasma have not shown any significant effect on the SX peak intensity although a significant reduction of adsorbed oxygen is expected in the case of ZnO nanostructure surfaces, similar to the films.

XPS studies of UV illuminated sample do not show any direct evidence of adsorbtion or desorbtion of O, but show clear increases in OH peak levels after illumination in the O1s spectrum region, which indicates the difficulty in removing OH species from the ZnO surface. The increase of OH levels also indirectly indicates that desorbtion of O from the surface happens due to UV illumination, whereby the surface desorbed of O reacts quickly with ambient H_2O and thus increases the OH species.

Furthermore, we have applied high voltages (~60V) to local regions of the sample to see the effects on the SX peak. In this study the SX peak increases and decreases

with respect to untreated samples and treatment in different gas atmospheres yields consistent changes confirming the relationship of the SX peak with surface treatment in defects. Furthermore, TEM studies of ZnO nanorod/nanowall samples where the SX peak is strongest show the clear evidence of extended defects within the wall structure and suggests a relationship of the SX peak to such defects.

6.2 Experimental description

The growth technique of the ZnO nanostructures studied is already described in previous chapters. In summary, for the experiments done in this chapter, ZnO nanostructures were grown on *a*-plane (11-20) sapphire, *n*-type and *p*-type Si substrates by the VPT method. ZnO and graphite powders were mixed in 1:1 ratio by mass for use as a source powder, and the growth temperatures used were either 900^{o}C or 950^{o}C. The sample was placed in the middle of a horizontal single zone furnace on top of the source powder which was placed in either an alumina or a multisil boat.

Electron microscopy images have been taken using FESEM (Hitachi S-4300 field emission system) and SEM (Karl-Zeiss EVO series). XRD has been performed using a Bruker AXS D8 advance texture diffractometer. PL spectra have been acquired using a Bomem Hartmann & Braun DA8 FT spectrometer. For all the spectra taken in this study, the same instrumental setup was used. The aperture of the detector in all cases enabled a spectral resolution of 5 cm^{-1}. The detector gain was set at 1 for all measurements. In terms of eV units, the spectral resolution was ~0.4 meV and the number of co-added scans was 100. In all PL spectra the SX peak has been compared to the other two main peaks (I_6 and I_9) in terms of peak intensity (not integrated intensity) because spectral linewidths were largely unchanged for all features.

Material surface composition before and after UV illumination has been studied using XPS at base pressures in the preparation and analysis chambers of 2x10^{-6} mbar

and $1x10^{-9}$ mbar, respectively, using an Al Kα (hγ =1486.6 eV) X-ray source[*]. The pass energy of the analyser was set at 20 eV yielding a resolution of approximately 1.0 eV. The XPS peaks were fitted with mixed ratio of Gaussian and Lorentzian line shapes and a Shirley background function. The TEM study has been done using a JEOL2000FX system operating at 200 kV. TEM specimens have been prepared in the same way as described previously in section 3.4.2[†]. The surface treatments study which has been done to investigate the effect on SX peak intensity is described in more detail below.

6.2.1 Plasma treatment

Plasma treatments have been performed using O and Ar plasmas[‡]. At the beginning O plasma was used, but no changes have been observed in the SX peak. Following this, an Ar plasma treatment has been performed on subsequent samples. The O plasma was produced with an inductively coupled plasma reactive ion etching (ICP–RIE) system (Unaxis 790 ICP-RIE) with an ICP power of 50 W and an RF power of 125 W, O pressure of 15 mTorr, and a flow rate of 30 sccm for 30 minutes. The Ar plasma was produced using the same instrument and conditions except the RF power and time was reduced to 5.0 W and 5 minutes. The ZnO nanostructures were exposed to the plasma without intentional heating of the sample.

6.2.2 UV illumination

UV illumination has been performed using a hand held 250W iron doped metal halide UV lamp (UV-H 253 BL). The spectral output of the lamp is from 280 nm-450 nm (2.75 eV-4.42 eV), and thus has a fraction of its photons with energy above the room temperature bandgap of ZnO (~3.3 eV). To study the effect of desorbtion of surface species the sample has been placed inside the cryostat (Janis research Co.

[*] XPS experiments and line-fitting/identification analysis was done by Mr. Kumar Kumarappan from School of Physical Sciences, NCSR, Dublin City University.
[†] TEM study was performed by Dr. Simon Newcomb from Glebe Scientific Ltd. Tipperary, Ireland.
[‡] Plasma treatments were performed by Prof. Hong Koo Kim's group from the School of Engineering, University of Pittsburgh, USA.

Inc.) and maintained at low temperatures (~18K) PL spectra have been taken before illumination. After this the cryostat temperature was raised to room temperature and the vacuum pump has been switched on until the pressure of the inner chamber of the cryostat (where the sample was placed) reached to 10^{-6} mbar. We have found 2.6×10^{-6} mbar is the lowest pressure the cryostat used in this study can attain.

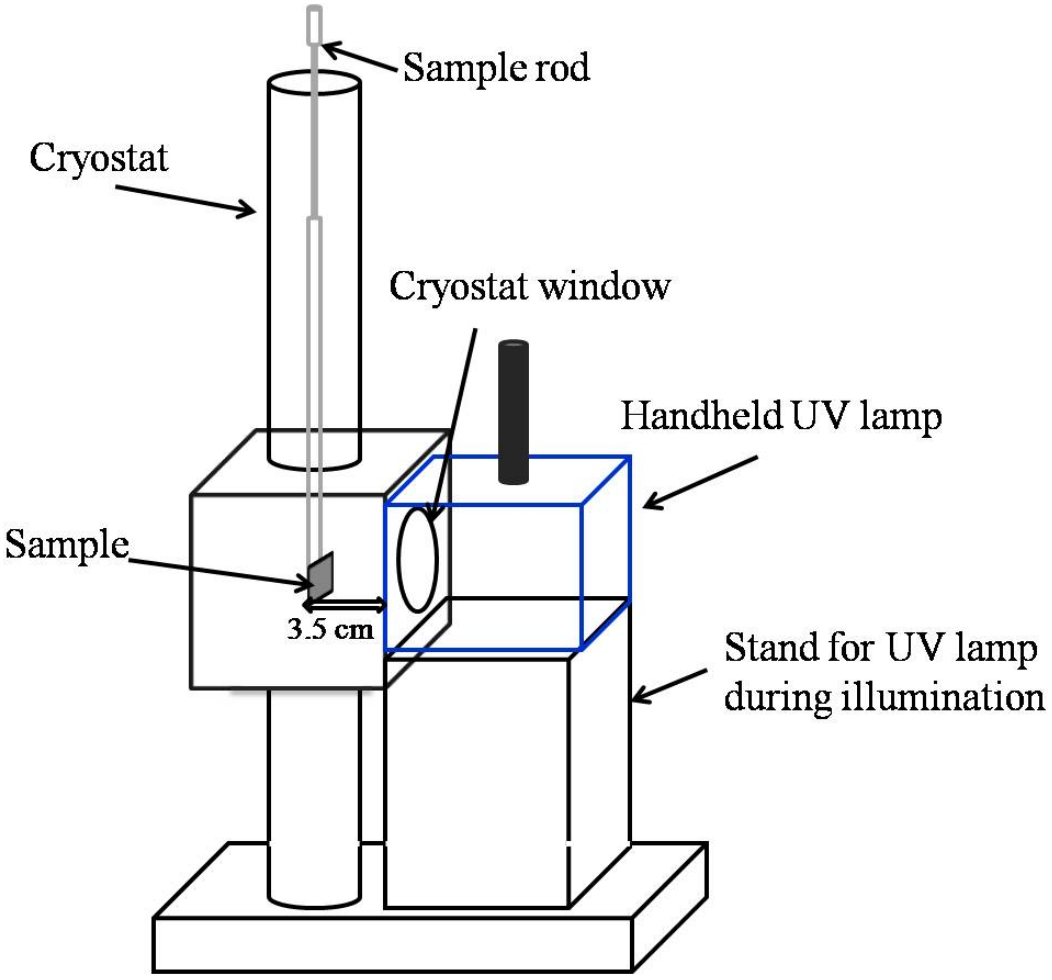

Fig 6.1: Schematic diagram of the arrangement of the UV illumination system at high vacuum on ZnO nanostructure samples within the PL cryostat.

The PL chamber has been chosen for in-situ UV illumination to avoid any further adsorbtion of O or any other species from air while transferring from one chamber to another. For the illumination the UV light source has been placed in front of the cryostat window facing directly at the sample as shown in *Fig 6.1* below with no focusing optics. After the illumination the chamber has been filled with He gas prior

to starting the compressor to reach low temperatures, which are essential as the SX PL peak is visible only at temperatures below ~25K.

The distance of the lamp to the sample was 3.5 cm. The UV illumination has been done for different times (6 hours, 8 hours, 20 hours and 24 hours). The power density of the UV lamp has been measured using a Newport digital power meter (model 815), a photodiode (Newport; model 818-SL) and neutral density filter in front of the photodiode. The power densities of the UV lamp have been measured at 0 cm distance, at 3.5 cm (the sample distance within PL chamber) and at 18 cm (sample distance within the XPS chamber) from the lamp, with the power meeting wavelength set to the highest (450 nm), lowest (280 nm) and middle wavelength (365 nm) values of the UV lamp spectrum.

6.2.3 Electrical voltage application

To apply electrical voltages in vacuum and in different gas atmospheres the PL cryostat has again been used, as it is important to check the PL spectrum without exposing the sample to air (in case of vacuum and He gas atmosphere experiments) similar to the UV illumination experiments. The electrical wires have been sent to the sample within the cryostat through the temperature controller feedthrough of the cryostat.

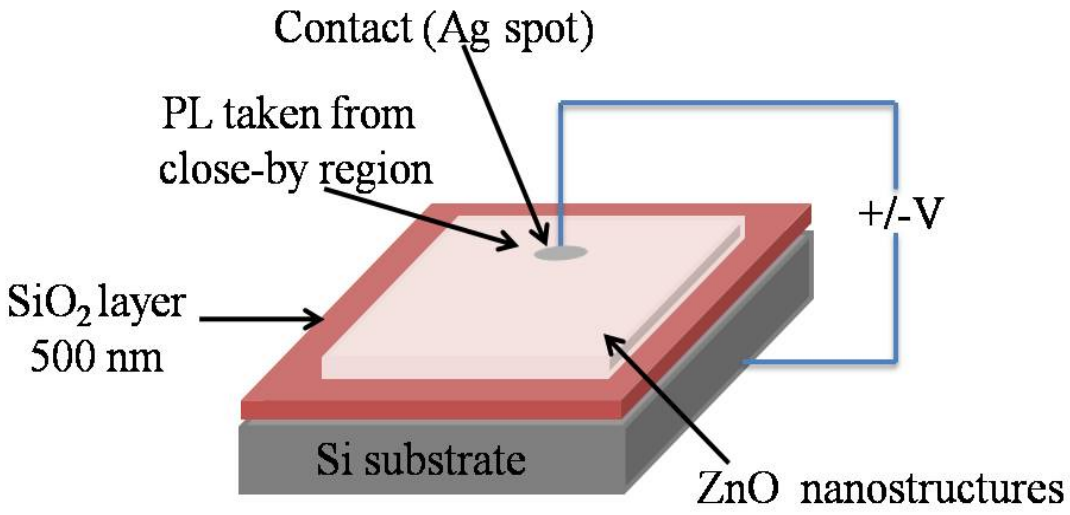

Fig 6.2: Sample structure for electrical voltage application.

To apply voltages the above structure in *Fig 6.2* has been realised. All samples used for this electrical study have been grown on Si as sapphire is an insulator. The SiO_2 layer has been deposited using plasma enhanced chemical vapour deposition techniques, and thickness was ~500 nm[§]. The SiO_2 layer acts as an insulator between the Si and ZnO nanostructures. Using conductive silver (Ag) paste one wire has been placed at top of ZnO nanostructure deposited area, and another at back of the sample on Si. The voltage has been applied for 1 hour in all experiments. To investigate any differences in the SX peak intensity behaviour the experiments have been done using both *n*- and *p*-type Si, using both positive and negative voltages applied to the nanostructures and with different voltage levels ranging from 40V to 70V. Initially all the above mentioned experiments have been done at high vacuum in the range of 10^{-6} mbar (which is maximum vacuum capability of our cryostat as mentioned in the previous section).To investigate the effects of voltage applications in other atmospheres, the voltage has been applied in air (immediately before checking PL) and in pure He gas atmospheres. Like the UV illumination experiments, in these experiments also the chamber has been filled with He before cooling the system to make low temperature PL measurements after voltage application.

[§] The SiO_2 deposition has been performed by Dr. Ram Prasad Gandhiraman from the BDI, Dublin City University.

6.3 Results

6.3.1 Relationship of SX peak with nanostructure morphology

Fig 6.3 shows the SEM and PL spectra of ZnO nanorod/nanowall and nanorod samples grown at 900^{o}C and 950^{o}C. The data from these two samples and similar data from many other samples grown at 900^{o}C and 950^{o}C in our laboratory have helped us form a general conclusion about a relationship between the SX peak intensity at ~3.367 eV and the ZnO nanostructure morphology.

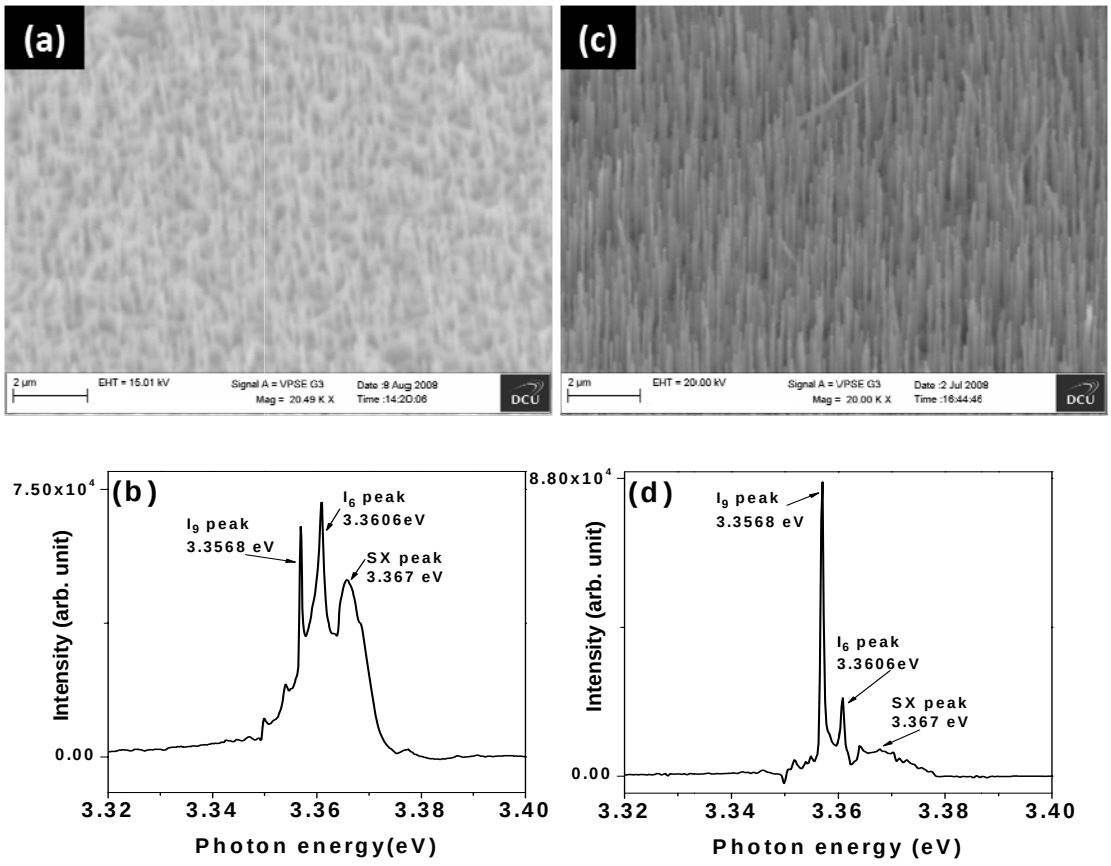

Fig 6.3: SEM image (a) and PL spectrum (b) of ZnO nanorod/nanowall sample grown at 900^{o}C; SEM image (c) and PL spectrum (d) of ZnO nanorod sample grown at 950^{o}C.

As mentioned in chapter 3, for growth at 900^{o}C we always observe a nanorod/nanowall morphology and for growth at 950^{o}C a nanorod morphology is

almost always observed. For growth at 950^{o}C occasionally some short basewalls or sidewalls, as shown in *Fig 6.4,* are observed.

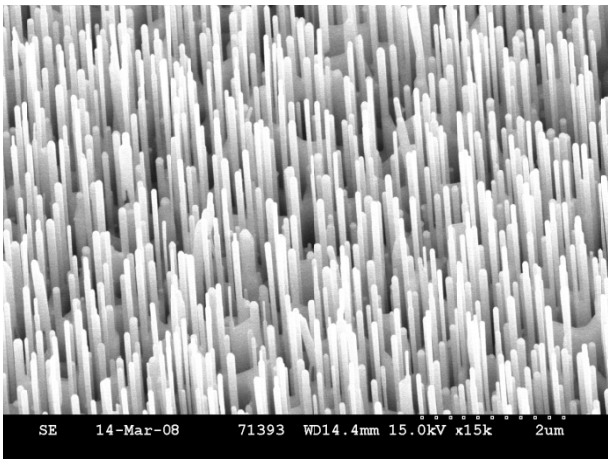

Fig 6.4: ZnO nanorod samples grown at 950^{o}C, with some basewalls and sidewalls.

From *Fig 6.3 (a)* and *(b)* we can see for the nanorod/nanowall morphology (where the diameter of nanorods are in the range of ~95 nm and their lengths are in the range of ~500 nm) the large and broad SX peak is observed. From *Fig 6.3 (c)* and *(d)* we see for the nanorod only morphology (i.e. mostly nanorods, occasionally with some short walls at the base of nanorods) the SX peak intensity is quite low. The diameter of nanorods for the 950 ^{o}C sample is similar or slightly less than for the 900 ^{o}C and their length is ~1.5 μm, indicating an equal or larger surface-to-volume ratio for the 950 ^{o}C sample compared to the 900 ^{o}C sample. These conclusions are supported by observations of a large number of samples grown in our laboratory (~60).

It has been reported that the SX peak is the dominant peak for ultrathin nanowires of diameter less than 10 nm, and that the SX peak intensity decreases with increasing diameter and the SX peak is attributed to a surface related defect on this basis entirely [3]. From our study the main point to be noted is that a high intensity SX peak is never seen for the 950 ^{o}C grown samples, where only weak or no SX emission is observed. A high intensity SX peak is observed only in samples grown at 900^{o}C showing nanorod/nanowall morphology, despite the fact that the surface-to-

volume ratio of the nanorod/nanowall structures is similar to or less than that of the nanorod only structures. Based on our observations of many samples grown at both 900^{o}C and 950^{o}C we conclude that the relative intensity of the SX peak is not solely dependent on the surface-to-volume ratio of the ZnO material (the factor which determines site density for adsorbtion of impurity species), i.e. the conventional explanation that the SX peak intensity level is due solely to adsorbed species such as O on large surface-to-volume ratio morphologies is clearly incomplete.

A closely related point is the question of what determines presence and absence of the SX peak in terms of nanostructure morphology. From *Fig 6.3* and also from many other samples, we have observed that the SX peak (whether strong or weak) is visible only in samples with clear evidence of a nanorod/nanowall morphology as shown in *Fig 6.3 (a)* or with a nanorod morphology with base or side walls (similar to the example shown in *Fig 6.4*), but, conversely, all ZnO nanostructure samples with nanorod/nanowall morphology do not show SX peak.

In summary it can be conclude that the existence of the SX peak in PL spectra is always dependent on the presence of nanowalls, but the presence of nanowalls does not guarantee the presence of the SX peak. Consequently there must be one or more other factors responsible for the appearance of this peak in the PL spectra in addition to the nanorod/nanowall morphology.

6.4.2 Relationship of SX peak with XRD of nanostructure

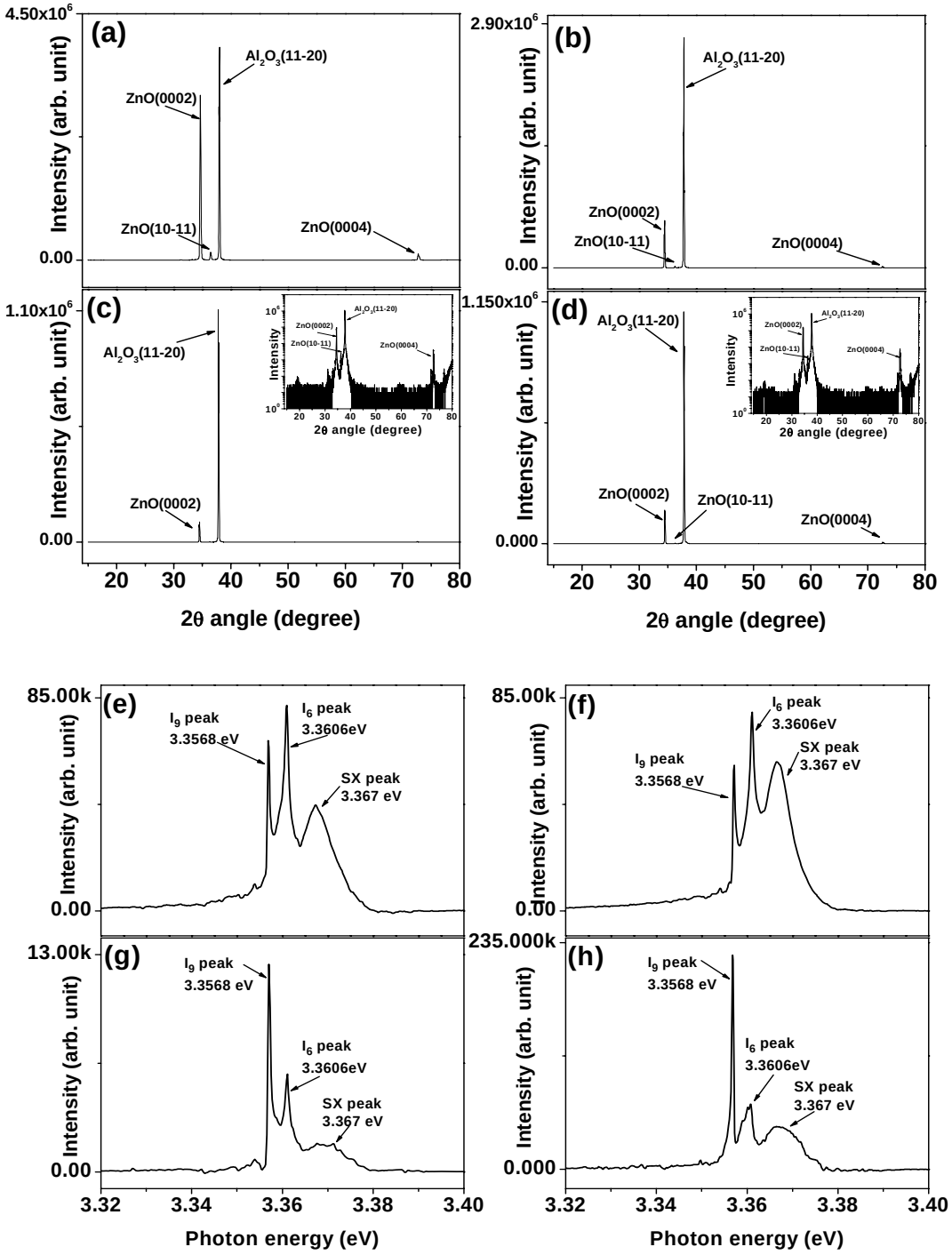

Fig 6.5: *2θ-ω* XRD scans and PL spectra of ZnO nanostructure samples on *a*-sapphire; (a)-(b) are *2θ-ω* scans of samples grown at 900°C and (e)-(f) are PL spectra of the same two samples, (c)-(d) are *2θ-ω* scans of samples grown at 950°C and (g)-(h) are PL spectra of the same two samples.

The XRD 2θ-ω scan of a selection of ZnO nanorod/nanowall samples on *a*-sapphire all show the (10-11) reflection of ZnO in addition ZnO (0002), ZnO (0004) and sapphire (11-20) peaks. As mentioned before in chapter 3 the (10-11) peak of ZnO may be related to wall-like structures and some crystallite misalignment. In this section we discuss the possible relationship between the presence of the (10-11) peak in XRD 2θ-ω scans and the presence of the SX peak in PL spectra of ZnO nanostructures.

In *Fig 6.5 (a)* and *(b)*, we see the 2θ-ω scans of ZnO nanorod/nanowall samples grown at 900^{o}C, and in *Fig 6.5 (c)* and *(d)* the 2θ-ω scan of ZnO nanorod samples grown at 950^{o}C. All samples show the Al_2O_3 (11-20) peak from the *a*-sapphire substrate, the ZnO (0002) peak from the aligned nanostructures and the ZnO (0004) peak (second order of (0002) peak) is also visible for all samples except *Fig 6.5 (c)*. In *Fig 6.5 (a)* and *(b)* the (10-11) peak is visible on a linear scale, while in *Fig 6.5 (d)* it is very weak and barely visible on linear scale, while in *Fig 6.5 (c)* the (10-11) peak is only visible on a log scale, as shown in the inset of this figure. The PL spectra of the samples shown in *Fig 6.5 (a)* and *(b)* show a high intensity SX peak as shown in *Fig 6.5 (e) and (f)*, and PL spectra of samples shown in *Fig 6.5 (c)* and *(d)* show small SX peak as shown in *Fig 6.5 (g) and (h)*. We have studied a range of samples where the intensity of the SX peak is small, and we have found in all cases a correlation between a weak or invisible SX peak and the (10-11) XRD peak also being weak and only visible on a log scale. For samples with intense SX peaks the (10-11) XRD peak is clearly visible on linear scales intensity.

In the ZnO nanostructure samples grown either by active carbon or carbon black instead of graphite as a source powder, the 2θ-ω XRD scan of all samples show higher intensities of this (10-11) XRD peak (e.g. the 2θ-ω XRD scan shown in *Fig 4.8 (a)-(c)*) compared to the samples shown in *Fig 6.5* grown with graphite). But surprisingly PL investigations of many of these active carbon and carbon black grown samples with strong (10-11) XRD peaks do not show strong SX peak emissions, but rather show only weak or no SX peaks (data not shown).

The data in this section lead us to conclude that the presence of the (10-11) peak in XRD data from any one class of ZnO nanostructured samples may correlate with the SX peak emission strength, but that the SX emission must also be determined by other factors which may change in a different class of samples (e.g. grown with other carbon sources apart from graphite) and where the SX peak intensity and its degree of correlation to the (10-11) XRD peak intensity differs substantially.

6.3.3 Plasma treatment experiments

Plasma treatments have been performed on ZnO nanostructure samples grown on *a*-sapphire. All samples used for these experiments have been grown on *a*-sapphire at 900^{o}C.

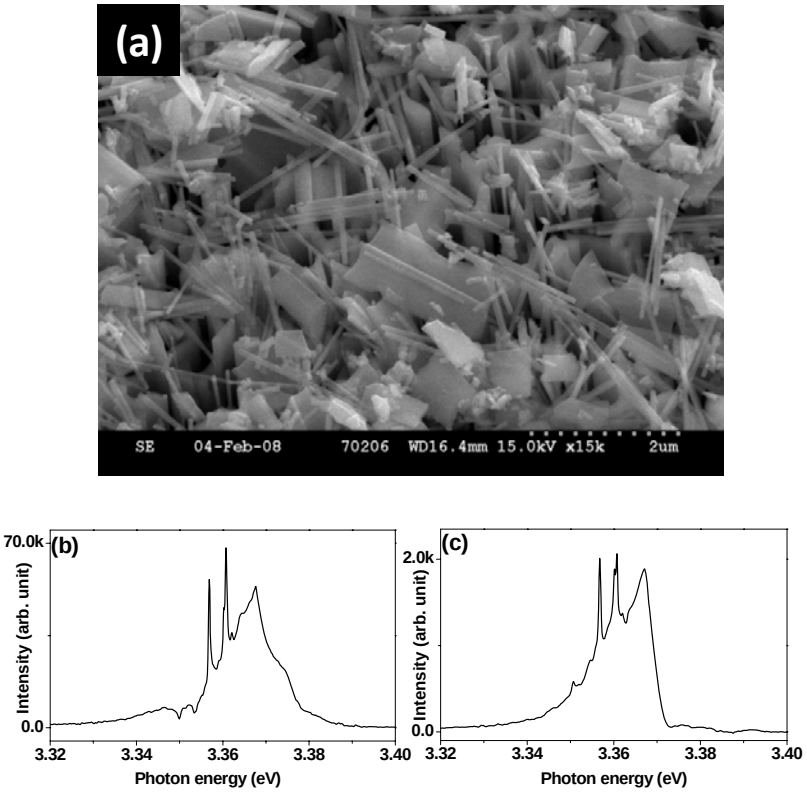

Fig 6.6: O plasma treated sample with RF power of 125W for 30 minutes, (a) FESEM image after plasma treatment, (b) and (c) are PL spectra before and after plasma treatment, respectively.

Initially plasma treatments were performed using an O plasma, as previously it was proved as a successful procedure to desorb O from the surface of ZnO thin films and to prevent further chemisorbtions of O [33]. In this case a high RF power of 125 W has been applied during plasma treatment.

From the FESEM image in *Fig 6.6 (a)* we can see the nanorods have been physically damaged during the plasma treatment. Almost all nanorods and some nanowalls have been displaced from the substrate. However PL spectra in *Fig 6.6 (b) and (c)* show no significant change in the SX peak compared to the other I line peaks. In fact it has increased little.

Following these initial plasma experiments we considered the fact that the SX peak is possibly due to O at the surface of the nanostructures and hence O plasma treatment might not be effective in reducing the SX peak. Consequently an Ar plasma treatment has been undertaken as the next step. To eliminate or reduce the nanorod damage the RF power has been reduced to 5W from 125W and the treatment time has been reduced to 5 minutes from 30 minutes. From the FESEM images of two samples in *Fig 6.7 (a)* and *(b)* we can observe that, in this experiment the damage to the nanorods is much less than that seen the previous time, but nevertheless some nanorods are still physically displaced. The PL spectra after plasma treatment for both samples in *Fig 6.7 (d)* and *(f)* show no significant decrease in the SX peak intensity compared to the as grown sample spectra in *Fig 6.7 (c)* and *(e)*, respectively. The I_9 peak decreases compared to other peaks and we also can see a slight downshift of the SX peak in energy (downshift of ~3.2 meV in *Fig 6.7 (d)* for first sample and ~1 meV in *Fig 6.7 (f)* for second sample). We note that the change in I_9 (In-related) peak intensity may be related to the surface aggregation nature of In in ZnO nanostructures proposed by Fan *et al.* [34] which could be affected by some surface treatments. However, we also note little effect on the I_9 line for O plasma treatments in *Fig 6.6*. From these data we can see the main initial purposes of the plasma treatment experiment has not been achieved and no reduction in the SX peak intensity was seen due to the desorbtion of O.

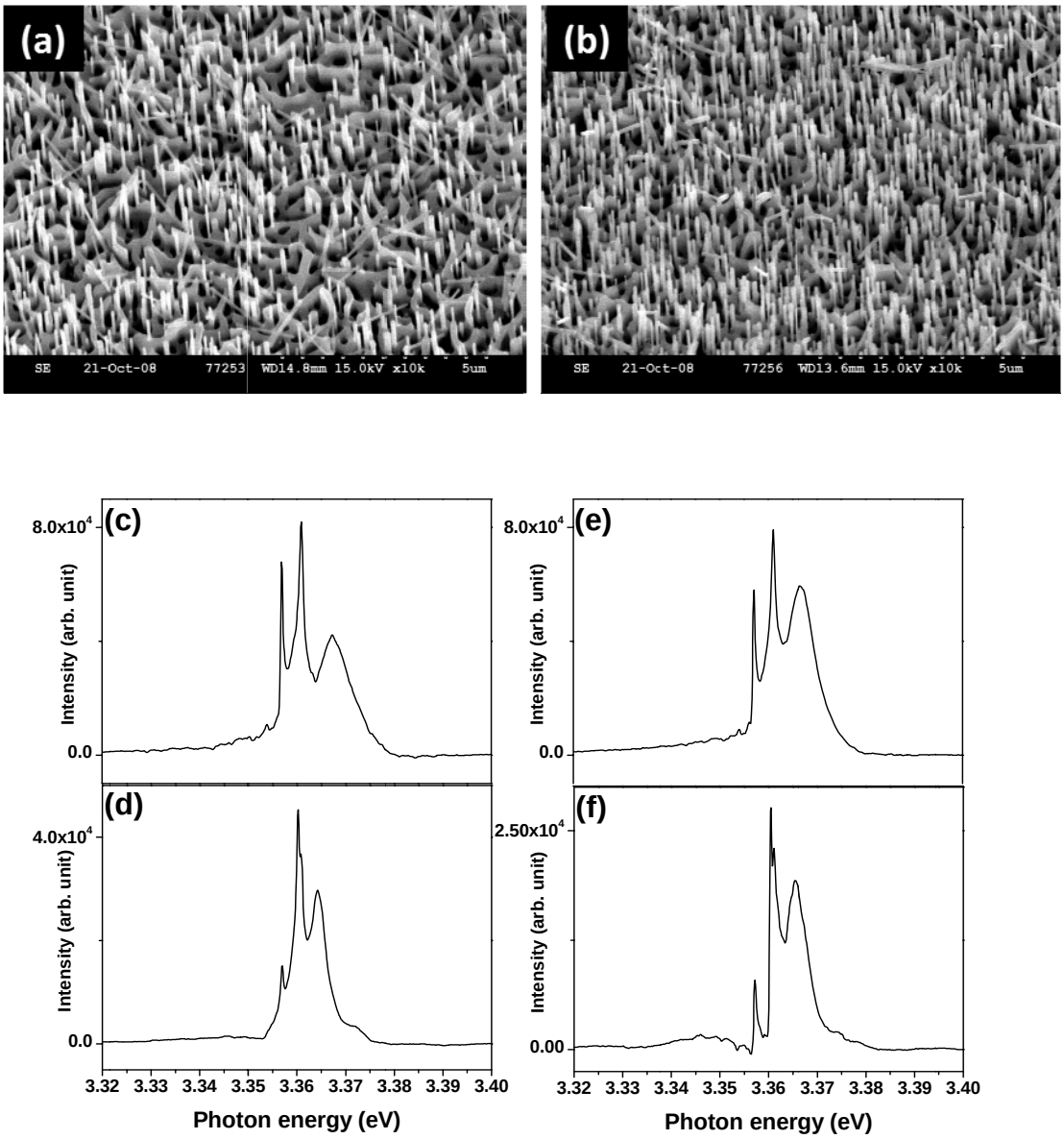

Fig 6.7: Ar plasma treated samples with RF power of 5W for 5 minutes; (a) and (b) FESEM of two samples after plasma treatment. (c) and (d) PL spectra of the sample shown in (a) before and after plasma treatment, respectively. (e) and (f) are the PL spectra of the sample shown in (b) before and after plasma treatment, respectively.

6.3.4 UV illumination experiments

UV illumination has been performed on ZnO nanostructure samples grown on both *a*-sapphire and Si substrates. The power density measurements of the UV lamp are listed below at different callibration wavelength values for the laser power meter used in the lamp spectrum range and at different distances as mentioned in section 6.2.2. The power measurements have been performed in an identical manner to the way the sample was exposed to UV light (i.e. without focussing). The setup of all experiments done in this study is as described in section 6.2.2.

Table 6.1: Power density of UV lamp at different distances from lamp and at different callibration wavelengths of the laser power meter used in the lamp spectrum range

Distance (cm)	**Wavelength (nm)**	**Power (mW/cm^2)**
0	280	16.48
3.5	280	11.56
18	280	2.36
0	365	21.6
3.5	365	15.28
18	365	3.16
0	450	27.4
3.5	450	18.68
18	450	3.9

PL spectra of four sets of experiments are shown below in *Fig 6.8*. Four sets of data of four different samples have been taken using four illumination times of 6 hours, 8 hours, 20 hours and 24 hours (shown from first row to fourth row in *Fig 6.8*, respectively). The vertical columns from left to righ show the PL spectra before

illumination, after illumination and after air exposure, respectively, for the same sample.

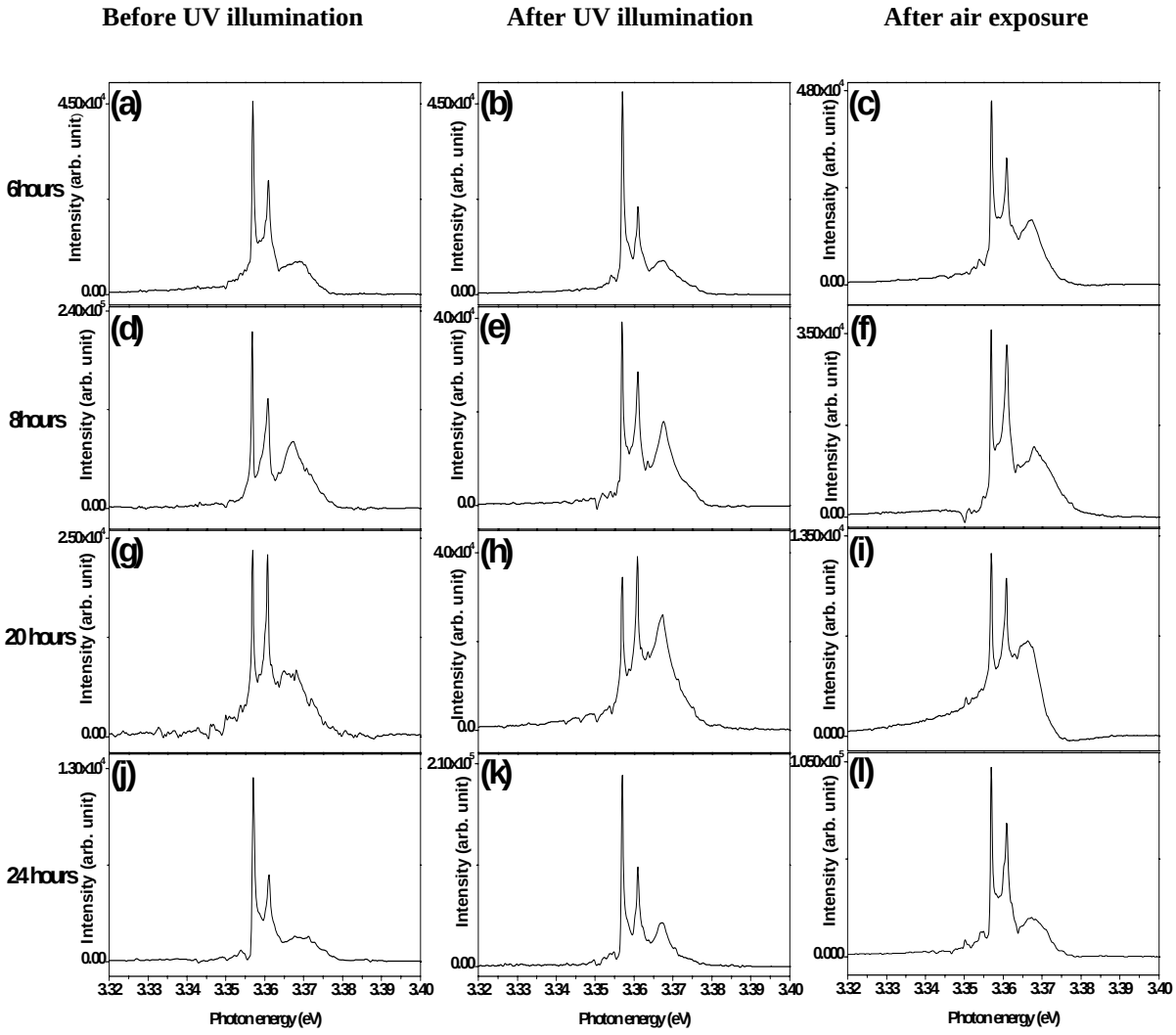

Fig 6.8: PL spectra of ZnO nanostructure samples illuminated with UV light for different time durations. Illumination time; (a)-(c) 6hours, (d)-(f) 8 hours, (g)-(i) 20 hours, (j)-(l) 24 hours. The first column indicates the spectra before illumination, the second column after illumination, and the third column after exposure to air (post UV illumination).

The broad peak ~3.367 eV in all spectra in *Fig 6.8* is the SX peak and the purpose of this study is to compare the relative peak intensity of this peak with respect to other I lines after UV illumination. For the 6 hours illumination period we can see the relative intensity of the SX peak is almost the same (*Fig 6.8 (b)*), while for 8 hours and 20 hours illumination this peak intensity increases (*Fig 6.8 (e)* and *(h)*, respectively) after UV light illumination. For 24 hour illumination the SX peak intensity is almost the same in all spectra, but the linewidth has narrowed slightly after UV illumination (*Fig 6.8 (k)*).

After UV illumination when these samples have been taken out to air, and the PL spectra have been measured again, no drastic changes are observed. After exposure to air the 6 hours illuminated sample shows a slight increase in SX peak intensity (*Fig 6.8 (c)*), for the 8 hours and 20 hours illuminated samples the SX peak intensity decreased slightly (*Fig 6.8 (f)* and *(i)*), respectively), and for the 24 hours sample the SX peak was almost identical (*Fig 6.8 (l)*). From these spectra we conclude that there are no significant or consistent changes in the SX peak after illuminating with UV light in high vacuum, although this is an effective and established method to desorb O from ZnO surfaces.

Further experiments have been done using post-illumination exposure to pure O_2 gas, rather than air where O_2 gas has been introduced to the chamber after UV illumination in the chamber, to investigate the SX peak behaviour. The PL spectra are shown below in *Fig 6.9*.

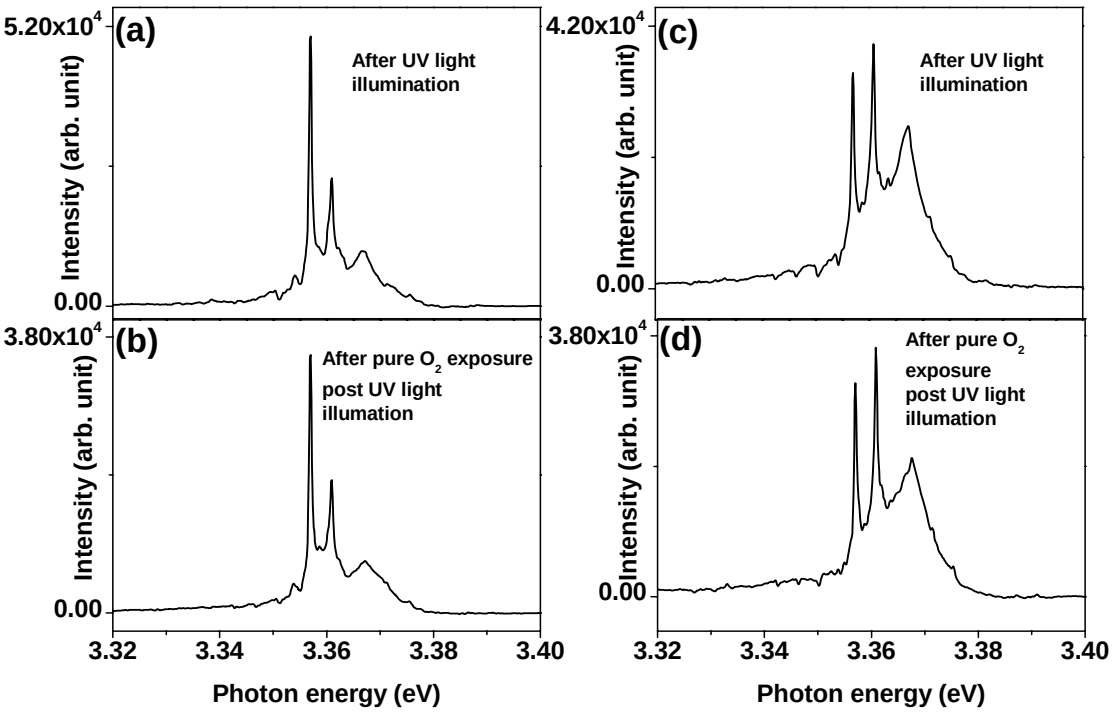

Fig 6.9: PL spectra of pure O_2 exposed ZnO nanostructure samples immediately after UV illumination. (a) and (c) are the spectra taken for two samples after UV illumination, and (b) and (d) are the spectra taken for the same two samples after exposing to pure O_2.

From *Fig 6.9* we can see there is no significant change in the SX peak intensity after pure O_2 exposure in both samples. In both cases the peak is almost identical after pure O_2 exposure. UV illumination in vacuum should desorb the adsorbed O, hence the bare ZnO nanostructure surfaces should adsorb the pure O_2 introduced in the chamber very readily. However, the SX peak behaviour is essentially identified in this experiment to that in the previous experiments where samples have been exposed to air after UV illumination.

6.3.5 Experiment studying electrical voltage application to ZnO nanostructures

Electrical voltage application experiments have been done using the arrangement described in section 6.2.3. The experiments have been done using different voltage amplitudes, using positive (positive terminal of power supply was connected to the nanostructures) and negative (negative terminal of power supply was connected to nanostructures) biases, using *n*- and *p*- type Si substrates and using different gas atmospheres.

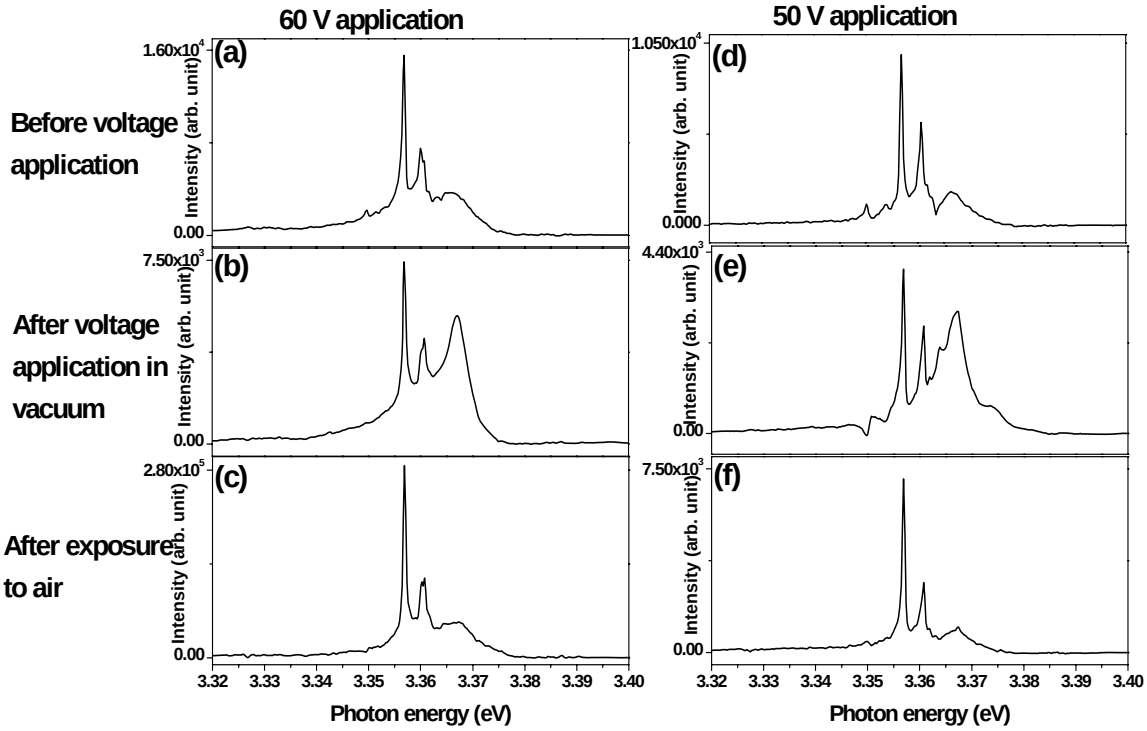

Fig 6.10: PL study of ZnO nanostructure by electrical voltage application of two different amplitudes at high vacuum. At 60V (a) before voltage application, (b) after voltage application, and (c) after exposure to air. At 50V (d) before voltage application (e) after voltage application, and (f) after exposed to air.

Firstly experiments with different voltage amplitudes have been performed, where 30 V-70 V has been applied in 10V intervals. Changes in peak intensity of the SX peak have been observed from 50V upwards. In *Fig 6.10* PL spectra for two samples where voltages of 50V and 60V have been applied are shown. Only for these two

voltages has any changes in the SX peak been seen. Below 50V no change in the SX peak has been observed, and above 60V the sample has been damaged. In our sample structure application above 60 V was not successful due to the breakdown of the insulating SiO_2 layer in between nanostructure and Si. With only 500 nm thickness the SiO_2 layers were unable to withstand voltages more than 60V and allow current to flow. This current flow, which is basically due to loss of dielectric isolation, caused localized heating and damaged the nanostructures. From *Fig 6.10 (b)* and *(e)* it is observed that the SX peak intensity has increased significantly compared to the I peaks after voltage application. The notable point is, the peak intensity dropped down again to its initial condition after exposure to air, as shown in *Fig 6.10 (c)* and *(f)*.

For the experiments with positive and negative voltages, both positive and negative biases of 60V have been applied to the nanostructures. In both cases the change in the SX peak has been the same. *Fig 6.10 (a)-(c)* show the PL spectra for the experiment with positive 60V. For negative biases of 60V also the change in the SX intensity is exactly the same (data not shown), i.e. on increase in vacuum after voltage application and a drop back to initial levels after exposing to air.

For the experiments with *n*- and *p*-type Si, changes in the SX intensity are the same for an applied 60V. The sample used in *Fig 6.10 (a)-(c)* was a *p*-type Si substrate, and the same experiment has been done using an *n*-type Si substrate, where identical changes in the SX peak have been observed (data not shown).

In the experiments using different gas atmospheres voltages have been applied to the sample in air and He gas atmospheres, and compared with the experiments done at high vacuum similar to the one shown in *Fig 6.10 (a)-(c)*. As we had previously observed changes in the SX peak for 60V, in these experiments a fixed voltage of positive 60V has been applied in the different gas atmospheres. The PL spectra of these experiments are shown below in *Fig 6.11*. These experiments show interesting and reproducible results, where we observe significant and differing responses of the SX peak intensity to voltage application in different atmospheres. *Fig 6.11 (a) and*

(b) show the spectra before and after voltage application in high vacuum, respectively, similar to the spectra shown in *Fig 6.10 (a) and (b)* where we can see the increase in the intensity of the SX peak after voltage application, as previously noted. *Fig 6.11 (c)* and *(d)* represent the spectra taken before and after voltage application in air, respectively, where the relative intensity of the SX peak has decreased after voltage application. Finally we observe in *Fig 6.11 (f)* for the voltage application in He gas showing that the relative intensity of the SX peak remains identical to that before voltage application shown in *Fig 6.11 (e)*. For the study of voltage applications in air, after the PL spectrum is acquired, shown in *Fig 6.11 (d)*, the sample has been exposed to the air atmosphere without any applied voltage, after which it is observed that the SX peak increases again and returns to the level in *Fig 6.11 (c)* (data not shown).

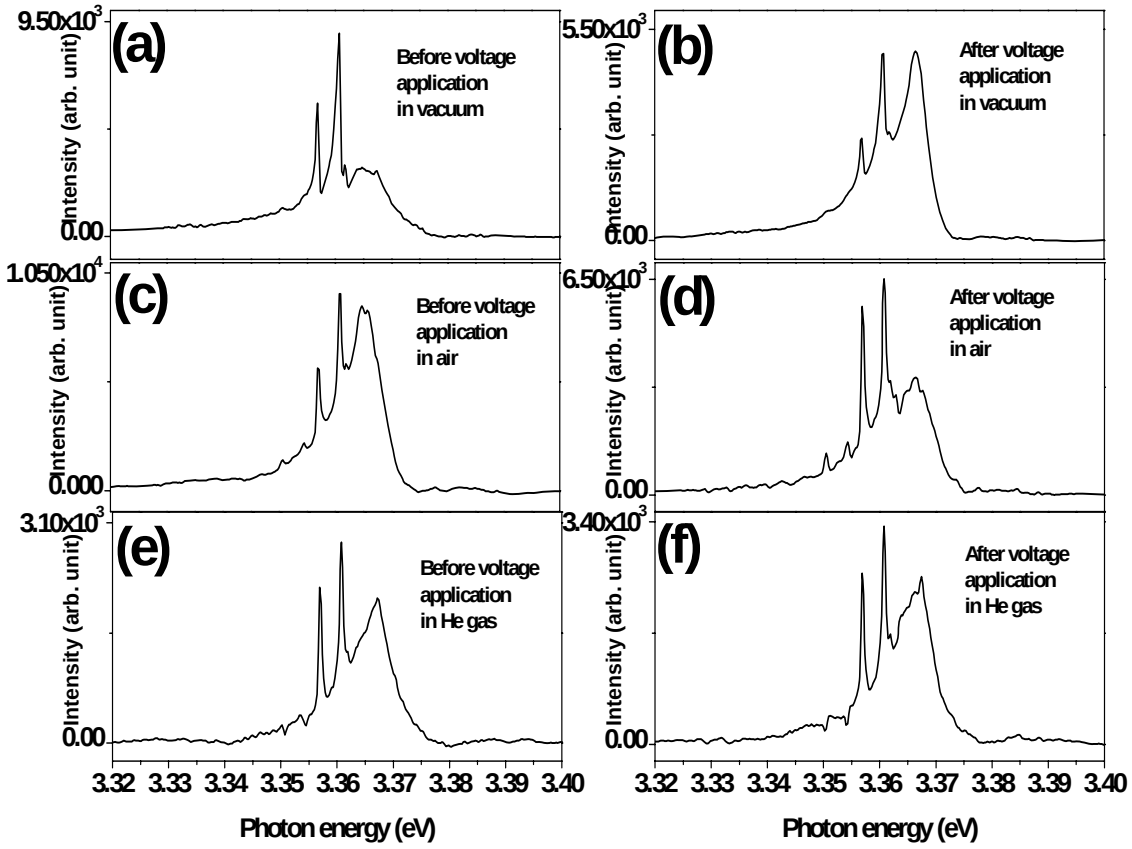

Fig 6.11: PL study by electrical voltage (60V) application in vacuum (a)-(b), air (c)-(d) and He gas (e)-(f). (a), (c) and (e) are PL spectra taken before voltage application, and (b), (d) and (f) are PL spectra taken after voltage application, respectively.

It is clear that the relative intensity of the SX peak changes in differing but reproducible ways as a result of high voltage application at room temperature in various gas atmospheres and the changes can be reversed by re-exposure to air with no applied voltage. These results strongly attest to the surface nature of the defect responsible for the SX emission in PL.

6.4 Discussion

Plasma treatment of ZnO thin films has been reported as a very effective method of suppressing O chemisorbtion on ZnO [33]. In this process the positive ions of the plasma are expected to neutralize the negatively charged O species adsorbed or chemisorbed on the ZnO surface, desorbing them from the surface. In reported experiments on ZnO films, the photocurrent has been improved dramatically after plasma treatment, indicating desorbtion of adsorbed O leading to an increase in photocurrent levels. UV illumination is also a well-known method to desorb adsorbed O species sites as mentioned in section 6.1. In this process the desorbtion effects on ZnO are strongly affected and is dependent on the ambient gas conditions, being optimal in vacuum and inert gases compared to air. In air the re-adsorbtion process happens very quickly again and reduces the free electron concentration in ZnO, which reduces the conductance. In contrast it is found that O plasma treatments significantly alter the electrical property and are largely insensitive to the ambient condition after processing. The temporal photocurrent responses of plasma treated ZnO thin films measured in air and vacuum show almost similar (differences below the detection limit of the instrument) decay time constants in both cases [33].

In our plasma experiments we have transferred the plasma treated sample from the one laboratory to another for PL study, but based on the report in [33] this transferring process at ambient should not lead to significant re-adsorbtion on the ZnO surface because the chemisorbtion sites are effectively suppressed by the plasma and are subsequently insensitive to ambient conditions.

On the basis that, no re-adsorbtion occurred after plasma treatment and since, we have not seen any changes in the SX peak intensities in PL after plasma treatments, even with Ar plasma (*Fig 6.3* and *6.4*) we believe that we can exclude the possibility that the SX peak is due to adsorbed O species on the surface of ZnO.

To provide further support for this conclusion a UV illumination study has been done on similar types of samples. The desorbtion of O is dependent on ambient conditions, and in air the adsorbtion happens again quickly so we have performed UV illumination in the PL chamber, so that PL spectra can be taken without exposing the samples to air.

Most of the reports on UV illumination of ZnO are based on photocurrent measurements in vacuum, air etc. [20, 23, 27, 29, 31], which show direct evidence of desorbtion of surface O. In our study a vacuum pressure in the cryostat in the 10^{-6} mbar range has been used, which is similar or better than the vacuum level used in most of the reports of UV illumination studies of ZnO [18, 20, 23, 35]. The power or power density levels of UV light used in this study (power 250W, power density >10 mW/cm^2, as shown in *Table 6.1*) is also similar to or higher than most of the previous reports [23, 25, 29, 31, 36]. Hence the experimental setup used in this study should be more than sufficient to desorb O from the surface of ZnO nanostructures, which should affect the SX peak intensity if the proposal that adsorbed O is the cause of the SX peak is true. In fact we find that there are no consistent changes in the SX peak intensity in different samples with different illumination times as shown in *Fig 6.5*. None of the experiments show significant decreases in the SX peak intensity. Even samples exposed to pure O_2 after illumination did not show any changes in the SX peak (*Fig 6.6*).

Thus we believe that the assignment of adsorbed O species as the microscopic origin of the SX peak in PL is almost certainly not correct and certainly cannot be the whole story where the peak's origin is concerned.

Thus the involvement of other species at the ZnO surface must also be considered. Therefore an XPS study of ZnO nanostructure samples showing intense SX peaks in PL has been undertaken. The XPS spectra have been taken before UV illumination and after UV illumination in ultra-high vacuum (~10^{-9} mbar) within the XPS chamber to investigate any surface compositional changes.

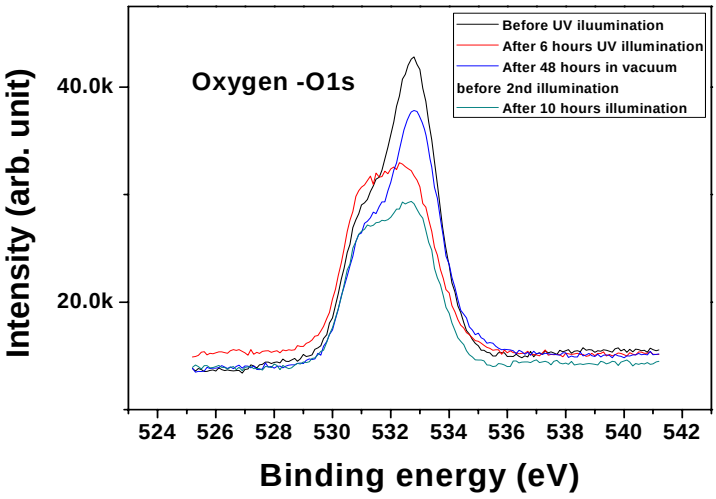

Fig 6.12: XPS Spectra showing the change in peak shape due to UV illumination in the O1s region of the spectrum.

The sample was kept inside the XPS chamber during illumination and the power density at the sample (18 cm from source) was ~2.5 mW/cm^2, as shown in *Table 6.1*. The calibration of the binding energy scale was performed with the C1s line (285 eV) from the adventitious carbon contamination layer [37]. The O1s spectra before and after illumination show significant changes as shown in *Fig 6.12*, whereas the Zn2p$_{3/2}$ spectra do not show much difference (data not shown). It has always been observed in XPS studies of various ZnO samples that the O peak is more sensitive to compositional changes compared to the Zn peak. So any desorbtion effects are expected to be more readily visible in the O region of the spectrum.

In the XPS data shown in *Fig 6.12* we can see significant changes in the peak shape in the O1s region spectrum due to UV illumination. The overall (peak amplitude) relative intensity of the O1s peak has increased before the second illumination after being left in the vacuum for 48 hours, which can be explained by re-adsorbtion of

some H_2O or OH species (which is expected even in ultra high vacuum). The sample was in the same place while taking the spectra after the first illumination and after leaving the sample in vacuum for extended periods (shown in red and blue in *Fig 6.12*), so all intensities can be compared directly.

The detailed peak fitting of the O1s spectra are shown in *Fig 6.13*. For the case of O bonded to Zn, we found it very difficult to obtain unambiguous fits for the various possible states (like O bonded to Zn stoichiometrically and non- stoichiometrically) due to the variety of reports of many peaks of similar energies in this energy range. For example, according to the NIST database there are 10 reported peak values for O bonded to Zn in the range of 529.90eV-530.90eV [38]. So it is very difficult to compare the exact percentage change of the surface-adsorbed O from peak fitting. XPS therefore only gives a approximate idea about the possible reactions occurring based on the peak shape change. The peak position which is usually chosen from standard databases is O bonded to Zn in pure ZnO at ~531 eV [39]. This peak shows some changes in intensity in our samples but these may be due to surface cleaning effects of UV illumination which increase the signal from the underlying ZnO. This peak does not provide any significant information about adsorbed O in our samples.

Among the other fitted peaks, the peak at ~532.4 eV can be attributed to O bonded as OH [40, 41], and it has increased slightly after both UV illumination. The increment in OH peak in XPS due to UV illumination is already reported by other groups [42-44], and explained as follows: after the desorbtion of O from the surface of ZnO, the bare surface becomes very reactive and reacts quickly with the available water vapour in vacuum (water vapour is the most common contaminant in any high vacuum or ultra high vacuum system), and forms OH groups on the surface, and this reaction increases the total number of OH groups on the surface. From these XPS studies it is clear that OH groups on the surface are not removed (and even slightly increased in numbers) by UV illumination, and this increase gives indirect evidence of the desorbtion of surface O from ZnO. The SiO_2 signal in the O spectrum is from the native oxide layer of the substrate, which has decreased after each illumination, due to the desorbtion or releasing of O from the SiO_2 layer [45].

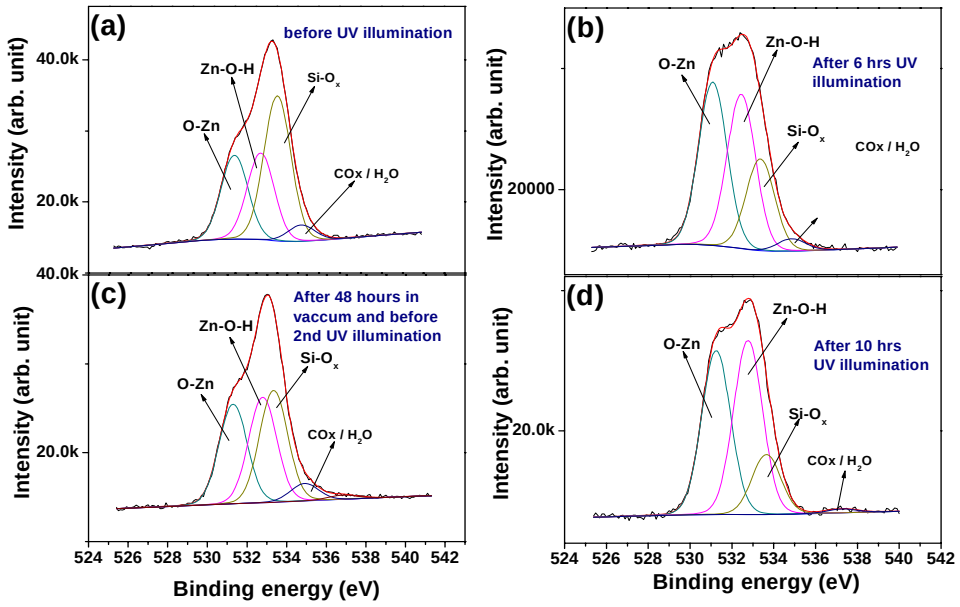

Fig 6.13: Peak fitted O1s spectra at different stages of the illumination experiment. (a) before illumination, (b) after 6 hours illumination, (c) after leaving sample in vacuum for 48 hours before second illumination and (d) after 10 hours illumination.

Table 6.2: Atomic percentages of the O bonded compound calculated from the peak fitting of O1s spectra at different stage of the experiment

Element/ Compound	Before 1st UV illumination (%)	After 6 hours UV illumination (%)	After 48 hours in vacuum andBefore 2nd UV illumination (%)	After 10 hours UV illumination (%)
O-Zn	12.37	16.58	13.74	16.37
O-H	12.79	15.65	14.51	17.39
O-Si	21.44	9.31	15.43	5.99
CO_x/H_2O	2.42	1.26	2.39	0

Our conclusions from the plasma treatment and UV illumination at high vacuum studies indicate that the SX peak at ~3.367 eV is not due to adsorbed O on the surface of ZnO nanostructures, and the XPS study gives some indication of a possible relationship with the much more stable OH surface species.

The electrical voltage experiments also show very interesting results. Significant changes in the SX peak in different gas atmospheres have been observed. One can remove and recover the SX PL peak via voltage application, removal and re-exposure to air with different but reproducible behaviour in various gas atmospheres. These experiments have been done at room temperature or below, and the temperature has been monitored during voltage application so annealing or diffusion effects of defects can be ignored. Furthermore, after discharging the electrical probes in the gas atmosphere, the SX peak has not shown any changes, i.e. when voltage is applied in vacuum the SX peak relative intensity increased, but after discharging and while still in vacuum the SX peak relative intensity has remained at its increased level. So the possibilities of any charge state or depletion layer effects are also unlikely. Voltage applications in air and vacuum lead to the SX peak reacting exactly opposite ways and we feel this clearly shows some relationship with some adsorbed surface species, but not O given that the possibility of O as the microscopic origin of the SX peak has been excluded by the other experiments reported in this chapter.

Finally, a selection of TEM images of nanorod/nanowall structures which show varying degrees of SX emission are presented to study the structure of these morphologies.

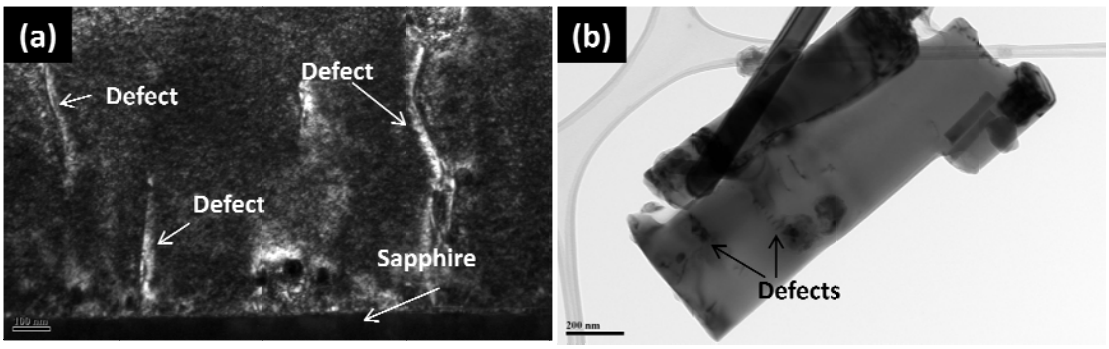

Fig 6.14: TEM images of ZnO nanorod/nanowall samples grown at 900^{o}C. Image (a) shows some defects in-situ in cross-section at the wall structure at the base of nanorods and near the substrate, image (b) shows defects in one mechanically removed wall structure.

TEM studies have been undertaken on both nanorod/nanowall and nanorod morphology samples. In *Fig 6.14* only TEM images of nanorod/nanowall samples grown at 900^{o}C are shown, as these clearly show the wall structures with structural defects. Most of the nanorods in both samples are found to be free of structural defects, as shown in *Fig 3.5*. This TEM data is important, as it shows the nature and extent of defects in the wall structures. From the study of the relationship between nanostructure morphology and SX peak relative intensity in section 6.3.1 it has been noted that the highest relative intensity SX peak is found only in nanorod/nanowall samples grown at 900^{o}C and the presence of the SX peak is dependent on the presence of wall structures in both 900^{o}C and 950^{o}C grown samples. Thus, the presence of the SX peak in nanostructures with dominant wall morphology gives a strong indication of some possible relationship with the structural defects seen in the wall structures in TEM. The nature and amount of such defects will certainly be dependent on the growth environment and the growth technique. These defects sites may act as preferential sites for strong chemisorbtion of certain surface species by the wall structure (e.g. such as OH species), and thus facilitate the creation of the defect responsible for the SX peak. In addition, the defects may help increase the relative SX peak strength via the mechanism discussed below.

In normal as-grown, *n*-type, ZnO nanostructures surface states at such defects located within the bandgap can be occupied by electrons, which lead to band bending effect [46]. This band bending results in a lower number of excitons reaching the surface and thus reducing the SX relative intensity. In ref [9] and [5] it has been shown by Richters *et al.* that a dielectric medium (in those reports polymer and Al_2O_3 coatings) reduce this band bending allowing a higher density of excitons at the surface and thus an increase in the SX peak. In those reports the ZnO nanowire and the coating thereon act as a core-shell structure. In our case we can envisage that the ZnO material on either side of the structural defects shown in *Fig 6.14* acts as the dielectric medium to screen the ZnO on the other side of the defect and thus the screening effects allow a larger density of excitons to reach the structural defect surfaces, and thus lead to an increased SX emission.

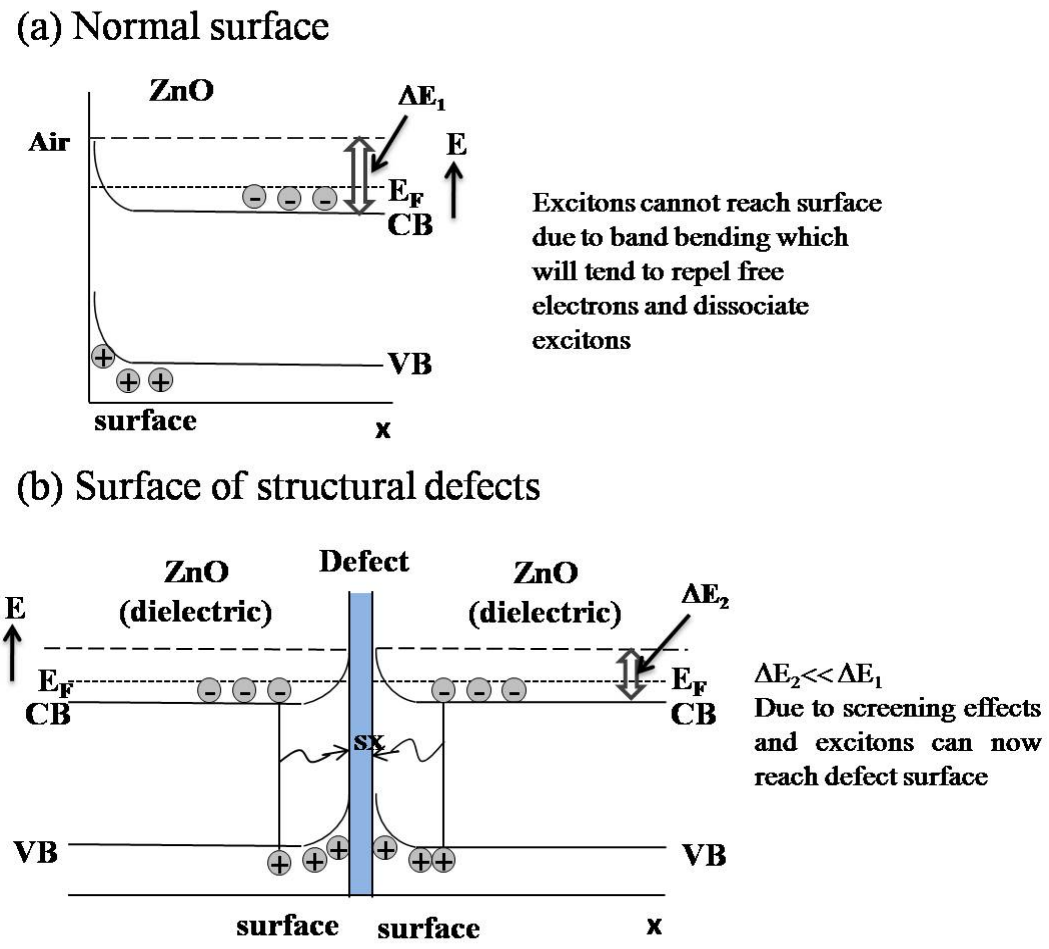

Fig 6.15: Model of band structure of ZnO nanostructure with extended defect with surrounding ZnO which acts as a dielectric medium using an extension of the model shown in ref [9]. Figure (a) showing the band structure for normal surface of ZnO nanostructures and (b) showing ZnO nanostructure surface with structural defects where both sides of the defect act as surfaces for the excitons (with reduced band bending compared to normal surface due to screening).

The extended structural defects, such as grain boundaries and dislocations act as preferential sites for chemisorbtion of e.g. OH species which may lead to SX emission. Normally a surface depletion layer reduces the SX concentration and the amount of excitons captured by these adsorbed species and thus reduce the SX emission intensity. However in our case due to the screening effect of the ZnO dielectric medium in the region of the structural defects there will be an increase in the number of excitons close to the surface, as shown in *Fig 6.15*.

So the overall relative intensity of the SX peak in our model is dependent on the number of defects associated with the nanostructure surface (including internal surface), the surface environment (internal screened or external unscreened) and also on the concentration of adsorbed species. The relationship of morphology to the SX peak intensity is explained by this model. Normally structural defects are mostly seen in nanowall structures, as shown by TEM. With fewer and smaller walls in 950^{o}C grown samples we have never seen high intensity SX emission, which can be explained by a smaller number or the absence of structural defects.

The voltage application studies indicate the emission intensity from these defects change with electrical voltage in different gas atmospheres. The increase of the SX peak intensity in vacuum upon voltage application may be related to the increase of the OH species in vacuum, observed in XPS studies. The relationship of the SX peak with OH-related surface defects is also supported by the fact that with increasing temperature the PL quenches strongly in samples which show a large SX peak [7], due to increased NR recombination with increasing temperature due to these defects. This is supported by a report that OH groups present on the surface of ZnO quantum dots are responsible for the quenching of bandedge excitonic emission [47]. So the quenching of PL of ZnO nanostructures which show strong SX emission at higher temperatures can be related to the presence of OH groups, which may thus be the microscopic origin of this SX peak. The broad width of the SX peak can be explained in terms of slightly differing local defect environments for the OH adsorbate, due to which the defect energy position is shifted slightly and makes the peak broader.

So we suggest that the SX peak may be due to an exciton bound to a strongly chemisorbed surface species, at extended defects in ZnO nanostructures. The presence and relative intensity of the SX peak will be dependent on the concentration of structural defects and the concentration of adsorbed species present in the nanostructures. The exact adsorbed species responsible for this peak is not fully confirmed, but from this work it is confirmed that adsorbed O species are not responsible for it. From the XPS study, based on the behaviour of the OH adsorbed

species; we suggest that adsorbed OH may be the species responsible for the SX emission. OH has been found to be a very stable chemisorbed species, which is very difficult to remove by any surface treatment consistent with the results of UV illumination and plasma treatments. Further detailed surface treatment studies are needed to confirm the microscopic origin of the SX peak however. The SX peak intensity in our samples is also strongly affected by the environment at the structural defects, where screening effects will allow a larger exciton concentration to reach the defect surface and thus lead to a larger SX emission intensity.

6.5 Conclusion

The microscopic origin of the SX peak has been studied by various surface treatment methods. Previously it was assumed that the adsorbed O species are responsible for this peak. We have undertaken plasma treatments and UV illumination at high vacuum, which are established surface treatment methods to desorb surface O. From these studies we conclude that O is not the species responsible for the SX peak in ZnO PL. Electrical voltage application in high vacuum, air and He gas show significant changes in the peak intensity in the different gas atmospheres, which suggests a relationship with adsorbed surface species. XPS data show it is very difficult to remove adsorbed OH species and this species increases in vacuum due to re-adsorption and reaction. TEM data show the amount and nature of structural defects in the nanowall structures. Our final conclusion from this whole range of studies is that the SX peak is due to an exciton bound to a strongly chemisorbed surface species, probably at extended defects in ZnO nanostructures. The chemisorbed surface species is tentatively suggested to be OH-related.

This model of the origin of the SX peak can explain the entire range of prior experimental data in the literature and also in our results, including the large peak width and effect such as higher temperature PL quenching.

6.6 References

[1] B. K. Meyer, H. Alves, D. M. Hofmann, W. Kriegseis, D. Forster, F. Bertram, J. Christen, A. Hoffmann, M. Straßburg, M. Dworzak, U. Haboeck, and A. V. Rodina, Physica Status Solidi (b) 241 (2004) 231.

[2] L. Wischmeier, T. Voss, I. Ruckmann, J. Gutowski, A. C. Mofor, A. Bakin, and A. Waag, Physical Review B 74 (2006) 195333.

[3] C. R. D Stichtenoth, T Niermann, L Wischmeier, T Voss, Chung-Jen Chien, Pai-Chun Chang and Jia Grace Lu Nanotechnology 18 (2007) 435701.

[4] O. Brandt, C. Pfüller, C. Chèze, L. Geelhaar, and H. Riechert, Physical Review B 81 (2010) 045302.

[5] J.-P. Richters, T. Voss, L. Wischmeier, I. Ruckmann, and J. Gutowski, Applied Physics Letters 92 (2008) 011103.

[6] Y. Yang, B. K. Tay, X. W. Sun, J. Y. Sze, Z. J. Han, J. X. Wang, X. H. Zhang, Y. B. Li, and S. Zhang, Applied Physics Letters 91 (2007) 071921.

[7] J. Grabowska, A. Meaney, K. K. Nanda, J. P. Mosnier, M. O. Henry, J. R. Duclere, and E. McGlynn, Physical Review B 71 (2005) 115439.

[8] V. V. Travnikov, A. Freiberg, and S. F. Savikhin, Journal of Luminescence 47 (1990) 107.

[9] J. P. Richters, T. Voss, D. S. Kim, R. Scholz, and M. Zacharias, Nanotechnology 19 (2008) 305202.

[10] T. Voss and L. Wischmeier, Journal of Nanoscience and Nanotechnology 8 (2008) 228.

[11] R. Tenne, V. M. Nabutovsky, E. Lifshitz, and A. F. Francis, Solid State Communications 82 (1992) 651.

[12] V. V. Travnikov, Journal of Crystal Growth 101 (1990) 579.

[13] V. V. Travnikov, Izvestiya Akademii Nauk Sssr Seriya Fizicheskaya 52 (1988) 758.

[14] G. J. Lapeyre and J. Anderson, Physical Review Letters 35 (1975) 117.

[15] L. Wischmeier, T. Voss, I. Ruckmann, and J. Gutowski, Nanotechnology 19 (2008) 135705.

[16] Y. Z. Zhang, H. P. He, Y. Z. Jin, B. H. Zhao, Z. Z. Ye, and H. P. Tang, Journal of Applied Physics 104 (2008) 103529.

[17] C. Klingshirn, physica status solidi (b) 71 (1975) 547.

[18] J. Lagowski, J. E. S. Sproles, and H. C. Gatos, Journal of Applied Physics 48 (1977) 3566.

[19] D. Wang, H. W. Seo, C.-C. Tin, M. J. Bozack, J. R. Williams, M. Park, N. Sathitsuksanoh, A.-j. Cheng, and Y. H. Tzeng, Journal of Applied Physics 99 (2006) 113509.

[20] D. H. Zhang, Journal of Physics D: Appl. Physica 28 (1995) 1273.

[21] R. J. Collins and D. G. Thomas, Physical Review 112 (1958) 388.

[22] J. D. Ye, S. L. Gu, S. M. Zhu, F. Qin, S. M. Liu, W. Liu, X. Zhou, L. Q. Hu, R. Zhang, Y. Shi, and Y. D. Zheng, Journal of Applied Physics 96 (2004) 5308.

[23] Q. H. Li, T. Gao, Y. G. Wang, and T. H. Wang, Applied Physics Letters 86 (2005) 123117.

[24] F. Steinbach and R. Harborth, Faraday Discussions of the Chemical Society 58 (1974) 143.

[25] J. Cunningham, E. Finn, and N. Samman, Faraday Discussions of the Chemical Society 58 (1974) 160.

[26] C. Jin, A. Tiwari, and R. J. Narayan, Journal of Applied Physics 98 (2005) 083707.

[27] W. H. Hirschwald, Account of Chemical Research 18 (1985) 228.

[28] D. R. I. Bickley, P. G. Heiland, D. W. Hirschwald, D. E. Thull, P. F. Steinbach, M. R. Harborth, D. W. Bauer, P. A. Hausmann, D. A. J. Tench, P. J. Cunningham, P. M. W. Roberts, D. T. B. Grimley, P. D. Menzel, and P. H. P. Boehm, Faraday Discussions of the Chemical Society 58 (1974) 175.

[29] K. Keem, H. Kim, G.-T. Kim, J. S. Lee, B. Min, K. Cho, M.-Y. Sung, and S. Kim, Applied Physics Letters 84 (2004) 4376.

[30] D. C. R. Brundle, D. S. Evans, P. M. W. Roberts, D. D. Briggs, D. J. C. Fuggle, P. D. Menzel, D. F. R. Smith, P. J. M. Thomas, D. D. E. Parry, D. A. M. Bradshaw, D. P. Biloen, D. E. W. Plummer, D. T. B. Grimley, D. D. R.

Lloyd, D. R. W. Joyner, D. J. Küppers, and D. H. Killesreiter, Faraday Discussions of the Chemical Society 58 (1974) 125.

[31] H. Kind, H. Yan, B. Messer, M. Law, and P. Yang, Advanced Materials 14 (2002) 158.

[32] N. Golego, S. A. Studenikin, and M. Cocivera, Physical Review B 61 (2000) 8262.

[33] M. Liu and H. K. Kim, Applied Physics Letters 84 (2004) 173.

[34] H. J. Fan, A. S. Barnard, and M. Zacharias, Applied Physics Letters 90 (2007) 143116.

[35] E. V. a. D. Kohl, Journal of Physics C: Solid State Physics 14 (1981) 2395.

[36] S. A. Studenikin and N. Golego, Journal of Applied Physics 87 (2000) 2413.

[37] J. F. Moulder, W. F. Stickle, P. E.Sobol, and K. D. Bomben, *Handbook of X-Ray Photoelectron Spectroscopy*, 1st ed., ed. J. Chastain, Perkin-Elmer Corporation: Eden Prairie, Mn., 1992.

[38] http://srdata.nist.gov/xps/,

[39] C. D. Wagner and G. E. Muilenberg, *Handbook of x-ray photoelectron spectroscopy*, Physical Electronics Division, Perkin-Elmer Corp., 1979.

[40] D. Elizabeth Pugel, R. D. Vispute, S. S. Hullavarad, T. Venkatesan, and B. Varughese, Applied Surface Science 254 (2008) 2220.

[41] T. L. Barr, The Journal of Physical Chemistry 82 (1978) 1801.

[42] R.-D. Sun, A. Nakajima, A. Fujishima, T. Watanabe, and K. Hashimoto, The Journal of Physical Chemistry B 105 (2001) 1984.

[43] N. Asakuma, T. Fukui, M. Toki, K. Awazu, and H. Imai, Thin Solid Films 445 (2003) 284.

[44] N. Asakuma, H. Hirashima, T. Fukui, M. Toki, K. Awazu, and H. Imai, Japanese Journal of Applied Physics Part 1-Regular Papers Short Notes & Review Papers 41 (2002) 3909.

[45] X. Lin, G. Liao, C. Information, Z. Tang, and T. Shi, Microsystem Technologies 15 (2009) 317.

[46] Y.-J. Lin and C.-L. Tsai, Journal of Applied Physics 100 (2006) 113721.

[47] H. Zhou, H. Alves, D. M. Hofmann, W. Kriegseis, B. K. Meyer, G. Kaczmarczyk, and A. Hoffmann, Applied Physics Letters 80 (2002) 210.

Chapter 7

Post-growth passivation techniques of ZnO nanostructures

In this chapter, methods for post-growth chemical passivation of ZnO nanostructures have been studied, to enhance luminescence emission by suppressing NR recombination. Two chemical agents, polyvinylpyrrolidone (PVP) and hydrofluoric acid (HF) have been used. Variations in PL intensity for passivation with different solution strengths of PVP and HF is shown and the optimum recipe to improve PL signal for both passivating agents is been discussed.

7.1 Introduction

The optical quality of ZnO nanostructures is generally better, compared to bulk ZnO, due to the excellent crystal quality and absence of strain effects, making such structures very attractive for optoelectronic devices. Although these structures are good optical materials, their luminescence intensity often drops significantly with increasing temperature (more than might be expected due to FE dissociation only), becoming significantly attenuated at room temperature [1]. To utilise ZnO for optical devices efficient room temperature luminescence is very important, as such devices must operate at room temperature. The main purpose of this aspect of my work is to

establish methods which will increase the luminescence intensity of ZnO nanostructures, particularly the room temperature luminescence intensity.

As discussed in detail in chapter 2, NR recombination can compete with photon emission, which is detrimental for optical device applications. Defects in semiconductors e.g. native defects, foreign atoms, broken or dangling bonds at surfaces etc. create single or multiple energy levels within the forbidden bandgap of the semiconductor, which can function as efficient NR centres, quenching UV luminescence emission. For nanostructures, the broken and dangling surface bonds, and surface impurities and defects can be especially damaging due to the high surface-to-volume ratio of nanostructures. If these defects can be chemically capped by some other material or compound, the effect of the NR recombination centres may be reduced. Passivation mechanisms work by introducing a suitable chemical element or compound onto the surface of a semiconductor. These compounds bond to the surface, in particular, they react and terminate the broken or dangling bonds (these broken bonds create the mid bandgap levels at the surface, which act as deep NR recombination centres) at the surface in such a way as to render the surface chemically stable.

Passivation techniques for different types of ZnO materials such as thin films [2], quantum dots [3, 4], nanoparticles [5-8], sub-micron particles [9], nanowire FETs [10] and nanowire transistors [11] have already been reported. In all previous reports above either pre-growth or during growth passivation methods were used, which enhanced the UV emission for these structures. The majority of reported works have concentrated on nanoparticles as they are mostly grown by solution based methods where it is easier to introduce a passivation agent during the growth process. In addition nanoparticles can be transferred easily to a passivation solution, where the nanoparticles can be capped with the corresponding agent. Very few reports on surface passivation of ZnO nanorods have been published until now [12, 13]. In these recent reports, solution based methods [12] or a hydrothermal method [13] of growth was used, where the passivation agent was introduced during growth process. To date, to our knowledge, almost no reports have been published on post-growth surface passivation of any ZnO nanostructured sample. The presence of passivating

agents during growth would naturally, affect both the passivation efficiency and the nanostructure morphology and dimensions simultaneously. Hence the nanostructure morphology and degree of passivation are interdependent, which is undesirable. For efficient use of ZnO nanostructures in devices, it is very important to grow the required morphology (nanorods, nanowalls, quantum dots etc.) and then treat the surface suitably so as to eliminate or reduce the NR recombination effects. In the case of vapour deposition methods, it is very difficult or almost impossible to introduce any passivating agent due to the very high operating temperature of the deposition system, as most of the passivating agents are organic chemicals with low melting and boiling points and are therefore generally only used in solution. For vapour phase deposited samples, the passivation agent is easier to introduce after growth.

Different elements and organic compounds such as PVP [3, 4, 6, 11, 14, 15], fluorine (F) containing compound [2, 16], SiO_2 [10] and methacryloxypropyl-trimethoxysilane (MPS) [7] are used as passivation agents in the above mentioned reports. Among these passivation agents, PVP has been most widely used, probably due to the ease of synthesis from a commercial point of view, the availability of a range of molecular weights, solubility in water, alcohols and many organic acids and ketones, biocompatibility and non-toxicity. As PVP is soluble in many liquids it can be easily introduced in solution based ZnO nanostructure growth methods. PVP is also used to control the growth kinetics e.g. particle size control of nanostructures [12]. The chemical characteristics of PVP are discussed in more detail in the next section. F^- is another passivating elements used by some research groups, where enhancements in the UV emission intensity of ZnO treated by F-containing compounds has been observed [2, 16]. In these cases F was also introduced during growth using the F- based Zn compound ZnF_2. Alternatively F^- was introduced as a dopant in ZnO thin films during growth using HF [17].

For the VPT grown samples in our laboratory, PVP and HF have been selected for post-growth passivation agents as both are water soluble. PVP has already been established as a passivation agent for ZnO nanostructures as mentioned above, while HF can be expected to be a good method for introducing F^-, which is an effective

passivation agent. The aqueous solutions of HF containing F^- ions are reactive with ZnO and F is a good passivation agent like other halogens especially for preventing species adsorption on the surface.

Some improvements in luminescence intensity for some ZnO samples have been achieved in this work using both compounds for post-growth passivation. In the next section, before describing the experimental results, the PVP and HF compounds are introduced briefly.

7.2 Passivation agents

7.2.1 PVP

PVP is a polymeric N-vinyl lactam (lactam is cyclic amide), known chemically as poly-1-vinyl-2-pyrollidone $(C_6H_9NO)_n$ [18].

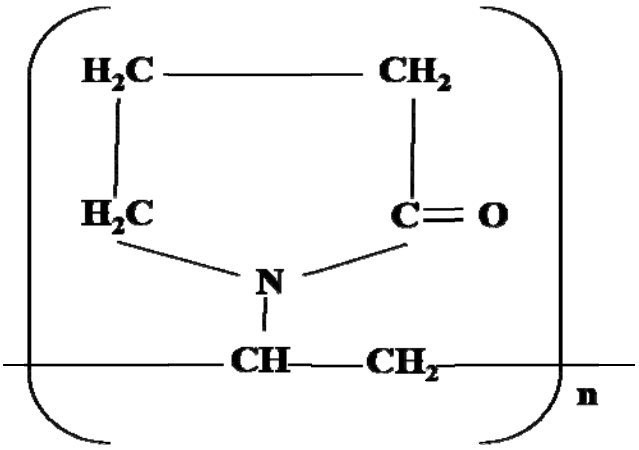

Fig 7.1: Chemical structure of PVP; n is the number of repeating units of the base monomer structure in the polymer chain [18].

It is produced commercially by a purely synthetic route involving acetylene, formaldehyde, ammonia and hydrogen [19]. PVP is a comparatively recent arrival in the field of industrial water soluble polymers. It was developed by W. Reppe in Germany in late 1930's.

PVP is a very versatile organic compound and offers various functional properties for a range of scientific and industrial applications such as pharmaceuticals, cosmetics, textiles, adhesives, coatings, material science and ceramics. Usually it is an odourless, tasteless white powder or transparent solution with excellent solubility. The commercial versatility of PVP has led to an increasing usage of this polymer in a wide variety of fields is primarily due to the following characteristics [18]–

- Wide solubility
- Good hydroscopicity
- Complexing and detoxifying abilities
- Protective colloid action
- Good film-forming properties
- Chemical and surfactant stability
- Non-toxicity
- Biocompatability

Under ordinary conditions PVP is chemically stable as a solid or in solution. PVP is marketed for its various uses at different average molecular weights. The different weight average molecular weights PVP solutions are distinguished by a K-number (usually K-12 for MW of 2000-3000, K17 for MW of 7000-11000, K-30 for MW of 44000-54000, K60 for MW of 160000-400000, K90 for MW of 1000000-1500000 etc. [20]) where increasing K value denotes a higher average molecular weight [21]. The material properties vary according to the average molecular weight.

In ZnO materials research, PVP is mostly used for nanomaterial preparation to control the morphology [4, 10, 12]. For example the length and diameter of ZnO nanorods, prepared by a solution method may be controlled by the amount of PVP added [12]. From *Fig 7.1* we can observe that PVP has polyvinyl skeleton with polar groups. The lone pairs of electrons on the nitrogen and oxygen atoms in the polar groups of one PVP unit may occupy the orbital of a metal ion. The formation of coordinate bonds between PVP and metal ions such as Ag^{+} and Zn^{2+} has already been reported [22, 23]. Zn^{2+} can coordinate with PVP, which results in the decrease of Zn^{2+} concentration available for growth. Thus grain size and morphology can be

controlled due to the reduction of the reaction rate [15, 24, 25]. Higher PVP concentrations lead to a lower Zn^{2+} concentration during solution based deposition. This results in a reduction in the reaction rate between Zn^{2+} ions and hydroxide ions. This process also helps decrease grain aggregation as the adsorption of PVP on ZnO crystal face reduces grain boundary interactions. It is also believed that PVP passivates the (10-10) plane of ZnO and facilitates crystal growth along the *c*-axis when its concentration is moderate. The higher the concentration, the more PVP adsorbs on to the (10-10) plane. In this case, ZnO rods grow easily on (0001) plane while growth on the (10-10) plane is suppressed. The suppression of growth along the lateral facets results in a reduction of the diameter of the rods and an increase in the rod aspect ratio. [25].

Apart from its uses during preparation to influence the material morphology however, PVP is also widely used as a capping agent of ZnO nanomaterials, where it passivates the surface adsorbed species and enhance the UV emission as mentioned earlier. For example, in ZnO quantum dots the visible emission has been suppressed and UV peak enhanced by surface passivation using PVP [3].

7.2.2 HF

Hydrogen fluoride, often in the aqueous form as hydrofluoric acid, is a source of F^-. It is unique in its ability to dissolve many metal and semimetal oxides. For post-growth treatment of ZnO nanostructures, a solution based F compound is preferable, which should also be reactive with ZnO. HF is a well-known acid which is very reactive with ZnO in aqueous solution. HF dissociates in aqueous solution in a similar fashion to other acids in the following manner –

$$HF + H_2O \leftrightarrow H_3O^+ + F^- \qquad \text{Eqn. 7.1}$$

When the concentration of HF approaches its maximum solubility, the acidity increases dramatically due to the following equilibrium -

$$2\ HF \rightarrow H^+ + FHF^- \qquad \text{Eqn. 7.2}$$

The FHF^- anion is stabilized by the very strong hydrogen–fluorine hydrogen bond.

As HF acid is a strong etching agent, only very diluted solutions of HF are used for passivation of ZnO in this work to avoid destruction of the nanostructured deposit. In HF solutions F^- is readily available, and this has been expected to be the passivation agent for ZnO nanostructures.

Interactions between the surface of ZnO and F^- have not been investigated extensively, however an XPS study of F^- interactions with ZnO nanocrystals has been previously reported [16]. This study suggests that F^- reacts with and passivates dangling surface bonds thus preventing subsequent adsorption of species from the ambient atmosphere. This results in an increase in the carrier mobility of the nanostructures. The use of HF acid as a passivation agent of ZnO has not been reported yet, probably due to the ease at which HF etches metal oxides, and its technical and handling difficulties in the laboratory.

7.3 Experiments

In this work PVP passivation has been studied mainly on ZnO nanostructure samples grown by chemical bath deposition (CBD) method in our group[*]. Initially our experiments were performed on VPT grown samples. As the optical quality of the VPT grown samples is very high, particularly at low temperatures, the FT-PL detector was easily saturated. In this situation it is very difficult to observe changes in the PL intensity before and after passivation, as any small changes in the optical alignment causes a significant signal variation for these samples. The optical alignment is usually done by varying the angle at which sample is placed within cryostat, the lens position and the aperture diameter to obtain the highest possible intensity from the sample. The optical quality of the PL emission for CBD grown samples is much poorer and the emission linewidths also larger compared to VPT grown samples. As the emission intensity of the CBD samples is a lot smaller than

[*] Chemical bath deposition (CBD) growth of ZnO nanostructures has been performed by Mr. Daragh Byrne in our group.

those of VPT grown samples, it is easier to acquire spectra using same instrumental setup (e.g. aperture, gain) before and after passivation, both for room and low temperature experiments. The passivation methods are also more effective for increasing the signal of CBD samples, which are poorer than VPT samples always.

In the CBD method first a thin seed layer (thin film) of ZnO was deposited by drop coating a solution of zinc acetate in ethanol on a Si/SiO_2 substrate. This process results in a thin film of zinc hydroxide which is subsequently decomposed at 350°C to yield a thin ZnO seed layer. ZnO nanorods were then deposited by a chemical bath method [26]. The seeded substrates were submerged in a 25 mM solution of zinc nitrate and hexamethylenetetramine and heated at 85-90°C for 30 minutes. During heating the hexamethylenetetramine slowly decomposes to yield hydroxide ions which react with the zinc ions to form zinc oxide which deposits on the seeded substrate to yield a *c*-axis aligned nanorod array. Some experiments were also performed on ZnO nanostructures grown by VPT on *a*-sapphire substrate. The growth process is exactly same as described in chapter 2 and 3. Briefly again, nanostructures have been grown using ZnO and graphite powder thoroughly mixed in 1:1 ratio as the zinc source. The mixed powders were placed in an alumina/multisil boat and the substrate was placed directly above the source powder. The growth temperature was $900^oC/950^oC$ and the growth duration was 60 minutes for all samples studied in this work.

A simple dipping method has been used for passivation. At the beginning of the work PVP K-60 solution (Sigma Aldrich) was used. As received it is diluted to 45% concentration by volume in H_2O and the average chain molecular weight is 160000. Several experiments have been performed initially with this solution both by diluting it to various degrees and using different times. We did not get any significant improvement in the PL signal with this PVP product, probably due to the solution's high viscosity, which restricts the diffusion of PVP molecules through the nanostructures and prevents the aggregation with the defects in crystal. The passivation was subsequently performed using PVP powder (Alfa Aesar) with an average molecular weight of 1,300,000. Different weight/volume solutions of PVP powder were prepared by dissolving the powder in de-ionized (DI) water in a beaker,

and stirring the mixer for 30 minutes using magnetic stirrer. Samples were then coated by dipping them into the PVP solution. Weight/volume solution is the mass of the solute in gm per 100 mL of the resulting solution.

For HF passivation experiments, HF acid of 48% concentration by weight in water (Sigma Aldrich) was diluted in DI water in a beaker. In the experiment with HF volume/volume solutions have been prepared, which can be defined as the volume of the solute in mL per 100 mL of the resulting solution. A range of different concentrations of HF in DI-water were prepared so as to ascertain whether HF etched ZnO or not. The study of HF passivation on ZnO nanostructures was started at the concentration at which HF does not significantly etch ZnO nanostructures. After the HF solution was prepared, ZnO nanostructured samples were dipped into the solution. For both passivation techniques, the samples were dried with a nitrogen stream once removed from the passivation solution.

Samples were characterized by a FT-PL spectrometer (Bomem Hartmann & Braun DA8 FT spectrometer) and EDX system with detection limits down to 0.1% concentration, attached to a SEM (Karl-Zeiss Evo series). The PL setup was identical for all the CBD grown samples. The spectral resolution for the FT-PL was 0.4 meV for all the spectra shown in this work. For the CBD grown samples, the number of co-added scan was 1000 at room temperature and 500 for scans at low temperature. For the VPT grown samples the number of co-added scan was 100 in all cases. The low temperature scans were performed at ~18K.

7.4 Results and discussion

7.4.1 PVP passivation

As mentioned in section 7.3, passivation has been studied mainly on CBD grown samples. The PL data shown in *Fig 7.2* have been taken both at room temperature and at low temperature for different concentrations of PVP solutions. As mentioned in the experimental section, initially a PVP K60 solution of molecular weight 160000 was used for passivation, but because no improvement was observed, a PVP powder of higher molecular weight (1300,000) was chosen.

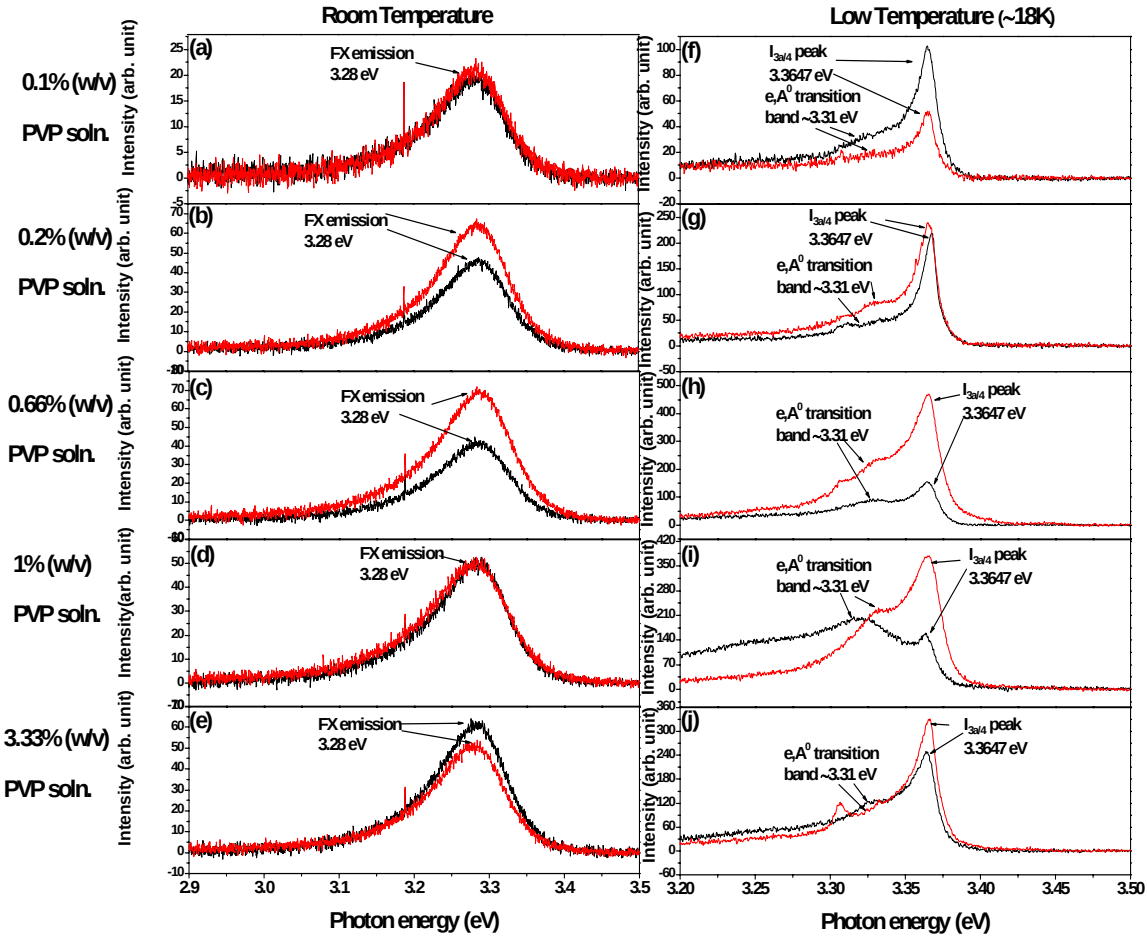

Fig 7.2: PL spectra of PVP passivated CBD grown samples on Si, (a)-(e) room temperature, (f)-(j) low temperature (~18K) PL for five w/v solutions of PVP for 30 minutes dipping. The black curve is the emission spectrum before passivation data while post passivation is shown in red.

PVP passivation has been studied using different concentrations and for different dipping times in the passivation solution. First a particular concentration with dipping time of 30 minutes where some favourable changes in the PL intensity were observed was chosen. This solution was then used as the basis for the time based experiments. The time durations used for dipping the sample in that concentration are 30 minutes, 2 hours and 24 hours. It is observed that there is no significant change in the PL signal for the longer passivation times compared to 30 minutes. Therefore the passivation time was reduced to 30 minutes for all subsequent experiments. In the next phase of the analysis, different concentration solutions of PVP were prepared and the corresponding variation in PL emission was examined for samples dipped in different concentration solutions for the optimised time of 30 minutes. In this chapter PL data is shown for samples dipped in five different concentration PVP solutions for 30 minutes.

Fig 7.2 (a)-(e) shows the room temperature spectra and *Fig 7.2 (f)-(j)* shows the low temperature spectra taken at ~18K for the range of different solutions. From the room temperature data we see that for 0.1% solution, after passivation the PL intensity of the FX peak at ~3.28 eV is almost the same as before passivation (*Fig 7.2 (a)*). The FX peak emission intensity increased for samples passivated in the 0.66% solution (*Fig 7.2 (c)*). FX intensity remains the same after passivation for the sample passivated in the 1% solution (*Fig 7.2 (d)*), and decreases for samples passivated in the 3.33% solution (*Fig 7.2 (e)*). In the low temperature spectra, it is observed that after passivation , the intensity of the bandedge emission (as lablelled here $I_{3a/4}$ peak according to Meyer et. al [27]) decreased for the lowest concentration solution i.e. 0.1% (*Fig 7.2 (f)*), then increased when the PVP concentration was increased to 0.2% and 0.66% (*Fig 7.2 (g)* and *(h)*, respectively). Considering the line broadening of the $I_{3a/4}$ peak (as labelled in *Fig 7.2*) and deviation from the literature value of the energy position of I_{3a} or I_4, we can also consider the possibility that this broad peak is the SX peak mentioned in chapter 6. Increasing the concentration further (1% and 3.33%) also resulted in an increase in the intensity but at a reduced percentage as compared to the 0.2% and 0.66% solutions (*Fig 7.2 (i)-(j)*, respectively). The broad peak due to stacking fault related (e,A^o) transition beside the $I_{3a/4}$ line at ~3.31 eV [28], was suppressed with respect to the $I_{3a/4}$ line after

passivation. This suppression is mostly visible for the sample passivated with 0.66% and 1% solution, where $I_{3a/4}$ intensity increased most relative to the 3.31 eV emission. The percentage of changes in intensity before and after passivation is listed in *Table 7.1*.

Table 7.1: Percentage of change in intensity (peak intensity) at different concentrations of PVP in room and low temperatures FT-PL after passivation with a passivation period of 30 minutes

Concentration of solutions weight/volume percentage	**Approximate change in FX peak intensity at room temperature compared to unpassivated sample (%) (standard error ±14.5)**	**Approximate change in $I_{3a/4}$ peak intensity at low temperature compared to unpassivated sample (%) (standard error ±19.51)**
0.1%	0	-50
0.2%	41	10
0.66%	64	200
1%	0	135
3.33%	-17.5	31

The '-' sign in *Table 7.1* indicates a decrease in the signal intensity after passivation. From *Table 7.1* we can see the numerical values of the increase and decrease in emission intensity for the different concentrations of PVP. The 0.66% solution can be regarded as the critical concentration, after which the intensity decreases with decreasing or increasing concentration. As the FX emission intensity decreases for 3.33% solutions and bandedge emission at low temperature decreases for 0.1% solutions, no further study on the PVP concentration was performed above 3.33% or below 0.1%. EDX analysis shows the presence of carbon (C), nitrogen (N), O, Zn and Si for all the samples. Carbon is detectable from the surrounding even if it has not been incorporated on the sample during passivation, and O is a component of ZnO, however the presence of N confirms the incorporation of the PVP onto the

samples. The atomic percentage of N for the five samples mentioned above (starting from lowest 0.1% to highest 3.33% concentration) are 0.12%, 0.19%, 1.38% and 7.62%, respectively.

The concentration of PVP is very important when it is used to control morphology and when it is used as a stabilizer or passivating agent. The growth control of ZnO nanorods with different concentrations has already been reported [25], where it has been observed that the density and length of the nanorods deposited increases with increasing PVP concentration, but beyond a certain concentration the density decreases with increasing concentration. It is known that water can be bound by PVP in aqueous solutions containing high PVP concentrations [29]. With very high concentrations of PVP in water, both the viscosity and bond strength of water in the liquid phase increases [30]. The viscosity of the solution greatly restricts the diffusion of PVP molecules through the nanostructures and prevents the aggregation with the defects in crystal. In this work, increasing the PVP concentration increases the number of PVP molecules available in the solution which in turn react with ZnO surface dangling or broken bonds. When the critical concentration (in this work 0.66% w/v) is exceeded water is bound by the PVP restricting the reaction of PVP with ZnO nanostructures.

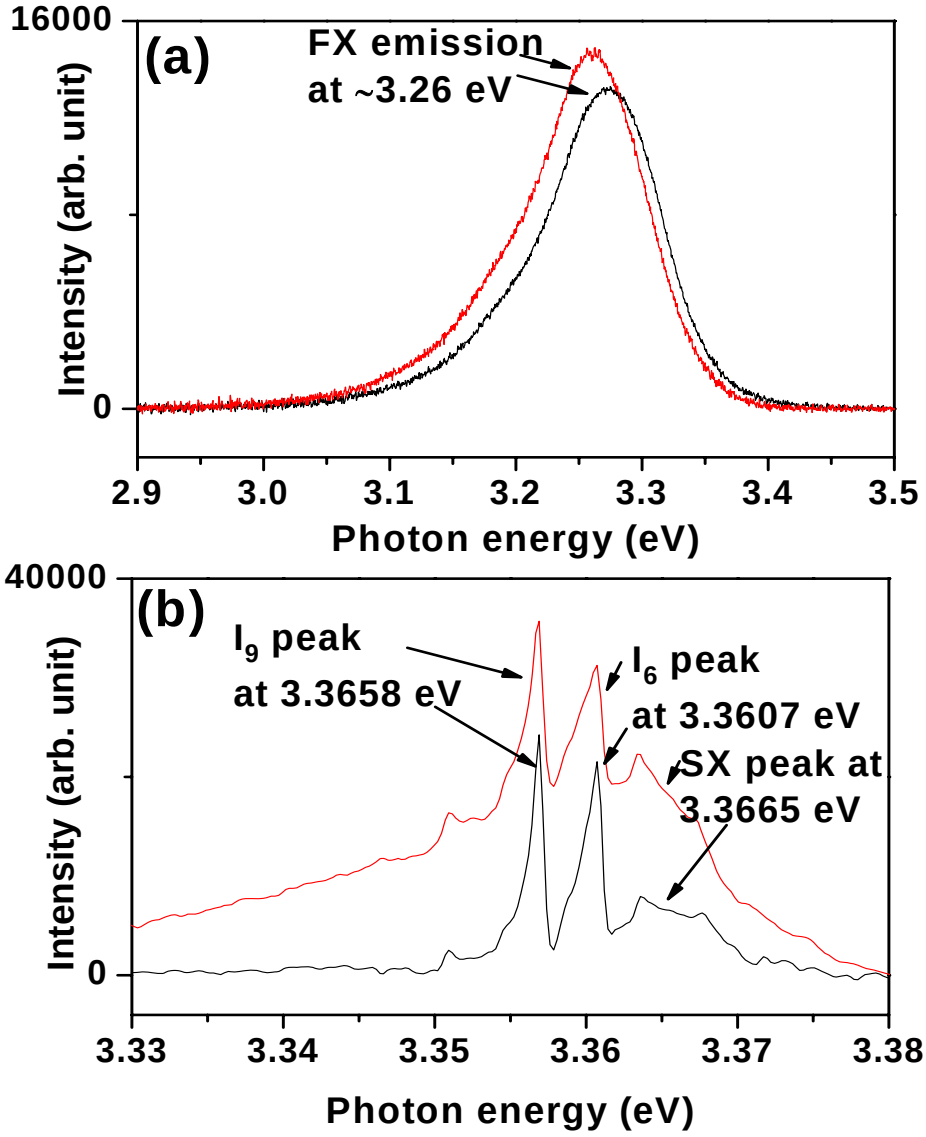

Fig 7.3: PL spectra of PVP passivated VPT grown samples on *a*-sapphire; (a) at room temperature, (b) at low temperature for 0.66% w/v solutions of PVP for 30 minutes dipping time. The black curve is presenting data before passivation and the red curve is presenting data after passivation.

PVP passivation was also performed on VPT grown samples using 0.66% PVP solution to see if any significant changes in intensity similar to those observed in CBD grown samples occurs. For the VPT grown sample at low temperature, the linewidths (I_6 linewidth ~2.5 meV and I_9 linewidth ~1 meV) of the PL peaks are very narrow compared to those of the CBD samples. The width of the spectral envelope

of the near bandedge emission for the CBD sample is ~156 meV – the individual lines are narrower but not resolved, but are still certainly much broader than the individual lines in the VPT sample. The peak intensities of the CBD samples are also smaller, at least an order of magnitude less, than those of the VPT grown samples. As previously mentioned, for VPT grown samples it is very difficult to compare the intensity before and after passivation due to the strong luminescence signal, especially at low temperature. The PL spectra shown in *Fig 7.3* are of ZnO nanorods grown on an *a*-sapphire substrate. The room temperature luminescence signal (FX peak intensity) increased ~11% (*Fig 7.3 (a)*) which is quite insignificant compared to the enhancement observed with the CBD grown sample. The low temperature intensity (peaks intensity) (*Fig 7.3 (b)*) also increased, but again not as significantly as the CBD sample, and no changes of spectral shape are seen.

7.4.2 HF passivation

To study passivation using HF solutions, the first stage of the investigation was to find an appropriate solution concentration where the ZnO nanostructures will not be strongly or completely etched (which can be observed visually or by SEM). The starting HF concentration for this work was 0.5% v/v and time was 10 minutes. The concentration was then decreased further until it could be observed that for 0.01% v/v solution of HF, the ZnO nanostructures were not completely etched. The presence of proper lineshapes in the PL spectrum further indicates that the nanostructures were not completely etched by HF. The HF passivation was studied further using more dilute solutions of HF. Different passivation time durations were also studied. The time durations examined were 10 minutes, 20 minutes and 30 minutes. It was found however that for etching times of 20 minutes or greater the nanostructure deposits were completely etched even with the 0.01% v/v solution, so 10 minutes etching times were chosen for all further HF passivations. In *Fig 7.4* PL spectra have been presented for three solutions of HF (indicated on the left side of the graphs) at both room and low temperatures (indicated at the top of the graphs), dipped for 10 minutes.

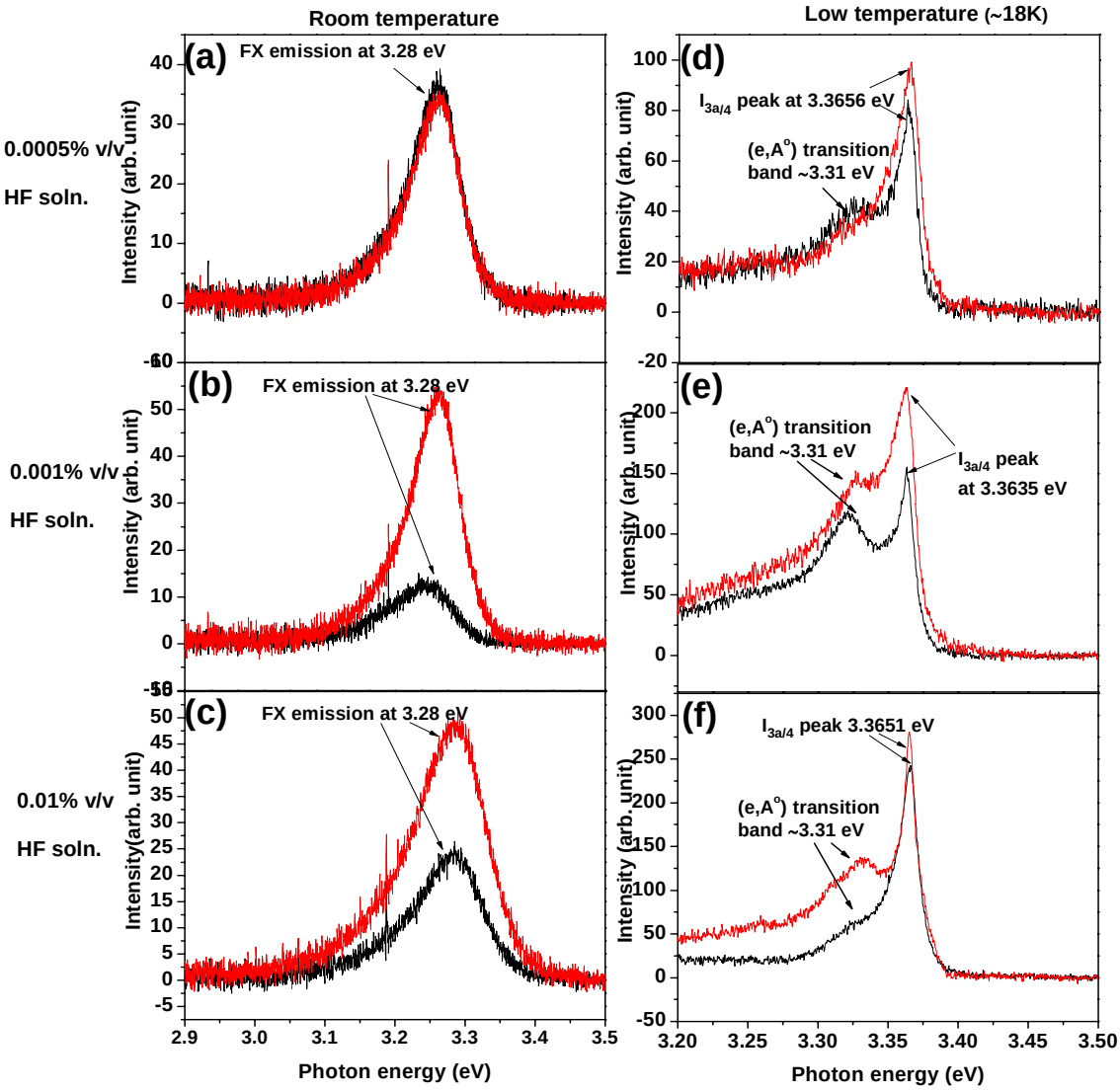

Fig 7.4: PL spectra of HF passivated CBD grown samples on Si; (a)-(c) at room temperatures, (d)-(e) at low temperatures for three different v/v solutions of HF. The emission spectrum prior to passivation is represented by the black curve while post passivation emission is represented by the red curve.

Table 7.2: Percentage change in the emission intensity (peak intensity) for different concentrations of HF used during passivation in room and low temperature FT-PL with a passivation period of 10 minutes

Concentration of solutions volume/volume percentage	**Approximate change in FX peak intensity at room temperature compared to unpassivated sample (%) (standard error ±66)**	**Approximate change in $I_{3a/4}$ peak intensity at low temperature compared to unpassivated sample (%) (standard error ±3.5)**
0.0005%	0	18
0.001%	315	41
0.01%	97	17

From the PL data at *Fig 7.3* and from *Table 7.2* we can see that the largest increase in PL intensity occurred after passivation using a 0.001% solution of HF (*Fig 7.3 (b)* and *(e)*). For the lower concentration of 0.0005% the FX emission at room temperature was unchanged (*Fig 7.3 (a)*) and the bandedge emission increased just 18% (*Fig 7.3 (d)*) after passivation. For higher concentrations (0.01%) both room and low temperature PL intensity increases (*Fig 7.3 (c)* and *(f)*) but much less than the increase observed using the 0.001% solution. Hence for HF passivation, of these three solutions, the 0.001% solution can be considered as the critical concentration. The EDX analysis for all three passivated CBD grown samples shows presence of F in trace amounts. The atomic percentage of F for the 0.005%, 0.001% and 0.01% solutions were 0.24%, 0.35% and 0.59%, respectively. This confirms the reaction of F^- with ZnO nanostructures.

The higher concentrations of HF solution increases the number of F^- ions in the solution, which in turn will increase the degree of reaction of F^- with ZnO. If this degree is higher it is expected F will passivate the broken ZnO bonds more effectively and will prevent adsorption of unwanted species, which will increase the luminescence by suppressing NR recombination. For our data the anticipated increase in luminescence was not observed for the highest concentration (0.01%) used for passivation. Visually, the ZnO nanostructures deposit showed no signs of etching, but from the FESEM images in *Fig 7.5* we can see that the structures were etched to some extent, especially at 0.01% v/v solution.

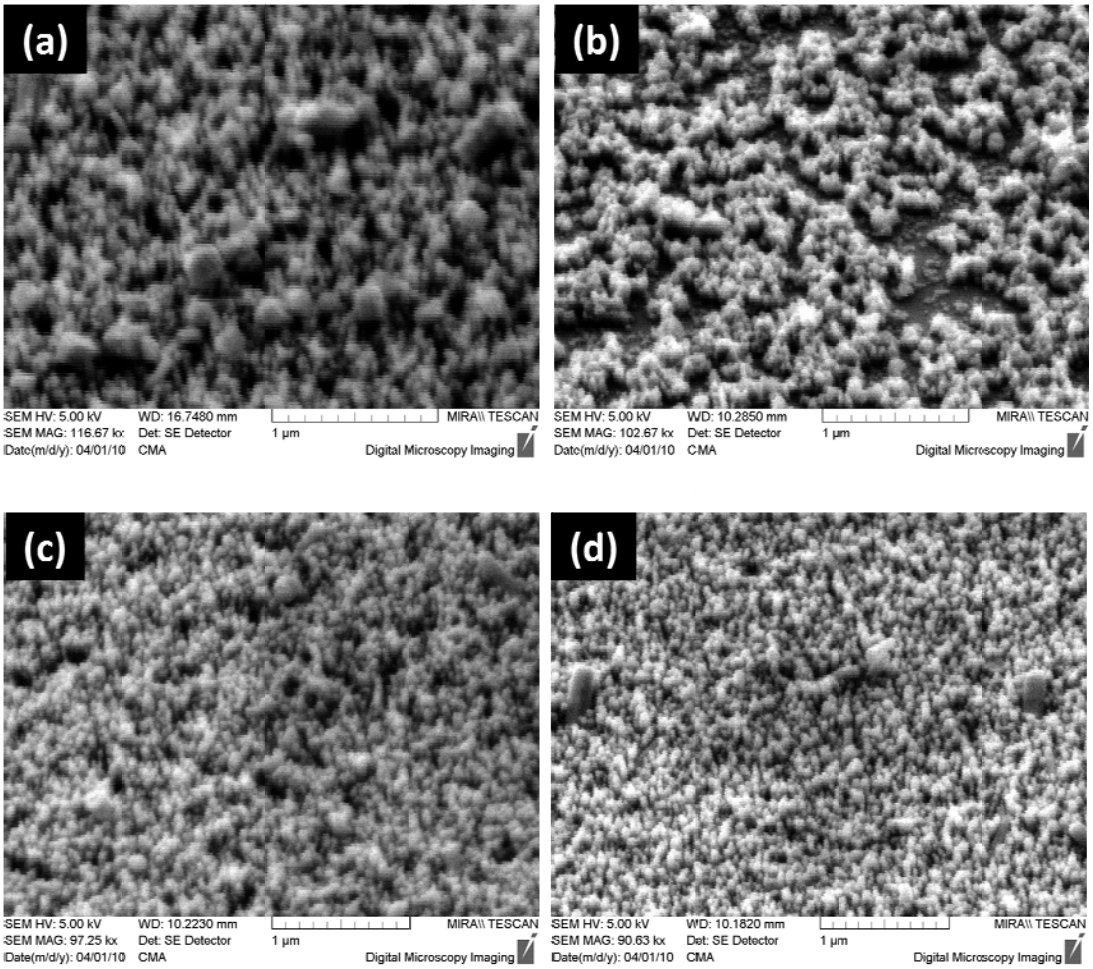

Fig 7.5: FESEM images CBD grown nanostructures; (a) Unpassivated, (b), (c) and (d) passivated by HF solutions of 0.01% v/v, 0.001% v/v, 0.0005% v/v, respectively for 10 minutes.

This etching was not significant enough so as to noticeably reduce the PL intensity and deteriorate the lineshape, however changes in the lineshapes of the peaks at low temperature were seen, specifically the broad peak due to the stacking fault-related (e,A^o) transition at ~3.32 eV increased compared to the band edge $I_{3a/4}$ emission (note that for the other two concentrations the 3.32 eV emission was suppressed). This observation is consistent with the observation that a very small amount of etching occurred and the band edge peak intensity has not increased more than seen for the 0.001% solution. The FESEM images shown in *Fig 7.5 (b)* and *(c)* of passivated nanostructures using 0.001% and 0.0005% concentration, respectively show no sign of etching.

The HF passivation on the VPT grown sample has been performed using 0.001% HF solution, as we found significant improvement in the PL intensity for that solution compared to other concentrations for the CBD samples. The room temperature PL signal in *Fig 7.6 (a)* increased by a factor of almost 3 after passivation, in agreement with the CBD sample data. The low temperature spectra in *Fig 7.6 (b)* do not show any increment in intensity.

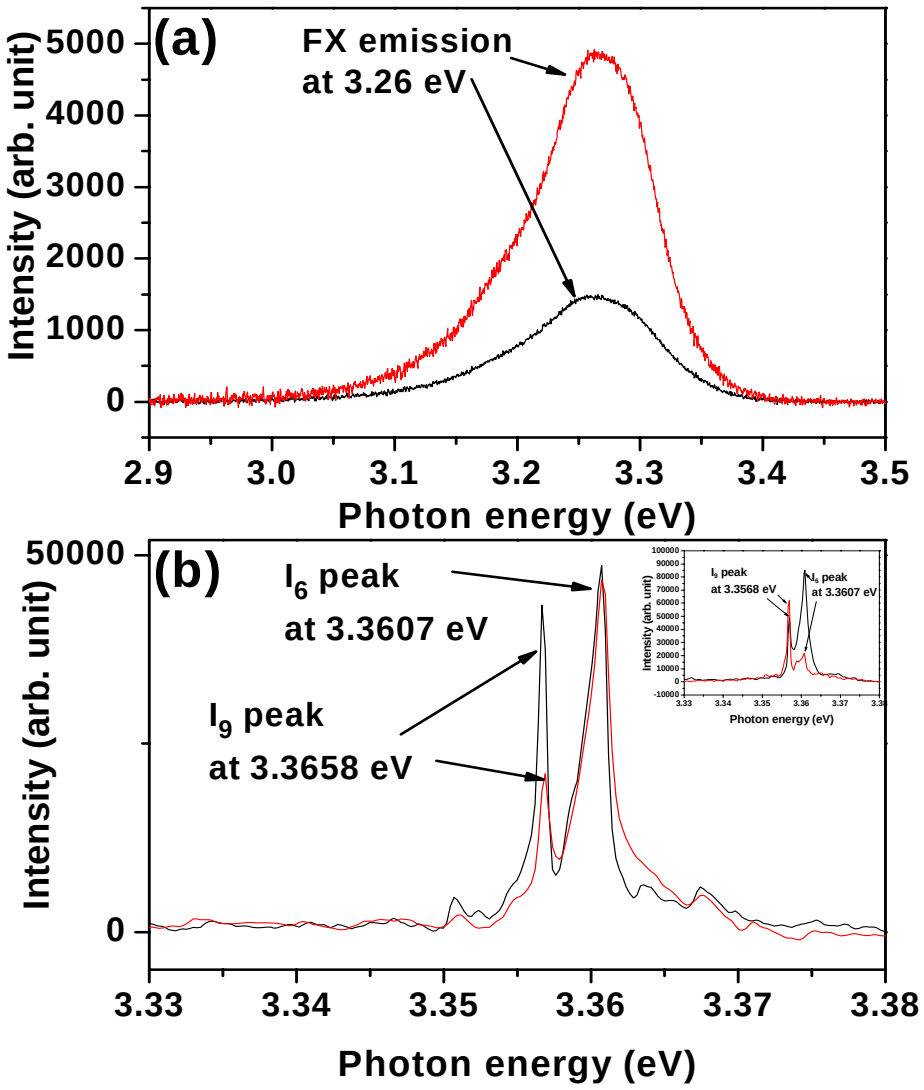

Fig 7.6: PL spectra of HF passivated VPT grown samples on *a*-sapphire; (a) at room temperature, (b) at low temperature for 0.001% v/v solutions of HF. Inset of (b) shows low temperature PL spectra of another 0.001% HF solution passivated sample. The black curve is data before passivation and the red curve is data after passivation.

The notable point in the low temperature spectra is the decrease in the I_9 peak as compared to the I_6 peak instead of a drop or increase in overall intensity. To check whether or not only the I_9 peak is affected by the HF reaction, another sample was studied (spectra have shown in inset of *Fig 7.6 (b)*) using the same solution, where the I_6 peak was decreased as compared to I_9 after passivation. In this sample, shown in the inset, the I_9 peak shows little change in intensity after passivation. The linewidth of the peaks after passivation is not affected which indicates no significant etching effect.

From the PL data shown above for both the PVP and HF passivated samples, it can be concluded that for PVP and HF passivation routes the use of 0.66% and 0.001% solutions, respectively, can be considered as the optimal solutions (from the range of concentrations we have studied) to gain improvement in the luminescence at room and low temperatures (though mostly notably at room temperatures). Among these two passivating agents, HF shows significant improvement in room temperature PL intensity, which is usually more effectively suppressed by NR recombination [1]. In case of PVP passivation the low temperature intensity improves significantly compared to the room temperature intensity for all concentrations. It can be concluded that HF is a more effective passivating agent to increase room temperature PL signal and PVP is more effective for low temperature signal improvement. This might be tentatively explained as follows; HF may be more effective to react with and passivate deep defects such as broken or dangling bonds within the nanostructures, which create the deep mid- bandgap levels at the surface and sub-surface regions and act as deep NR recombination centres, especially at room temperature. This is due to the action of the small and isolated F^- ion which may be able to diffuse into ZnO surface & sub-surface regions at room temperature. The much larger PVP molecules mainly act as a surface cap and may remove shallow surface traps more effectively leaving behind the deeper surface traps or sub-surface defects. Further dual passivation studies using both the passivating agents would be an interesting line of enquiry.

7.5 Conclusion

A simple dipping method for post-growth passivation has been studied using solutions of PVP and HF as passivating agents. From the experiments performed using these two passivating agents, we see certain selective concentrations and time durations which are optimal for passivation resulting in the largest variations in PL intensity. From the concentrations and times used in this work it can be concluded that dipping ZnO nanostructure samples in 0.66% w/v PVP solutions for 30 minutes and in 0.001% v/v HF solutions for 10 minutes results in a significant improvement in the PL intensity. HF passivation has more effect in improving room temperature PL intensity and PVP has greater effect on low temperature PL intensity. This simple passivation method is a useful finding, since it is potentially applicable to any type of ZnO nanomaterial. Because it can be performed after growth, one may concentrate on the passivation process independently without concerns about altering the growth morphology. Further post-growth passivation studies on same sample using both passivating agents and on other types of ZnO nanostructures separately using these agents will be interesting to elucidate the exact nature of the passivation mechanisms for PVP and HF, and why these two agents affect room temperature and low temperature PL emission intensities differently.

7.6 References

[1] J. Grabowska, A. Meaney, K. K. Nanda, J. P. Mosnier, M. O. Henry, J. R. Duclere, and E. McGlynn, Physical Review B 71 (2005) 115439.

[2] H. Y. Xu, Y. C. Liu, R. Mu, C. L. Shao, Y. M. Lu, D. Z. Shen, and X. W. Fan, Applied Physics Letters 86 (2005) 123107.

[3] C. L. Yang, J. N. Wang, W. K. Ge, L. Guo, S. H. Yang, and D. Z. Shen, Journal of Applied Physics 90 (2001) 4489.

[4] X. H. Li, C. L. Shao, Y. C. Liu, X. Y. Chu, C. H. Wang, and B. X. Zhang, Journal of Chemical Physics 129 (2008) 114708.

[5] L. Guo, S. Yang, C. Yang, P. Yu, J. Wang, W. Ge, and G. K. L. Wong, Applied Physics Letters 76 (2000) 2901.

[6] W. Feng, H. C. Tao, Y. Liu, and Y. C. Liu, Journal of Materials Science & Technology 22 (2006) 230.

[7] Z. H. Guo, S. Y. Wei, B. Shedd, R. Scaffaro, T. Pereira, and H. T. Hahn, Journal of Materials Chemistry 17 (2007) 806.

[8] T. Strachowski, E. Grzanka, W. Lojkowski, A. Presz, M. Godlewski, S. Yatsunenko, H. Matysiak, R. R. Piticescu, and C. J. Monty, Journal of Applied Physics 102 (2007) 9.

[9] Y. Harada, H. Kondo, N. Ichimura, and S. Hashimoto, Journal of Luminescence 87-89 (2000) 405.

[10] J. Sanghyun, L. Kangho, Y. Myung-Han, F. Antonio, J. M. Tobin, and B. J. David, Nanotechnology 18 (2007) 155201.

[11] J.-H. Choi, D.-Y. Khang, and J.-M. Myoung, Solid State Communications 148 (2008) 126.

[12] F. Bai, P. He, Z. Jia, X. Huang, and Y. He, Materials Letters 59 (2005) 1687.

[13] Y. F. Huang, H. N. Xiao, and S. G. Chen, in High-Performance Ceramics V, Pts 1 and 2, Vol. 368-372 (W. Pan and J. H. Gong, eds.), Trans Tech Publications Ltd, Stafa-Zurich, 2008, p. 329.

[14] J. Zhang, H. Liu, Z. Wang, N. Ming, Z. Li, and A. S. Biris, Advanced Functional Materials 17 (2007) 3897.

[15] A. I. Inamdar, S. H. Mujawar, V. Ganesan, and P. S. Patil, Nanotechnology 19 (2008) 325706.

[16] H. Y. Xu, Y. C. Liu, J. G. Ma, Y. M. Luo, Y. M. Lu, D. Z. Shen, J. Y. Zhang, X. W. Fan, and R. Mu, Journal of Physics: Condensed Matter 16 (2004) 5143.

[17] X. Zhou, D. Jiang, F. Lin, X. Ma, and W. Shi, Physica B: Condensed Matter 403 (2008) 115.

[18] B. V. Robinson, F. M. Sullivan, J. F. Borzelleca, and D. L. Schwartz, *PVP A critical Review of the Kinetics and Toxicology of Polyvinylpyrrolidone* Lewis Publishers, Inc. Michigan, 1990.

[19] V. Buhler, *Polyvinylpyrrolidone Excipients for Pharmaceuticals*, Springer-Verlag, Germany, 2005.

[20] V. Buhler, *Polyvinylpyrrolidone Excipients for Pharmaceuticals*, Springer-Verlag, Germany, 2005.

[21] S. Jason and B. T. Jan, Journal of Applied Polymer Science 90 (2003) 1153.

[22] G. Li, Y. Luo, and H. Tan, Journal of Solid State Chemistry 178 (2005) 1038.

[23] C. Wang, E. Wang, E. Shen, L. Gao, Z. Kang, C. Tian, C. Zhang, and Y. Lan, Materials Research Bulletin 41 (2006) 2298.

[24] Z. Chen, Y. Tang, L. Zhang, and L. Luo, Electrochimica Acta 51 (2006) 5870.

[25] S. F. Wei, J. S. Lian, and Q. Jiang, Applied Surface Science 255 (2009) 6978.

[26] L. E. Greene, M. Law, D. H. Tan, M. Montano, J. Goldberger, G. Somorjai, and P. Yang, Nano Letters 5 (2005) 1231.

[27] B. K. Meyer, H. Alves, D. M. Hofmann, W. Kriegseis, D. Forster, F. Bertram, J. Christen, A. Hoffmann, M. Straßburg, M. Dworzak, U. Haboeck, and A. V. Rodina, Physica Status Solidi (b) 241 (2004) 231.

[28] M. Schirra, R. Schneider, A. Reiser, G. M. Prinz, M. Feneberg, J. Biskupek, U. Kaiser, C. E. Krill, K. Thonke, and R. Sauer, Physical Review B (Condensed Matter and Materials Physics) 77 (2008) 125215.

[29] Z. Jianhui, L. Huaiyong, W. Zhenlin, and M. Naiben, Chemistry - A European Journal 14 (2008) 4374.

[30] Y. D. Cui, G. B. Yi, and L. W. Liao, *The Synthesis and Applications of Polyvinylpyrrolidone*, Science Publishing Company, Beijing, 2001.

Chapter 8

Conclusions and future works

8.1 Summary and conclusions of the thesis

The thesis combines five distinct but related experimental studies on ZnO nanostructure growth and properties using a variety of experimental techniques. The important works of the thesis are discussed briefly below and the conclusions from these works are restated. Finally, some comments on potentially interesting and useful further studies are given.

To summarise the experiments performed in early part (chapter 3) of this thesis which formed a platform for later work of these nanostructures, the VPT growth method of ZnO nanostructures has been studied in detail to obtain various reproducible growth morphologies. Optical spectroscopy, electron microscopy and X-ray diffraction techniques have been used to study the nanostructure morphologies, crystalline and optical properties and surface behaviour of these nanostructures. Although survey studies of nanostructure properties have been investigated for many types of nanostructures, the most interesting and useful morphologies were found to be the nanorod and nanorod/ nanowall structures. The conditions necessary to grow well-aligned nanorod and nanorod/nanowall structures using the VPT method have been established.

In chapter 4, different carbon powders have been used in the growth system as a source powder along with ZnO powder to investigate the growth behaviour. Carbon acts as a catalyst in the VPT growth which triggers the reduction (CTR) of ZnO at comparatively low temperatures. Non-graphitic carbon like carbon black, active carbon, carbon nanotubes allow nanostructures to grow at much lower temperatures than graphite. In this thesis, carbon black and active carbon have been used to investigate the growth morphologies at much lower temperatures than using graphite powders, because a reduction of the temperature in VPT growth might be a useful factor in reducing the cost for mass production of ZnO nanostructures. ZnO nanostructures grown using non-graphitic carbon powder show different deposit yields and morphologies compared to graphite carbon. These carbons enable lower temperature growth than graphite. This fact cannot be explained by surface area, thermodynamics and purity differences alone. In our experiments the different surface activity of these carbons found to be responsible for enabling lower temperature growth. However the negative aspect of these results was the poor reproducibility in the deposit yields and morphologies with non-graphitic carbons, due to the inherent variability of surface activity and purity in available non-graphitic carbons.

Among the various research areas going on in the area of ZnO and ZnO nanostructures properties, the doping of ZnO is a crucial issue. To utilise nanostructures properly in bipolar and unipolar devices the achievement of desirable levels of carrier concentration and homogeneity of dopants are some of the most important steps. As-grown ZnO shows *n*-type conductivity and in low temperature PL emission, we usually find Al and In related DBE lines (at 3.3608 eV and 3.3568 eV, respectively) and a broad peak around 3.367 eV known as SX peak. In chapter 5, low temperature CL study has been performed on ZnO nanostructures grown on Si and sapphire to investigate the spatial distribution of these peaks, because Al and In are well-known and often used *n*-type dopants of ZnO. The Al-related DBE emission shows significant inhomogeneity in the CL emission of the nanostructures grown on Si, where we get unaligned nanostructures with nanosheets, nanorods, nanowalls. These inhomogeneities have been observed only at, but not at all, locations in nanorods and nanosheets where different nanostructures cross or coalesce. This

suggests Al aggregation occurs in regions of localized crystal disruption in the samples, such as grain boundaries, since no evidence for strain-induced lineshifts is observed in the CL emission.

Some significant experiments have been done on the SX peak as well which are reported in chapter 6. The SX peak has been studied thoroughly by PL to investigate its possible microscopic origin. Plasma treatment, UV light illumination in high vacuum have been performed which are established surface treatment method to desorb surface O. From these studies we conclude that O is not the species responsible for the SX peak in ZnO PL. Electrical voltage application in high vacuum, air and He gas show significant changes in the peak intensity in the different gas atmospheres, which suggests a relationship with adsorbed surface species. Additionally with the help of TEM data of nanorod/nanowall samples and XPS data of UV illuminated (in high vacuum) samples it is concluded that SX peak is due to an exciton bound to a strongly chemisorbed surface species, probably at extended defects in ZnO nanostructures. The chemisorbed surface species is tentatively suggested to be OH-related.

Finally, in chapter 7 post-growth passivation methods have been investigated to improve the luminescence emission intensity of ZnO nanostructures. ZnO nanostructures grown by the CBD method have been used mostly because their poorer optical quality, compared to VPT grown samples, makes it easier to notice small changes in the luminescence intensity. PVP and HF solutions have been used as the passivating agent, and samples have been dipped in the solutions of these two compounds. Two solutions of PVP and HF have been selected as the most effective passivation recipes from different solution concentrations studied in the work, where both CBD and VPT grown samples show significant improvement in the PL intensity.

8.2 Future works

There are several outstanding issues, which could not be fully concluded during the period of the work performed leading to this thesis. These issues may usefully form the basis of work to be carried out in the future and are listed below-

- In the growth study of ZnO nanostructures with non-graphitic carbons, the reason behind the unaligned nanostructure growth on lattice matched *a*-sapphire substrates was not satisfactorily resolved. It would be interesting to see the growth on aligned ZnO buffer layers on various substrates or on substrates which already have shorter aligned nanorods there on, since we get aligned nanorod growth using buffer layer on lattice mismatched Si substrate. Also, a detailed study on the reason behind the large number of crystal defects seen by TEM in the non-graphitic carbon grown samples is necessary, and may ultimately be related to the unaligned growth phenomenon.
- In the dopant distribution study, it would be interesting to see the distribution of the *n*-type dopants when the dopant concentration is much higher than we used because it was difficult to incorporate larger amounts of Al and In in our VPT system and large concentration may amplify the effects of clustering. Also further studies will be required to probe the microscopic details of the structural defects responsible for the Al aggregation and correlate them with the CL emission distributions.
- In the study of the microscopic origin of SX PL peak further detail surface treatment studies are necessary to confirm the exact origin of the SX peak, especially which will affect the surface adsorbed OH species.
- In the passivation work, it would be useful to try dual passivation approaches using PVP followed by HF or *vice versa*. It has been observed that HF is more effective in increasing room temperature PL intensity and PVP is more effective in increasing low temperature PL intensity, which hints that dual passivation approaches might be more productive in improving PL emission intensity over a broader temperature range.

Finally, the thesis can be concluded with the hope of ZnO nanostructure commercialisation in near future. Apart from the problem with the *p*-type doping, ZnO nanostructures have great potential in the unipolar devices like field emission devices and in sensors applications. Hence it is desirable to see some of these devices in market in next 5-10 years, especially in the field of sensor applications nanostructured ZnO already has shown promises.